



THE UNIVERSITY *of* EDINBURGH

This thesis has been submitted in fulfilment of the requirements for a postgraduate degree (e.g. PhD, MPhil, DClinPsychol) at the University of Edinburgh. Please note the following terms and conditions of use:

- This work is protected by copyright and other intellectual property rights, which are retained by the thesis author, unless otherwise stated.
- A copy can be downloaded for personal non-commercial research or study, without prior permission or charge.
- This thesis cannot be reproduced or quoted extensively from without first obtaining permission in writing from the author.
- The content must not be changed in any way or sold commercially in any format or medium without the formal permission of the author.
- When referring to this work, full bibliographic details including the author, title, awarding institution and date of the thesis must be given.

Dielectrophoretic Investigations of Internal Cell Properties

by

Colin Chung



Declaration

I have read and understood The University of Edinburgh guidelines on Plagiarism and declare that this written dissertation is all my own work, except where I indicate otherwise by proper use of quotes and references. No part of this thesis has been submitted for any other degree or professional qualification.

Signed : _____ (Candidate)

Date : _____

Lay Summary

Dielectrophoresis (DEP) refers to a phenomenon where uncharged particles subjected to an electric field experience a force. This force requires an electric field whose strength varies across space, and a particle which can be polarised. DEP has been studied in a variety of contexts, from the separation of mineral ores to the precise alignment of carbon nanotubes; however, the greatest effort has been directed towards unmet needs in the life sciences. Biological cells are polarisable particles with distinct electrical properties which allow for their characterisation and selective manipulation by DEP.

By alternating the electric field at different frequencies the DEP force becomes dependent upon different aspects of a cell's structure. At two characteristic frequencies this force undergoes a change of direction between attraction to, and repulsion from, regions of high electric field strength. The first frequency occurs in the 1 kHz to 1 MHz range and has been extensively researched, its value being a function of both the cell membrane's electrical properties and physical geometry. In the 10 MHz to 1 GHz range a second characteristic frequency is expected, whose value is thought to depend upon the electrical properties of the cell interior. Our knowledge of how cells behave at these higher frequencies is limited and provided the motivation for this work.

The electrical theory used to study DEP is examined in terms of the aforementioned second characteristic frequency, referred to as f_{x02} . A device is designed and built to operate at frequencies of up to 300 MHz, providing observations of f_{x02} in mammalian cells which are consistent with theory. The value of f_{x02} appears to be unstable, gradually decreasing in time as a function of temperature. It is also found that this value is correlated to the concentration of potassium in cells, a relationship which is explored by forcing water into the cells. Finally, the health of a cell culture is found to directly influence f_{x02} , a finding which suggests its analysis may be of practical benefit.

Abstract

Dielectrophoresis (DEP) is a term which describes the motion of polarisable particles induced by a non-uniform electric field. It has been the subject of research into a variety of fields including nanoassembly, particle filtration and biomedicine. The application of DEP to the latter has gained significant interest in recent years, driven by the development of microfluidic “Lab-on-a-chip” devices designed to perform sophisticated biochemical processes. It provides the ability to characterise and selectively manipulate cells based on their distinct dielectric properties in a manner which is non-invasive and label free, by using electrodes which can be readily integrated with microfluidic channels.

Under appropriate conditions a biological cell will experience a DEP force directing it either towards or away from concentrations in the electric field. At a so-called “crossover frequency” the cell is effectively invisible to the field resulting in no DEP force, a response typically observed in the 1 kHz to 1 MHz range. Its value is a function of cell membrane dielectric properties and has been the subject of research directed at devices capable of using it to both characterise and sort cells.

The aim of this work was to investigate the behaviour of a higher frequency crossover referred to as f_{x02} , predicted to occur in the 1 MHz to 1 GHz range. At these frequencies the electric field is expected to penetrate the cell membrane and behave as a function of intracellular dielectric properties. Standard lithography techniques have been used to fabricate electrodes carefully designed to operate at these frequencies. The existence of f_{x02} was then confirmed in murine myeloma cells, in good agreement with dielectric models derived from impedance spectroscopy. A temperature dependent decrease in its value was observed with respect to the time that cells were suspended in a DEP solution. This decrease is consistent with previous studies which indicated an efflux of intracellular ions under similar conditions.

An analytical derivation of f_{x02} demonstrates its direct proportionality to intracellular conductivity. Direct control of the crossover was achieved by using osmotic stress to dilute the intracellular compartment and thereby alter its conductivity. By using a fluorophore which selectively binds to potassium, a strong relationship has been demonstrated between the value of f_{x02} and the concentration of intracellular potassium. Measurements of f_{x02} for an unfed culture demonstrated a correlation with viability and subtle shifts in its distribution were caused by the early stages of chemically induced apoptosis.

Acknowledgements

I would like to thank Professor Ronald Pethig for introducing me to the field of dielectrophoresis, for providing his enthusiastic guidance and also his countless entertaining stories.

A special thank you to Dr Anoop Menachery and Dr Srinivas Velugotla, for guiding me in my first dielectrophoretic steps and for encouraging me throughout. I would also like to thank Dr Stewart Smith for his support and supervision throughout my time here.

Thank you to Dr Martin Waterfall for sharing his extensive knowledge, providing immense practical assistance and entertaining the ever changing bioelectronic thoughts of an engineer. Thanks must also go to Dr David Wright for his support with the culture of cells which literally kept my research alive. For their invaluable insights and guidance with cell biology I must thank both Dr Steve Pells and Dr Vlastimil Srsen.

Thank you to my family and to all my friends for being here throughout this, a special group of people whose support in so many of Edinburgh's pubs has meant the world to me.

Last, but not least, I would like to thank my wife Kathleen – I simply could not have done this without you.

Glossary

Apoptosis

Programmed cell death which results in the orderly destruction of a cell. Apoptosis is necessary in ensuring normal cell turnover, the development of embryos and the destruction of cells which may present a health risk.

B Cell

One of three lymphocyte sub- types, named after their source of production in the bone marrow. B cell's are specialised by their ability to bind to specific antigens - foreign substances which can include bacteria or viruses.

Colloid

A substance in which insoluble particles of one matter phase, typically of micron scale and below, are dispersed in a medium of another. Examples of this include solid foams such as styrofoam, liquid aerosols such as fog and sols such as human blood.

Conductivity

A measure of how easily electric current can flow in a material, defined in units of siemens per metre (S/m)

DEP (Dielectrophoresis)

The movement of polarisable particles which are subjected to a non-uniform electric field.

Dielectric

Materials which become polarised in an electric field with zero or low electrical conductivity. Bound charges in the dielectric are transiently displaced by an alternating electric field.

Dipole

An object containing two opposing poles that, at large distances, is characterised by a vector quantity known as the dipole moment.

DMSO (Dimethyl Sulfoxide)

A widely used solvent in molecular biology which is water-miscible.

Electrokinetic

Techniques used to induce motion in particles by the application of an electric field.

Erythrocyte

Red blood cells which are circulated around the human body and that of most vertebrate animals. Erythrocytes provide a means of delivering oxygen to tissues via a circulatory system.

Etoposide

Also known as VP-16, etoposide is a chemotherapy drug which is used to treat a range of cancers by inducing apoptosis.

FACS (Fluorescence-Activated Cell Sorting)

A method of sorting cells based upon the light scattering and fluorescent properties of cells.

Fibroblast

Cells responsible for forming most of the connective structural framework in animal tissues.

Fluorophore

A fluorescent compound that absorbs light at one wavelength and re-emits it at a longer one. Fluorophores are often used to stain cell structures or as a probe for specific ions.

Genistein

A chemical found in soy beans which has been studied as a potential anticancer drug. Genistein is known to affect the progression of cancer by several mechanisms including the induction of apoptosis and arrest of the cell cycle.

Haemocytometer

A device used to count cells consisting of an indented thick glass slide and a thinner counterpart which are sealed together. The indent is filled with cell solution and a grid used to perform a count for a set volume of fluid.

Hybridoma

Cell lines which are created by fusing plasma cells that produce a desired antibody with myeloma cells selected for their ability to grow and absence of antibody production. The resulting line can then be used to mass produce the specific antibody.

Hypoxic

A condition in which cells are deprived of oxygen.

IDE (Interdigitated Electrode)

Comb-like electrode structures often used in thin-films material research and electrochemical analysis.

Intracellular

Referring to the contents of a cell, it's cytoplasm, nucleus and organelles.

Lossy

Dielectric materials which also dissipate energy, typically as heat, are described as lossy. These losses are generally a combination of both the material conductivity and a frequency dependent component of the permittivity.

Lymphocyte

One of five white blood cell types which comprise the immune system of a body. Three subtypes of lymphocyte exist, known as B (Bone marrow), T (Thymus) and NK (Natural Killer).

Monocyte

One of five white blood cell types which comprise the immune system of a body. Monocytes can differentiate into macrophages which ingest both neutrophils and dead cell debris.

Murine

Of or relating to mice and associated rodents.

Myeloma

A cancer of plasma cells which are normally responsible for the controlled production of infection fighting antibodies. Genetic damage results in cells which are capable of evading senescence, allowing them to grow indefinitely.

Neutrophil

One of five white blood cell types which comprise the immune system of a body. Neutrophils provide a rapid immune response, ingesting foreign material by phagocytosis.

PBFI (Potassium-Binding Benzofuran Isophthalate)

Fluorescent dye which selectively binds to potassium ions, often used in the AM (acetoxymethyl) ester form which allows the molecule to pass through cell membranes.

PBS (Phosphate Buffered Saline)

A buffer which is commonly used to wash and handle cells in biological research.

Permittivity

A measure of how easily a material is polarised by an electric field, defined in units of farads per metre (F/m)

Plasma Cell

A type of B cell responsible for the production of antibodies, proteins which bind to foreign antigens such as bacteria and viruses. These targets are either neutralised directly or tagged for immune attack. Plasma cells are normally short lived, for a specific immune response.

Pluronic F-127

A dispersal agent used with the AM esters of dyes, such as PBFI-AM, to enhance their solubility in water and facilitate the loading of cells in aqueous solutions.

Propidium Iodide

A fluorescent dye which is impermeant to viable cells with intact membranes.

RPMI-1640

A medium developed for the culture of leukemic cells.

SPICE

An industry standard analogue electrical circuit simulator.

Trypan Blue

Often used during cell counts to determine viability, trypan blue is a stain which is excluded by intact cells.

TWD (Travelling Wave Dielectrophoresis)

The movement of polarisable particles which are subjected to a travelling electric field.

ROT (Electrorotation)

The rotation of polarisable particles which are subjected to a rotating electric field.

RVD (Regulatory Volume Decrease)

A decrease in cell volume which occurs in response to hypotonically induced swelling, returning the cell towards its isotonic volume.

Senescence

In the context of cells, senescence refers to cells which cease to divide after a number of previous divisions.

Staurosporine

An anti-fungal agent which is also known to induce apoptosis in a wide variety of cell lines.

Contents

Declaration		i
Lay Summary		ii
Abstract		iii
Acknowledgements		iv
Glossary		v
Table of Contents		viii
Chapter One	Bio-dielectrics	1
Introduction		1
Impedance Spectroscopy		2
AC Electrokinetics		2
Thesis Outline		8
References		12
Chapter Two	Technical Theory	16
Introduction		16
The Dipole		16
The Lossless Dielectric Sphere		20
Conductive Losses		22
The Single-Shelled Sphere		26
Electrorotation		33
Conclusion		35
References		37
Chapter Three	Device Requirements, Design & Fabrication	39
Introduction		39
The Multi-Shelled Spherical Model of a Cell		39
Interdigitated Electrode Modelling		42
Variation in Conductivity		47
Variation in Mark-Space Ratio		48
Variation in Array Size		49
Levitation		50
Device Design		54
Conclusion		57
References		58

Chapter Four	Measuring the Second Crossover Frequency	59
	Introduction	59
	Method	59
	Initial Results	61
	Instability	63
	Osmolality	65
	Phosphate Buffered Saline	66
	Temperature	68
	Salts	72
	Flow Cytometry	74
	Conclusion	78
	References	80
Chapter Five	Controlling the Second Crossover Frequency	81
	Introduction	81
	An Analytical Derivation of f_{xo2}	81
	Validating the Behaviour of f_{xo2}	87
	Method	87
	Cell Volume	89
	First Crossover and Membrane Capacitance	91
	Second Crossover	92
	Intracellular Potassium	94
	Conclusion	96
	References	98
Chapter Six	Cell Death and the Second Crossover Frequency	100
	Introduction	100
	Cell Growth and Death	100
	Apoptosis in an Unfed Culture	102
	Apoptosis Induced by Etoposide	110
	Conclusion	116
	References	118
Chapter Seven	Methods	120
	Electrode Fabrication	120
	Measurement of Linewidth and Sheet Resistance	122
	Preparation of DE P Solutions	125
	Cell Suspension	127
	DEP Experiment	128
	Measurement of Cell Size	131
	References	132

Chapter Eight	Conclusions & Future Work	134
	Introduction	134
	Summary of Thesis and Results	134
	Future Work	138
	Conclusion	139
	References	140
Appendix	Publications	141

Chapter One

Bio-dielectrics

Introduction

In recent years the idea of microsystems which are capable of performing chemical and biological analysis have gained significant interest¹. Biomedical applications represent one of the most interesting areas where microsystems are being exploited; where microfluidic devices incorporate novel approaches to identify and manipulate bio-particles such as cells based on a desired parameter. These microfluidic devices have the potential to transform healthcare by allowing personnel to perform diagnostics which may otherwise require a clinical laboratory, on small samples and at a low cost¹. The detection of early stage cancer is one example of an area where significant advances could be made in hospitals, a process which currently requires personnel trained in both the usage and interpretation of specialist techniques outside of the clinic².

It is the developing world, however, which may provide the greatest demand based on the detection of infectious diseases such as tuberculosis³ and HIV⁴. The usefulness of microfluidic devices is dependent upon their ability to detect the relevant signs of disease, or biomarkers. Fluorescence-Activated Cell Sorting (FACS) is a technique commonly used by hospitals to analyse and sort cells, involving the attachment of fluorophore labels to surface proteins expressed by specific cell sub-populations⁵. FACS has been useful in identifying both the presence of stem cells⁶ and a range of immunodeficiency diseases⁷; however the equipment is immobile, expensive and requires specialised training. Microfluidic devices are able to exploit these label based approaches whilst holding the potential to avoid their drawbacks^{8,9}. They also provide the ability to exploit other physical characteristics such as the mechanical^{10,11} and electrical properties^{12,13} of cells without the use of labels, both separately and in combination. Electrical devices based on both impedance spectroscopy and electrokinetics are capable of discriminating cells on the basis of their size and dielectric properties, in a manner which is both non-invasive and label-free¹⁴. It is research into these electrical techniques which forms the basis of this thesis.

Impedance Spectroscopy

Impedance spectroscopy is a method by which the electrical properties of particles can be determined across a range of frequencies. The electrical impedance of an object is described as the ratio of the voltage applied across it divided by the current induced through it¹⁴. By suspending cells between electrodes their impedance can be measured as a function of frequency, allowing us to infer their electrical structure. In the 1910s Höber performed the first impedance measurements of erythrocytes at both low and high frequencies to estimate their intracellular conductivity¹⁵⁻¹⁷. During the 1920s Fricke developed an electrical description of disperse colloidal systems, or cell suspensions, based on the work of Maxwell which provided estimates for both the cell membrane capacitance and thickness of 8.1 mF/m² and 3.3nm, respectively¹⁸⁻²⁰ – values which are close to those accepted today.

The development of multi-shelled models has since been exploited by several researchers to extract detailed dielectric properties for suspended cells²¹⁻²⁴. By incorporating electrodes into microfluidic channels Ayliffe *et al.*²⁵ were able to perform the first single-cell impedance measurements within a microfluidic device. This impedance based approach has provided a means of evaluating the size, membrane capacitance and intracellular conductivity of individual cells, although the throughput rate is typically limited to hundreds of cells per second¹⁴. The biological importance of these properties remains an area of ongoing research, underpinning the relevance of all electrically based techniques. Although unable to rival the specificity of fluorophores, the potential simplicity of these devices and their label-free operation are attractive. An encouraging achievement has been the identification of lymphocytes, monocytes and neutrophils by single-cell impedance measurements using microlitres of whole human blood²⁶. Impedance measurements are able to provide a detailed electrical analysis of cells however their ability to sort them *en masse* remains a key challenge.

AC Electrokinetics

AC electrokinetic techniques are based on the movement of particles subjected to alternating electric fields^{27,28}. High strength electric fields are capable of translating and rotating particles in a manner dependent upon their dielectric properties, a characteristic which relates these techniques to the measurements of impedance spectroscopy. Dielectrophoresis (DEP) is a term coined by Pohl in the 1950s which refers to the translation of particles under the influence of a non-uniform electric field, a field which exhibits a spatial divergence in magnitude²⁹. The ancient Greek philosopher Thales observed this phenomenon circa 600 BC

when straw became attracted to amber which had been rubbed vigorously³⁰; however this was not exploited until the work of Hatfield in the 1920s for the extraction of tin ore³¹. Pohl later applied the same technique towards the characterisation and separation of cells and bacteria³², the study of which remains a principal focus of research to the present day.

An understanding of DEP first requires an appreciation of how electric charge becomes redistributed in a material when an external electric field is applied. Many particles can be analysed in an approximate manner by simplifying their geometry as spheres or ellipsoids constructed from lossy dielectrics. These materials possess both free and bound charges which govern quantities referred to as their conductivity and permittivity, respectively. Conductivity quantifies the ability of a material to pass direct current (DC), providing a measure of how free charges are able to migrate under the influence of a static electric field. Permittivity quantifies the ability of a material to pass alternating current (AC), providing a measure of how bound charges are able to re-distribute under the influence of a time-varying electric field. A lossy dielectric particle will experience a re-distribution of charge when an electric field is applied, inducing the formation of a dipole which may be quantified in terms of an effective polarisability as a function of frequency²⁷.

As the electric field frequency changes so does the dominant mechanism of polarisation, each mechanism inducing a distinct change in the permittivity referred to as a dielectric dispersion. It is these mechanisms which dictate how particles such as cells become polarised when suspended in a fluid and subjected to an external electric field. At frequencies approaching DC the polarisability of materials tends to be governed by their conductivity. As the field frequency is increased the accumulation of charge at the boundary of dielectric materials becomes increasingly important, a mechanism known as interfacial polarisation. The conductivity, permittivity and geometry of the particle all act to determine how it becomes polarised at these frequencies, typically between 10 kHz to 10 MHz when considering the lipid membranes of biological cells. As the frequency is increased into the GHz range the behaviour of molecular dipoles, such as water, becomes important as they undergo orientational polarisation. In the THz range, crystalline materials experience ionic polarisation due to small displacements in their ionic bonds, and in the PHz range the distribution of electron clouds within atoms change as they undergo electronic polarisation.

Consider a solid, spherical, dielectric particle suspended in an aqueous electrolyte between two electrodes. When a voltage is applied to the electrodes an electric field is set up which induces a dipole on the particle due to the redistribution of charge. If the particle is more polarisable than the surrounding medium, as shown in Fig. 1.1 (left), more charge is built up

on the inside of the particle-medium boundary and the induced dipole acts to oppose the applied electric field. If the particle is less polarisable than the surrounding medium, as shown in Fig. 1.1 (right), more charge builds up on the outside of the boundary and the dipole reinforces the electric field. The electric fields being considered here are completely symmetrical between the electrodes and thus no net force is induced upon either particle. If one of the electrodes were reduced to a point the electric field would be concentrated towards one side of the particle, resulting in a net force. A particle which is more polarisable than the surrounding medium will move towards this field concentration, a response described as positive DEP. If the particle is less polarisable than the surrounding medium it will move away from the concentration, a response described as negative DEP.

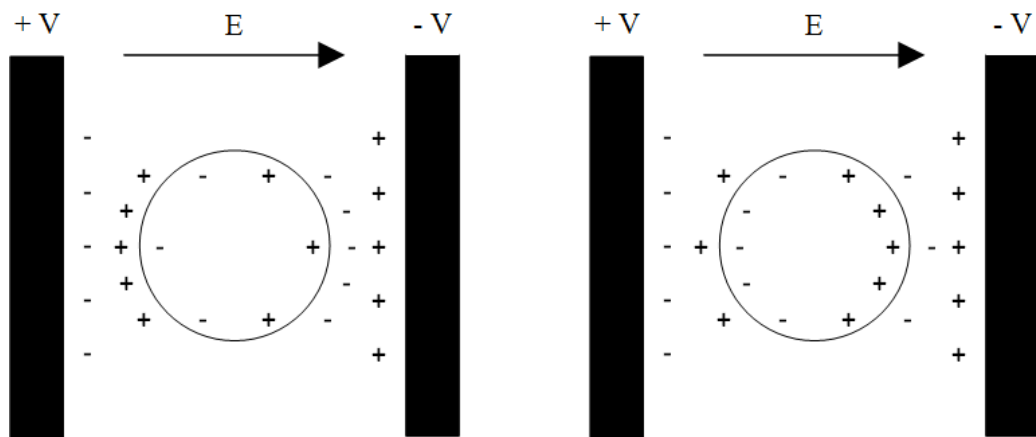


Figure 1.1 – Polarisation of dielectric spheres which are more (left) and less (right) polarisable than their surrounding medium. The positive and negative symbols illustrate the accumulation of charge at the electrode-medium and particle-medium boundaries.

When considering biological cells, which possess a conductive interior surrounded by an insulating membrane, the situation becomes more complex. The multi-shelled dielectric models developed by Fricke and others, with the impedance spectroscopy of cell suspensions in mind, are directly relevant to DEP as they describe the same fundamental geometry and dielectric parameters. These models provide an estimate of both the low frequency conductivity and high frequency (~ 100 MHz) permittivity for constituent parts of the cell structure. At low frequencies free charges are able to migrate in the field but at frequencies significantly above the interfacial dispersion it is the bound charges, or the effective particle permittivity, which dominates. Analysis of the cell model in terms of polarisability describes a transition from negative to positive DEP in the region of 100 kHz, based on intact cells suspended in a medium of sufficiently low conductivity (typically less than 100 mS/m). The

value of this crossover frequency is primarily a function of cell size, membrane capacitance and medium conductivity³³. It is these frequency dependent transitions between negative and positive DEP which provide the basis for isolating dielectrically distinct cells. The impact of suspending cells in a low conductivity medium for extended periods of time is not well understood however evidence has emerged of a decrease in viability after several hours³⁴. Nevertheless, the ease of evaluating and exploiting crossover frequencies offer clear benefits when operating under these conditions³⁵.

A variety of DEP electrode geometries have been developed to selectively trap or deflect cells in a microfluidic channel for downstream investigation. Interdigitated electrodes as shown in Fig. 1.2 (left) patterned on a single plane are often employed and are useful for measuring crossover frequencies. Under a negative DEP force of sufficient strength cells are able to levitate above the electrodes as gravitational, buoyancy and DEP forces sum to zero in the vertical axis. On transitioning to positive DEP the cells then become attracted to electric field concentrations which exist along the electrode edges. The strength of the electric field can be increased further by incorporating castellations³⁶ as shown in Fig. 1.2 (right) which generate regions of intense field non-uniformity at the corners.

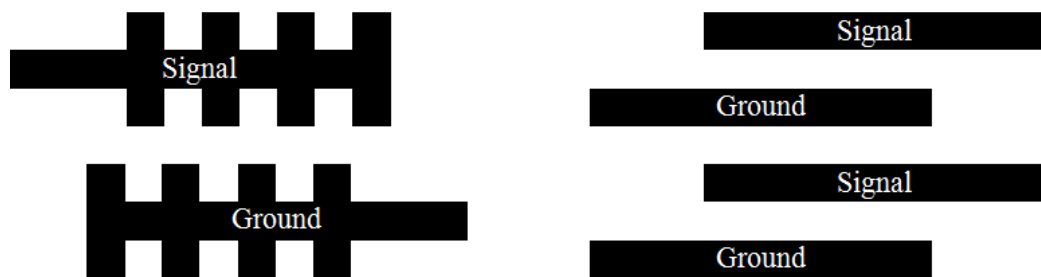


Figure 1.2 – Interdigitated (left) and castellated (right) DEP electrode geometries fabricated on a single plane.

By constructing a microfluidic channel over these electrodes it is possible to trap a target sub-population of cells under positive DEP by exploiting differences in their crossover frequencies. This selective trap can be achieved by applying a frequency which is intermediate to the crossover frequencies of both sub-populations, an approach which has already been demonstrated in the separation of live from dead cells³⁷, cancer cells from blood³⁸ and differentiated myotubes from their multipotent progenitors³⁹. By comparison to the hundreds of cells per second typical of single-cell impedance spectroscopy a DEP based device can exceed this by a factor of at least ten²⁸ and is easily adapted to parallelisation.

A spatially rotating electric field can be generated by using a quadrupolar electrode arrangement as displayed in Fig. 1.3, where quadrupolar refers to the use of four independent electrodes surrounding a cell. By introducing phase shifts to each of the, otherwise identical, electrode signals an electric field which rotates in space is generated, the example showing it moving in a counter-clockwise direction. If the charge relaxation time – permittivity divided by conductivity – of the medium exceeds that of the particle, a situation displayed in Fig. 1.3 (left), the particle will rotate in the same direction as the field with a lag related to the torque induced upon it. If the charge relaxation time of the particle exceeds that of the medium the particle will rotate in the opposite direction, as displayed in Fig. 1.3 (right).

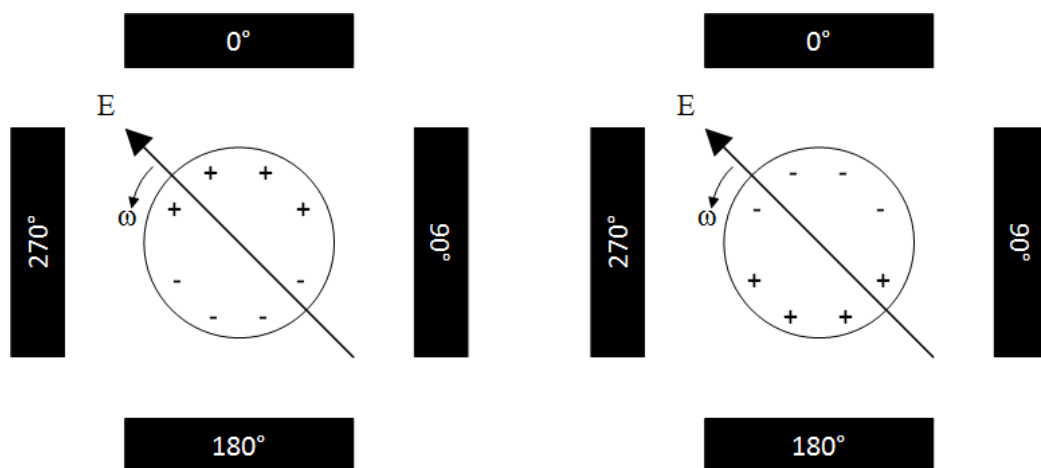


Figure 1.3 – Polarisation of a dielectric particle in a rotating electric field of angular velocity ω when the charge relaxation time of the medium exceeds that of the particle (left) and vice versa (right).

Early experiments by Pohl suggested that this electrorotation (ROT) behaviour was related to that of DEP³², for which the theoretical basis was later developed⁴⁰. An advantage of this technique is the ability to characterise the behaviour of a cell across a wide range of frequencies whilst in suspension for an extended period of time. The ability to measure the response of cells across a broad frequency spectrum allows for the extraction of dielectric parameters using a multi-shelled model, in a manner similar to that of impedance spectroscopy. This approach has been successfully used to characterise the differences between viable and non-viable cells⁴¹, the onset of chemically induced apoptosis⁴², the activation of neutrophils⁴³ and changes to membrane capacitance as a result of protein expression⁴⁴. As with impedance spectroscopy the analysis of individual cells is time consuming and the cells also need to be located in the small area between quadrupolar

electrodes. Although DEP devices do not typically provide the same level of dielectric detail they have the advantage of being simple to implement across a large area and integrate with microfluidics.

It is, however, possible to convert the electro-rotational torque induced by phase shifted quadrupolar electrodes to a translational force, a technique known as travelling wave DEP (TWD). Instead of quadrupolar electrodes surrounding the cell they may instead be arranged as interdigitated electrodes which repeat periodically, a setup which is illustrated in Fig. 1.4. The particle will move as its dipole continually aligns with the travelling field, providing a means of moving cells without the use of fluid flow.

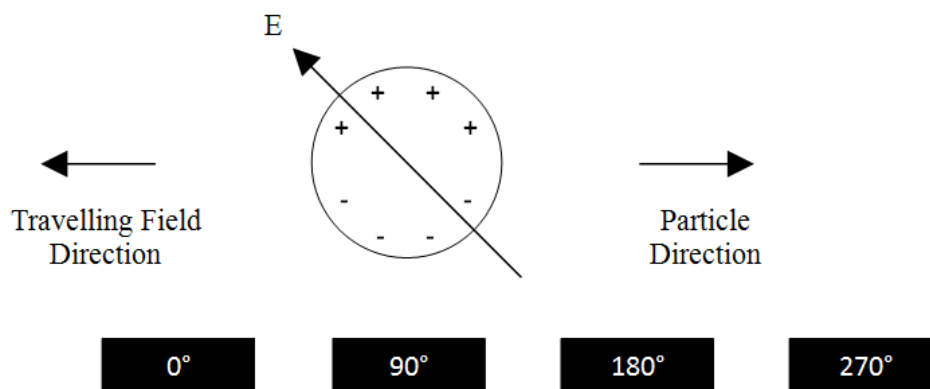


Figure 1.4 – Polarisation of a dielectric particle in a travelling electric field of angular with the charge relaxation time of the particle exceeding that of the medium.

In 1988, Masuda *et al.*⁴⁵ applied travelling fields to erythrocytes (red blood cells) at frequencies of between 0.1 and 10 Hz using parallel electrodes and observed their translational movement. At such low frequencies electrophoretic forces need to be considered, however Hagedorn *et al.*⁴⁶ later demonstrated this behaviour using particles of pollen and cellulose at frequencies of between 10 kHz and 30 MHz. At these frequencies the induced dipole moments and DEP become more important than surface charge and electrophoretic effects. TWD has since been used to separate viable from non-viable yeast cells⁴⁷ and specific sub-types of white blood cell⁴⁸. The eventual development of theoretical modelling relating the behaviour of TWD, ROT and DEP has consolidated our understanding of AC electrokinetics as a whole⁴⁹.

A great deal is now known about the theory underlying AC electrokinetics, the electrode geometries required to exploit it and the microfluidics with which it can be combined. The potential for high-throughput cell sorting based on these electrical techniques exists but

requires an understanding of the biological differences which can be detected, a non-trivial biophysical question. It is therefore important to fully exploit these electrokinetic phenomena and a gap in our understanding remains regarding the DEP behaviour of cells at very high frequencies, beyond 100 MHz. At such frequencies the electric field is expected to effectively short-circuit the capacitive membrane and interact directly with the cell interior²⁸. Based on parameters extracted by impedance spectroscopy it is expected that a high frequency crossover exists marking a transition from positive back to negative DEP. Practical measurements of this transition have, to the authors knowledge, not been undertaken for mammalian cells and its behaviour remains unexplored. In principal its value should be a function of both intracellular conductivity and permittivity, parameters which may be useful in evaluating the physiological health of cells. Although high frequency dielectric properties can be examined by either impedance spectroscopy or electrorotation a DEP crossover could enable the construction of microfluidic separation devices which are both simple to implement and scale upwards. The aim of this thesis is to both verify the existence of this crossover and determine how it can be exploited.

Thesis Outline

In Chapter Two the fundamental theory underlying DEP is presented, beginning with a calculation of the force induced upon an infinitesimal dipole when subjected to a non-uniform electric field. An expression for the electric potential surrounding a dipole is derived which forms the general basis for determining the DEP force in any given situation. The DEP force on a lossless dielectric sphere is derived and modified to account for the presence of conductive losses which introduce frequency dependent dispersions. By incorporating an additional shell it becomes possible to model the behaviour of a particle which is conceptually similar to a mammalian cell, possessing a conductive interior surrounded by an insulating membrane.

The operation of adding shells is generalised in Chapter Three and used to develop a triple-shelled model incorporating the nucleoplasm, nuclear envelope, cytoplasm and cell membrane as distinct entities. By substituting values for these dielectric parameters, derived from published broadband impedance spectroscopy measurements, the DEP spectrum of a mammalian cell suspended in a low conductivity medium is predicted. This analysis suggests the presence of a high frequency crossover, referred to as f_{xo2} , which exists in the region of ~ 215 MHz. The design of electrodes capable of applying voltages at these frequencies across an aqueous electrolyte requires careful consideration. A distributed RCR network is

introduced as a model and validated using interdigitated electrode and Greek cross test structures fabricated from platinum on glass. Accurate crossover measurements require a transition from levitation under negative DEP to electrode attachment under positive DEP. The frequency and voltage necessary for effective levitation is discussed and modelled using an electrostatic finite element simulation. These requirements are used to design and fabricate electrodes which are, in principle, capable of evaluating f_{x02} for mammalian cells.

Chapter Four describes the first measurements of murine (mouse) myeloma cells suspended in a low conductivity isosmotic solution and loaded into the DEP device. By mounting the device in an inverted microscope and applying a high frequency signal the cells are initially levitated above the electrodes as predicted. Sweeping the frequency downwards causes cells to become attracted to the electrode edges in a manner which is consistent with f_{x02} . An unexpected observation is an apparent decrease in this frequency over time which suggests the cells are not in a state of equilibrium when suspended in the DEP solution. This behaviour is also shown to occur for red blood cells and appears consistent with previously published observations of intracellular ion efflux for both cell types under similar conditions. Increasing the salinity of the solution reduces this initial efflux of ions which appears to occur immediately on suspension however the subsequent decrease over time remains identical. Temperature controlled experiments reveal that this process possesses an activation energy which is identical to an existing reported value for red blood cells. By exposing murine myeloma cells to DEP solutions with various combinations of salts the absence of potassium chloride is identified as a critical factor in this instability. Flow cytometry reveals that although the solution is isosmotic it is not isotonic and results in cell shrinkage on suspension, consistent with the initial efflux of ions. Cell viability is also shown to collapse on suspension but does not appear to trend in time with the associated decrease in f_{x02} for intact cells. Based on these experiments the decision is taken to undertake subsequent DEP measurements within 30 minutes of suspension.

In Chapter Five an analytical derivation of f_{x02} is performed which indicates a direct proportionality to intracellular conductivity under the experimental conditions used. It therefore provides a complementary measurement to f_{x01} which provides information regarding the morphological state and integrity of the cell membrane. An experiment is devised to directly control the value of f_{x02} by applying hyposmotic stress to the cells such that water is driven into them to dilute their intracellular compartment. Measurements of f_{x01} , f_{x02} and cell size are performed in tandem with flow cytometry using a potassium sensitive intracellular fluorophore. An osmolality of 215 mOsm/kg is identified as isotonic, significantly lower than that of the culture media. Relative to the isotonic datum, hypertonic

stress is shown to drive an efflux of potassium from the cell, a response which is reflected in measurements of $f_{x_{o2}}$. Hypotonic stress is shown to cause an increase in cell size with reductions to both $f_{x_{o2}}$ and intracellular potassium concentration which are both accounted for by the associated dilution. Both $f_{x_{o2}}$ and intracellular potassium display a strong correlation over the entire osmotic range explored, suggesting that $f_{x_{o2}}$ may be an effective parameter to evaluate the intracellular ionic health of cells.

The viability of a cell culture is one of the most important parameters concerning a cell biologist. Murine myeloma cells are themselves now grown on an industrial scale for the production of monoclonal antibodies, an active area of research with implications for the treatment of diseases including multiple sclerosis, severe asthma and malignant tumours. A means of continually evaluating the health of cells for batch cultures, which are financially expensive, is desirable to both ensure their viability and to maximise productivity. A method of detecting changes to the intracellular ionic health of cells may provide an early warning system before the collapse of such cultures. Murine myeloma cells are maintained in an unfed culture for a period of six days over which the viability of the culture, determined by the exclusion of trypan blue, collapses. Over a subsequent period of five days the cells are then fed every two days resulting in the full recovery of culture viability. The mean value of $f_{x_{o1}}$ provides no clear trend over this experiment with uncertainty over the interpretation of membrane capacitance due to the potential for increased membrane conductivity with the onset of apoptosis. By comparison, the mean value of $f_{x_{o2}}$ correlates well with viability over the entire experiment and displays promise as a means of gauging the health of a culture. Whether it is capable of detecting subtle changes related to the onset of apoptosis, rather than that of necrosis as measured by viability, remains a question. Murine myeloma cells are exposed to etoposide, an anticancer drug which is known to induce the apoptotic process^{33,50}, to determine if $f_{x_{o2}}$ is affected. No apparent correlation is found in the mean value of $f_{x_{o2}}$ with etoposide concentration after 6 or 24 hours. The mean value of $f_{x_{o1}}$ and estimated membrane capacitance, assuming low membrane conductivity, also show no correlation after 6 hours. After 24 hours the mean value of $f_{x_{o1}}$ increases noticeably with etoposide concentration and an associated decrease in the estimated membrane capacitance occurs, but at a stage where the onset of necrosis has already begun. Cumulative distribution plots of $f_{x_{o1}}$ and $f_{x_{o2}}$ suggest that both crossover frequencies experience a subtle shift after 6 hours of exposure, prior to any detectable change in cell viability. An apparent decrease in $f_{x_{o1}}$ with etoposide concentration appears to contradict previously published results however a concomitant decrease in $f_{x_{o2}}$ is consistent with an efflux of potassium ions associated with early stage apoptosis.

Chapter Seven provides a summary of the thesis and highlights observations which are of particular relevance to dielectrophoresis and AC electrokinetics as a whole. The questions which have been raised, potential for future research and for practical application are highlighted.

References

- 1 Whitesides G. M. (2006) The origins and the future of microfluidics. *Nature*, 442 (7101), 368-373.
- 2 Chen, J., Li, J. & Sun, Y. (2012) Microfluidic approaches for cancer cell detection, characterization, and separation. *Lab on a Chip*, 12 (10), 1753-1767.
- 3 Wang, S. & Demirci, U. (2013) Point-of-care assays for tuberculosis: role of nanotechnology/microfluidics. *Biotechnology Advances*, 31 (4), 438-449.
- 4 Chin, C. D., Laksanasopin, T., Cheung, Y. K., Steinmiller, D., Linder, V., Parsa, H., Wang, J., Moore, H., Rouse, R., Umvilighozo, G., Karita, E., Mwambarangwe, L., Braunstein, S. L., Wijgert, J., Sahabo, R., Justman, J. E., El-Sadr, W. & Sia, S. K. (2011) Microfluidics-based diagnostics of infectious diseases in the developing world. *Nature Medicine*, 17 (8), 1015-1019.
- 5 Shapiro, H. M. (2003) *Practical Flow Cytometry*, Hoboken: Wiley.
- 6 Wang, Z., Oron, E., Nelson, B., Razis, S. & Ivanova, N. (2012) Distinct lineage specification roles for NANOG, OCT4, and SOX2 in human embryonic stem cells. *Cell Stem Cell*, 10 (4), 440-454.
- 7 Illoh, O. C. (2004) Current applications of flow cytometry in the diagnosis of primary immunodeficiency diseases. *Archives of Pathology & Laboratory Medicine*, 128 (1), 23-31.
- 8 Osman, O., Toru, S., Dumas-Bouchiat, F., Dempsey, N. M., Haddour, N., Zanini, L. F., Buret, F., Reyne, G. & Frénéa-Robin, M. (2013) Microfluidic immunomagnetic cell separation using integrated permanent micromagnets. *Biomicrofluidics*, 7 (1), 054115.
- 9 Chen, Y., Wu, T. H., Kung, Y. C., Teitell, M. A. & Chiou, P. Y. (2013) 3D pulsed laser-triggered high-speed microfluidic fluorescence-activated cell sorter. *Analyst*, 138 (24), 7308-7315.
- 10 Preira, P., Grandné, V., Forel, J. M., Gabriele, S., Camara, M. & Theodoly, O. (2013) Passive circulating cell sorting by deformability using a microfluidic gradual filter. *Lab on a Chip*, 13 (1), 161-170.
- 11 Sun, J., Liu, C., Li, M., Wang, J., Xianyu, Y., Hu, G. & Jiang, X. (2013) Size-based hydrodynamic rare tumor cell separation in curved microfluidic channels. *Biomicrofluidics*, 7 (1), 011802.
- 12 Song, H., Wang, Y., Rosano, J. M., Prabhakarpanian, B., Garson, C., Pant, K. & Lai, E. (2013) A microfluidic impedance flow cytometer for identification of differentiation state of stem cells. *Lab on a Chip*, 13 (12), 2300-2010.

- 13 Shim, S., Stemke-Hale, K., Noshari, J., Becker, F. F. & Gascoyne, P. R. C. (2013) Dielectrophoresis has broad applicability to marker-free isolation of tumor cells from blood by microfluidic systems. *Biomicrofluidics*, 7 (1), 011808.
- 14 Sun, T. & Morgan, H. (2010) Single-cell microfluidic impedance cytometry: a review. *Microfluidics and Nanofluidics*, 8 (4), 423-443.
- 15 Höber, R. (1910) Eine Methode, die elektrische Leitfähigkeit im Innern von Zellen zu messen. *Pflügers Archiv: European Journal of Physiology*, 133 (4-6), 237-253.
- 16 Höber, R. (1912) Ein zweites Verfahren, die Leitfähigkeit im Innern von Zellen zu messen. *Pflügers Archiv: European Journal of Physiology*, 148 (4-5), 189-221.
- 17 Höber, R. (1913) Messungen der inneren Leitfähigkeit von Zellen. *Pflügers Archiv: European Journal of Physiology*, 150(1-2), 15-45.
- 18 Fricke, H. (1925) The electric capacity of suspensions of red corpuscles of a dog. *Physical Review*, 26, 682-687.
- 19 Fricke, H. (1925) The Electric capacity of suspensions with special reference to blood. *The Journal of General Physiology*, 9 (2), 137-152.
- 20 Fricke, H. (1925) The electric resistance and capacity of blood for frequencies between 800 and 4½ million cycles. *The Journal of General Physiology*, 9 (2), 153-167.
- 21 Hanai, T. (1960) Theory of the dielectric dispersion due to the interfacial polarization and its application to emulsions. *Kolloid-Zeitschrift*, 171 (1), 23-31.
- 22 Pethig, R. (1979) *Dielectric and Electronic Properties of Biological Materials*, Chichester: Wiley.
- 23 Asami, K. (2002) Characterization of heterogeneous systems by dielectric spectroscopy. *Progress in Polymer Science*, 27 (8), 1617-1659.
- 24 Sun, T. (2007) Dielectric spectroscopy of single cells: time domain analysis using Maxwell's mixture equation. *Journal of Physics D: Applied Physics*, 40 (1), 1-8.
- 25 Ayliffe, H. E. (1999) Electric impedance spectroscopy using microchannels with integrated metal electrodes. *Journal of Microelectromechanical Systems*, 8 (1), 50-57.
- 26 Holmes, D., Pettigrew, D., Reccius, C. H., Gwyer, J. D., Berkel, C. V., Holloway, J., Davies, D. E., Morgan H. (2009) Leukocyte analysis and differentiation using high speed microfluidic single cell impedance cytometry. *Lab on a Chip*, 9 (20), 2881-2889.
- 27 Morgan, H. & Green, N. G. (2003) *AC Electrokinetics: Colloids and Nanoparticles*, Baldock: Research Studies Press.
- 28 Pethig, R. (2010) Review Article-Dielectrophoresis: status of the theory, technology and applications. *Biomicrofluidics*, 4 (2), 022811.

- 29 Pohl, H. A. (1951) The motion and precipitation of suspensoids in divergent electric fields. *Journal of Applied Physics*, 22 (7), 869-871.
- 30 Mottelay, P. F. (1922) *Bibliographical History of Electricity and Magnetism*, London: Charles Griffin.
- 31 Hatfield, H. S. (1924) Dielectric separation: a new method for treatment of ores. *Institution of Mining and Metallurgy Bulletin*, 233, 335-342.
- 32 Pohl, H. A. (1978) *Dielectrophoresis*, Cambridge: Cambridge University Press.
- 33 Pethig, R. and Talary, M. S. (2007) Dielectrophoretic detection of membrane morphology changes in Jurkat T-cells undergoing etoposide-induced apoptosis. *IET Nanobiotechnology*, 1 (1), 2-9.
- 34 Yang, L., Banada, P. P., Bhunia, A. K. & Bashir, R. (2008) Effects of dielectrophoresis on growth, viability and immuno-reactivity of listeria monocytogenes. *Journal of Biological Engineering*, 2 (6), 1-14.
- 35 Voldman, J. (2006) Dielectrophoretic traps for cell manipulation. IN: Ferrari, M. (Ed) *Biomolecular sensing, processing and analysis*, New York: Springer, pp173-186.
- 36 Pethig, R., Huang, Y., Wang, X. & Burt, J. P. H. (1992) Positive and negative dielectrophoretic collection of colloidal particles using interdigitated castellated microelectrodes. *Journal of Physics D: Applied Physics*, 25(5), 881-888.
- 37 Doh, I. and Cho, Y. H. (2005) A continuous cell separation chip using hydrodynamic dielectrophoresis (DEP) process. *Sensors and Actuators A: Physical*, 121 (1), 59-65.
- 38 Gascoyne, P. R. C., Wang, X. B., Huang, Y. & Becker, F. F. (1997) Dielectrophoretic separation of cancer cells from blood. *IEEE Transactions on Industry Applications*, 33 (3), 670-678.
- 39 Muratore, M., Srsen, V., Waterfall, M., Downes, A. & Pethig, R. (2012) Biomarker-free dielectrophoretic sorting of differentiating myoblast multipotent progenitor cells and their membrane analysis by Raman spectroscopy. *Biomicrofluidics*, 6, 034113.
- 40 Arnold, W. M. & Zimmermann, U. (1988) Electro-rotation: development of a technique for dielectric measurements on individual cells and particles. *Journal of Electrostatics*, 21 (2-3), 151-191.
- 41 Huang, Y., Hölzel, R., Pethig, R. & Wang, X. B. (1992) Differences in the AC electrostatics of viable and non-viable yeast cells determined through combined dielectrophoresis and electrorotation studies. *Physics in Medicine and Biology*, 37 (7), 1499-1518.

- 42 Huang, C., Chen, A., Wang, L., Guo, M. & Yu, J. (2007) Electrokinetic measurements of dielectric properties of membrane for apoptotic HL-60 cells on chip based-device. *Biomedical Microdevices*, 9 (3), 335-343.
- 43 Griffith, A. W. & Cooper, J. M. (1998) Single cell measurements of human neutrophil activation using electrorotation. *Analytical Chemistry*, 70(13), 2607-2612.
- 44 Zimmermann, D., Zhou, A., Kiesel, M., Feldbauer, K., Terpitz, U., Haase, W., Schneider-Hohendorf, T., Bamberg, E. & Sukhorukov, V. L. (2008) Effects on capacitance by overexpression of membrane proteins. *Biochemical and Biophysical Research Communications*, 369(4), 1022-1026.
- 45 Masuda, S., Washizu, M. & Kawabata, I. (1988) Movement of blood cells in liquid by nonuniform traveling field. *IEEE Transactions on Industry Applications*, 24 (2), 217-222.
- 46 Hagedorn, R., Fuhr, G., Müller, T. & Gimsa, J. (1992) Traveling-wave dielectrophoresis of microparticles. *Electrophoresis*, 13 (1), 49-54.
- 47 Talary, M. S., Burt, J. P. H., Tame, J. A. & Pethig, R. (1996) Electromanipulation and separation of cells using travelling electric fields. *Journal of Physics D: Applied Physics*, 29(8), 2198-2203.
- 48 Pethig, R., Talary, M. S. & Lee, R. S. (2003) Enhancing traveling-wave dielectrophoresis with signal superposition. *IEEE Engineering in Medicine and Biology Magazine*, 22 (6), 43-50.
- 49 Wang, X. B., Huang, Y., Becker, F. F. & Gascoyne, P. R. C. (1994) A unified theory of dielectrophoresis and travelling wave dielectrophoresis. *Journal of Physics D: Applied Physics*, 27 (7), 1571-1574.
- 50 Hande, K. R. (1998) Etoposide: four decades of development of a topoisomerase II inhibitor. *European Journal of Cancer*, 34 (10), 1514-1521.

Chapter Two

Technical Theory

Introduction

The phenomenon of dielectrophoresis was briefly described in Chapter One. However a thorough mathematical analysis is necessary to gain a deeper understanding. In this chapter the relevant theory is introduced and is largely based on texts written by Jones¹ and Pethig². The foundations of this field do, however, stretch back to studies made by Herbert Pohl, James Clerk Maxwell and further. The concept of an infinitesimal dipole is first introduced and an expression derived for the dielectrophoretic force acting upon it when exposed to a non-uniform electric field. By deriving an expression for the surrounding electric potential the effective dipole moment will be introduced as a general means of determining this force. A lossless dielectric sphere is first considered and subsequently expanded to incorporate the effect of conductive losses under the action of an AC field. The addition of a spherical shell yields a model which is conceptually similar to the physical structure of mammalian cells, providing a firm foundation on which we can build an understanding of cellular dielectrophoresis.

The Dipole

An appropriate point to begin understanding dielectrophoresis is by considering an electric dipole and estimating the force exerted upon it when a DC electric field is applied. Consider the small dipole illustrated in Fig. 2.1 where two equal but opposite charges, $+q$ and $-q$, are separated by a short distance \mathbf{d} and located at a position \mathbf{r} . An electric field \mathbf{E} is applied which, if uniform, will induce a torque causing the dipole to align but result in no net force. A non-uniform field will also induce a net force which is the basis for dielectrophoresis. It is assumed that the arrangement of charge necessary to create such a field is unaffected by the presence of the dipole itself. If the displacement vector \mathbf{d} is infinitesimal in length by comparison to the field non-uniformities then a Taylor expansion around the position \mathbf{r} may be applied to determine the net force^{1,3}:

$$\mathbf{F} = q\mathbf{E}(\mathbf{r} + \mathbf{d}) - q\mathbf{E}(\mathbf{r}) = q[\mathbf{E}(\mathbf{r}) + \mathbf{d} \cdot \nabla\mathbf{E}(\mathbf{r}) + \dots] - q\mathbf{E}(\mathbf{r}) \quad (2.1)$$

The Taylor expansion allows us to express the net force on a dipole as an infinite sum of terms, each one calculated by applying successively higher spatial derivatives of the electric field around a given position. It is therefore possible to consider only the most significant terms and derive an effective approximation to an otherwise complicated function. The electrophoretic first term is algebraically cancelled out, leaving the remaining terms which depend upon spatial derivatives of the electric field and therefore its non-uniformity.

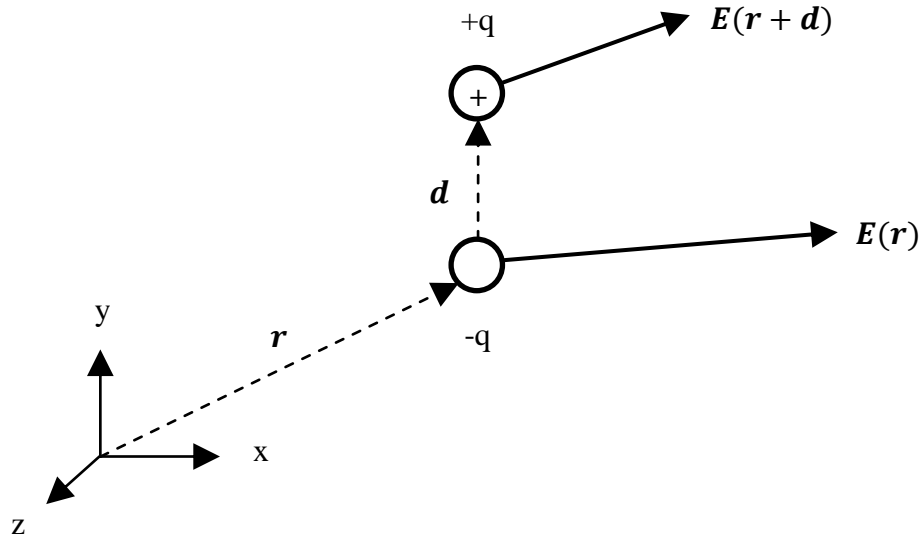


Figure 2.1 – A small dipole placed in a divergent electric field, the latter being defined at each of the dipole charges by the thickened vector arrows. The position vector \mathbf{r} defines the location of a negative dipole charge, whose corresponding positive charge is displaced by the vector \mathbf{d} .

A standard approximation, when considering the electric field around a dipole, is to neglect the second and higher order derivatives if the external field non-uniformities are significantly larger in scale^{2,4}. By neglecting these higher order terms and applying the limit of $|\mathbf{d}| \rightarrow 0$ such that the dipole moment $\mathbf{p} = q\mathbf{d}$ remains finite we arrive at an expression for the resultant force on an infinitesimal dipole:

$$\mathbf{F}_{dipole} = \mathbf{p} \cdot \nabla \mathbf{E} \quad (2.2)$$

The above expression is known as the dipole approximation to the dielectrophoretic (DEP) force. It states that no net force is exerted upon a dipole unless an electric field gradient due to a non-uniform field is applied. In deriving this expression it is assumed that these non-uniformities are sufficient to induce a force but not so great that the higher order terms neglected in Eq.(2.1) are required. In quadrupolar designs the higher order terms are required

to correctly calculate the force applied on a particle located in the centre, which would otherwise be zero⁵. At locations which are close to the edge of electrodes – and when considering crossover frequencies, discussed on p29 – the first order dipole approximation of Eq.(2.2) is often considered to be of sufficient accuracy^{6,7}.

The dipole itself may arise due to an arrangement of permanent charges, a polar molecule for example, or be induced upon a particle by the applied field itself. A derivation of the effective dipole moment therefore depends upon the physical situation being considered. Before modelling a given situation we need to identify the general form of this dipole in terms of the electric potential surrounding a particle. The electric potential for any given situation can then be solved for, the effective dipole moment identified for substitution into Eq.(2.2) and the induced DEP force determined. Let us therefore consider the generalised situation displayed in Fig. 2.2:

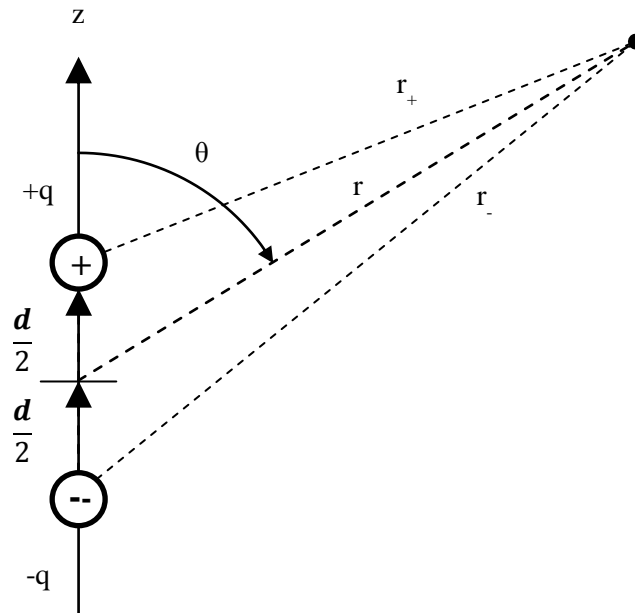


Figure 2.2 – A small dipole in a dielectric solution of permittivity ϵ_s aligned to the z-axis where the origin is situated equidistantly between the two charges. Spherical coordinates are used with symmetry assumed about the z-axis, defined by an azimuthal angle ϕ (not displayed) in the out-of-page third dimension.

A small but finite dipole constructed from two point charges positioned along the z-axis at $z = \pm d / 2$ in a homogenous and isotropic dielectric of permittivity ϵ_s will set up an

axisymmetric electric potential $\Phi(r,\theta)$, where r and θ are the radial distance and polar angle in spherical coordinates to an observation point. At this observation point the net electrostatic potential may be determined by superposition of the electric fields due to the two charges:

$$\Phi(r, \theta) = \frac{q}{4\pi\epsilon_s r_+} - \frac{q}{4\pi\epsilon_s r_-} \quad (2.3)$$

Both r_+ and r_- may be expressed as a function of d , r and θ by considering the geometry of the situation displayed in Fig. 2.2:

$$\left(\frac{r}{r_{\pm}}\right) = \left[1 + \left(\frac{d}{2r}\right)^2 \mp \frac{d}{r} \cos \theta\right]^{-\frac{1}{2}} \quad (2.4)$$

which can be expanded using a Maclaurin series - a Taylor series expansion of a function around zero - of the form⁸:

$$(1 + x)^{-\frac{1}{2}} = 1 - \frac{x}{2} + \frac{3x^2}{8} - \frac{5x^3}{16} + \dots \quad (2.5)$$

Legendre polynomials may then be used to further simplify this expression, expressed concisely by Rodrigues' formula as⁹:

$$P_n(x) = \frac{1}{2^n n!} \frac{d^n}{dx^n} [(x^2 - 1)^n] \quad (2.6)$$

where x is substituted by $\cos \theta$ for each term possessing an order n . These arise due to the spherical co-ordinates defining the effective multi-polar geometry of the potential. By combining Eq.(2.4) with Eq.(2.5) and Eq.(2.6) it may therefore be re-written as:

$$\begin{aligned} \left(\frac{r}{r_{\pm}}\right) &= P_0(\cos \theta) \pm \left(\frac{d}{2r}\right) P_1(\cos \theta) + \left(\frac{d}{2r}\right)^2 P_2(\cos \theta) \\ &\quad \pm \left(\frac{d}{2r}\right)^3 P_3(\cos \theta) \dots \end{aligned} \quad (2.7)$$

Based on (2.3) and (2.7) the net electrostatic potential resulting from the two charges may be expanded as:

$$\Phi(r, \theta) = \frac{qdP_1(\cos \theta)}{4\pi\epsilon_s r^2} + \frac{qd^3P_3(\cos \theta)}{16\pi\epsilon_s r^4} + \dots \quad (2.8)$$

The first term of this expansion being the dipole term of the electrostatic potential:

$$\Phi_{dipole}(r, \theta) = \frac{qdP_1(\cos \theta)}{4\pi\epsilon_s r^2} \equiv \frac{p_{eff} \cos \theta}{4\pi\epsilon_s r^2} \quad (2.9)$$

where p_{eff} may represent any effective dipole moment which arises from the polarisation of a particle in a dielectric medium. Higher order terms of odd order also exist in Eq.(2.8) for the finite dipole. These are the corrections necessary given a finite spacing between the two charges as opposed to the principal term of Eq.(2.9) which, by itself, represents that of an infinitesimal point dipole. By solving for the electrostatic potential surrounding a particle and comparing it against this form we can identify the effective dipole moment – and therefore the induced DEP force of Eq.(2.2).

The Lossless Dielectric Sphere

The first situation which we should consider is that of a non-conducting sphere of radius R and permittivity ϵ_p suspended in a solution of permittivity ϵ_s , as displayed in Fig. 2.3. Such a particle is not only equivalent in terms of its external geometry to many cells suspended in solution, it can be further refined to more accurately reflect the behaviour of a cell. It is assumed that a uniform field of magnitude E_0 , oriented in the z direction, existed prior to the sphere being inserted and that no free charges are present anywhere.

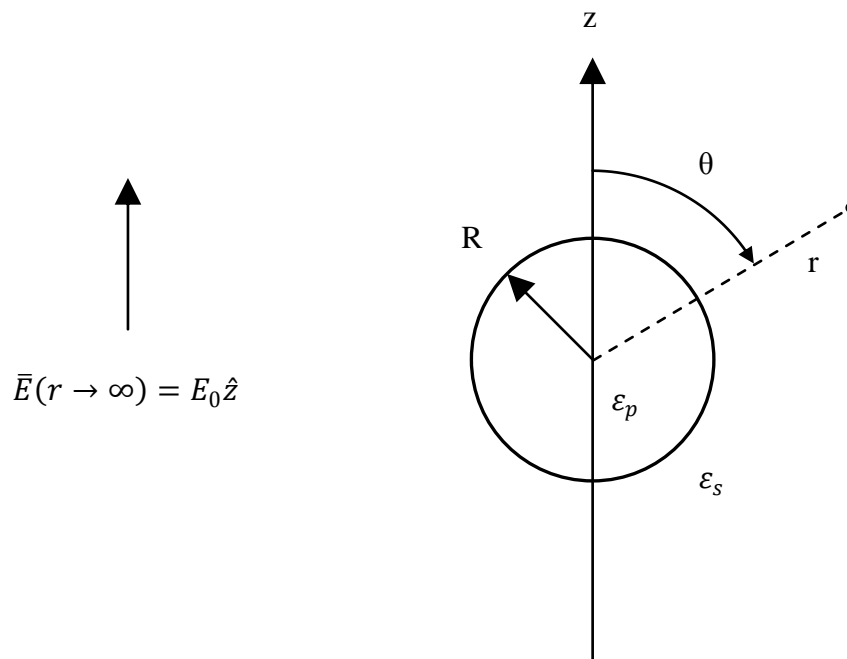


Figure 2.3 – A non-conducting dielectric sphere in a dielectric solution of permittivity ϵ_s , subjected to a uniform electric field parallel to the z -axis. Spherical coordinates are used with symmetry assumed about the z -axis, defined by an azimuthal angle ϕ (not displayed) in the out-of-page third dimension.

As the sphere is dielectrically both isotropic and homogenous it will become polarised symmetrically around the z-axis. Subject to an electrostatic potential satisfying Laplace's equation ($\nabla^2\phi = 0$) a potential arises both inside ϕ_i and outside ϕ_o the sphere where the following solution form is assumed¹⁰:

$$\phi_i = -Br \cos \theta \quad (r \leq R) \quad (2.10)$$

$$\phi_o = -E_0 r \cos \theta + \frac{A \cos \theta}{r^2} \quad (r \geq R) \quad (2.11)$$

In the above equations A and B are coefficients which need to be solved by applying appropriate boundary conditions at the surface of the sphere. Inside of the sphere, described by Eq.(2.10), a single component acts along the same axis as the applied electric field. The outside of the sphere is described by Eq.(2.11), where the first term corresponds to the applied electric field itself and the second term accounts for the effective dipole, induced by the former. By solving for the coefficient A we can therefore identify the effective dipole moment and determine the induced DEP force. The solution of this electrostatic problem requires the following constraints at the surface of the sphere:

$$\phi_i(r = R, \theta) = \phi_o(r = R, \theta) \quad (2.12)$$

$$\epsilon_p \frac{\partial \phi_i}{\partial r}(r = R, \theta) = \epsilon_s \frac{\partial \phi_o}{\partial r}(r = R, \theta) \quad (2.13)$$

Eqs.(2.12) and (2.13) ensure that both the electric potential and normal component of the displacement flux vector are continuous across the spherical boundary. The former is required for a solution which is consistent across the interior to exterior dielectric boundary. The latter must be satisfied as the dielectric materials are non-conducting and therefore prevent the accumulation of charge at the interface. By combining Eqs.(2.10) through (2.13) we can determine the coefficients A and B:

$$A = \frac{\epsilon_p - \epsilon_s}{\epsilon_p + 2\epsilon_s} R^3 E_0 \quad (2.14)$$

$$B = \frac{3\epsilon_s}{\epsilon_p + 2\epsilon_s} E_0 \quad (2.15)$$

By substituting Eq.(2.14) into the external electric potential expression of Eq.(2.11) we can, by comparison to Eq.(2.9), identify the effective dipole moment:

$$p_{eff} = 4\pi\epsilon_s R^3 K E_0 \quad (2.16)$$

where:

$$K(\varepsilon_p, \varepsilon_s) = \frac{\varepsilon_p - \varepsilon_s}{\varepsilon_p + 2\varepsilon_s} \quad (2.17)$$

which is known as the Clausius-Mossotti factor, the effective polarisability of the cell being equivalent to this factor multiplied by $3\varepsilon_s^{11}$. Substitution of Eqs.(2.16) and (2.17) into Eq.(2.2) yields an expression for the DEP force exerted upon a lossless and homogenous dielectric sphere in a dielectric medium:

$$\mathbf{F}_{DEP} = 4\pi\varepsilon_s R^3 \left(\frac{\varepsilon_p - \varepsilon_s}{\varepsilon_p + 2\varepsilon_s} \right) \mathbf{E} \cdot \nabla \mathbf{E} = 2\pi\varepsilon_s R^3 \left(\frac{\varepsilon_p - \varepsilon_s}{\varepsilon_p + 2\varepsilon_s} \right) \nabla E_0^2 \quad (2.18)$$

Eq.(2.18) states that the DEP force is zero in a uniform field, that it is proportional to the particle volume and that the induced dipole moment may be directed either with or against the applied field. The latter is dependent upon whether the particle permittivity is greater or less than that of the surrounding medium, dictating whether the particle is attracted to or repelled from concentrations in the electric field. This behaviour is encapsulated in the Clausius-Mossotti factor $K(\varepsilon_p, \varepsilon_s)$ and commonly referred to as either positive DEP in the attractive and negative DEP in the repulsive cases. A key consideration in the development of DEP devices is the generation of an electric field which is sufficiently non-uniform to move particles of interest. The use of high field strengths can lead to thermal, electrochemical or dielectric breakdown issues. By reducing the distance between electrodes the generation of large field gradients becomes possible at low voltages. At the microscopic scale this induced DEP force may orders of magnitude higher than both gravity and Brownian motion, making it suitable for the manipulation of biological cells¹¹.

Conductive Losses

Our analysis of spherical particles thus far is only applicable to lossless particles. There are many cases where we need to account for conductive losses which, in the case of biological cells, will arise due to the presence of free ions throughout their intracellular structure. When considering a homogenous but conductive dielectric subjected to an AC field such losses may be accounted for by an expression referred to as the complex permittivity:

$$\varepsilon^* = \varepsilon - \frac{j\sigma}{\omega} \quad (2.19)$$

where ε is the permittivity in F/m, σ the DC conductivity in S/m, ω the angular frequency of the electric field in rad/s and j is the imaginary unit vector $\sqrt{-1}$. The Clausius-Mossotti

factor of Eq.(2.17) may be re-written as a complex function incorporating these frequency dependent conductive losses:

$$K^*(\varepsilon_p^*, \varepsilon_s^*) = \frac{\varepsilon_p^* - \varepsilon_s^*}{\varepsilon_p^* + 2\varepsilon_s^*} \quad (2.20)$$

At low frequencies the current flowing is principally conductive and caused by the movement of free ions which act in phase with the applied AC field. At higher frequencies a displacement current associated with the perturbation of bound dielectric charges begins to dominate. The materials forming the particle-solution interface behave as a capacitor with displacement current leading the field by up to $\pi / 2$ radians. A charge relaxation time of $\tau_r = \varepsilon/\sigma$ is associated with these lossy dielectrics and may be used to estimate the frequency at which the displacement exceeds the conductive current as $f_r = 1/2\pi\tau_r$. Based on an aqueous solution of 50 mS/m conductivity f_r is in the region of 10 MHz but rises significantly in physiological media of 1.5 S/m conductivity to over 300 MHz.

As the Clausius-Mossotti factor of Eq.(2.20) is complex both its magnitude and phase vary with ω , the latter implying that the applied electric field and dipole moment exhibit a separation in phase. This separation is due to charging effects which occur at the surface of the sphere, a process known as Maxwell-Wagner interfacial polarisation^{12,13} which exhibits a characteristic time constant:

$$\tau_{MW} = \frac{\varepsilon_p + 2\varepsilon_s}{\sigma_p + 2\sigma_s} \quad (2.21)$$

A lossless dielectric of relative permittivity 2.5, representative of a polystyrene sphere, suspended in an aqueous solution of 50 mS/m conductivity exhibits a relaxation frequency at approximately 10 MHz. By increasing the particle conductivity to introduce loss we reduce τ_{MW} and increase the frequency at which this relaxation occurs. The DEP behaviour of lossy particles, as a function of frequency, should therefore account for these relaxations. In order to estimate the DEP force induced on a lossy particle in conductive media we first need to consider the applied AC electric field, expressed as a complex phasor. Fig. 2.4 displays a phasor of magnitude $E_0(\mathbf{r})$ at an angle of ωt radians from the horizontal axis, where E_0 is the electric field magnitude as a function of position \mathbf{r} and t is the time in seconds. As time proceeds the phasor rotates in a counter-clockwise direction, the horizontal and vertical components varying with the cosine and sine of the phasor angle, respectively. The situation is mathematically equivalent to the complex number $E_0(\mathbf{r})e^{j\omega t}$, where the real and imaginary components are plotted on the horizontal and vertical axes according to Euler's formula: $e^{jx} = \text{Cos}(x) + j\text{Sin}(x)$.

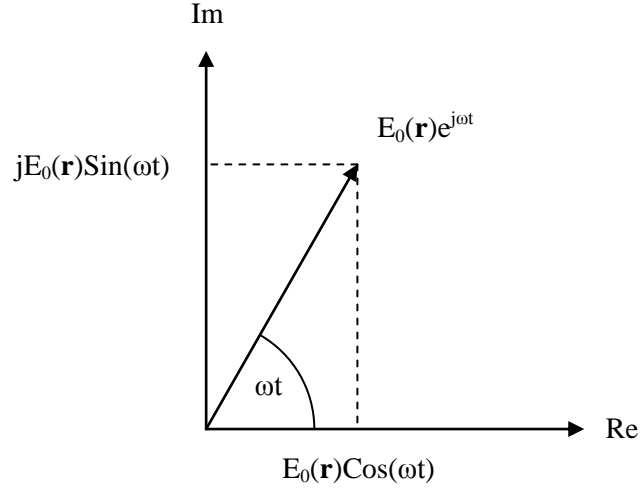


Figure 2.4 - Representation of a phasor in Cartesian form where the horizontal and vertical axes represent the real and imaginary components, respectively.

We arbitrarily define the real component of the complex phasor, displayed in Fig. 2.4, to be its instantaneous value in reality:

$$E(\mathbf{r}, t) = \text{Re}[E_0(\mathbf{r})e^{j\omega t}] \quad (2.22)$$

where “Re” indicates that the real component of the phasor is being used. Based on Eq.(2.22), and using the complex Clausius-Mossotti factor of Eq.(2.20), the effective dipole moment of Eq.(2.16) may be re-written to account for frequency dependent conductive losses as:

$$p_{eff}^*(\mathbf{r}, t) = 4\pi\epsilon_s R^3 \frac{\epsilon_p^* - \epsilon_s^*}{\epsilon_p^* + 2\epsilon_s^*} E_0(\mathbf{r})e^{j\omega t} \quad (2.23)$$

The instantaneous effective dipole moment is therefore:

$$p_{eff}(\mathbf{r}, t) = \text{Re}(p_{eff}^*(\mathbf{r}, t)) = \text{Re}\left(4\pi\epsilon_s R^3 \frac{\epsilon_p^* - \epsilon_s^*}{\epsilon_p^* + 2\epsilon_s^*} E_0(\mathbf{r})e^{j\omega t}\right) \quad (2.24)$$

Eq.(2.24) allows us to understand the DEP behaviour of such a particle. The induced, time-dependent, DEP force for a lossy sphere may be calculated based by assuming it is a point dipole subjected to a time-varying electric field of magnitude E_0 based on Eqs.(2.24) and (2.2):

$$F_{DEP}(\mathbf{r}, t) = \text{Re}\left(4\pi\epsilon_s R^3 \frac{\epsilon_p^* - \epsilon_s^*}{\epsilon_p^* + 2\epsilon_s^*} E_0(\mathbf{r})e^{j\omega t}\right) \cdot \nabla \text{Re}[E_0(\mathbf{r})e^{j\omega t}] \quad (2.25)$$

The RMS average of the electric field for any general position allows us to derive the time-averaged DEP force acting upon this homogenous but lossy dielectric sphere:

$$\langle F_{DEP}(t) \rangle = 2\pi\epsilon_s R^3 \text{Re} \left(\frac{\epsilon_p^* - \epsilon_s^*}{\epsilon_p^* + 2\epsilon_s^*} \right) \nabla E_{rms}^2 \quad (2.26)$$

Since the real part of the Clausius-Mossotti factor $\text{Re}\{K\}$ varies with the angular frequency ω so does the average DEP force. All of the frequency dependent behaviour is encapsulated in the Clausius-Mossotti factor with solution permittivity, particle size and field non-uniformity determining the precise force induced. The resulting behaviour is plotted in Fig. 2.5 for a sphere of relative permittivity 2.5 and a range of conductivities suspended in an aqueous solution of 50 mS/m conductivity. In the DC limit the magnitude and polarity of $\text{Re}\{K\}$ is determined by particle conductivity, as should be expected from Eq.(2.19). If the particle and solution conductivities are equal then no DEP force is induced in this limit. A lossless particle will experience strong negative DEP, with $\text{Re}\{K\}$ plateauing at -0.5. Above $\sim 100\text{MHz}$ the value of $\text{Re}\{K\}$ depends upon the relative difference in particle and solution permittivities. The point of transition - or relaxation - between these two regions is simply determined by the polarisation time constant of Eq.(2.21) in the case of a homogenous sphere.

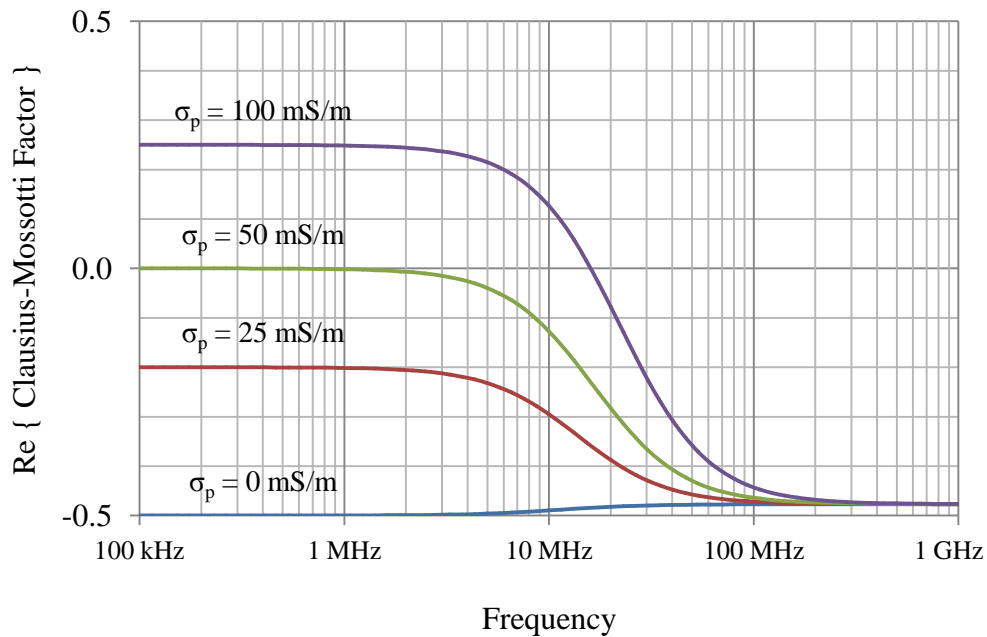


Figure 2.5 – The real part of the Clausius-Mossotti factor for a homogenous lossy dielectric sphere. Particle relative permittivity $\epsilon_p = 2.5$ and conductivity $\sigma_p = 0, 25, 50$ and 100 mS/m. Solution relative permittivity $\epsilon_s = 80.1$ and conductivity $\sigma_s = 50$ mS/m.

The Single-Shelled Sphere

DEP is often considered in the context of biological particles as opposed to simple homogenous spheres of polystyrene. Mammalian cells, for example, possess an elaborate intracellular structure built from dielectrically distinct components. The presence of a nucleus, nucleoplasm, cytoplasm, cell membrane and a variety of intracellular structures with their associated relaxation mechanisms serve to complicate any analysis. A simplified method is to model the cell in an approximate manner by the use of concentric dielectric shells, an approach based on the theory developed by Fricke¹⁴⁻¹⁶. Such a heterogeneous, multi-shelled, structure can then be analytically transformed into a homogeneous smeared out sphere that exhibits the same frequency dependent dielectric behaviour observed experimentally. To understand this procedure let us first consider the single-shelled sphere displayed in Fig. 2.6.

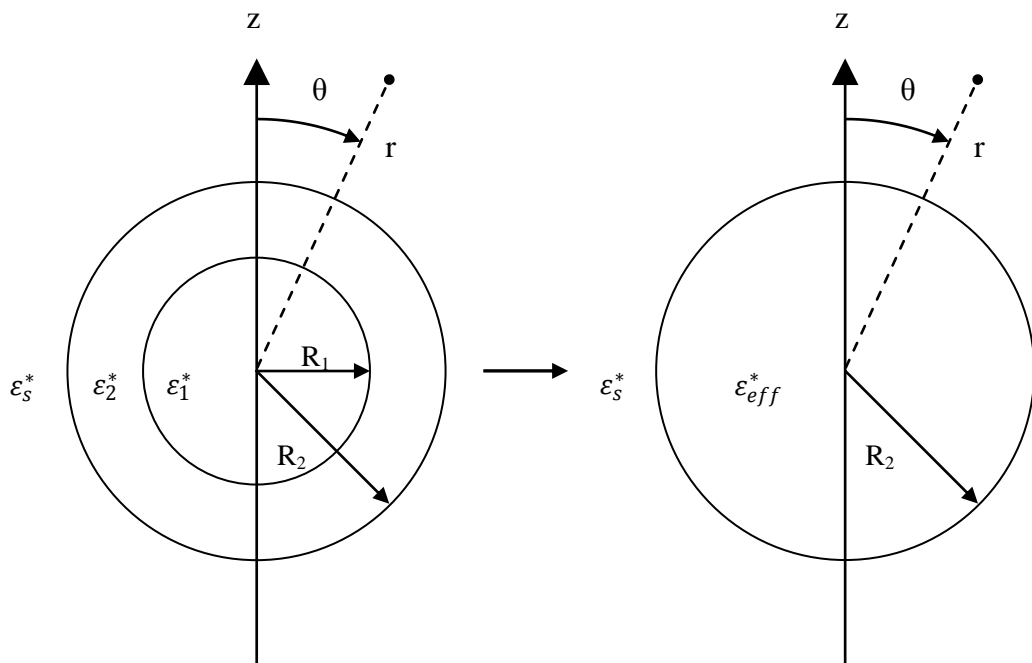


Figure 2.6 – A single shelled dielectric sphere built from a core and surrounding shell, possessing their own complex permittivities and “smeared” into an equivalent sphere of the same outer radius.

In a similar manner to the homogenous sphere of Fig. 2.3 we first assume a form for the solution of the electrostatic potential, subject to Laplace's equation:

$$\varphi_1 = -Dr \cos \theta \quad (r < R_1) \quad (2.27)$$

$$\varphi_2 = -Br \cos \theta + \frac{C \cos \theta}{r^2} \quad (R_1 < r < R_2) \quad (2.28)$$

$$\varphi_s = -E_0 r \cos \theta + \frac{A \cos \theta}{r^2} \quad (R_2 < r) \quad (2.29)$$

Boundary conditions are applied at the dielectric interfaces which correspond to continuity of the electric potential and normal component of the displacement field:

$$\varphi_1(r = R_1, \theta) = \varphi_2(r = R_1, \theta) \quad (2.30)$$

$$\varphi_2(r = R_2, \theta) = \varphi_s(r = R_2, \theta) \quad (2.31)$$

$$\varepsilon_1 \frac{\partial \varphi_1}{\partial r}(r = R_1, \theta) = \varepsilon_2 \frac{\partial \varphi_2}{\partial r}(r = R_1, \theta) \quad (2.32)$$

$$\varepsilon_2 \frac{\partial \varphi_2}{\partial r}(r = R_2, \theta) = \varepsilon_s \frac{\partial \varphi_s}{\partial r}(r = R_2, \theta) \quad (2.33)$$

Based on the forms of Eqs.(2.9) and (2.29) only the co-efficient $A = p_{\text{eff}} / 4\pi\varepsilon_s$ is required to determine the effective dipole moment as this dictates the solution outside of the particle. Solving the system of equations defined by Eqs.(2.30) through (2.33) yields:

$$A = \frac{\varepsilon_{\text{eff}} - \varepsilon_s}{\varepsilon_{\text{eff}} + 2\varepsilon_s} R_2^3 E_0 \quad (2.34)$$

where ε_{eff} is the smeared out effective permittivity representing the core and shell:

$$\varepsilon_{\text{eff}} = \varepsilon_2 \left[\frac{\left(\frac{R_2}{R_1}\right)^3 + 2\left(\frac{\varepsilon_1 - \varepsilon_2}{\varepsilon_1 + 2\varepsilon_2}\right)}{\left(\frac{R_2}{R_1}\right)^3 - \left(\frac{\varepsilon_1 - \varepsilon_2}{\varepsilon_1 + 2\varepsilon_2}\right)} \right] \quad (2.35)$$

Note that the co-efficient A contains the Clausius-Mossotti factor, similar to that derived for the lossless and homogenous dielectric sphere Eq.(2.17) with the substitution of a smeared out effective permittivity for the single-shelled sphere. As for the homogenous sphere, these expressions may be generalised further to account for conductive losses of the solution and particle by substituting in complex permittivities defined by Eq.(2.19). The resulting expression can then be compared against Eq.(2.9) to identify the effective dipole moment

and substituted into Eq.(2.2) for the instantaneous DEP force, thus allowing us to determine the time-averaged DEP force on a single-shelled lossy dielectric sphere:

$$\langle F_{DEP}(t) \rangle = 2\pi\epsilon_s R^3 \text{Re} \left(\frac{\epsilon_{eff}^* - \epsilon_s^*}{\epsilon_{eff}^* + 2\epsilon_s^*} \right) \nabla E_0^2 \quad (2.36)$$

where the single-shelled particle effective permittivity is given by:

$$\epsilon_{eff}^* = \epsilon_2^* \left[\frac{\left(\frac{R_2}{R_1} \right)^3 + 2 \left(\frac{\epsilon_1^* - \epsilon_2^*}{\epsilon_1^* + 2\epsilon_2^*} \right)}{\left(\frac{R_2}{R_1} \right)^3 - \left(\frac{\epsilon_1^* - \epsilon_2^*}{\epsilon_1^* + 2\epsilon_2^*} \right)} \right] \quad (2.37)$$

The single-shelled model is the simplest dielectric representation of a cell where the core is equivalent to the intracellular volume and the shell is equivalent to an insulating lipid membrane. Substituting representative values into the equations above yields the real part of the Clausius-Mossotti factor – $\text{Re}\{K\}$ – displayed in Fig. 2.7.

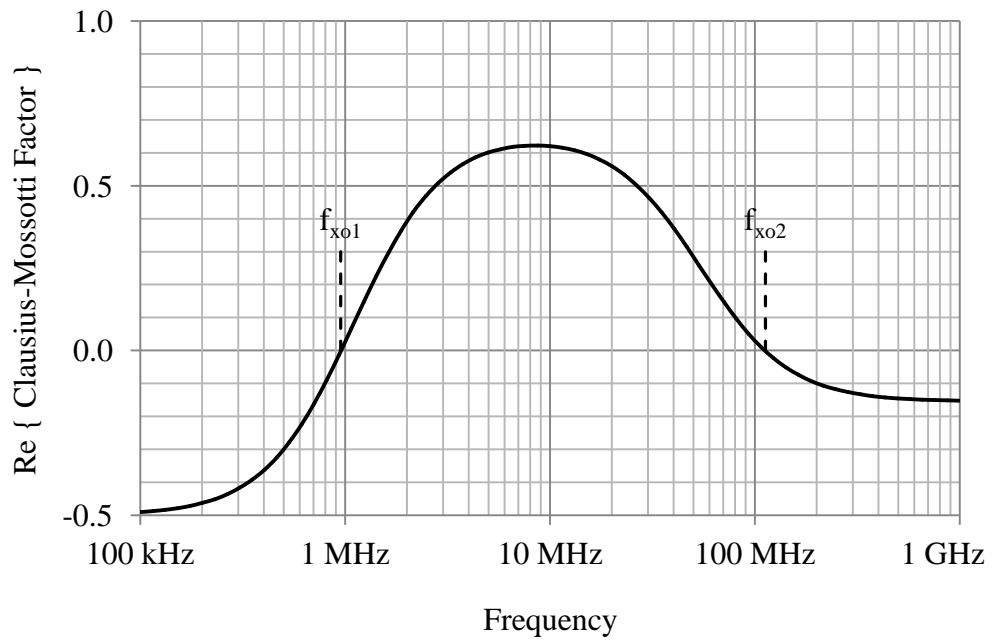


Figure 2.7 – The real part of the Clausius-Mossotti factor for a single-shelled lossy dielectric sphere. A transition from negative to positive DEP occurs at a frequency f_{xo1} followed by a transition back to negative DEP at f_{xo2} . Core relative permittivity $\epsilon_1 = 50$, conductivity $\sigma_1 = 0.5$ S/m and radius $r_1 = 2.5\mu\text{m}$. Shell relative permittivity $\epsilon_2 = 5$, conductivity $\sigma_2 = 0$ S/m and radius $r_2 = 2.51\mu\text{m}$. Solution relative permittivity $\epsilon_s = 80.1$ and conductivity $\sigma_s = 50$ mS/m.

At low frequencies the single shell model's behaviour is determined by conductivity which is effectively zero for the particle due to the insulating membrane. The real part of the Clausius-Mossotti factor K therefore tends towards a value of -0.5 and strong negative DEP. At higher frequencies the behaviour of cells is determined by both their interior permittivity and that of their suspending solution, the cell membrane acting as a capacitor which is effectively short circuited. The frequency at which the electric field begins to penetrate the cell interior is a function of the membrane conductivity, permittivity and thickness.

A useful method of analysing any multi-shelled dielectric cell model is to interpret it in terms of an equivalent electrical circuit¹⁷. The approach has been of use to researchers looking to fit data extracted by impedance spectroscopy¹⁸ and provides an insight into the frequency dependent electrical characteristics of the cell structure. In Fig. 2.8 this approach is shown for a triple-shelled model of a cell which includes a distinct nucleus, the full dielectric model for which is considered further in Chapter 3. It is the conductivities, permittivities and geometry of each shell that dictate the value of resistances and capacitances used in this equivalent model. The membrane is modelled by the equivalent resistors R_m in parallel with capacitances C_m , on both sides. The cytoplasm is modelled by a resistor R_{cp} which forms a branch parallel to that of the nucleus. A resistor R_{np} models the nucleus, or nucleoplasm, surrounded by the capacitors C_{ne} which form the nuclear membrane. The cell may be suspended in a conductive solution, between electrodes which apply an AC signal across the equivalent circuit of Fig. 2.8. It is therefore clear that the membrane forms a low-pass RC filter with the capacitor C_m bypassing the resistance R_m at sufficiently high frequencies. The analysis of this circuit model¹⁹ reveals that above ~ 1 MHz nearly all of the applied signal voltage is dropped across the cytoplasm and nucleus.

At intermediate frequencies the behaviour is a function of both Maxwell-Wagner membrane polarisation and dielectric relaxation of the core itself, processes which are a mixed function of the cell's constituent permittivities and conductivities. Positive DEP occurs between 1 and 100 MHz which results in a transition between the negative and positive regimes at two crossover frequencies termed f_{xo1} and f_{xo2} , respectively. The DEP force on the particle at these frequencies is zero and its effective dielectric properties exactly balance those of the solution displaced. Under these conditions the cell is indistinguishable from the local electric field, a situation which is equivalent to the effective dipole moment of Eq.(2.16) being equal to zero. In the high frequency limit it is intracellular permittivities which dictate the behaviour of cells, as described by Eq.(2.19). Both $\text{Re}\{K\}$ and the DEP force are negative in this limit as the core permittivity is lower than that of the suspending solution.

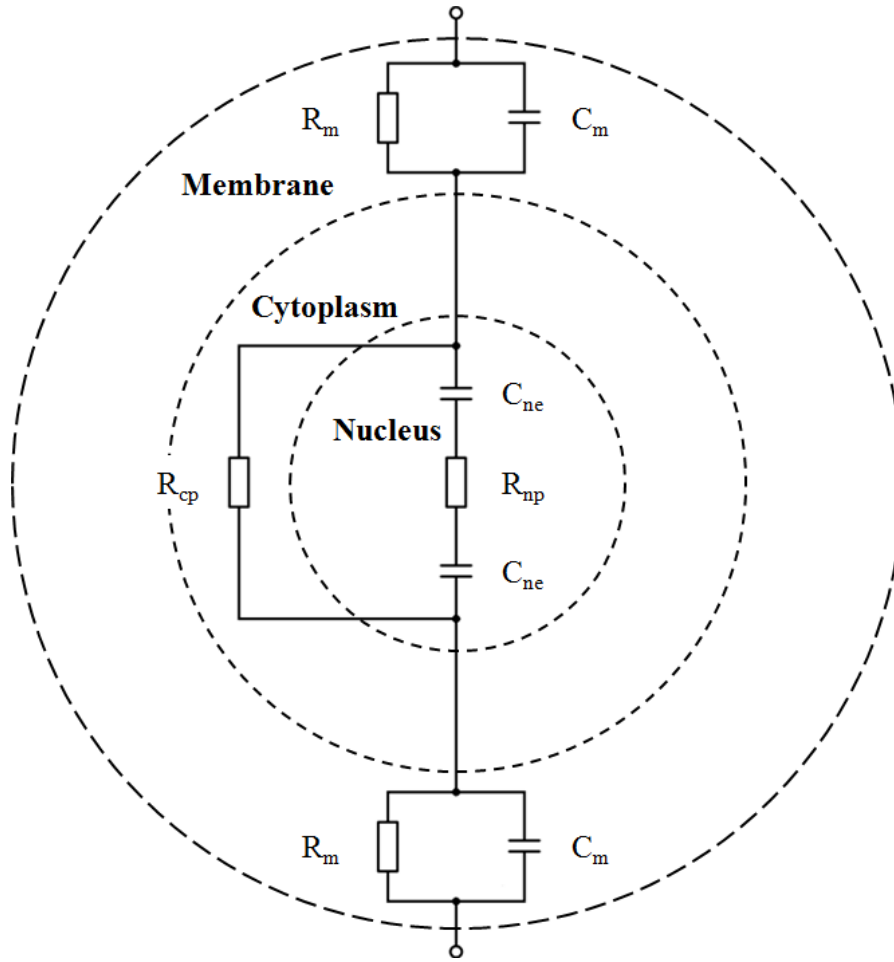


Figure 2.8 – An equivalent electrical circuit for a cell with nucleus. The membrane is modelled by the resistors R_m and capacitors C_m . The cytoplasm is modelled by a resistor R_{cp} in parallel with the nucleus, the membrane of which is modelled by the capacitors C_{ne} and nucleoplasm by the resistor R_{np} .

Crossover frequencies can provide an effective means of sorting cells if their value is related to a desired trait of the particle. Two particles which exhibit different values of f_{x01} , for example, may be differentiated by applying a frequency located between them. The low f_{x01} particle will be attracted towards an applied field concentration whilst the high f_{x01} particle is repelled. This approach has formed the basis for many microfluidic DEP sorting devices by either selectively attracting particles onto patterned electrodes or using more sophisticated deflection geometries. If crossover frequencies exist the real part of Eq.(2.20) must equal zero which, by substituting expressions for the particle and solution complex permittivity based on Eq.(2.19), yields Eq.(2.38).

$$\begin{aligned}
Re\{K^*\} &= Re\left\{\frac{\varepsilon_p^* - \varepsilon_s^*}{\varepsilon_p^* + 2\varepsilon_s^*}\right\} = Re\left\{\frac{\varepsilon_p - \frac{j\sigma_p}{\omega_{xo}} - \varepsilon_s + \frac{j\sigma_s}{\omega_{xo}}}{\varepsilon_p - \frac{j\sigma_p}{\omega_{xo}} + 2\varepsilon_s - 2\frac{j\sigma_s}{\omega_{xo}}}\right\} \\
&= \frac{1}{\omega_{xo}^2}(\sigma_p + 2\sigma_s)(\sigma_s - \sigma_p) - (\varepsilon_p - \varepsilon_s)(\varepsilon_p + 2\varepsilon_s) = 0 \\
\Rightarrow f_{xo} &= \frac{\omega_{xo}}{2\pi} = \frac{1}{2\pi} \sqrt{\frac{(\sigma_p + 2\sigma_s)(\sigma_s - \sigma_p)}{(\varepsilon_p - \varepsilon_s)(\varepsilon_p + 2\varepsilon_s)}} \tag{2.38}
\end{aligned}$$

When considering a single-shelled particle the conductivity σ_p and permittivity ε_p of the particle represent effective values which are determined by the smeared expression of Eq.(2.37). An analytical solution to Eq.(2.38) in the low frequency case was derived by Huang *et al.*²⁰ for mammalian cells by applying DC approximations proposed by Schwan²¹, where $\sigma_p = RG_m$ and $\varepsilon_p = RC_m$, yielding:

$$f_{xo1} = \frac{\sqrt{2}}{2\pi RC_m} \sigma_s - \frac{\sqrt{2}G_m}{8\pi C_m} \tag{2.39}$$

In this equation R is the radius of a spherical cell with membrane conductance G_m and capacitance C_m per unit area, respectively, suspended in a solution of conductivity σ_s . G_m accounts for both the passive conductance of ions across the membrane and the surface conductance associated with the electrical double layer which surrounds all cells. The second term of Eq.(2.39) is often neglected as it is typically 100x smaller than the first, thus allowing a determination of the membrane capacitance from f_{xo1} and cell radius alone for a known solution conductivity.

As the solution conductivity is increased f_{xo1} rises in a proportional manner, however the DEP spectrum, plotted in Fig. 2.9, is altered drastically. By quadrupling the solution conductivity from 50 to 200 mS/m the peak value for $Re\{K\}$ is roughly halved, severely reducing the applied DEP force. The practical impact of this force reduction depends on the device but may increase the time required or potentially lead to a complete failure in identifying any crossover. At 800 mS/m the particle will only experience negative DEP and prevents the possibility of using any crossover based separation. Mammalian cells are typically grown in culture media of ~1.5 S/m conductivity and therefore require re-suspension into a lower conductivity solution. DEP solutions based upon this approach are widely used and have presented few issues in the f_{xo1} regime, as long as they are isotonic and able to retain the integrity of cell membranes for the duration of experiments.

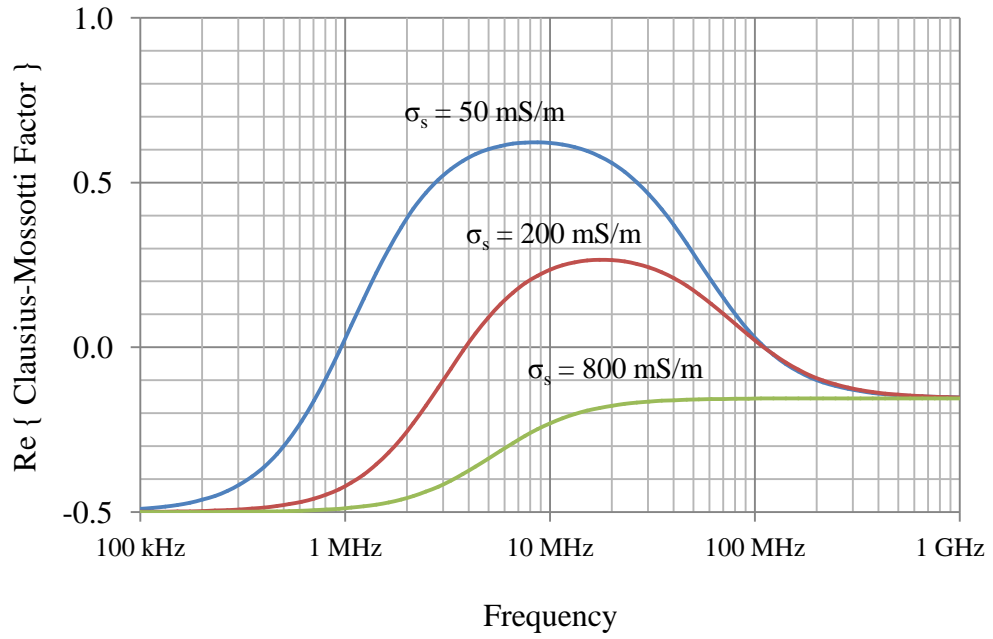


Figure 2.9 – The real part of the Clausius-Mossotti factor for a single-shelled lossy dielectric sphere. Parameters are as described for Fig. 2.6 with solution conductivities $\sigma_s = 50$ mS/m, 200 mS/m and 800 mS/m.

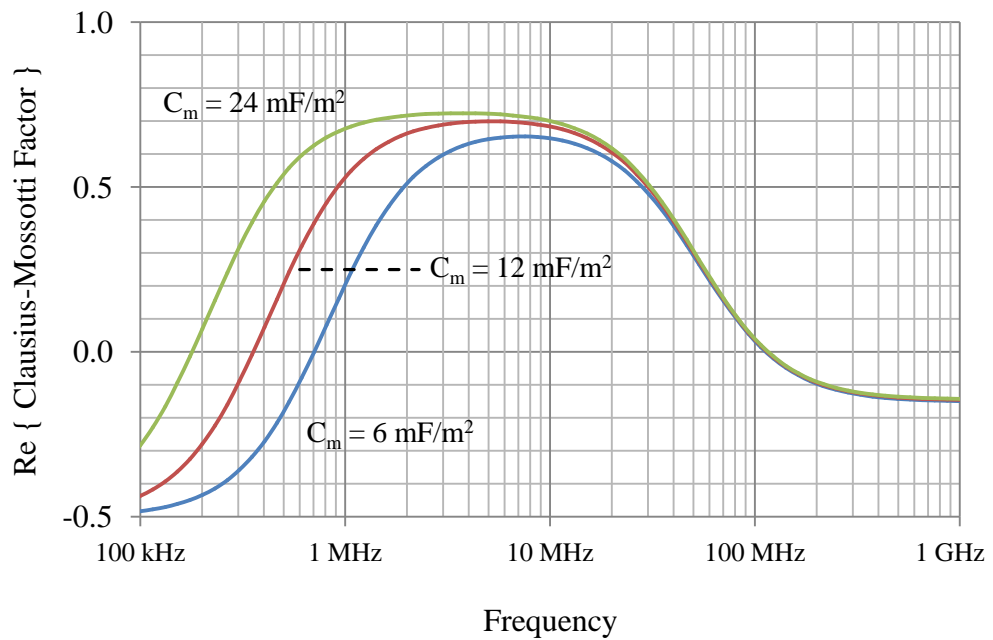


Figure 2.10 – The real part of the Clausius-Mossotti factor for a single-shelled lossy dielectric sphere. Parameters are as described for Fig. 2.6 with membrane capacitances $C_m = 6$ mF/m², 12 mF/m² and 24 mF/m².

Membrane capacitance is an important parameter to derive and is related to the topography of a cell membrane. The modelled cell-like structure assumes a perfect sphere; however real cells exhibit blebs, microvilli and ruffles which contribute to the membrane capacitance per unit area C_m . Fig. 2.10 displays the effect of varying this membrane capacitance on the DEP spectrum at values representative of actual cells. As predicted by Eq.(2.41), f_{x01} scales with the inverse of C_m but also indicates that these differences are largely restricted to the lower end of the spectrum. At higher frequencies this capacitance effectively short circuits the membrane at which point intracellular dielectric properties are expected to dominate the DEP response, leading to a higher frequency crossover.

Electrorotation

The DEP force acting on a dielectric particle was derived by considering an infinitesimal dipole in a non-uniform electric field. A torque may also be exerted upon a dipole due to the net forces acting about its centre, with contributions from each charge:

$$\bar{T}_{dipole} = \frac{\mathbf{d}}{2} \times q\mathbf{E} + \frac{-\mathbf{d}}{2} \times -q\mathbf{E} = q\mathbf{d} \times \mathbf{E} = \mathbf{p} \times \mathbf{E} \quad (2.40)$$

This torque is only dependent on the magnitude and direction of the applied electric field rather than its gradient, as is the case for the induced DEP force. A torque will therefore arise if the dipole moment and electric field are not in alignment, assuming that any non-uniformities in the electric field are significantly larger than the dipole itself. If the field is time-varying then the instantaneous torque may be expressed for the complex effective dipole vector \mathbf{p}_{eff}^* as:

$$\mathbf{T}(t) = \mathbf{p}_{eff}^*(\mathbf{r}, t) \times \mathbf{E}^*(\mathbf{r}, t) = Re(\mathbf{p}_{eff}^*(\mathbf{r})e^{j\omega t}) \times Re(\mathbf{E}^*(\mathbf{r})e^{j\omega t}) \quad (2.41)$$

Defining the electric field as being circularly polarized in the form $\mathbf{E}^* = E_0(\hat{x} - j\hat{y})$, the time-averaged torque based on the complex effective dipole of Eq.(2.23) is:

$$\langle \mathbf{T}(t) \rangle = \frac{1}{2} Re(\mathbf{p}_{eff}^* \times \overline{\mathbf{E}^*}) = -4\pi\epsilon_s R^3 Im\left(\frac{\epsilon_p^* - \epsilon_s^*}{\epsilon_p^* + 2\epsilon_s^*}\right) E_0^2 \hat{z} \quad (2.42)$$

The dependence of this electrorotation, or ROT, on the imaginary component of the Clausius-Mossotti factor clearly indicates its relationship to DEP and the real component. This relationship is governed by the Kramers-Krönig integrals²² which provide a unifying framework for these phenomena. If we consider a lossy dielectric particle in a rotating electric field, such as that generated by the quadrupolar electrodes described in Fig. 1.3, a dipole is induced which will continuously attempt to align itself with the field. If the charge

relaxation time $\tau_r = \epsilon / \sigma$ of the suspending solution exceeds that of the particle it will rotate with the electric field, if the opposite is true the particle will rotate against the field. Although the induced charges follow the field it is their continuous repulsion which generates a torque and as the particle surface rotates it pulls the surrounding solution with it. Since the solution adjacent to the particle rotates with it, but not the bulk further away, the adjacent layers of fluid must rotate at angular velocities which diminish with distance. These infinitesimal layers of fluid experience friction between themselves, leading to a drag force which is proportional to the particle's angular velocity. This proportional constant is known as the dynamic viscosity and allows for a derivation of the steady-state angular velocity¹:

$$\Omega = -\frac{\epsilon_s}{2\eta_s} \text{Im} \left(\frac{\epsilon_p^* - \epsilon_s^*}{\epsilon_p^* + 2\epsilon_s^*} \right) E_0^2 \quad (2.43)$$

where η is the fluid dynamic viscosity in PaS. By this method it is possible to derive the imaginary part of the Clausius-Mossotti factor from the measured angular velocity of a cell across a range of frequencies, allowing for the fit of a multi-shelled dielectric model. Although not considered in this thesis the approach is noteworthy as it has already been used in the extraction of membrane capacitance and intracellular conductivity values^{23,24}.

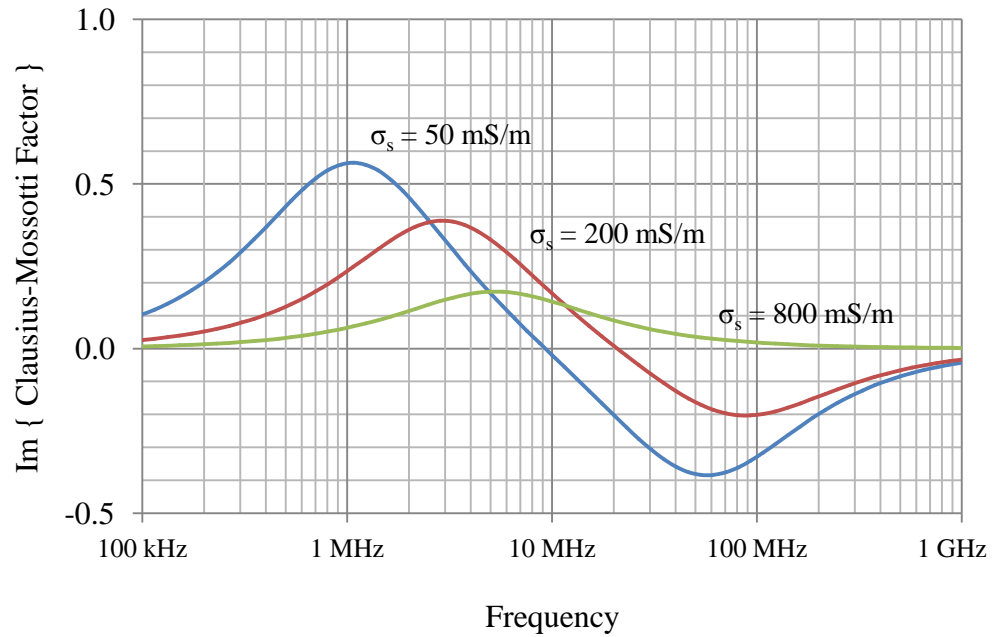


Figure 2.11 – The imaginary part of the Clausius-Mossotti factor for a single-shelled lossy dielectric sphere. Parameters are as described for Fig. 2.6 with solution conductivities $\sigma_s = 50 \text{ mS/m}$, 200 mS/m and 800 mS/m .

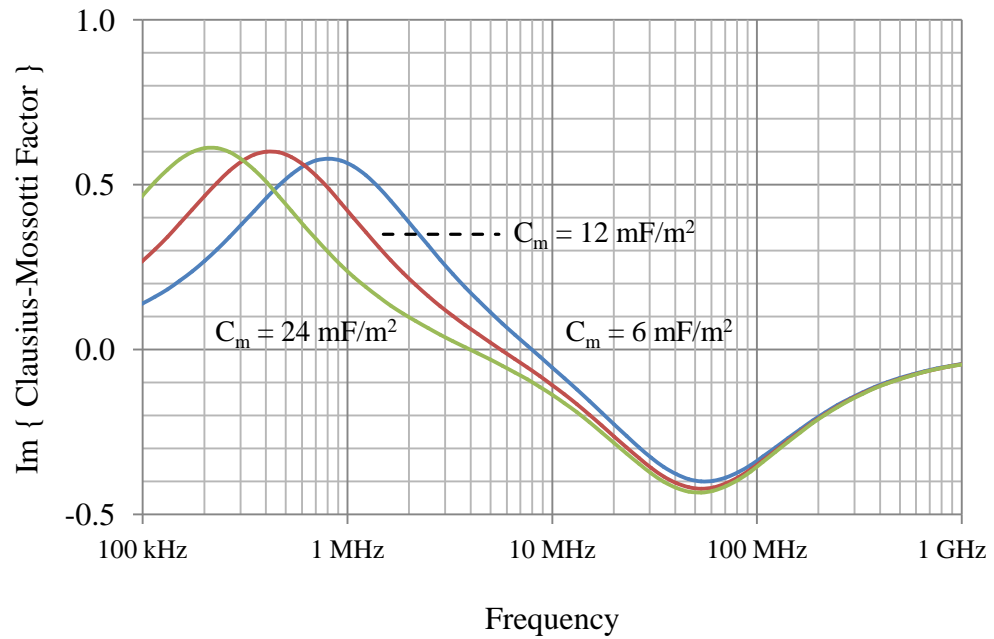


Figure 2.12 – The imaginary part of the Clausius-Mossotti factor for a single-shelled lossy dielectric sphere. Parameters are as described for Fig. 2.6 with membrane capacitances $C_m = 6 \text{ mF/m}^2$, 12 mF/m^2 and 24 mF/m^2 .

In Fig. 2.11 the imaginary part of the Clausius-Mossotti factor is plotted for the particle and solution conductivity values of Fig. 2.9. The peaks of the ROT spectrum correspond to the points of steepest gradient in the DEP spectrum, a direct result of the Kramers-Krönig relationship which also holds for the membrane capacitance in Figs. 2.10 and 2.12. In principle a separation system based on TWD could be used to exploit differences in intracellular conductivity that affect the zero-rotation point of the ROT spectrum. The primary drawback of this approach is the associated influence from the cell membrane at these frequencies, an issue which should be avoided at the higher frequency DEP crossover.

Conclusion

The infinitesimal dipole has been introduced and used to derive a general expression for the DEP force acting upon it. By using the effective dipole method an expression for this force has been derived for a lossless and homogenous dielectric sphere. This expression indicates that the DEP force is proportional to particle volume, requires a non-uniform electric field and has behaviour dependent upon the difference in dielectric properties between the particle and suspending solution. The incorporation of complex permittivities to account for loss and the addition of a shell via an effective smearing method yielded a model which is analogous

to mammalian cells. This model exhibits two crossover frequencies marking the transition between regions of negative and positive DEP. An expression for the first crossover f_{x01} provides important information regarding membrane topography and the basis for selectively characterising and separating cells. The higher frequency crossover f_{x02} is expected to be a function of intracellular dielectric properties which are not accurately described by the single shell model.

References

- 1 Jones, T. B. (1995) *Electromechanics of Particles*, Cambridge: Cambridge University Press.
- 2 Pethig, R. (2010) Review Article-Dielectrophoresis: status of the theory, technology and applications. *Biomicrofluidics*, 4 (2), 022811.
- 3 Struik, D. J. (1969) *A Source Book in Mathematics, 1200-1800*, Cambridge: Harvard University Press.
- 4 Halliday, D., Resnick, R. & Walker, J. (2005) *Fundamentals of Physics*, Hoboken: John Wiley & Sons.
- 5 Washizu, M. & Jones, T. B. (1994) Multipolar dielectrophoretic force calculation. *Journal of Electrostatics*, 33 (2), 187-198.
- 6 Pethig, R., Bressler, V., Carswell-Crumpton, C., Chen, Y., Foster-Haje, L., Garcia-Ojeda, M. E., Lee, R. S., Lock, G. M., Talary, M. S. & Tate, K. M. (2002) Dielectrophoretic studies of the activation of human T lymphocytes using a newly developed cell profiling system. *Electrophoresis*, 23 (13), 2057-2063.
- 7 Pethig, R., Lee, R. S. & Talary, M. S. (2004) Cell physiometry tools based on dielectrophoresis. *Journal of Laboratory Automation*, 9 (5), 324-330.
- 8 Zwillinger, D. (2002) *CRC Standard Mathematical Tables and Formulae, 31st Edition*, Boca Raton: CRC Press.
- 9 Altmann, S. L. & Ortiz, E. L. (2006) *Mathematics and Social Utopias in France: Olinde Rodrigues and His Times (History of Mathematics)*, Providence: American Mathematical Society.
- 10 Stratton, J. A. (1941) *Electromagnetic Theory*, New York: McGraw-Hill.
- 11 Morgan, H. & Green, N. G. (2003) *AC Electrokinetics: Colloids and Nanoparticles*, Baldock: Research Studies Press.
- 12 Maxwell, J. C. (1891, reprinted 1998) *A treatise on electricity and magnetism*, 3rd ed., New York: Oxford University Press
- 13 Wagner, K. W. (1914) Erklärung der dielektrischen nachwirkungsvorgänge auf Grund Maxwellscher Vorstellungen. *Archiv für Elektrotechnik*, 2 (9), 371-387.
- 14 Fricke, H. (1925) The electric capacity of suspensions of red corpuscles of a dog. *Physical Review*, 26, 682-687.
- 15 Fricke, H. (1925) The Electric capacity of suspensions with special reference to blood. *The Journal of General Physiology*, 9 (2), 137-152.
- 16 Fricke, H. (1925) The electric resistance and capacity of blood for frequencies between 800 and 4½ million cycles. *The Journal of General Physiology*, 9 (2), 153-167.

- 17 Schoenback, K. H., Buescher, E. S. & Beebe, S. J. (2002) Bioelectrics - New applications for pulsed power technology. *IEEE Transactions on Plasma Science*, 30 (1), 293-300.
- 18 Pethig, R. & Schmuesser, I (2012) Marking 100 years since Rudolf Höber's discovery of the insulating envelope surrounding cells and of the β -dispersion exhibited by tissue. *Journal of Electrical Bioimpedance*, 3, 74-79.
- 19 Ellappan, P. & Sundararajan, R. (2005) A simulation study of the electrical model of a biological cell. *Journal of Electrostatics*, 63 (3-4), 297-307.
- 20 Huang, Y., Wang, X. B., Becker, F. F. & Gascoyne, P. R. C. (1996) Membrane changes associated with the temperature-sensitive P85gag-mos-dependent transformation of rat kidney cells as determined by dielectrophoresis and electrorotation. *Biochimica et Biophysica Acta (BBA) - Biomembranes*, 1282 (1), 76-84.
- 21 Schwan, H. P. (1957) Electrical properties of tissue and cell suspensions. *Advances in Biological and Medical Physics*, 5, 147-209.
- 22 Pastushenko, V. P., Kuzmin, P. I. & Chizmadzhev, Y. A. (1985) Dielectrophoresis and electrorotation: a unified theory of spherically symmetrical cells. *Studia biophysica*, 110, 51-57.
- 23 Gimsa, J., Müller, T., Schnelle T. & Fuhr, G. (1996) Dielectric spectroscopy of single human erythrocytes at physiological ionic strength: dispersion of the cytoplasm. *Biophysical Journal*, 71 (1), 495-506.
- 24 Han, S. I., Joo, Y. D. & Han, K. H. (2013) An electrorotation technique for measuring the dielectric properties of cells with simultaneous use of negative quadrupolar dielectrophoresis and electrorotation. *Analyst*, 138 (5), 1529-1537.

Chapter Three

Device Requirements, Design & Fabrication

Introduction

The concept of a crossover frequency, where the dielectrophoretic force induced upon a cell is zero, was introduced in Chapter Two. To simplify the theoretical discussion a single-shelled model of a cell was used. Under experimental conditions which are typical for DEP - i.e. for mammalian cells suspended in an isosmotic solution of less than 50mS/m conductivity at room temperature - a crossover referred to as f_{x01} occurs below a frequency of 1 MHz. This crossover has been a principal focus of research to date and widely understood to be a function of the cell membrane's composition¹, topology² and integrity³. At higher frequencies a crossover referred to as f_{x02} is predicted and is expected to be a function of intracellular dielectric properties.

In this chapter the theory is further developed by incorporating additional shells to the model which thereby allow us to represent the intracellular structure of a cell, an approach used to provide an estimate of the expected frequency range for f_{x02} . These higher frequencies require the careful design of a device which itself needs to be modelled appropriately. A distributed RCR network is proposed for this purpose and validated against a range of test structures by measurement of their impedance spectra. The levitation of cells is discussed as a practical necessity for the accurate measurement of their crossover frequencies, one which dictates the minimal operating voltage and thus bandwidth of a device. Based on these requirements a device is designed and fabricated which is able to operate over the expected frequency range of f_{x02} .

The Multi-Shelled Spherical Model of a Cell

A high frequency crossover marking a transition from positive to negative DEP is predicted by the single-shelled cell model introduced in Chapter Two. Referred to as f_{x02} , the behaviour of a cell at these high frequencies is determined by intracellular dielectric properties which are only approximately modelled by the simple core volume. By adding further shells to this model it is possible to incorporate the nucleoplasm, nuclear envelope, cytoplasm and cell membrane as distinct – albeit simplified – entities. By generalising the smearing operation of a single shell and core described by Eq.(2.35) any effective core may

be merged with its surrounding shell⁴, a procedure which may be summarised by the following expression for the resultant smeared complex permittivity:

$$\varepsilon_{eff}^* = \varepsilon_{n+1}^* \frac{\left(\frac{r_{n+1}}{r_n}\right)^3 + 2\left(\frac{\varepsilon_n^* - \varepsilon_{n+1}^*}{\varepsilon_n^* + 2\varepsilon_{n+1}^*}\right)}{\left(\frac{r_{n+1}}{r_n}\right)^3 - \left(\frac{\varepsilon_n^* - \varepsilon_{n+1}^*}{\varepsilon_n^* + 2\varepsilon_{n+1}^*}\right)} \quad (3.1)$$

where the n^{th} shell of complex permittivity ε_n^* and radius r_n is merged with the surrounding $(n+1)^{\text{th}}$ shell of complex permittivity ε_{n+1}^* and radius r_{n+1} . The complex permittivity ε_n^* may be expressed in the form of Eq.(2.19) for the first shell and more generally as the result of a previous smearing operation. This transformation creates a sphere of complex permittivity ε_{eff}^* and radius r_{n+1} which can then act as the core for a subsequent transformation, a procedure which may be repeated to homogenise an entire particle. A diagram of its use is displayed in Fig. 3.1 where the effective permittivity of an n-shelled sphere is derived by n successive applications of Eq.(3.1).

The expected DEP spectrum for murine lymphocytes derived from electro-impedance measurements made by Asami *et al.*⁵ is shown in Fig. 3.2. It assumes suspension into a solution of 50 mS/m conductivity with fitted parameters as described in the figure legend. DEP crossovers exist where the real part of the Clausius-Mossotti factor is equal to zero, a condition which first occurs at 400 kHz for the low frequency crossover f_{x01} . Of particular importance is the expected value for f_{x02} of 215 MHz. Several parameters are likely to affect its position and distribution however the ratio of nucleus to cytoplasm is amongst the most significant, a parameter which can vary greatly over the cell-division cycle. By varying the modelled nucleus volume from zero up to the entire intracellular space it is suggested that f_{x02} could potentially range from 90 to 300 MHz. This analysis is simplified as intracellular variations in both ionic concentration and organelle structure could have a significant effect, nevertheless it is informative and should be considered a minimal requirement. A DEP device was therefore required which could apply an electric field of sufficient strength and non-uniformity across this entire range.

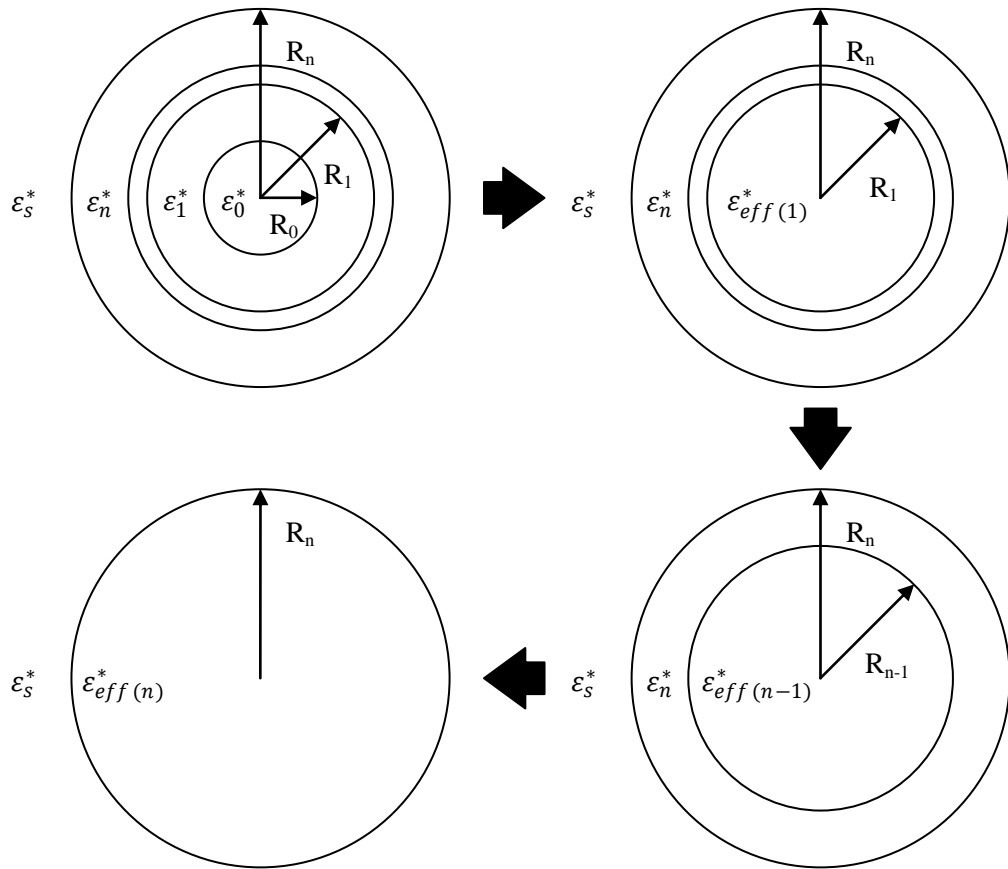


Figure 3.1 – A multi shelled dielectric sphere built from a core and n shells, each possessing their own complex permittivity, progressively transformed by n smearing operations into an equivalent homogenous sphere.

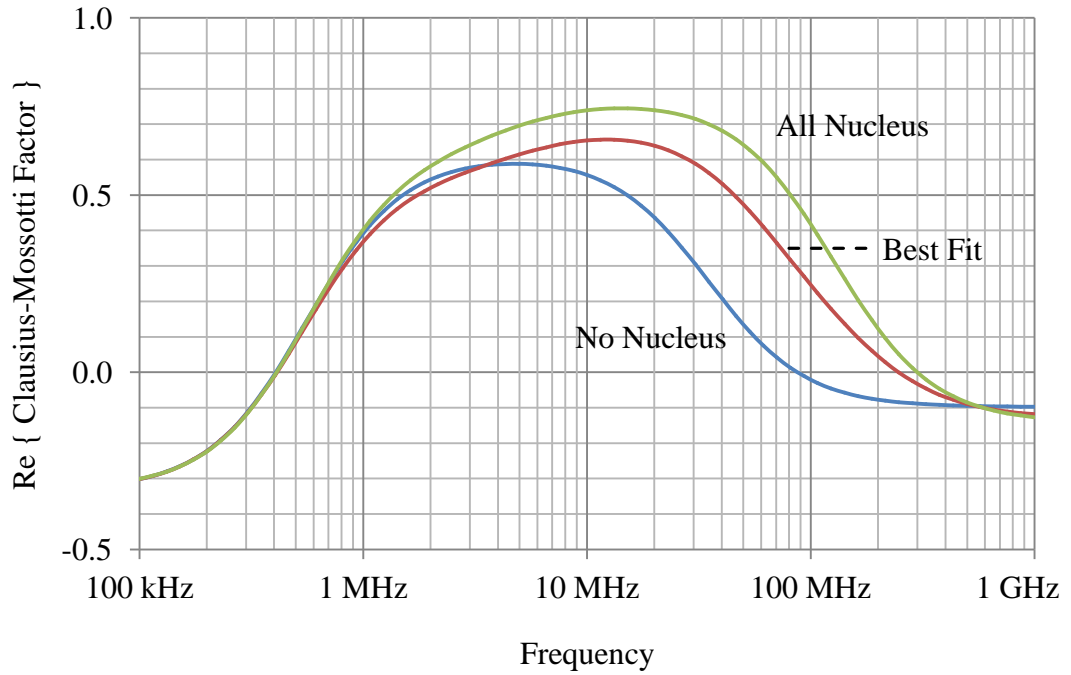


Figure 3.2 – The real part of the Clausius-Mossotti factor for a triple-shelled lossy dielectric sphere based on the fitted electro-impedance measurements of murine lymphocytes made by Asami *et al.* Nucleoplasm relative permittivity $\epsilon_1 = 52$, conductivity $\sigma_1 = 1.35$ S/m and radius $r_1 = 2.460\mu\text{m}$. Nuclear envelope relative permittivity $\epsilon_2 = 28$, conductivity $\sigma_2 = 6$ mS/m and radius $r_2 = 2.500\mu\text{m}$. Cytoplasm relative permittivity $\epsilon_3 = 60$, conductivity $\sigma_3 = 0.32$ S/m and radius $r_3 = 2.893\mu\text{m}$. Membrane relative permittivity $\epsilon_4 = 6.8$, conductivity $\sigma_4 = 32$ $\mu\text{S/m}$ and radius $r_2 = 2.900\mu\text{m}$. Solution relative permittivity $\epsilon_s = 80.1$ and conductivity $\sigma_s = 50$ mS/m.

Interdigitated electrodes are ubiquitous in DEP research, possessing a geometry which is simple to fabricate and capable of generating fields of high non-uniformity at the micron scale. Such fields inherently involve the use of high capacitances with small geometries that allow the use of low operating voltages. At the operating frequencies of f_{x01} – typically below 1 MHz – the design of such electrodes is relatively trivial. In addition, the requirement of low solution conductivities allows for the definition of a large electrode area without great concern for loading or bandwidth. At the high frequencies being considered for f_{x02} , however, the need arises for an accurate model capable of predicting the precise electrical behaviour of the electrodes.

Interdigitated Electrode Modelling

Interdigitated electrodes (IDEs) are often considered as lumped capacitances; however this approximation may break down under various conditions. A pair of IDEs is displayed in Fig. 3.3, each formed by a conductive pad and track deposited onto a substrate. Under typical DEP conditions a conductive aqueous solution is deposited over the electrodes and an AC voltage is applied across the two pads. This voltage generates a non-uniform electric field across the gap with field concentrations situated along their opposing edges. The gap itself constitutes a load which is both resistive and capacitive, due primarily to the ionic conductivity and permittivity of the solution, respectively. Assuming a glass substrate is being used, its contribution to the net conductivity across the gap is negligible. Likewise, glass will not contribute significantly to the capacitance across the gap as its permittivity is significantly lower ($\epsilon_r = 6.8$ for glass versus $\epsilon_r = 80.1$ for water).

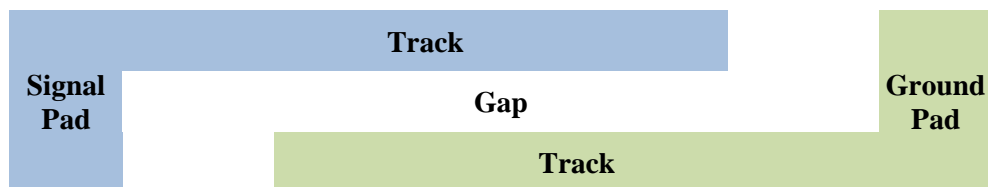


Figure 3.3 – Geometry for a pair of IDE tracks deposited on a substrate.

In practice the tracks possess a resistance per unit length and therefore require a distributed RC network to account for the load placed across them. It is clearly desirable to minimise the voltage dropped along the length of these tracks. Unfortunately, solving for the frequency response of these networks involves hyperbolic functions which do not readily lend themselves to a simple analysis⁶. Alternatively, the geometry may be broken down into unit sections of circuit which still provide a good approximation. The RCR network displayed in Fig. 3.4 was selected for this approach where lumped components represent the track resistance R_t , gap resistance R_g and gap capacitance C for each unit section – by simply increasing the number of units used the accuracy of this model may be improved. Zhu *et al.*⁷ suggested the use of a distributed network to account for the apparent DEP induced translation of particles around spiral electrodes, a phenomenon which was exploited in the construction of particle chains; a thorough analysis of which was not undertaken. An important advantage of this approach is its ease of implementation in circuit simulators, such as SPICE, and the incorporation of realistic drive conditions. Before using this approach to design an “ f_{xO_2} -capable” device, test structures were required to determine how

representative such an RCR network model would be. The measurement of voltage distributions within such structures, as a means of comparison, is desirable but technically difficult to achieve. Instead, their impedance spectra were used as an alternative means of comparison.

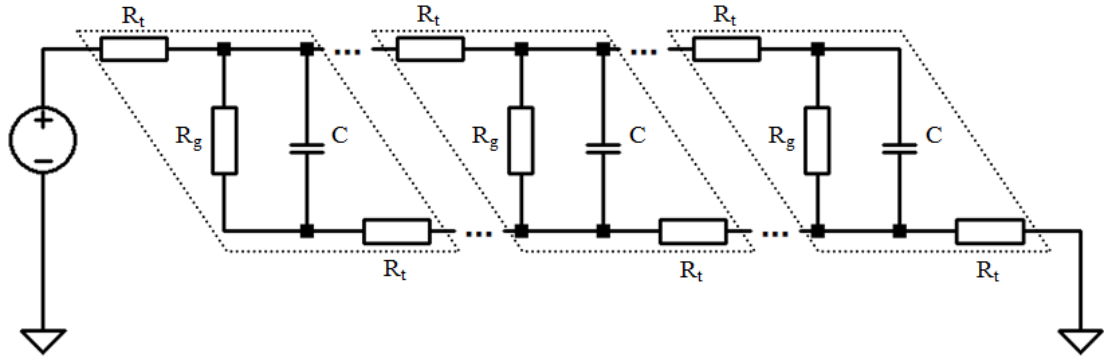


Figure 3.4 – A distributed RCR network representation of an IDE array, dashed lines surround each unit section.

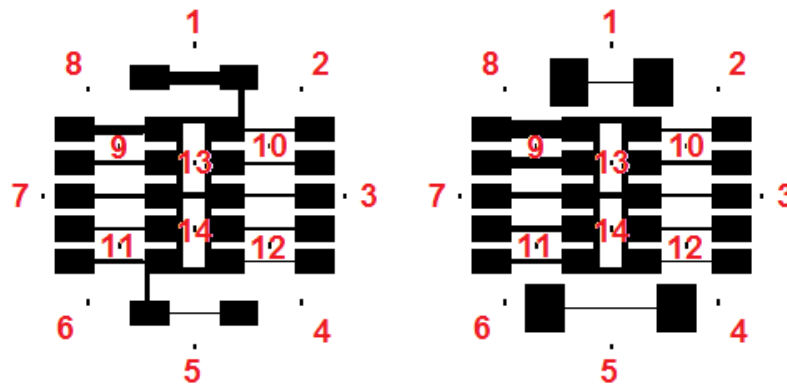


Figure 3.5 – Mask layouts for IDE testing with 20:20 and 20:40 μm mark-space ratio devices on the left and right, respectively. The locations of Kelvin cross bridge resistors are numbered.

The layout of two test masks used to determine the validity of the RCR network model is displayed in Fig. 3.5. These masks consisted of IDE test structures of up to sixty electrode tracks, each 10mm in length with mark-space ratios, representing the track width and separation gap, of 20:20 and 20:40 μm . Such dimensions are typical of cell-based DEP devices as cells generally possess a radius of between 3 and 10 μm . The structure is therefore large enough to determine which cells are undergoing positive rather than negative DEP. These IDE structures were interspersed by Kelvin cross bridge resistors which possessed

tracks of an identical width. By using standard test methods the electrical linewidth and sheet resistance could therefore be determined across the wafers and used to inform the model.

The fabrication process began with a bare 10cm glass wafer which was cleaned in piranha solution, rinsed with deionised water and dried. Electron beam evaporation of a 10nm titanium adhesion layer followed by 100nm of platinum was performed. In this process a metal target is bombarded by electrons from a tungsten filament operating in a high vacuum, evaporating metal atoms which then precipitate on all of the chamber surfaces within their line of sight, thereby coating the glass wafer. A photoresist was deposited onto the metal surface, exposed through the layout mask, developed and hard baked. The exposed platinum was then removed by reactive-ion etching with a subsequent wet etch of the titanium. A plasma barrel ash was used to remove the remaining photoresist, exposing the devices for electrical analysis.

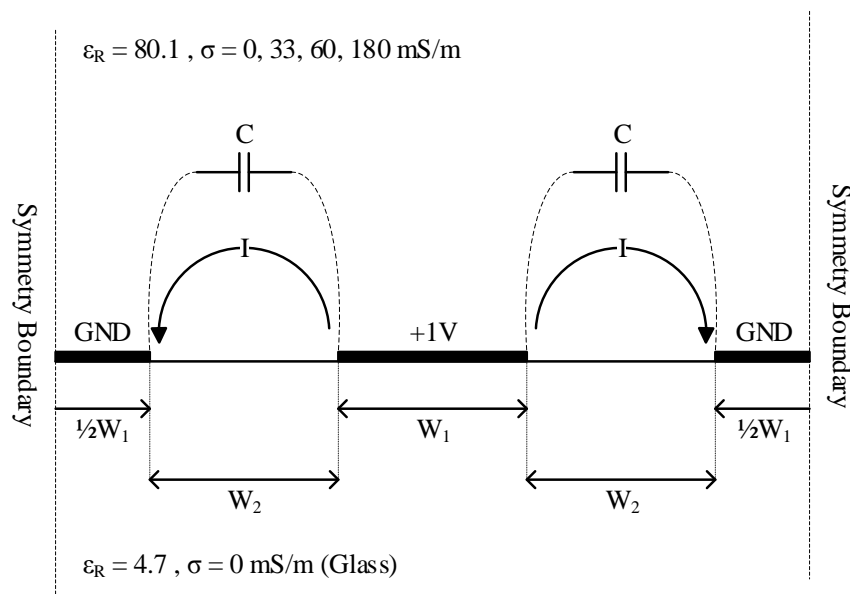


Figure 3.6 – Finite element simulation cross-section of the IDE tracks which run perpendicular to the page. The displayed values for relative permittivity ϵ_r and conductivity σ are applied with periodicity assumed in the horizontal axis.

COMSOL was used to perform electrostatic finite element simulations of electrode cross-sections for both mark-space ratios, to determine their gap resistance R_g and capacitance C . The mark-space ratios were determined from their mean electrical linewidths, measured as $24\mu\text{m}$ for the 20:20 μm devices and $21\mu\text{m}$ for the 20:40 μm devices. Their sheet resistances were determined to be 1.8 and 1.7 Ω/\square , respectively. Tracks bounded by other tracks were assumed to be spatially periodic in both directions, as displayed in Fig. 3.6, whereas those at

the edge were considered as a standalone pair. An aqueous solution of 33 mS/m conductivity was simulated for both mark-space ratios with additional values of zero, 60 and 180 mS/m for the 20:20 μm ratio. The resulting capacitance values are displayed in Table 3.1 with the current – induced by a 1V potential difference – shown in Table 3.2, both per unit metre of the track length.

Track Width (μm)	Track Spacing (μm)	Gap Capacitance, C (F/m)	
		Centre	Edge
24	16	4.413×10^{-10}	6.475×10^{-10}
21	39	3.078×10^{-10}	4.658×10^{-10}

Table 3.1 – Gap capacitances, per unit metre of track length, estimated at the centre and edge.

Track Width (μm)	Track Spacing (μm)	Solution Conductivity (mS/m)	Gap Current (A/m)	
			Centre	Edge
24	16	33	1.930×10^{-2}	2.860×10^{-2}
24	16	60	3.510×10^{-2}	5.199×10^{-2}
24	16	180	1.053×10^{-1}	1.560×10^{-1}
21	39	33	1.333×10^{-2}	1.978×10^{-2}

Table 3.2 – Gap currents induced by a 1V potential difference, per unit metre of track length, estimated at the centre and edge. The gap resistance is calculated by dividing the simulated 1 volt by the product of gap current and section length.

Electrical connections were established with the test structures by soldering the ground of an SMA connector directly to one electrode pad with the enclosed signal pin wired across to the opposing pad. An Agilent E4991A impedance analyser was calibrated up to the point of connection and used to determine the impedance magnitude of the IDE structures between 1 MHz and 1 GHz. Conductive aqueous solutions were prepared by adding phosphate buffered saline to deionised water and measured using an Oakton 510 conductivity meter. The majority of the electric field is concentrated within $\sim 100\mu\text{m}$ of the electrodes therefore, to ensure the validity of simulations, a PDMS gasket was used to ensure a solution depth of at least $500\mu\text{m}$. SPICE simulations of the IDEs replicated the distributed network of Fig. 3.4 with the use of twenty unit sections along each track, an effective length of $500\mu\text{m}$ per section. The gap capacitance and resistance values were calculated for these sections based on the values of Tables 3.1 and 3.2. Likewise, track resistances were calculated from the

aforementioned sheet resistances, derived from cross-bridge measurements. An inductance of 13nH was placed in series to simulate the length of wire used for the signal pad to SMA connection.

Variation in Conductivity

A 20:20 μm mark-space ratio test structure with eighteen interdigitated electrodes was prepared using solution conductivities of 0, 60 and 180 mS/m. The measured and modelled impedance magnitudes are displayed in Fig. 3.7.

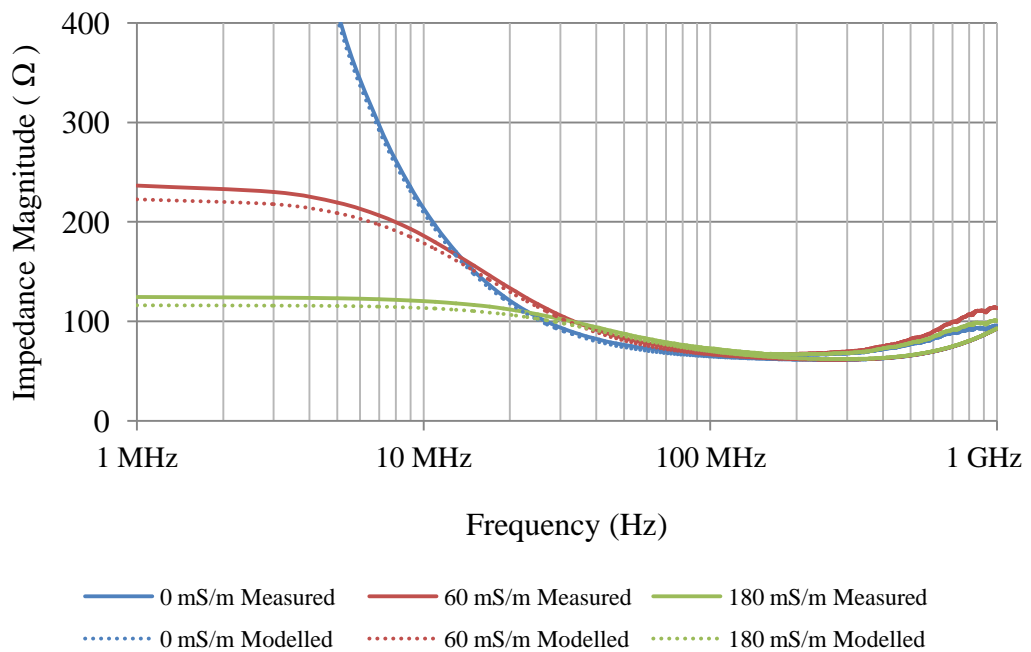


Figure 3.7 – Measured and modelled impedance magnitudes for a 20:20 μm mark-space ratio device with nine pairs of electrodes and three solution conductivities. The impedance magnitude error is less than $\pm 5\%$ across the displayed range.

The impedance of pure deionised water approaches infinity in the DC limit and plateaus at distinct values for conductivities of 60 and 180 mS/m. An effective fit is generally provided by the model in all three cases with a minor deviation emerging towards 1 GHz. At the device level the distributed RCR network appears to provide an accurate representation of the conductive loading between the tracks.

Variation in Mark-Space Ratio

Devices with mark-space ratios of 20:20 and 20:40 μm with ten interdigitated electrodes were prepared and covered by a solution of 33 mS/m conductivity. The measured and modelled impedance magnitudes are displayed in Fig. 3.8. Increasing the separating gap between electrodes produced a higher impedance magnitude at low frequencies as expected from the distributed RCR network model. The modelled impedance magnitude at 1 MHz increases from a value of 605 Ω to 840 Ω for separating gaps of 20 and 40 μm , respectively. Experimental measurements revealed a corresponding shift from 727 Ω to 972 Ω , an increase of 245 Ω which compares well to the modelled increase of 235 Ω . Differences between the absolute values of these modelled and experimental values may be due to surface contaminants or connection resistances which were unaccounted for. The measured impedance magnitude of the IDE with 20 μm separating gap remains within $\pm 5.1\%$ of its modelled value between 90 and 300 MHz. Increasing the separating gap to 40 μm caused the measured values to vary from the model by up to $\pm 26.5\%$. The general form of the modelled curves appears to be correct but further refinements approaching the GHz region could be achieved by accounting for inductances, both along and between tracks, and a dielectric relaxation for water which is centred near 10 GHz⁸.

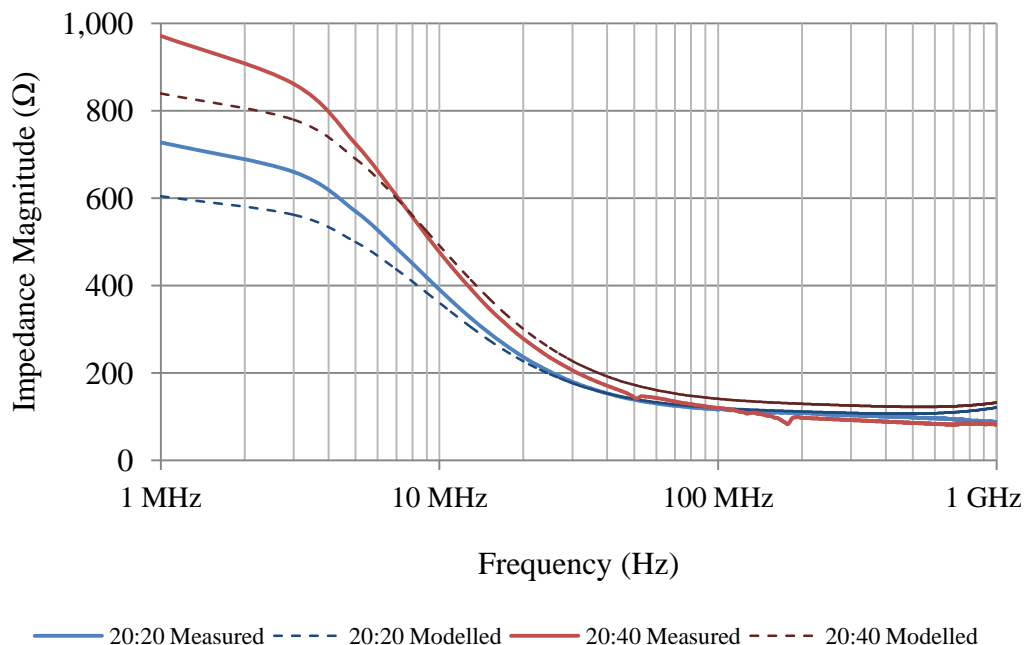


Figure 3.8 – Measured and modelled impedance magnitudes for 20:20 and 20:40 μm mark-space ratio devices using 33 mS/m conductivity with ten electrodes. The impedance magnitude error is less than $\pm 5\%$ across the displayed range.

Variation in Array Size

Devices with two, ten and twenty interdigitated electrodes with a mark-space ratio of 20:20 μm were prepared using a 33 mS/m conductivity solution. The measured and modelled impedance magnitudes are displayed in Figure 3.9. Based on one pair of electrodes the general form is correct, but deviates significantly at both the low and high frequency ends with $R^2 = 0.263$. As the number of electrodes increases the fit improves, with $R^2 = 0.899$ for ten electrodes and $R^2 = 0.906$ for twenty. As discussed for measurements related to mark-space ratio, the model deviates from measured values at low frequencies. At 300 MHz the measured impedance magnitude differs from the model by -45% and suggests that the symmetrical approximations applied in Fig. 3.6 are no longer appropriate. The measured values for 10 and 20 electrodes remain within $\pm 5.1\%$ and $\pm 6.4\%$ of their models, respectively, from 90 to 300 MHz.

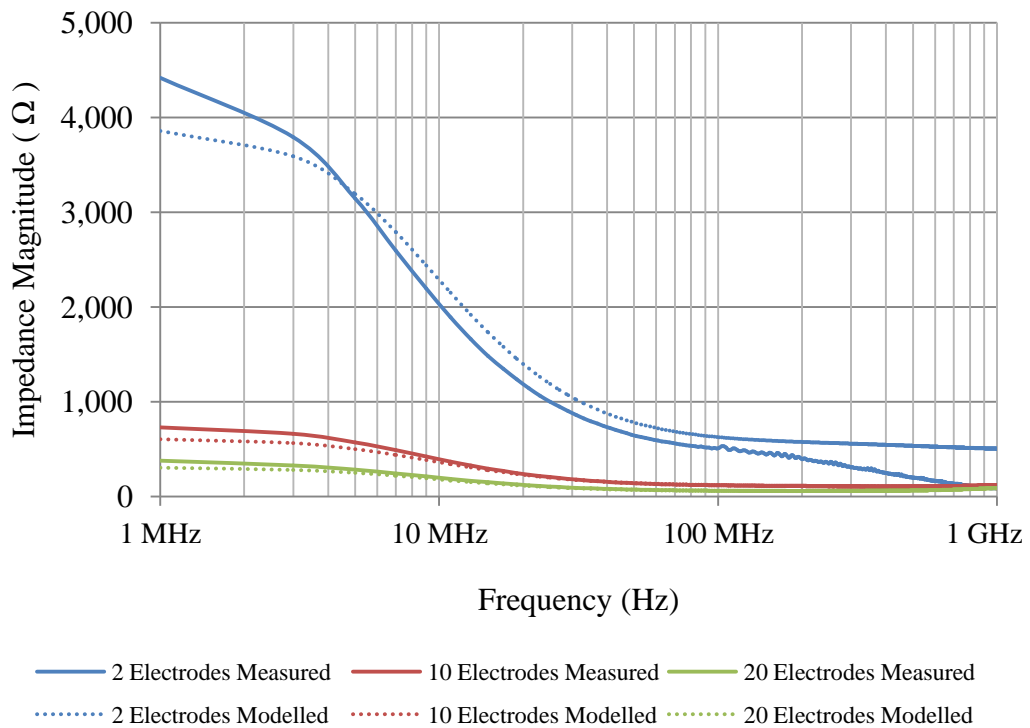


Figure 3.9 – Measured and modelled impedance magnitudes for 20:20 μm mark-space ratio devices using 33 mS/m conductivity solution with two, ten and twenty electrodes. The impedance magnitude error is less than $\pm 5\%$ across the displayed range.

Levitation

A circuit model capable of modelling the behaviour of an IDE structure has been demonstrated over the expected frequency range for f_{x02} , based on a distributed RCR network. This approach is powerful as it provides an indication of the voltage difference between adjacent tracks when driven by a realistic model of the voltage source and its connecting impedances. A minimum operating voltage is, however, still required to determine the design necessary for a practical “ f_{x02} -capable” device. The measurement of f_{x01} is typically performed by initially applying a low frequency signal which causes cells to levitate under negative DEP along the gap between tracks. This frequency is increased until cells experience a transition at f_{x01} to the positive DEP regime, resulting in the attraction of cells to electric field concentrations along the track edges. The initial levitation prevents cells from adhering to the device surface and therefore allows for an accurate determination of the crossover frequency. In the case of f_{x02} an initial high frequency needs to be applied to levitate cells, before being decreased to observe their attachment below it. A critical parameter is therefore the minimum voltage required to levitate cells above the device surface whilst operating at frequencies higher than f_{x02} .

The multi-shelled murine lymphocyte model developed earlier provides an estimate of -0.12 for the real part of the Clausius-Mossotti factor in the high frequency limit, as shown in Fig. 3.2. A finite element model of an IDE cross section may be used to solve for the DEP force of Eq.(2.36) by computing the electric field gradient surrounding the tracks. An electrostatic simulation based on the RMS voltage is sufficient for this purpose as a real value for the complex Clausius-Mossotti factor is assumed. At a point of levitation, the vertical gravitational, buoyancy and DEP forces will balance and yield a net force of zero – a situation displayed in Fig. 3.10 which may be expressed as:

$$0 = 2\pi\epsilon_s R^3 \text{Re}(K^*) \frac{\partial}{\partial y} E_0^2 + \frac{4}{3} \pi R^3 (\rho_c - \rho_s) g \quad (3.1)$$

where R is the cell radius, $\text{Re}(K^*)$ is the real part of the Clausius-Mossotti factor, E_0 is the electric field magnitude, ρ_c is the cell density, ρ_s is the solution density and g is the gravitational acceleration, oriented in the positive z -direction. A value for cell density may be derived from measurements made by Grover *et al.*⁹ of murine lymphocytes using a microfluidic mass sensor.

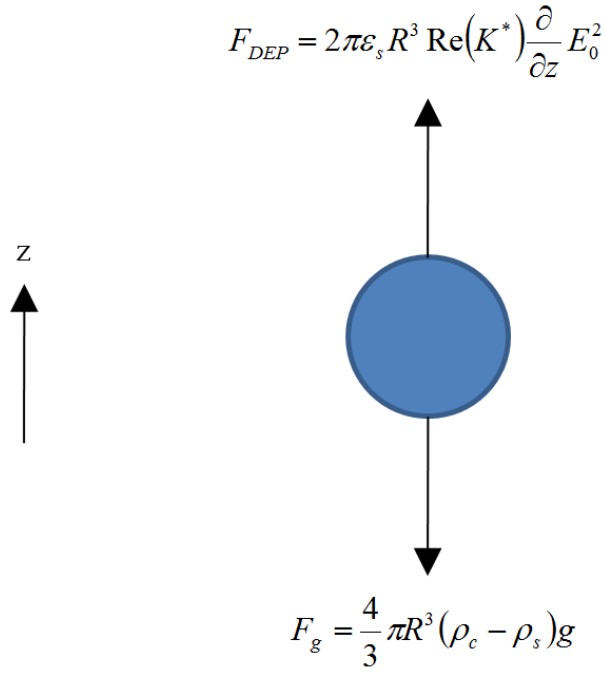


Figure 3.10 – Force body diagram for a levitated polarisable particle at rest above an array of DEP electrodes.

A simulated cross-section of a 20:40 μm mark-space ratio device was used to solve Eq.(3.1) based on the modelled cell values and a voltage of 5 V_{pp} as shown in Fig. 3.11. In the high-frequency limit the Clausius-Mossotti function of the multi-shelled model tends towards the value used here of -0.12. This value may be derived from the high-frequency Clausius-Mossotti factor which is proportional to the difference in nucleus and solution permittivities. Cells will move in the direction indicated by the net force arrows until they settle at the levitation contour, roughly 32 μm above the device surface. The use of an uneven mark-space ratio, where track spacings are greater than their width, results in a levitation contour with minima located along the gaps between tracks where cells will aggregate under negative DEP. This geometry is an advantage when performing visual inspections using an inverted microscope from beneath the glass substrate as the cells are in full view. The applied voltage may be decreased until the levitation contour is no longer continuous, a situation achieved in Fig. 3.12 at 2.33 V_{pp} . At this voltage the vertical DEP force is unable to balance the gravitational force acting on the particle at the centre of the gap, resulting in the undesirable situation where cells drop into contact with the substrate. A minimum potential difference of 2.33 V_{pp} between adjacent tracks therefore needs to be considered in the device design.

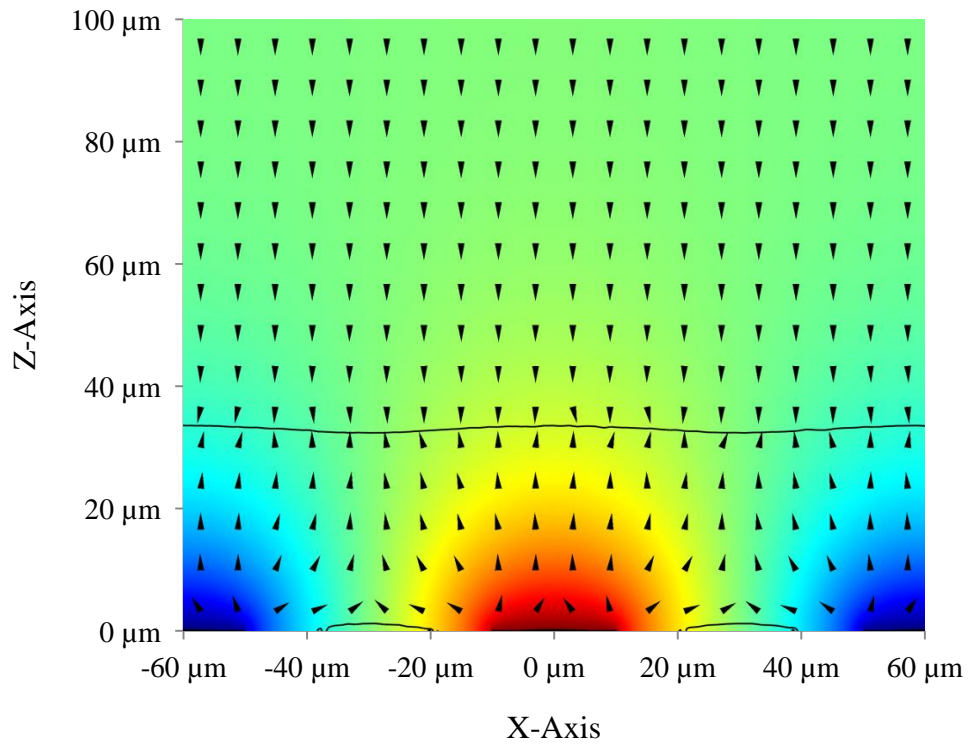


Figure 3.11 – IDE cross-section and electric field contour due to a $5 V_{pp}$ (red) potential difference applied with respect to ground (blue). $R = 2.9\mu\text{m}$, $\text{Re}(K^*) = -0.12$, $\rho_c = 1080 \text{ kg/m}^3$, $\rho_s = 1000 \text{ kg/m}^3$ and $g = -9.81 \text{ m/s}^2$. Arrows display the net force experienced by a modelled cell under negative DEP with the contour at $32\mu\text{m}$ representing the line of levitation.

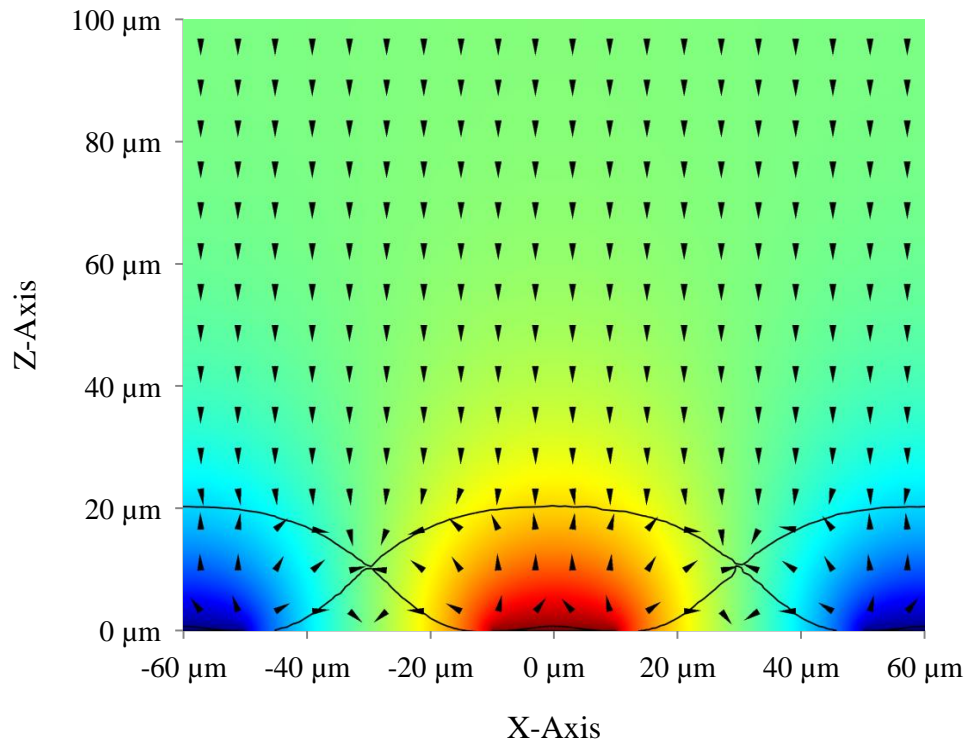


Figure 3.12 – IDE cross-section and electric field contour due to a $2.33 V_{pp}$ (red) potential difference applied with respect to ground (blue). Cell parameters are as used for Fig. 3.10. Arrows display the net force experienced by a modelled cell under negative DEP. The contour beginning at $20\mu\text{m}$ on the left hand side represents the line of levitation.

Device Design

The geometry shown in Fig. 3.13 was designed for the characterisation of $f_{x_{o2}}$ and consisted of sixteen 100nm thick, platinum interdigitated electrodes. Deposition onto a glass microscope slide provided a device suitable for mounting into, and observation using, an inverted microscope. A mark-space ratio of 20:40 μm and length of 2mm provided an active area of 1.84mm² which is sufficient to levitate up to 3000 cells, assuming cells of $\leq 10\mu\text{m}$ diameter levitated along the gaps. Large pads provided a soldering point for a BNC connector, into which a standard signal generator could be connected using a 15cm BNC cable. Signal generators are often designed with an output impedance of 50 Ω , necessitating the use of a corresponding surface mount resistor at the point of termination. The effective capacitance of the IDE is in parallel with this resistance and results in a low-pass RC filter response, a key parameter which restricts its total active area when high bandwidth is critical. This approach has the advantage of ensuring a constant electric field strength is applied across the pass band.

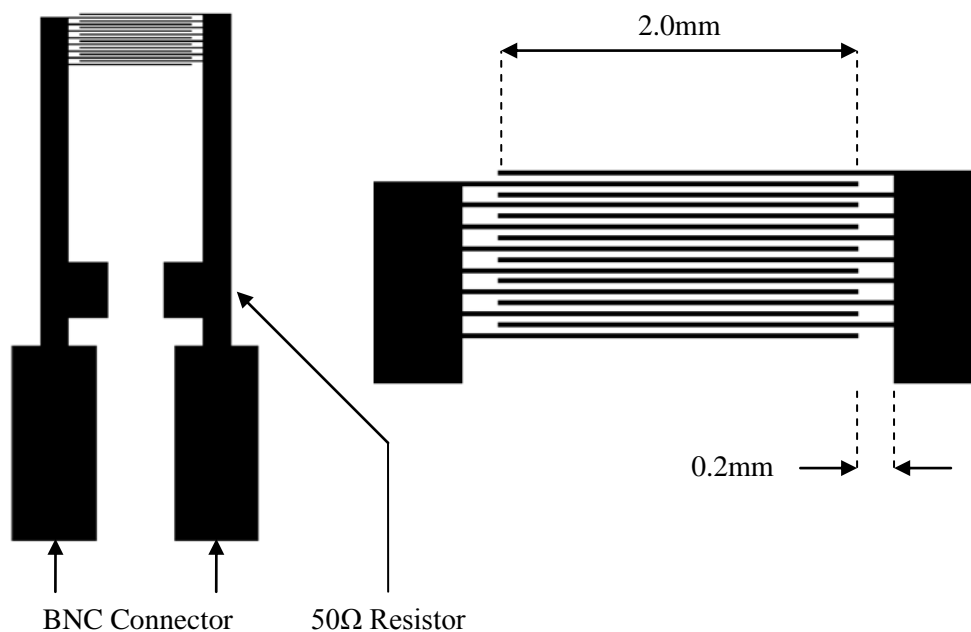


Figure 3.13 – Device geometry

A SPICE simulation of the device based on a 5 V_{pp} source and an RCR network representation of the IDE was performed, resulting in the signal pad voltage spectrum of Fig. 3.14. The small reduction in voltage at low frequencies of 79 mV is dependent upon the

solution conductivity used but is negligible for an array of this size at 50 mS/m. The corner frequency occurs where the signal power drops to half the pass band level, also known as the -3dB point. At 1 MHz the device is operating in the pass band with a signal voltage of $4.92 V_{pp}$. Signal power is proportional to voltage squared thus dividing the pass band voltage by $\sqrt{2}$ gives a -3dB level of $3.48 V_{pp}$ which occurs at ~ 500 MHz. The device is therefore capable of providing the required $2.3 V_{pp}$ across the predicted range of 90 to 300 MHz. Below this frequency the flat pass-band ensures that the applied electric field strength remains the same. Fig. 3.15 displays the voltage difference between adjacent tracks at the centre of the device, plotted along their length at four different frequencies. The length and conductivity of the tracks are such that effectively no drop in voltage occurs along them. At 800 MHz a catenary - or hanging chain-like structure - begins to appear in the voltage difference profile due to increased loading by the capacitive displacement current, a result of the hyperbolic solution discussed previously.

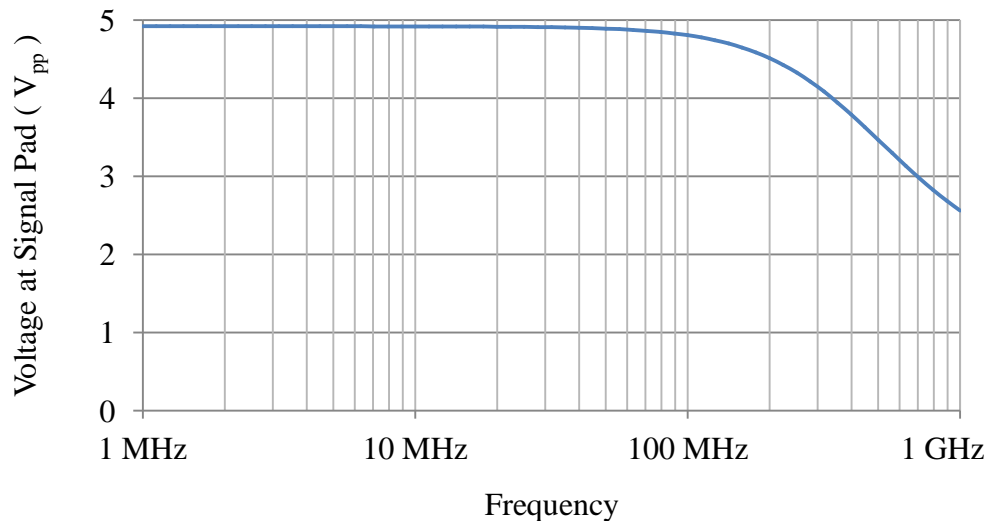


Figure 3.14 – Signal pad voltage at the device when driven at $5 V_{pp}$ by a 50Ω source. Track section lengths of $100\mu\text{m}$ with a sheet resistance of $1.7\Omega/\square$ and a solution conductivity of 50 mS/m were used.

The modelling provided a degree of confidence that the final device would perform as required. Fabrication was performed in the same manner as the test chips with a surface-mount 50Ω resistor and BNC connector soldered on. By locating these components close to the IDE itself the impact of track inductances and parasitic capacitances was minimised. A two-part epoxy resin was used to secure the BNC connector, providing mechanical strength to prevent track damage when connecting the device shown in Fig. 3.16.

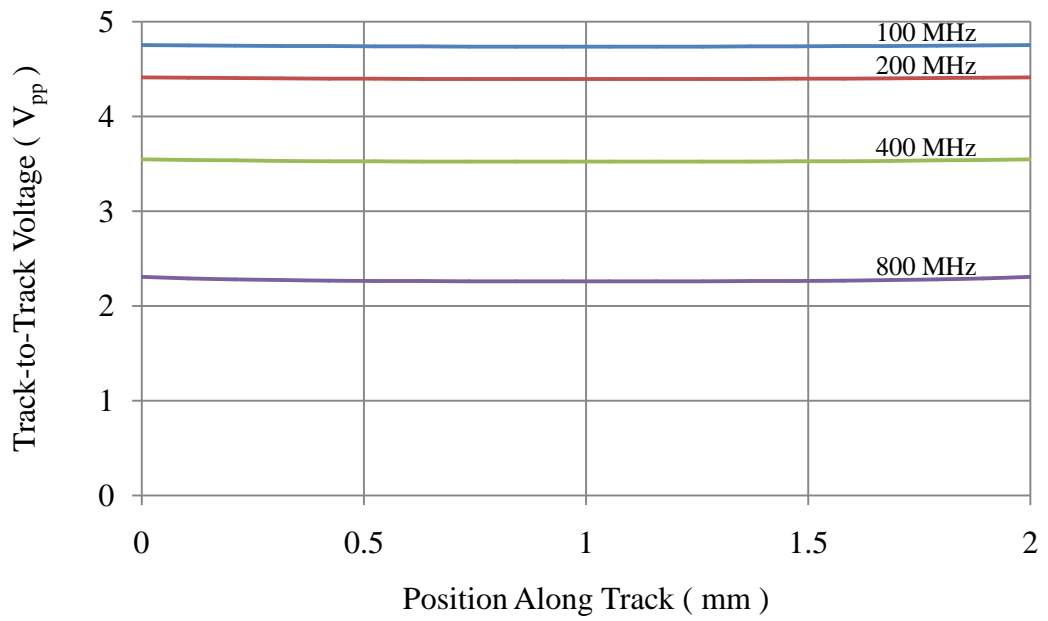


Figure 3.15 – Simulated voltage difference between adjacent tracks at the centre of the device with four frequencies.

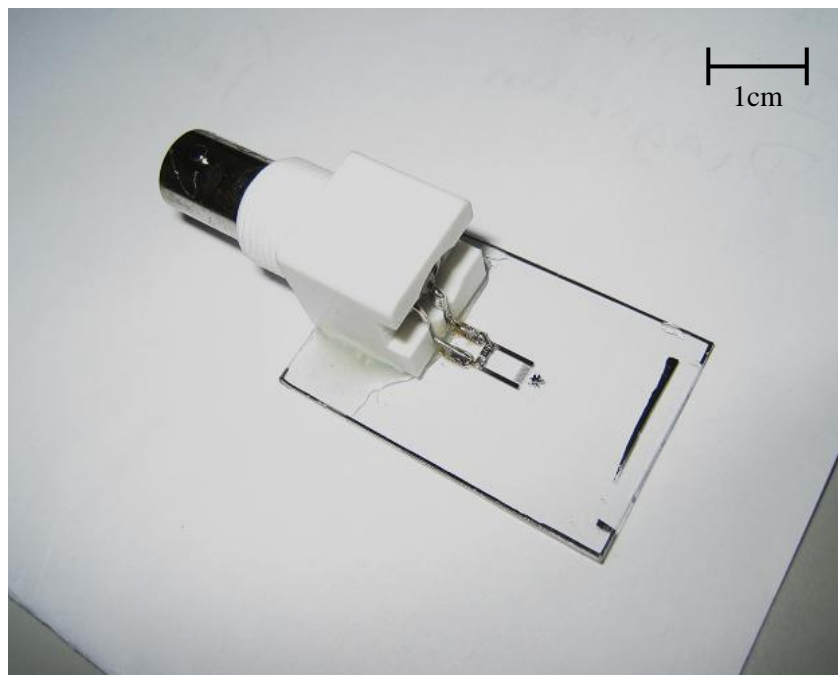


Figure 3.16 – The final fabricated device with BNC connection and 50Ω terminating resistor.

Conclusion

A multi-shelled model has been discussed which, based on published electro-impedance data for murine lymphocytes, suggests a possible range of 90 to 300 MHz for f_{x02} . These frequencies are significantly higher than those typically used in DEP, which are often less than 1 MHz, and as such require careful consideration with respect to the electrode design. The use of a distributed RCR network to model interdigitated electrodes was explored by fabricating test structures and validating their impedance spectra against those of simulations. These results provided a high degree of confidence in the model, particularly in the frequency range required, which was subsequently used in the development of an “ f_{x02} -capable” DEP characterisation device. Finite element modelling was used to predict the levitation height of cells at frequencies above f_{x02} , an important consideration in terms of practical cell characterisation. The model identified an absolute minimum operating voltage of 2.33 V_{pp} between adjacent electrode tracks, a limit which the final design exceeds across the required frequency range. Fabrication of the device was undertaken based on platinum interdigitated electrodes with a small active area to maximise bandwidth and matched termination that provides a flat frequency response.

The interdigitated electrode modelling work undertaken in this chapter has been published at the IEEE International Conference on Microelectronic Test Structures¹⁰.

References

- 1 Muratore, M., Srsen, V., Waterfall, M., Downes, A. & Pethig, R. (2012) Biomarker-free dielectrophoretic sorting of differentiating myoblast multipotent progenitor cells and their membrane analysis by Raman spectroscopy. *Biomicrofluidics*, 6 (3), 034113.
- 2 Pethig, R. & Talary, M. S. (2007) Dielectrophoretic detection of membrane morphology changes in Jurkat T-cells undergoing etoposide-induced apoptosis. *IET Nanobiotechnology*, 1 (1), 2-9.
- 3 Moisescu, M. G., Radu, M., Kovacs, E. Mir, L. M. & Savopol, T. (2013) Changes of cell electrical parameters induced by electroporation. A dielectrophoresis study. *Biochimica et Biophysica Acta*, 1828 (2), 365-372.
- 4 Jones, T. B. (1995) *Electromechanics of Particles*, Cambridge: Cambridge University Press.
- 5 Asami, K., Takahashi, Y. & Takashima, S. (1989) Dielectric properties of mouse lymphocytes and erythrocytes. *Biochimica et Biophysica Acta*, 1010 (49), 49-55.
- 6 Balabanian, S. (1959) *Linear Network Analysis*, New York: Wiley.
- 7 Zhu, X., Gao, Z., Yin, Z. & Ni, Z. (2010) Electrode-rail dielectrophoretic assembly effect: formation of single curvilinear particle-chains on spiral microelectrodes. *Microfluidics and Nanofluidics*, 9 (4-5), 981-988.
- 8 Buchner, R., Barthel, J. & Stauber, J. (1999) The dielectric relaxation of water between 0°C and 35°C. *Chemical Physics Letters*, 306 (1-2), 57-63.
- 9 Grover, W. H., Bryan, A. K., Diez-Silva, M., Suresh, S., Higgins, J. & Manalis, S. R. (2011) Measuring single-cell density. *Proceedings of the National Academy of Sciences of the United States of America*, 108 (27), 10992-10996.
- 10 Chung, C., Smith, S., Menachery, A., Bagnaninchi, P., Walton, A. J. & Pethig, R. (2011) Interdigitated electrode modelling for applications in dielectrophoresis. *2011 IEEE International Conference on Microelectronic Test Structures. 4-7 April 2011. Amsterdam, Netherlands. pp74-79.*

Chapter Four

Measuring the Second Crossover Frequency

Introduction

A device has been created which is capable of operating over the estimated frequency range for f_{x02} , based on the published electro-impedance measurements of murine myeloma cells. The development of a test system was then necessary to determine the existence and behaviour of f_{x02} using actual cells. By suspending cells similar to those modelled in low conductivity DEP solution, and observing their reaction to electric fields generated by the device, electrokinetic behaviour consistent with f_{x02} was successfully observed. Its value was observed to decrease over the time suspended – an instability which has ramifications for the measurement and health of cells. A similar behaviour was observed with the value of f_{x02} for human red blood cells and relevant comparisons have been made to studies published on both cell types, studies which implicate the efflux of intracellular ions. Flow cytometry was used to provide an optical insight to this phenomenon and determine how the viability of cells was affected by the DEP solution. By investigating its osmolality, salinity and temperature an understanding of the observed decrease has been developed and a means to minimise its impact proposed. Elements of the work performed in this chapter have been published in the Journal of Electrical Bioimpedance¹.

Method

The characterisation device developed in Chapter Three was mounted into an inverted microscope which provided illumination from above. As the objective lens points upwards from beneath the device only the cells situated between electrodes could be viewed. An Agilent ESG-D4000A signal generator connected to a Mini-Circuits ZHL-1A amplifier was used to generate a signal voltage of $5 V_{pp}$ over the required frequency range. A separate amplification stage was necessary as the signal generator provided a maximum output of $2.8 V_{pp}$ ($1 V_{RMS}$) between 250 kHz and 1 GHz. The amplifier applied an additional voltage gain of ~ 7.4 with the ability to drive a load exceeding 640 mW or $8.2 V_{pp}$ into our 50Ω terminating device. A semi-autonomous test system was developed by using a PC to control the signal generator over a GPIB interface with microscope images captured via a USB connected Lumenera Infinity 2-3 digital camera and 20 \times objective. The control system was

programmed using LabVIEW which applied an initial levitation frequency of 425 MHz prior to stepping down in 25 MHz decrements, at 10 second intervals, to a final frequency of 25 MHz. By manually inspecting images for cell attachment at the edge of tracks, the distribution of f_{x02} crossover frequencies for a sample of cells was built up.

SP2/0-Ag14 murine myeloma cells obtained from the American Type Culture Collection (Catalogue No. CRL1581) were cultured for these experiments. Myeloma cells are malignant plasma cells which originate as B lymphocytes, a type of white blood cell responsible for the production of antibodies in mammals. They are widely used as hybridoma fusion partners to produce large quantities of a target antibody. Both their rapid growth in suspension and similarity to the lymphocytes modelled in Chapter Two made them ideal candidates for initial measurements of f_{x02} . These were grown in RPMI-1640 medium supplemented with 100 units/ml penicillin-streptomycin and 10% foetal calf serum. The cultures were maintained in standard T75 flasks, incubated at 37°C with 5% CO₂ in air and grown to a maximum density of 1×10^6 cells/ml. The RPMI-1640 culture medium possessed an electrical conductivity of ~ 1.5 S/m which far exceeded the modelled values for DEP. Its use would effectively short circuit the device electrodes, with the potential to generate excessive heating in the sample due to I^2R losses through the medium. As with most culture media its primary constituent is sodium chloride, a salt which is important in maintaining the physical volume of cells and a state which is referred to as isotonic. Cells which are re-suspended into an isotonic solution will neither expand nor contract. Unfortunately, sodium chloride is also responsible for the high electrical conductivity and therefore requires substitution to allow for effective DEP measurements. A simple DEP solution was prepared by adding 100 g/L sucrose and 3 g/L glucose to deionised water. Phosphate buffered saline (PBS) was then added to achieve a conductivity of 33 mS/m, measured using an Oakton CON510 conductivity meter with the pH adjusted to 7.4 by using either sodium hydroxide or hydrochloric acid. These quantities produced a DEP solution with an osmolality of approximately 310 mOsm/kg, equal to that of the culture medium and therefore referred to as isosmotic – the value being measured using an Advanced Instruments Inc. Model 3300 osmometer. It should be noted that although the solution is isosmotic with respect to the culture media it does not imply isotonic, a determination which can only be made by observing the volume of cells once re-suspended.

The myeloma cells were harvested at a density of approximately 1×10^6 cells/ml, measured using a haemocytometer, and centrifuged at 100g for five minutes followed by aspiration of the supernatant. The cells were then washed twice by suspending them into 10 ml of fresh DEP solution, followed again by centrifugation and aspiration of the supernatant. The final

pellet was then re-suspended into ~1 ml of DEP solution to provide a target cell density of 1×10^7 cells/ml. These steps ensured that a single-cell suspension was created with a solution conductivity close to that intended. A square PDMS gasket surrounded the device electrodes, enclosing a 7×7 mm area, 200 μ m in height. By depositing a 10 μ l volume of the cell suspension inside this gasket and applying a glass cover slip on top the volume was effectively sealed. The loaded device was clamped into an inverted microscope and connected by BNC cable to the signal amplifier, ready for measurements. By focusing the microscope on the electrode plane the attachment of cells undergoing a transition from negative to positive DEP could be monitored easily, by observing their movement away from the central gap and into focus at the track edges.

Initial Results

Application of the signal at 425 MHz resulted in the levitation of cells as intended, shown in Fig. 4.1(A). Cells which appear significantly out-of-focus correspond to a high levitation height and are not constrained to any particular region of the device. Those which appear more in-focus are levitating at a lower height and tend to be constrained to the gap between electrode tracks. At these frequencies the spread in levitation heights is caused by differences in the density of cells and their Clausius-Mossotti factor, the latter dominated by both solution and cell permittivities. As the frequency was decreased the vast majority of cells became attracted to the electrode track edges, shown in Fig. 4.1(B) at 25 MHz and which, to the author's knowledge, represent the first published observations of f_{x02} in mammalian cells¹.

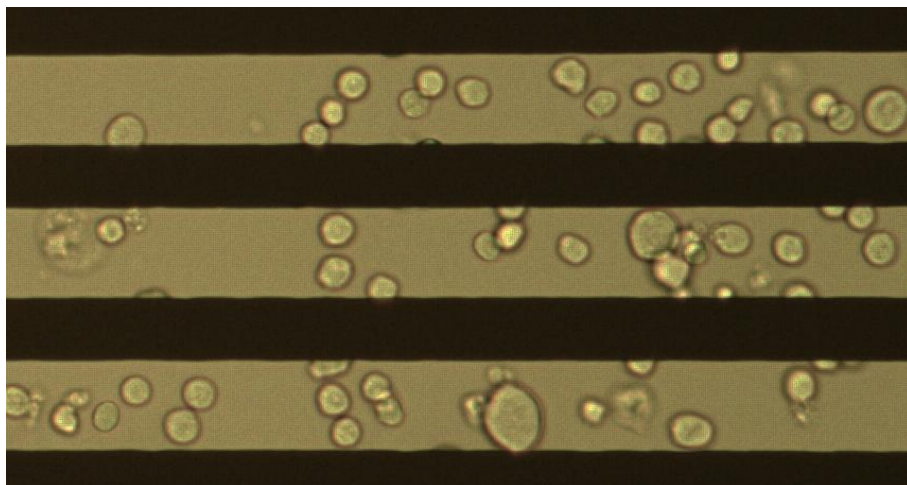


Figure 4.1(A) – Murine myeloma cells suspended in a 33 mS/m DEP solution with an applied electric field at 425 MHz.

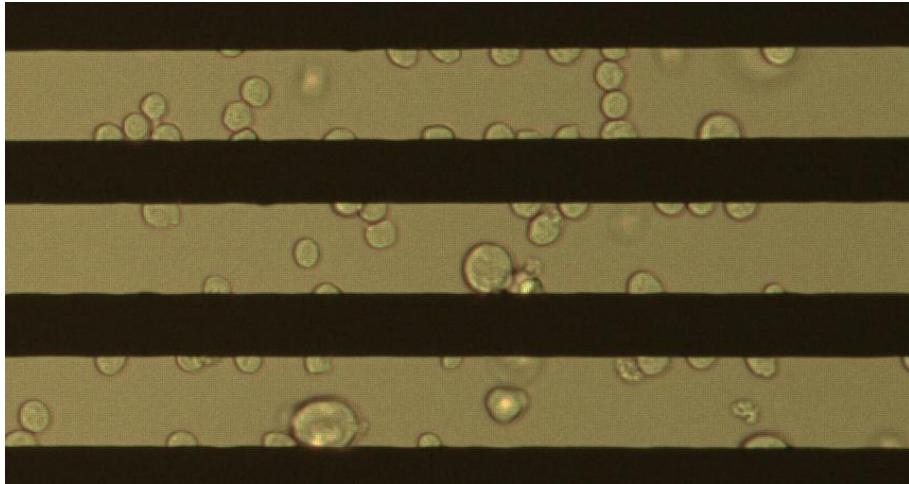


Figure 4.1(B) – Murine myeloma cells suspended in a 33 mS/m DEP solution with an applied electric field at 25 MHz.

By analysing the number of cells becoming attached in 25 MHz decrements from 425 MHz the f_{x02} distribution of Fig. 4.2 was generated based on a sample of 418 cells. The general range corresponded remarkably well to that anticipated by modelling – a range of 90 to 300 MHz – with the modelled value of 215 MHz corresponding to the measured mean frequency of 195 MHz with a 95% confidence interval (CI) of ± 6 MHz. The results of these cells and their levitation at 425 MHz suggested that the designed electrodes were fit for purpose.

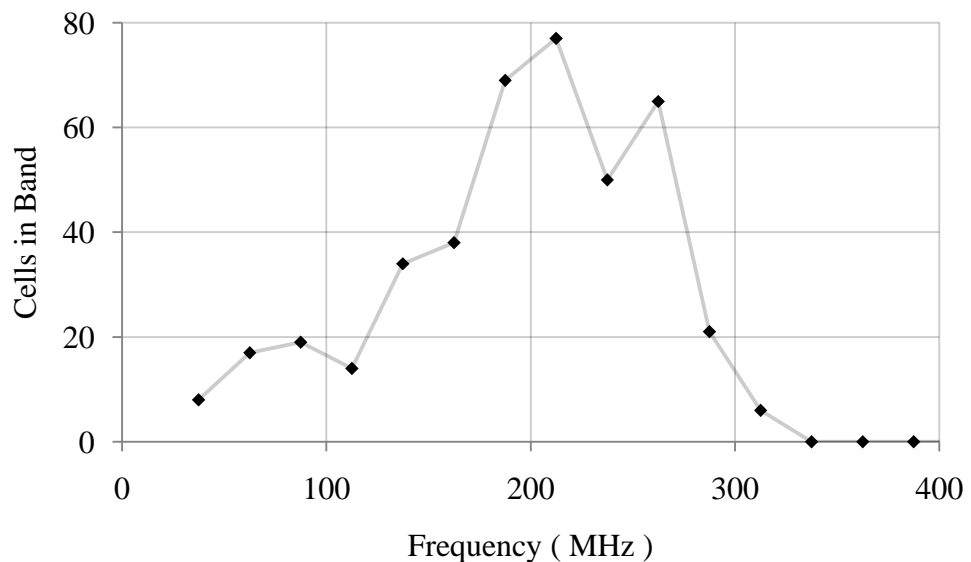


Figure 4.2 – The initial distribution of f_{x02} for murine myeloma cells, based on a sample of 418 cells.

Instability

An unanticipated finding was the apparent temporal instability exhibited by both f_{x01} and f_{x02} . In Fig. 4.3 a time course of murine myeloma cells held in DEP solution was performed at room temperature with measurements for both f_{x01} and f_{x02} . Over a three hour period f_{x01} increased and f_{x02} decreased; the latter trend being consistent with a decrease in intracellular conductivity. Based on the multi-shelled model of Chapter Three, the reduction in intracellular conductivity required for the observed decrease in f_{x02} of 15% would not account for the observed increase in f_{x01} , which should remain the same. A similar response had previously been observed by Gimsa *et al.*² with the value of f_{x01} for P3X63-Ag8 murine myeloma cells increasing over time. By measuring the conductivity of the solution in which cells had been suspended at over 100× the density used for DEP experiments, Gimsa *et al.* estimated that the cytoplasmic conductivity of their cells had halved after 80 minutes of suspension. It is, however, unclear whether this alone fully accounted for their observed increase in f_{x01} . Three apparent leakage processes were nevertheless identified with time constants of ~5, 20 and 200 minutes which were attributed, respectively, to the rapid equilibration of ions on suspension, a slower leakage phase and cell lysis. The observations of Gimsa *et al.* appear to agree with those made here for f_{x02} using cells of a similar nature, but differ on the cause of an observed increase to f_{x01} .

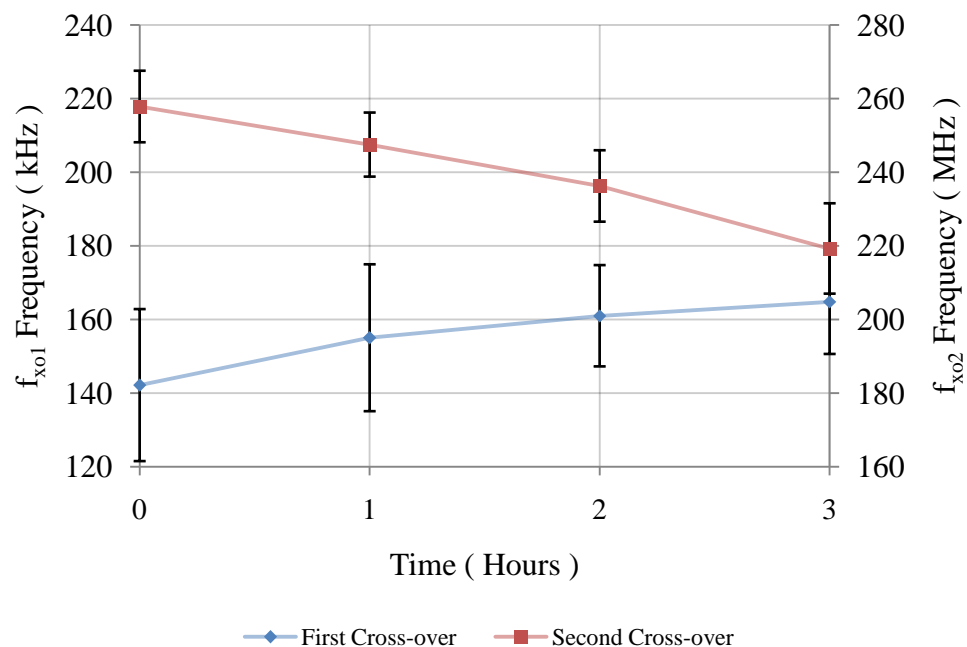


Figure 4.3 – Mean value of f_{x01} and f_{x02} for murine myeloma cells plotted at one hour intervals over a period of three hours. Error bars indicate the 95% confidence interval.

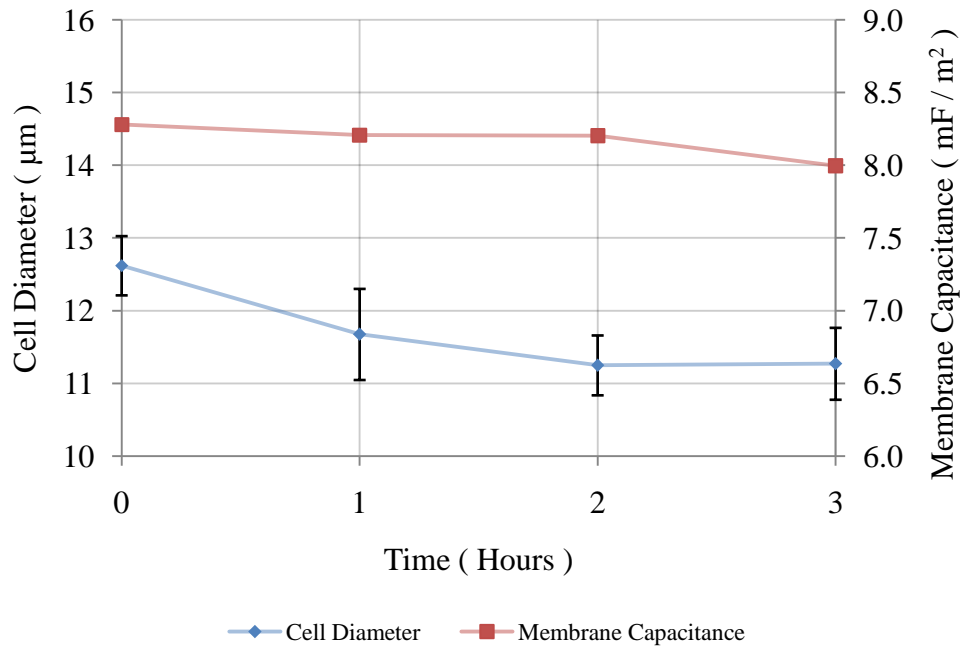


Figure 4.4 – Mean cell diameter and membrane capacitance based on fifty murine myeloma cells plotted at one hour intervals over a period of three hours. The membrane capacitance is calculated from the mean cell diameter, mean f_{x01} from Fig. 4.3 and the solution conductivity of 33 mS/m using Eq. 2.39. Error bars for cell diameter indicate the 95% confidence interval.

Measurements of cell diameter, shown in Fig. 4.4, were also made in conjunction with the discussed crossover measurements. These were performed by measuring a sample of fifty cells at each datum using a 40× objective. Based on the mean cell diameter, f_{x01} values of Fig. 4.3 and solution conductivity of 33 mS/m the membrane capacitance was determined using Eq.(2.39), with the assumption of zero membrane conductivity. Over a two hour period the cells lose an average of 29% in their cell volume with no significant change in membrane capacitance. It is this reduction in cell radius which can account for the observed increase in f_{x01} , an increase caused by the efflux of water from the cell but not directly by the reduction in intracellular conductivity due to the efflux of ions.

Human red blood cells were suspended in the same DEP solution and produced the f_{x02} distribution displayed in Fig. 4.4 immediately following suspension and two hours thereafter at room temperature. Their crossover frequency was observed to be significantly lower than that of murine myeloma cells, with frequency decrements altered accordingly to 10 MHz. Over the first two hours of suspension in DEP solution their mean frequency decreased by 28 MHz by comparison to the corresponding 22 MHz decrease of murine myeloma cells. These values differ slightly but suggest that the leakage of ions in DEP solution affects mammalian

cells more generally, behaviour which was not observed by Gimsa *et al.*² in their study of neurospora fungi cells. The leakage of salts from red blood cells in isosmotic sucrose has been investigated by several researchers including Lacelle *et al.*³, who concluded that the rate of efflux was determined by the ionic strength of a solution, increasing drastically below 0.2 mM of extracellular sodium chloride and exacerbated by higher temperatures.

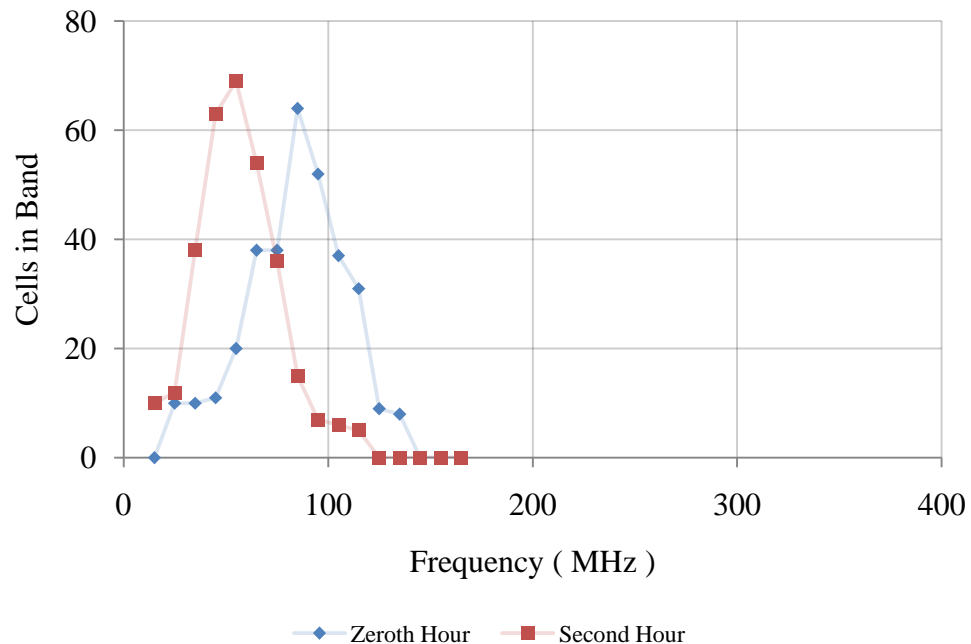


Figure 4.4 – The f_{x02} distribution for red blood cells based on samples of 328 and 315 cells at zero and two hours of suspension, respectively.

Ion homeostasis is a critical feature of cells. Their ability to carefully regulate intracellular concentrations is fundamental to their survival. Potassium itself is the most abundant intracellular ion and its efflux has been implicated as a driver of programmed cell death, a process referred to as apoptosis⁴. Although the long term suspension of cells in DEP solution is an issue for the characterisation of f_{x02} , the greater risk is in negatively affecting their viability or quality with such treatment. Efforts were therefore made to determine how this apparent efflux of ions could be prevented or mitigated in murine myeloma cells by using f_{x02} as a metric.

Osmolality

The construction of most DEP solutions is simple with osmolality being the most easy to control parameter, defined by the concentration of sucrose. An initial investigation of solution osmolalities ranging from 250 to 480 mOsm/kg was made and evaluated over time

as shown in Fig. 4.5. Immediately following suspension there is no significant difference between 250 and 390 mOsm/kg, however higher osmolalities display an apparent reduction in f_{x02} . These differences become exaggerated after six hours with higher osmolalities contributing to the apparent ion efflux, likely caused by the increased osmotic pressure driving water out of the cell. Reducing the osmolality did not make any appreciable difference and suggests that the underlying imbalance in ion concentration, described by Lacelle *et al.* for red blood cells, is still the fundamental limitation.

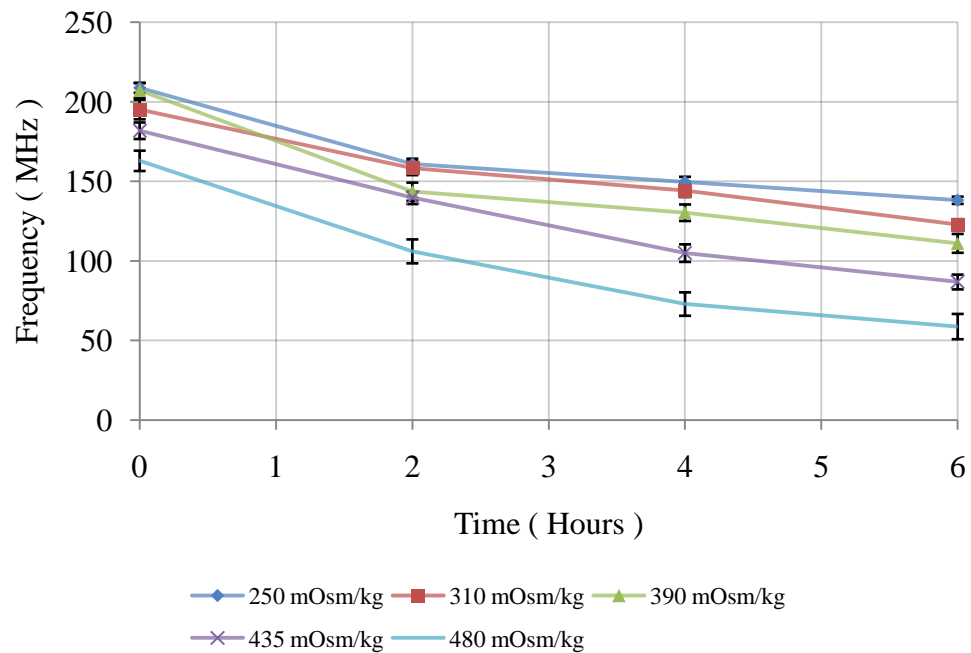


Figure 4.5 – Mean value of f_{x02} for murine myeloma cells over time at different solution osmolalities. Error bars indicate the 95% confidence interval.

Phosphate Buffered Saline

PBS is a commonly used buffer solution in cell biology and is designed to be isotonic with respect to most mammalian cells, sodium chloride being its primary constituent. Cells suspended in PBS are considered to be stable in the short term and as such raising its proportion in the DEP solution should provide a benefit. Any increase in the solution conductivity due to PBS will have a marked impact on the Clausius-Mossotti factor at frequencies in the region of f_{x01} . In Fig. 4.6 the simulated real part of the Clausius-Mossotti factor is plotted for solution conductivities of 33 and 330 mS/m. The impact of raising the conductivity by a factor of ten is a significantly reduced positive DEP force which increases the attachment time for cells to the electrode track edges. Both the levitation height and f_{x02}

remain unaffected, as this region of the Clausius-Mossotti factor is dictated by the extracellular permittivity, intracellular permittivity and intracellular conductivity. Therefore any significant shift in $f_{x_{O_2}}$ will be caused by fundamental differences in the biological response of cells to the increased salinity and not electrokinetic differences due to the solution conductivity itself. A DEP solution with additional PBS for a conductivity of 330 mS/m was created and an increased voltage of 7 V_{pp} was applied to mitigate the effect of both a reduced DEP force and increased electrical loading. The time interval between frequency decrements was also increased to thirty seconds as the attachment time was visibly increased. The result of increasing salinity is displayed in Fig. 4.7 which demonstrates a clear offset in $f_{x_{O_2}}$ across the entire six hour period when moving from a solution conductivity of 33 to 330 mS/m. The rate at which $f_{x_{O_2}}$ decreased over this period is nearly identical, suggesting the same underlying process is responsible. These observations are consistent with an initial rapid equilibration of ions governed by a time constant of less than 5 minutes which determines the first measured value of $f_{x_{O_2}}$. As the ionic shock induced by suspension from the culture medium into 330 mS/m DEP solution is less than that for 33 mS/m, it is logical for the initial ion efflux to be reduced as well resulting in a higher value for $f_{x_{O_2}}$. Thereafter a time constant associated with ionic leakage occurs resulting in the same profile in time for $f_{x_{O_2}}$ at both solution conductivities.

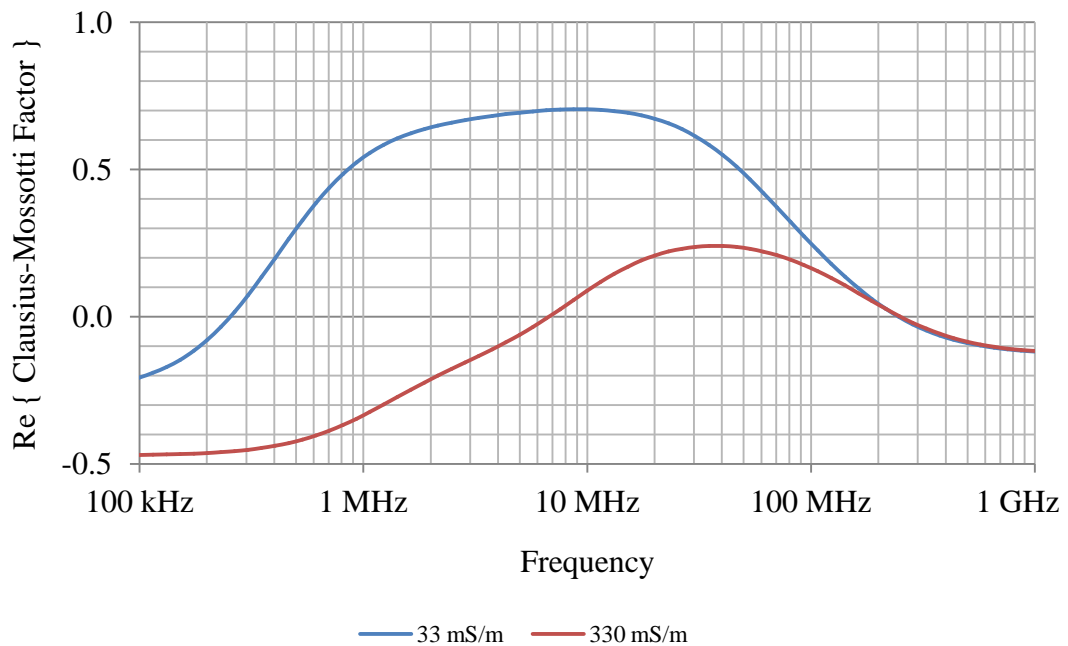


Figure 4.6 – The real part of the Clausius-Mossotti factor for the triple-shelled dielectric sphere based on the electro-impedance measurements of Asami *et al.*, with solution conductivities of 33 and 330 mS/m.

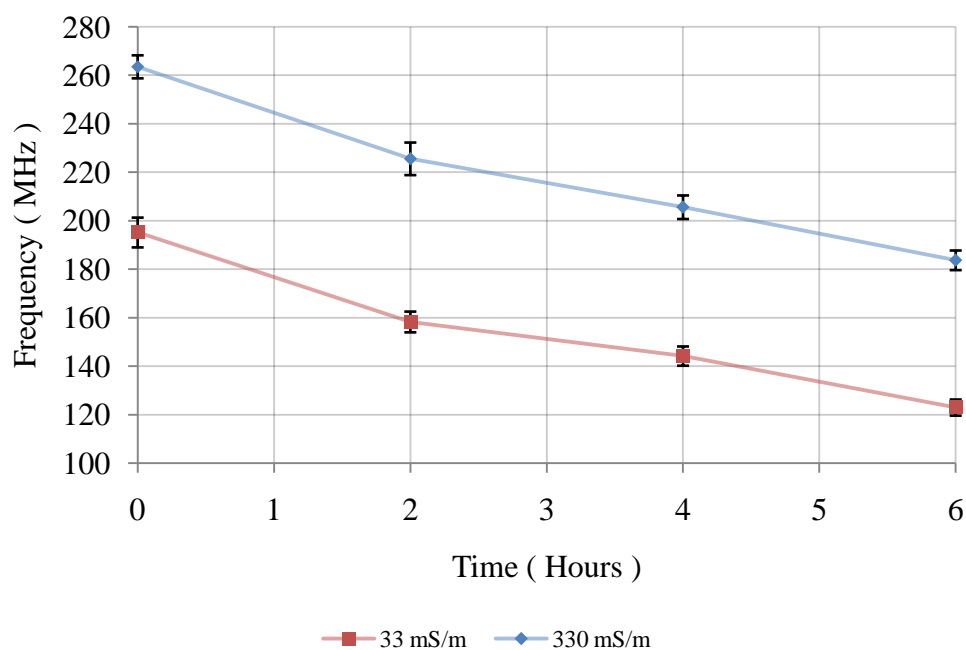


Figure 4.7 – Mean value of $f_{x_{o_2}}$ for murine myeloma cells over time at two solution conductivities. Error bars indicate the 95% confidence interval.

Temperature

The time constant governing the leakage, or diffusion, of ions across the cell membrane is fundamentally a temperature dependent kinetic phenomenon. Lowering the temperature at which the experiment is conducted was therefore expected to reduce the observed decrease in $f_{x_{o_2}}$. Mammalian cells are highly sensitive to reduced temperatures⁵ with their optimum growth occurring in the 35-37°C range, however many will continue to grow and divide down to 25°C but at a significantly reduced rate. Below 20°C the progression of cells through their cycle may be halted and can in fact be used as a method of synchronisation, with an hour of severe hypothermia (4°C) being particularly effective. Although such methods may be employed the intracellular homeostasis of ions requires the activity of pumping systems, such as Na^+/K^+ -ATPase, which may consume up to 80% of a cell's resting metabolic rate⁶. At reduced temperatures the absence of such mechanisms results in the leakage of ions across the cell membrane towards their thermodynamic equilibrium. A remarkable resistance to ion leakage is exhibited by hypoxia-tolerant cells which, although exhibiting a significant reduction in Na^+/K^+ activity, are capable of maintaining their intracellular ionic levels. This protective mechanism operates by suppressing the presence of ion leakage channels and thereby reducing membrane permeability, a process known as channel arrest. Research into myeloma cells has, in recent years, been directed at exploiting

their own requirement for a hypoxic environment which exists in bone marrow⁷. As such, their ability to maintain intracellular ionic levels may be further enhanced at low temperatures. An additional area of concern is the swelling of murine cells in response to hypothermia caused by the influx of sodium down its concentration gradient when conducted in standard culture media. DEP solution provides a fortunate environment in which to operate as the external sodium concentration is extremely low, typically less than 1 mM, and should therefore act to prevent such swelling⁸.

A DEP solution of 33 mS/m conductivity and 310 mOsm/kg osmolality was used for all temperature controlled measurements. Samples of the solution were cooled or warmed to the target temperature and used from the first wash stage onwards. The wash process resulted in the cells being exposed to the DEP solution for a maximum of 30 minutes prior to their initial measurement, defined as the “zero” time for each sample. Temperatures of 10, 29 and 37°C were selected for comparison against the 21°C benchmark, a refrigerated room at 5°C being used with a water bath to achieve the lowest target temperature in a controlled manner.

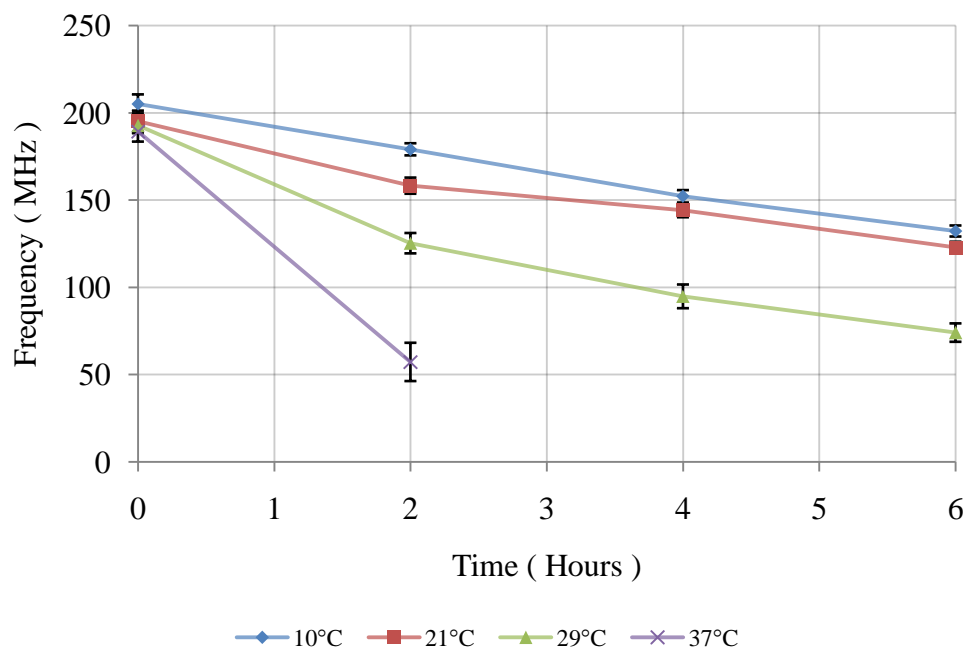


Figure 4.8 – Mean value of f_{x02} for murine myeloma cells over time at four temperatures. Error bars indicate the 95% confidence interval.

The trends displayed in Fig. 4.8 show that the decrease in f_{x02} over the first two hours is dependent upon temperature, as hypothesised. After four hours at 37°C the observed majority of cells did not exhibit any positive DEP, caused by the apparent severe drop in their intracellular conductivity. A precise count of the unattached cells was not possible as

they floated across a range of heights, out of the focal plane. At 10°C the rate of change appears to be constant over the entire time period. Elevating the temperature appears to introduce a process that exhibits a shorter time constant, with all trends below 37°C appearing identical after four hours. A useful method of interpreting the data over this initial two hour period is an Arrhenius plot, typically used to analyse the impact of temperature on chemical reactions but may be extended to cover any thermally induced process including diffusion through a membrane. The plot is based on the Arrhenius equation:

$$k = Ae^{-\frac{E_a}{RT}} \quad (4.1)$$

where k is the reaction rate constant, A is the pre-exponential factor, E_a is the activation energy in J/mol, R the universal gas constant of $8.314 \text{ J K}^{-1} \text{ mol}^{-1}$ and T the temperature in kelvin. We make the assumption that $f_{x_{O_2}}$ is linearly proportional to the free charge diffusing across the membrane, decreasing as they efflux, and therefore use the negative of its derivative with respect to time as the reaction rate constant. Taking the natural logarithm of this equation yields:

$$\ln(k) = -\frac{E_a}{R} \frac{1}{T} + \ln(A) \quad (4.2)$$

which is a straight line when plotted against $1/T$. If the reaction rate constant plotted against this can be fitted the physical situation is effectively described by the Arrhenius equation and the activation energy can then be calculated from the gradient:

$$E_a = -R \frac{\partial}{\partial \left(\frac{1}{T}\right)} \ln(k) \quad (4.3)$$

An Arrhenius plot based on the data of Fig. 4.8 is displayed in Fig. 4.9 with the corresponding best fit displayed assuming a linear form. This fit suggests an activation energy of approximately 44 kJ/mol or 10.5 kCal/mol, a value which is within 15% of the 12 kCal/mol value derived by Lacelle *et al.* for red blood cells by measuring their sodium chloride efflux³. The involvement of ammonium derivatives in membrane cation permeability was suggested due to their dissociation values in proteins being in the 9 to 13 kCal/mol range; however no clear consensus has emerged in this regard. The situation is similar as isosmotic sucrose was used in both cases, with a room temperature sodium chloride solution at a concentration of between 0.2 and 2 mM. It is reasonable to assume that the observed decrease in $f_{x_{O_2}}$ reflects the same underlying phenomenon, the efflux of sodium chloride. In addition to this loss, Lacelle *et al.* provided evidence for a simultaneous potassium efflux equivalent to 70% of the sodium based on the flame photometric analysis

of suspended solutions³. We may therefore expect the same efflux of potassium to occur for the murine myeloma cells used here.

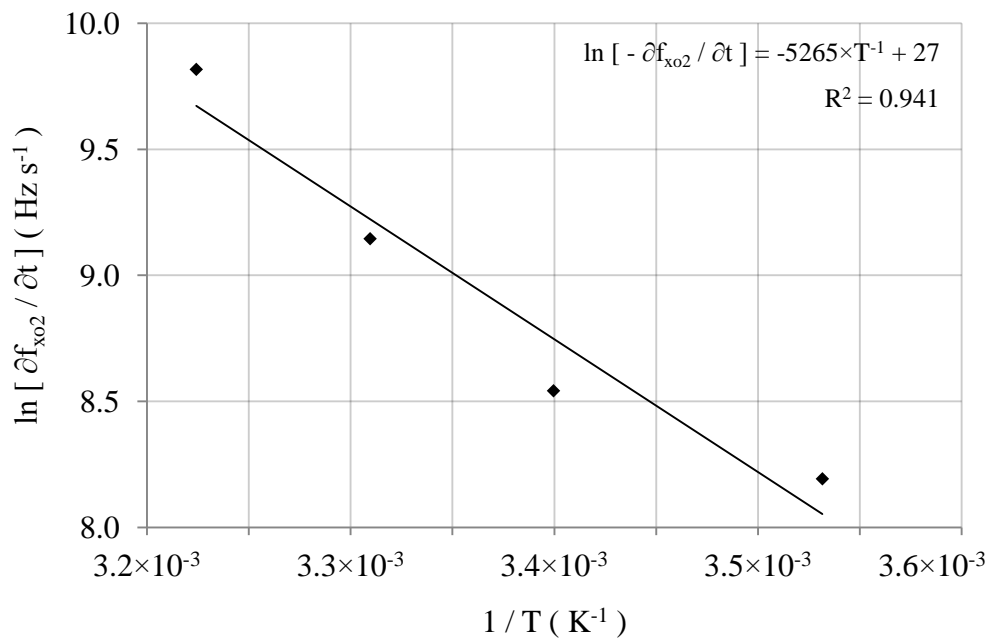


Figure 4.9 – An Arrhenius plot based on $f_{x_{o2}}$ with a straight line fit.

The temperature trends displayed in Fig. 4.8 suggest that, although we cannot prevent the efflux of ions and loss of cell volume, we can mitigate the impact of such behaviour by performing experiments at the lowest temperature and in the shortest time frame practical. All subsequent experiments were performed at room temperature – approximately 21°C – within thirty minutes of the first wash being conducted. DEP solutions were warmed to room temperature, rather than the standard incubation temperature of 37°C. By following these guidelines the decrease in $f_{x_{o2}}$ should be constrained to less than 10 MHz. It should be noted that the initial rapid equilibration of ions which is expected to occur within minutes of exposure to the DEP solution is still expected. With this procedure in mind an experiment was designed to further explore the importance of potassium and sodium chloride salts present in the culture medium, but missing from our DEP solution. Their impact on conductivity precludes their use at anything approaching physiological concentrations. However, an alternative is to expose them to solutions containing these salts over a period of time followed by subsequent re-suspension into the standard DEP solution for crossover measurement.

Salts

Four solutions were prepared which consisted of the standard solution with the addition of either potassium chloride, sodium chloride or both together. These were added at the same concentrations as RPMI-1640 medium with sucrose used to ensure isosmotic substitution up to the medium osmolarity of 310 mOsm/kg. The results for $f_{x_{o2}}$ displayed in Fig. 4.10 and based on the revised protocol show that three hours of exposure to the standard DEP solution at 21°C decreased its value by ~60 MHz. Such a result implies a significant decrease in intracellular conductivity, however the value for $f_{x_{o1}}$ also decreases which is inconsistent – with respect to both Fig. 4.3 and the work of Gimsa *et al.* In Fig. 4.11 the cell diameter for the control experiences a 6% reduction but the apparent capacitance increases by 30%. One explanation is that the wash steps used prior to the final measurement raised the solution conductivity, however this is identical in composition and any ions leaked would be diluted by a factor of over a hundred. An alternative explanation is that the additional handling which followed three hours of exposure compromised the membrane, a situation which would break the zero membrane conductivity used with Eq.(2.39) and cause $f_{x_{o1}}$ to decrease as observed. The results of $f_{x_{o1}}$ and $f_{x_{o2}}$ indicate that both provide a means of evaluating the health of cells relative to that of the initial control measurement.

Although the omission of any salt, neglecting the low level in the PBS added, results in $f_{x_{o2}}$ decreasing this effect is further exacerbated by the isosmotic addition of sodium chloride. Its presence may assist in the co-transport of intracellular ions such as potassium out of the cell, via the Na-K-Cl co-transporter NKCC1 which is almost universally present, for example. In principle, the presence of electrochemical sodium and chloride gradients directed into the cell could facilitate such co-transport. A more detailed analysis of the actual mechanism responsible for this ion efflux is desirable however the negative end result is clear and unambiguous. The associated collapse in $f_{x_{o1}}$ adds further to the detrimental effect of adding sodium chloride alone and is suggestive of a compromised membrane. By stark contrast the addition of potassium chloride, with or without sodium chloride, appears to be critical in maintaining the measured values of $f_{x_{o1}}$, $f_{x_{o2}}$ and cell diameter. Its concentration in RPMI-1640 represents less than 10% of the sodium chloride, by mass. At such levels the increase in conductivity is still significant, but the potential exists to add a fraction of the original potassium chloride as a compromise between biological stability and DEP efficacy.

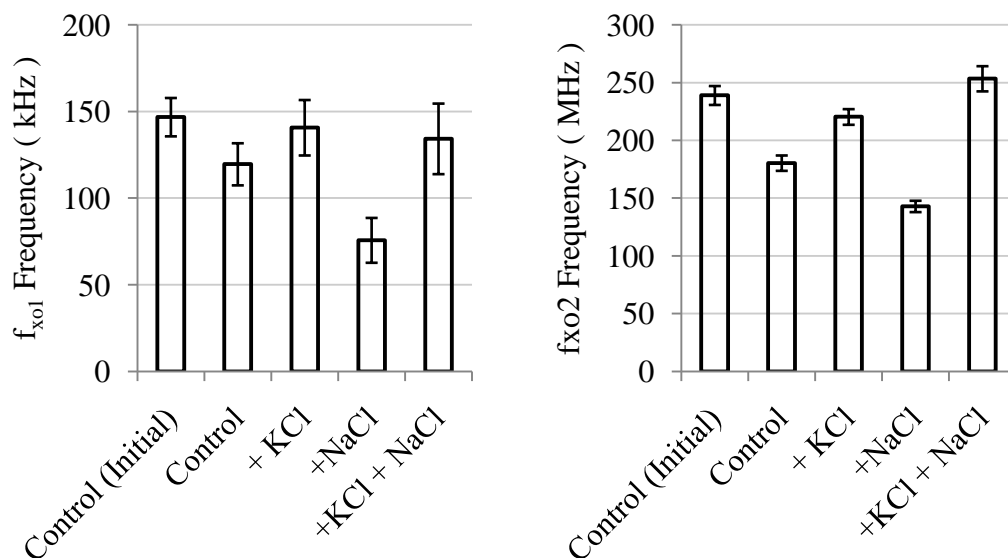


Figure 4.10 – Mean value of f_{xo1} and f_{xo2} for murine myeloma cells before and after three hours of exposure to various solutions. Error bars indicate the 95% confidence interval. Control (Initial) represents cells measured in the standard solution at zero hours. Control, +KCl, +NaCl and +KCl + NaCl represent measurement after three hours exposure to the standard solution with or without additional salts – immediately following re-suspension into the standard solution.

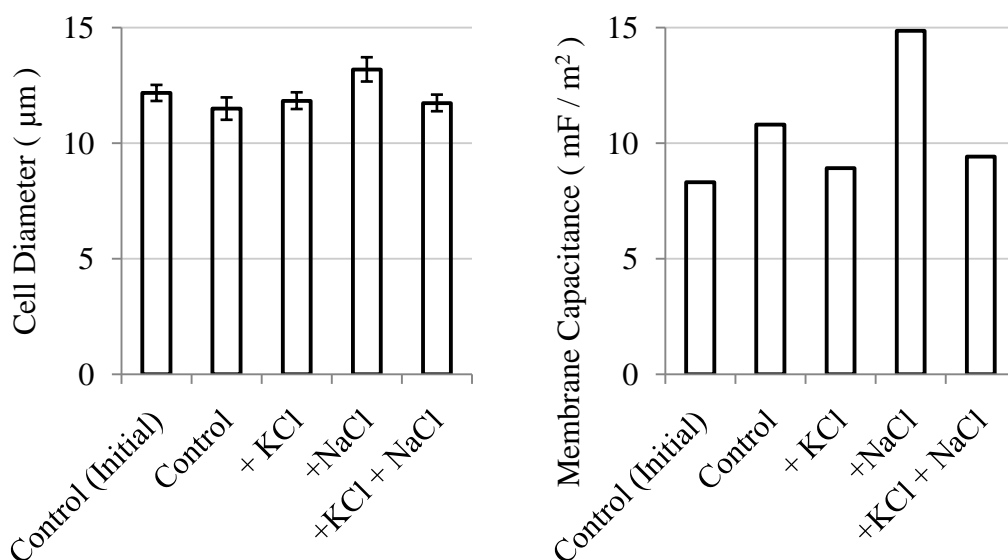


Figure 4.11 – Mean cell diameter and membrane capacitance based on fifty murine myeloma cells corresponding to the results of Fig. 4.10. Error bars indicate the 95% confidence interval. The capacitance is inferred from a combination of the diameters, mean f_{xo1} values of Fig. 4.10 and the solution conductivity of 33 mS/m.

Flow Cytometry

The large changes observed in both f_{x01} and f_{x02} when the cells are suspended in standard DEP solution are suggestive of major alterations to their physical structure. Flow cytometry is a tool which cell biologists have found useful in the investigation of cell viability and as an indicator of gross physical changes⁹. Cells are suspended in a solution which is fed through a flow cell, a device which generates a narrow stream of sheath fluid containing the cells. This stream of single cells is exposed to a laser beam at an observation point which is surrounded by lenses capturing light from both the forward and side (orthogonal) directions, illustrated in Fig. 4.12. An obscuration bar, present in the forward direction, blocks the oncoming laser beam from a subsequent photodiode detector. Light detected from the forward direction must therefore undergo either refraction or scattering around this bar and is commonly referred to as the forward scatter (FSC) signal. Larger cells will tend to refract a greater amount of light in this direction; however differences in their refractive indices will create additional complexity. The FSC light signal can therefore be interpreted as a rough guide to changes in cell volume but must be done so with care. Light is also scattered at wide angles from the beam direction which is partially collected by a lens positioned at right angles. Detection of light in this direction determines the side scatter (SSC) signal of the cell, a function of both the internal and surface structural complexities along with emitted light from fluorescent agents.

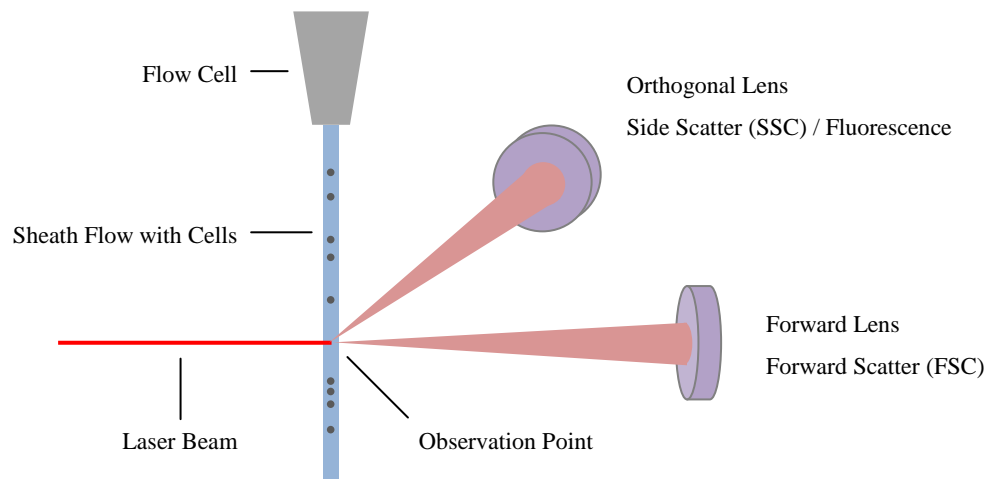


Figure 4.12 – Simplified schematic of the observation point and associated lenses in a flow cytometer.

Murine myeloma cells were processed by flow cytometry in both their culture medium and the isosmotic DEP solution, both immediately upon suspension and after four hours. An important feature of viable cells is an intact membrane, a consideration discussed earlier with respect to the first DEP crossover. A commonly used technique is the use of propidium iodide (PI) to determine the viability of cells¹⁰, a fluorescent molecule. The molecule is membrane impermeant and excluded from viable cells, allowing for the identification of whole cells which are physically compromised. It was therefore added to provide information regarding the stability of cells suspended in the DEP solution.

In Fig. 4.13 the forward scatter height versus side scatter height plot is gated to highlight ~60% of cells which appear intact and healthy, a similar distribution being reproduced after four hours. A band of apoptotic bodies and fragments exists below this region. The corresponding forward scatter height versus propidium iodide signal (FL-2 channel) height plots are similarly gated and indicate the same proportion of intact cells. Towards the right hand side of these plots are necrotic cells which have absorbed propidium iodide. When suspended into DEP solution the cells experience a drastic reduction in forward scatter height, from a median of ~500 to ~300 which suggests significant cell shrinkage, with a smaller reduction after an additional four hours. It indicates that although the DEP solution is isosmotic it is clearly not isotonic. Both side scatter and propidium iodide signal heights appear to increase following an additional four hours in DEP solution, with long term suspension leading towards cell death. These changes suggest a progressive break down of the membrane with time, which would logically be associated with an increase in membrane conductance. Such behaviour may be expected to reduce f_{x01} however the opposite was observed in Fig. 4.3 suggesting that either the uptake of propidium iodide is not associated with increased membrane conductance, or that those cells break down rapidly such that the DEP spectrum is collapsed entirely.

By varying the amount of sucrose used in the DEP solution the osmolality can be controlled. Three solutions with osmolalities of 270, 310 and 350 mOsm/kg were created to compare their effect on cells against a culture medium control. In Fig. 4.14 the forward scatter height versus propidium iodide signal (in the FL-3 channel) height plots display the effect of varying osmotic stress. The gated region highlights intact and healthy cells with 63.1% of the population in the original culture medium. Corresponding intact fractions of 48.7%, 36.9% and 31.4% result from immediate suspension into DEP solutions of 270, 310 and 350 mOsm/kg in osmolality, respectively. As the osmolality is reduced the median forward scatter is raised towards that of the culture medium and the proportion of whole cells, relative to fragments, is increased.

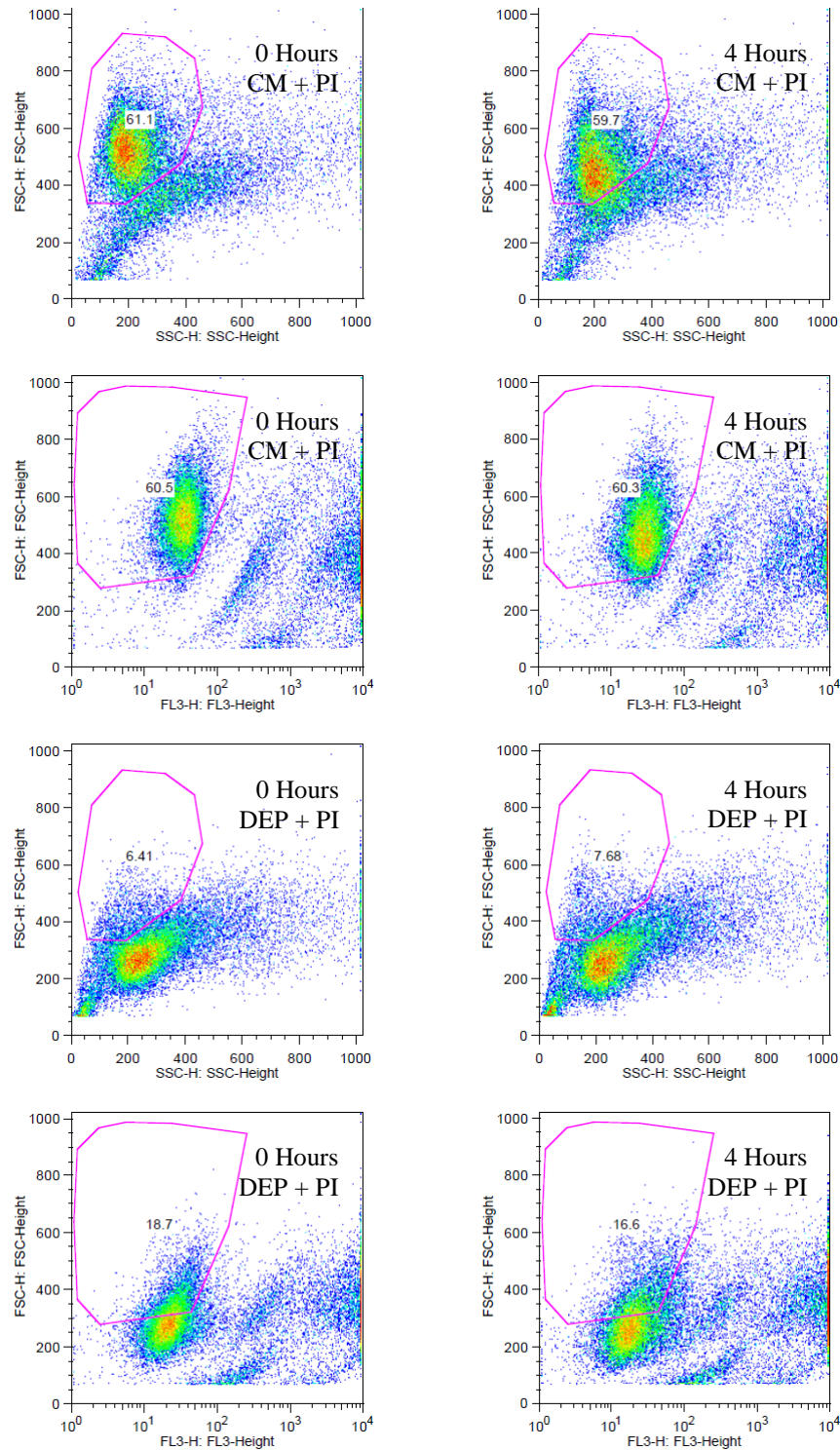


Figure 4.13 – Plots of forward scatter height versus both side scatter height and propidium iodide uptake (FL3-Height) by cells. Each plot represents 25,000 cells in either culture medium (CM) or isosmotic DEP solution (DEP) after zero and four hours of suspension. The gated region provides an estimate of the intact and healthy proportion of cells (in %).

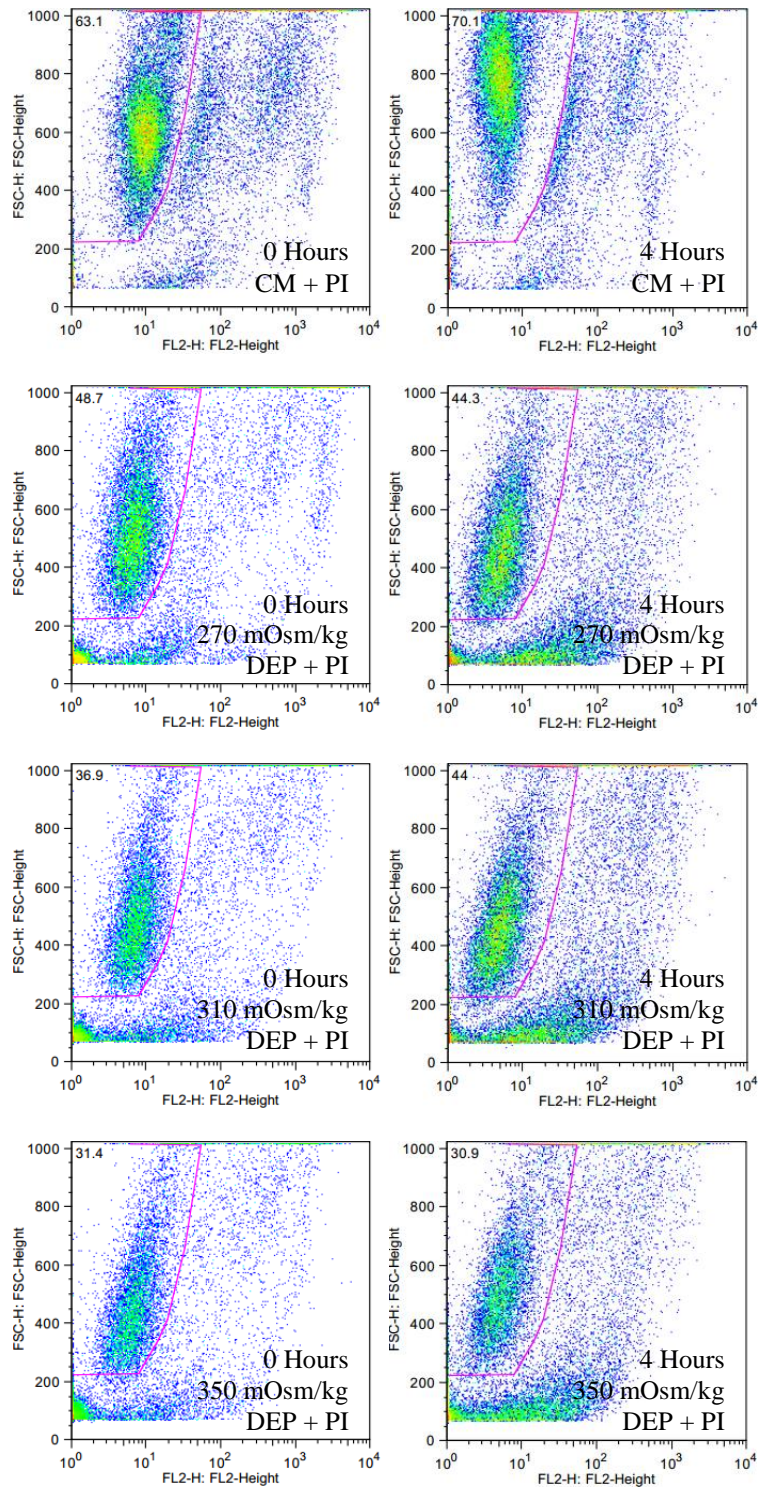


Figure 4.14 – Plots of forward scatter height versus propidium iodide uptake (FL2-Height) by cells. Each plot represents 25,000 cells in either culture medium (CM) or DEP solution (270/310/350 mOsm/kg) after zero and four hours of suspension. The gated region provides an estimate of the intact and healthy proportion of cells.

The forward scatter plots of Fig. 4.14 indicate a median value of 600 units for cells in culture media which drops to 400-500 units in the DEP solutions. An isotonic osmolality below 270 mOsm/kg is suggested which requires a lower concentration of sucrose than was used here. After four hours of suspension at 21°C the samples were re-measured. The culture media sample displayed an increase in median forward scatter to 800 units, a change which was unexpected but may have been due to a lack of sufficient agitation. Across all three DEP osmolalities the median forward scatter remained stable. It is clear that reducing the DEP solution osmolality towards an isotonic state increases the proportion of intact cells. Hyperosmotic stress is known to induce apoptosis in mammalian cells¹¹, a mechanism which appears to be responsible for the reduced proportion of intact cells seen in the DEP solution of 350 mOsm/kg osmolality.

Conclusion

In this chapter the first steps have been taken to measure and understand the second crossover, $f_{x_{o2}}$. A test system was developed and used to evaluate murine myeloma cells, successfully demonstrating the existence of $f_{x_{o2}}$ over the frequency range predicted by prior modelling. Further analysis revealed that $f_{x_{o2}}$ is unstable, decreasing over time when suspended in a standard isosmotic DEP solution. Red blood cells were also shown to exhibit the same behaviour providing some evidence that this instability, in solutions where the electrolyte has been isosmotically substituted, affects mammalian cells more generally. This phenomenon is consistent with observations made by both Gimsa *et al.* and Lacelle *et al.* using murine myeloma and red blood cells, respectively. Their observations indicate that the observed instability is a result of electrolyte efflux, a situation which would decrease intracellular conductivity and by extension $f_{x_{o2}}$.

Solution osmolality displayed no significant effect on the long term trend but did influence the initial value, consistent with a rapid equilibration of ions occurring on suspension but prior to measurement. A similar response was also observed by raising the proportion of phosphate buffered saline in the solution, but was detrimental to the applied DEP force. By decreasing temperature the stability of cells was shown to improve, a temperature of 10°C effectively eliminating an equilibration process associated with the first two hours of suspension, but unable to prevent its longer term decline. The activation energy of this former process was determined to be 44 kJ/mol and is consistent with a similar measurement made by Lacelle *et al.* based on the efflux of red blood cell electrolytes under comparable conditions. Although the decline in $f_{x_{o2}}$ could not be eliminated its effect can be mitigated by

operating at room temperature, or below, within a short period of time – i.e. within thirty minutes of the initial wash. Based on this approach the impact of returning sodium and potassium chloride to the solution over a three hour period was explored, with measurements of f_{xO_2} subsequently performed in the standard DEP solution. These indicated that the removal of potassium chloride is fundamental to the observed decline.

Flow cytometry has been performed using propidium iodide to assess membrane integrity, revealing that the DEP solution destroys a large proportion of cells on suspension. In addition, the isosmotic substitution of electrolytes by sucrose does not appear isotonic, with a significant reduction in cell volume occurring. Hypotonic stress is capable of reducing this cell shrinkage and increasing the proportion of cells which are both intact and viable.

References

- 1 Chung, C., Waterfall, M., Pells, S., Menachery, A., Smith, S. & Pethig, R. (2011) Dielectrophoretic characterisation of mammalian cells above 100 MHz. *Journal of Electrical Bioimpedance*, 2, 64-71.
- 2 Gimsa, J., Marszalek, P., Loewe, U. & Tsong, T. Y. (1991) Dielectrophoresis and electrorotation of neurospora slime and murine myeloma cells. *Biophysical Journal*, 60 (4), 749-760.
- 3 Lacelle, P. L. & Rothstein, A. (1966) The passive permeability of the red blood cell to cations. *The Journal of General Physiology*, 50 (1), 171-188.
- 4 Yu, S. P. (2003) Regulation and critical role of potassium homeostasis in apoptosis. *Progress in Neurobiology*, 70 (4), 363-386.
- 5 Rieder, C. L. & Cole, R. W. (2002) Cold-shock and the mammalian cell cycle. *Cell Cycle*, 1(3), 169-175.
- 6 Boutilier, R. G. (2001) Mechanisms of cell survival in hypoxia and hypothermia. *The Journal of Experimental Biology*, 204 (18), 3171-3181.
- 7 Hu, J., Valckenborgh, E. V., Menu, E., Bruyne, E. D. & Vanderkerken, K. (2012) Understanding the hypoxic niche of multiple myeloma: therapeutic implications and contributions of mouse models. *Disease Models & Mechanisms*, 5 (6), 763-771.
- 8 Plesnila, N., Müller, E., Guretzki, S., Ringel, F., Staub, F. & Baethmann, A. (2000) Effect of hypothermia on the volume of rat glial cells. *The Journal of Physiology*, 523, 155-162.
- 9 Shapiro, H. M. (2003) *Practical Flow Cytometry*, Hoboken: Wiley.
- 10 Vermes, I., Haanen, C., Steffens-Nakken, H. & Reutelingsperger, C. (1995) A novel assay for apoptosis. Flow cytometric detection of phosphatidylserine expression on early apoptotic cells using fluorescein labelled Annexin V. *Journal of Immunological Methods*, 184 (1), 39-51.
- 11 Copp, J., Wiley, S., Ward, M. W. & van der Geer, P. (2005) Hypertonic shock inhibits growth factor receptor signaling, induces caspase-3 activation, and causes reversible fragmentation of the mitochondrial network. *Cell Physiology*, 288 (2), C403-C415.

Chapter Five

Controlling the Second Crossover Frequency

Introduction

The observation of the second DEP crossover frequency, f_{x02} , has allowed us to validate the dielectric modelling used in its prediction and provided us with information regarding both its frequency distribution and stability. These are critical steps, but to seek practical applications for this technique we need to understand the physical factors which underpin it and then determine the corresponding biological factors of importance. This situation is similar to that encountered with the first DEP crossover frequency, f_{x01} , where mathematical analysis yielded an expression governing its behaviour, but practical experiments determined the relevance of biological features in light of this.

In this chapter an analytical derivation of f_{x02} is undertaken, a derivation which relies on assumptions that are both physical and biological. The features which govern f_{x01} are principally related to the cell membrane and it can therefore be explored by a number of biological techniques directly, those relating to surface charge and membrane integrity, for example. By contrast, f_{x02} is understood to be a function of principally intracellular properties, an environment which is not directly accessible and whose physical structure remains an area of intense research. An attempt is made here to control f_{x02} by applying hyposmotic stress that drives water into the cell, diluting the intracellular compartment and thereby reducing intracellular conductivity. Simultaneous flow cytometry using a fluorescent indicator which selectively binds to potassium is also undertaken to corroborate the ionic state of cells with their measured dielectric behaviour.

An Analytical Derivation of f_{x02}

Theoretical and experimental evaluations of f_{x01} have been extensive and exploited in various practical applications of DEP, such as the manipulation, separation and isolation of target cells from mixed suspensions¹⁻⁴. The derivation of Eq.(2.39) – an analytical expression for f_{x01} – has allowed researchers to understand the critical factors underlying its behaviour. By the same logic, an analytical expression is desirable for f_{x02} to provide a simple means of predicting and interpreting results. Electro-impedance measurements across a wide frequency range may be used to fit a multi-shelled model, simultaneously solving for the

radius, permittivity and conductivity in each shell⁵. As the crossover frequency provides only one point of reference this detail is not feasible, or appropriate. By using a single-shelled model to approximate the intracellular volume the situation can be simplified greatly, whilst still providing an insight into the trends observed. The effective permittivity for such a particle may be expressed⁶ as Eq.(2.35) and is repeated here for convenience:

$$\varepsilon_{eff}^* = \varepsilon_{mem}^* \left[\frac{a^3 + 2 \left(\frac{\varepsilon_{int}^* - \varepsilon_{mem}^*}{\varepsilon_{int}^* + 2\varepsilon_{mem}^*} \right)}{a^3 - \left(\frac{\varepsilon_{int}^* - \varepsilon_{mem}^*}{\varepsilon_{int}^* + 2\varepsilon_{mem}^*} \right)} \right] \quad (5.1)$$

where $a = (r_{int} / r_{mem})^3$, r_{mem} is the outer membrane radius, r_{int} is the intracellular radius, ε_{int}^* is the intracellular complex permittivity and ε_{mem}^* is the membrane complex permittivity, the latter two being defined by the form:

$$\varepsilon^* = \varepsilon - \frac{j\sigma}{\omega} \quad (5.2)$$

which describes a homogenous material of permittivity ε and conductivity at an angular field frequency of ω . Eq.(5.2) provides a general description of the real and imaginary parts for any complex permittivity. The real part of the effective complex cell permittivity described by Eq.(5.1) therefore corresponds to an effective permittivity whereas its imaginary part, multiplied by $-\omega$, corresponds to an effective cell conductivity. If we assume the best fitted values derived by Asami *et al.*⁵ for murine lymphocytes, but remove the nucleus and nuclear envelope as a simplifying assumption, the effective relative permittivity and conductivity behaviour of Fig. 5.1 is produced.

In the DC limit the effective cell conductivity is approximated⁷ by $\sigma_{eff(DC)} \approx r_{mem} \times \sigma_{mem} / t_{mem} = 13.3 \text{ mS/m}^2$, where $t_{mem} = r_2 - r_1$. The corresponding relative permittivity may be approximated by $\varepsilon_{eff(DC)} \approx r_{mem} \times \varepsilon_{mem} / t_{mem} = 2817$. Both of these values correspond well to the model and form the basis of Eq. 2.39, the analytical solution for f_{x01} . The high effective permittivity at low frequencies is a direct consequence of Maxwell-Wagner interfacial polarisation occurring across the cell membrane. As the frequency increases beyond 1 MHz the displacement exceeds the conductive current across the membrane and this polarisation mechanism breaks down. As the frequency continues to increase the effective values for conductivity and permittivity approach that of their intracellular volume, with both quantities within 10% of their intracellular values by 40 MHz.

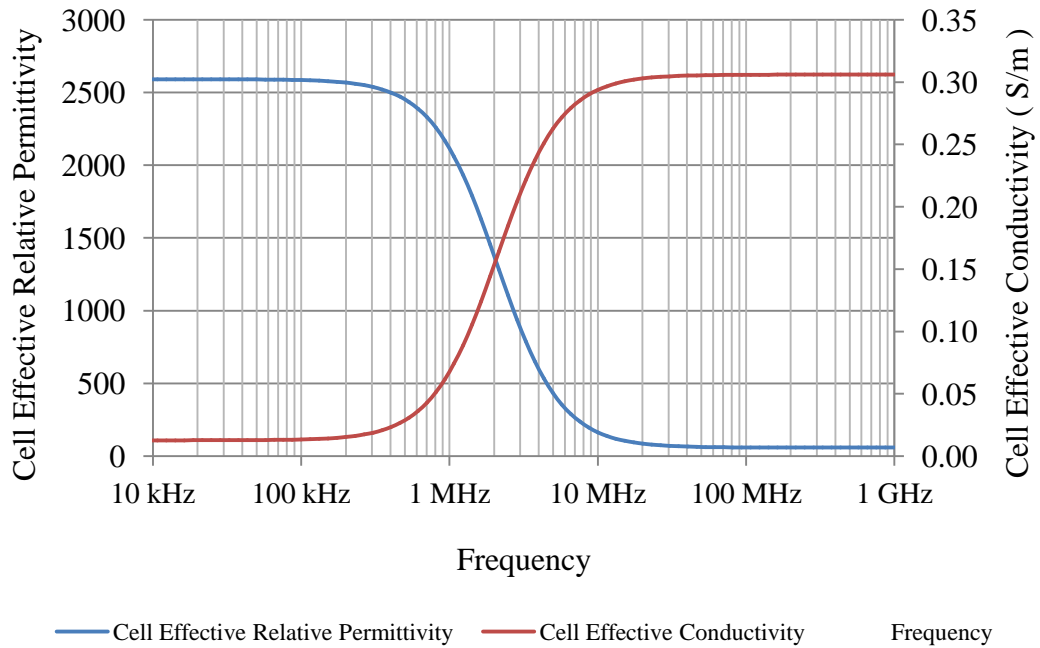


Figure 5.1 – The effective cell relative permittivity and conductivity based on a single-shelled sphere with parameters derived from the fitted electro-impedance measurements of murine lymphocytes made by Asami *et al.* Intracellular (cytoplasmic) relative permittivity $\epsilon_{\text{int}} = 60$, conductivity $\sigma_{\text{int}} = 0.32 \text{ S/m}$ and radius $r_{\text{int}} = 2.893\mu\text{m}$. Membrane relative permittivity $\epsilon_{\text{mem}} = 6.8$, conductivity $\sigma_{\text{mem}} = 32 \mu\text{S/m}$ and radius $r_{\text{mem}} = 2.900\mu\text{m}$.

The situation is complicated by the addition of a nucleus and nuclear envelope. However, the effective permittivity and conductivity of the cell will still approach their effective intracellular values at high frequencies, as displayed in Fig. 5.2. The introduction of a large nucleus results in a visible dispersion between 10 and 100 MHz, a function of both the nuclear envelope and differences between the cytoplasm and nucleus. As f_{x02} typically exists above this range for murine myeloma cells, which possess a high nucleus-to cytoplasm ratio, it is reasonable to expect its value to depend principally upon properties of the nucleus. Decreasing the size of the nucleus complicates matters significantly, requiring an analytical expression which incorporates an additional shell. Under such conditions the power of this approach is less clear, but may offer sensitivity to cell cycle or sufficient discrimination based on net properties. In Chapter Four the importance of intracellular ion efflux was discussed which, assuming the ions behave as strong electrolytes of sufficiently low concentration, will reduce the effective cell conductivity in a proportionate manner. Intracellular conductivity is therefore a critical parameter which requires consideration.

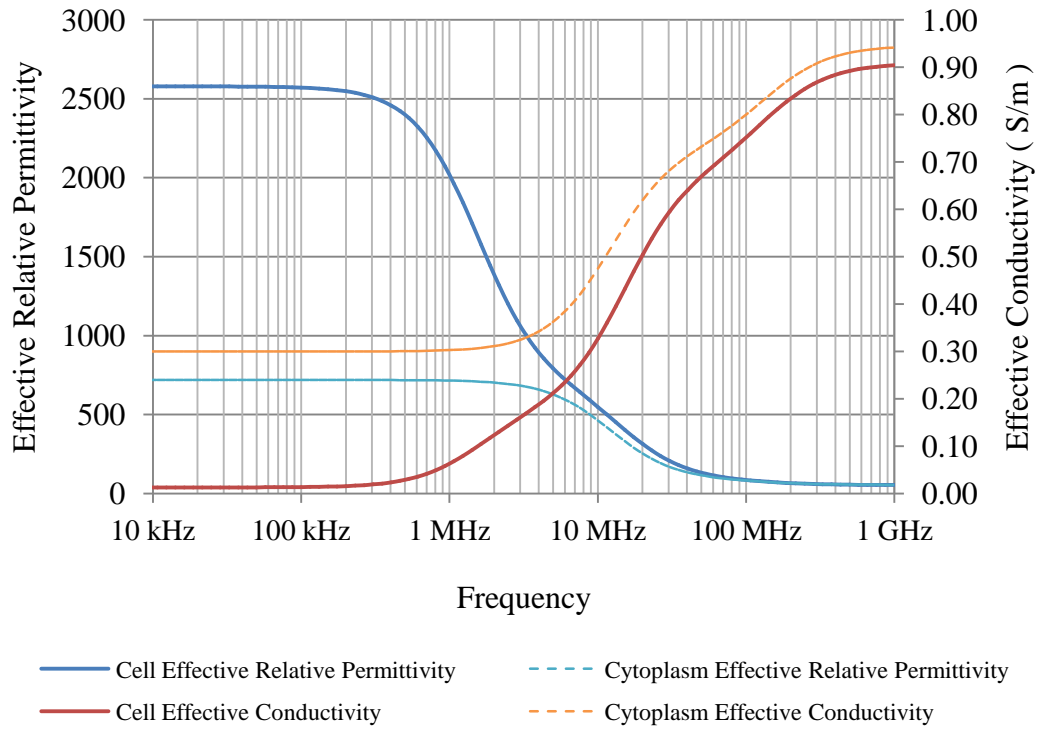


Figure 5.2 – The effective relative permittivity and conductivity for the triple-shelled sphere and its intracellular volume, with parameters derived from the fitted electro-impedance measurements of murine lymphocytes made by Asami *et al.* Nucleoplasm relative permittivity $\epsilon_1 = 52$, conductivity $\sigma_1 = 1.35$ S/m and radius $r_1 = 2.460\mu\text{m}$. Nuclear envelope relative permittivity $\epsilon_2 = 28$, conductivity $\sigma_2 = 6$ mS/m and radius $r_2 = 2.500\mu\text{m}$. Cytoplasm relative permittivity $\epsilon_3 = 60$, conductivity $\sigma_3 = 0.32$ S/m and radius $r_3 = 2.893\mu\text{m}$. Membrane relative permittivity $\epsilon_4 = 6.8$, conductivity $\sigma_4 = 32$ $\mu\text{S/m}$ and radius $r_2 = 2.900\mu\text{m}$. Solution relative permittivity $\epsilon_s = 80.1$ and conductivity $\sigma_s = 50$ mS/m.

In Fig. 5.3 the conductivities of the cytoplasm and nucleus have been individually varied in an aqueous solution of 50 mS/m conductivity and, based on the Clausius-Mossotti factor of Eq.(2.20), $f_{x_{02}}$ has been determined numerically. The behaviour appears to be highly linear with changing conductivity and we should therefore expect it to emerge as a principal coefficient in its analytical expression. Due to the large proportion of the intracellular volume taken up by the nucleus it dominates the cells dielectric response and therefore $f_{x_{02}}$. If an efflux of ions from the intracellular space occurs, a process that determines its electrical conductivity and by extension $f_{x_{02}}$, the question of how the nucleus will respond arises.

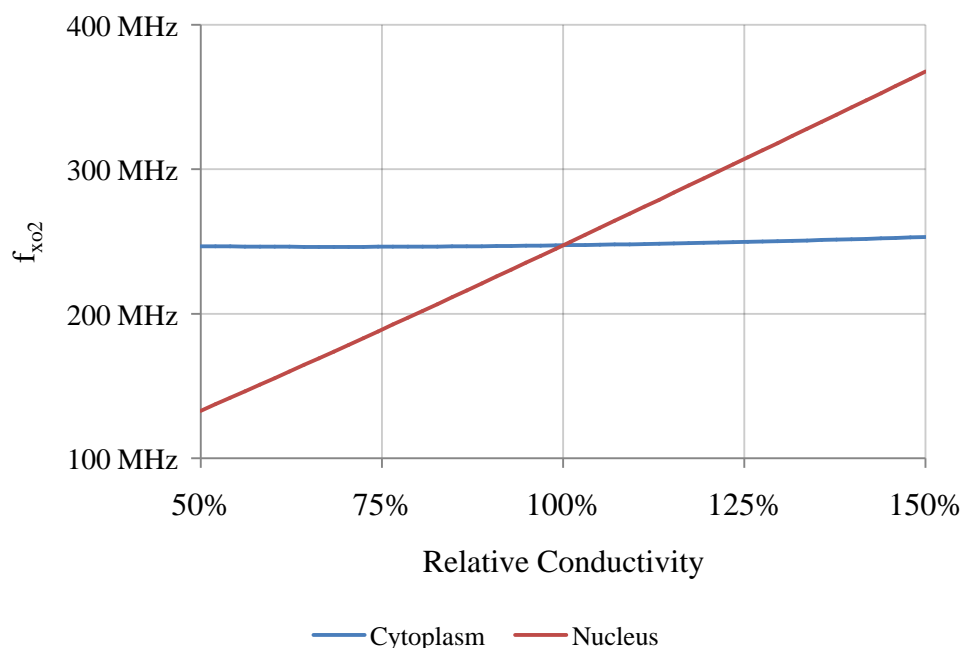


Figure 5.3 – Modelled values for $f_{x_{o_2}}$ based on the model used for Fig. 5.2. The conductivity of both the cytoplasm and nucleus has been varied by $\pm 50\%$ to illustrate their influence on $f_{x_{o_2}}$.

Thus far the nuclear envelope has been considered as a thin homogenous shell; however our current understanding has revealed a structure of significant complexity^{8,9}. An outer nuclear membrane which is continuous with the endoplasmic reticulum, a structure responsible for the synthesis and transport of proteins and lipids, surrounds an inner nuclear membrane. The region enclosed by these two membranes is known as the perinuclear space, the function of which remains unclear but may serve as a store for calcium and other inorganic ions. Ion channels have been discovered in recent years that connect this perinuclear space across both the inner and outer nuclear membranes, resulting in a structure which is analogous to a cell within a cell. Both the inner and outer nuclear membranes are fused together at so-called nuclear pore complexes (NPCs) which provide a direct link between the cytoplasm and nucleoplasm. It is likely that the response of these NPCs to the efflux of intracellular ions dictates the observed behaviour of $f_{x_{o_2}}$. Unfortunately there is currently no clear consensus on their permeability to ions and this particular issue remains contentious⁸. The practical difficulty associated with extracting pure samples of nuclear membrane and the alternate focus on macromolecular transport through these NPCs have limited progress in this area. The generally accepted view is of NPCs ~10nm in diameter that allow for the passive diffusion of both ions and other small molecules across the nuclear envelope which, in their hydrated form, are only angstroms in diameter. Studies have suggested that ion impermeable

states of the NPC may exist but given the sheer scale of changes observed here in f_{xo2} for cells suspended by a non-physiological solution the conventional viewpoint has been adopted. Based on the free diffusion of ions across the nuclear envelope, and the near complete dominance of the nucleus in determining f_{xo2} at high nucleus-to-cytoplasm ratios, an analytical solution restricted to a single shell is arguably appropriate for the murine myeloma cells under consideration. In such a single-shell model the nucleus is not ignored, its dielectric properties become incorporated as an overall ‘effective’ intracellular property.

The results of Chapter Four indicate values for f_{xo2} which are significantly higher than 10 MHz. Coupled with the analysis of Fig. 5.1, which suggests the membrane resistance is negligible at such frequencies, we may simplify Eq.(5.1) by defining the volume ratio $a = 1$. This procedure is purely one of mathematical convenience as the difference in conductivities between the intracellular and extracellular spaces clearly requires the membrane to physically exist. In doing so the effective complex permittivity of the cell ϵ_{eff}^* is simply reduced to that of the intracellular space ϵ_{int}^* . The crossover solution of Eq.(2.38) therefore simplifies at high frequencies to:

$$f_{xo2} = \frac{1}{2\pi} \sqrt{\frac{(\sigma_{int} + 2\sigma_s)(\sigma_s - \sigma_{int})}{(\epsilon_{int} - \epsilon_s)(\epsilon_{int} + 2\epsilon_s)}} \quad (5.3)$$

This formula was, to the author’s knowledge, first derived by Gimsa *et al.*¹⁰ and later by Broche *et al.*¹¹. In both cases the derivations were purely theoretical considerations whose validity remained unassessed. A further simplification can be made if the intracellular conductivity σ_{int} is significantly greater than the solution conductivity σ_s , a reasonable assumption as the modelled nucleoplasmic conductivity of 1.35 S/m is more than 20× the solution conductivity of 50 mS/m. Eq.(5.3) therefore simplifies to:

$$f_{xo2} = \frac{\sigma_{int}}{2\pi} \sqrt{\frac{1}{(\epsilon_{int} - \epsilon_s)(\epsilon_{int} + 2\epsilon_s)}} \quad (5.4)$$

The direct proportionality of f_{xo2} to intracellular conductivity is a result of particular interest. It suggests a means of evaluating the ionic state of a cell without resorting to the use of chemical probes or patch clamps which irrevocably alter cells and can be experimentally difficult to undertake. The solution permittivity is relatively stable and well characterised over the frequencies of interest. However, the parameters which affect intracellular permittivity, and more specifically that of the nucleus, are not well understood. The DNA of mammalian, and indeed all eukaryotic cells, is compacted into a dense structure known as chromatin. This condensation is achieved by a complex of the DNA with histones, proteins

around which the DNA is wrapped to create nucleosomes forming the chromatin structure. Histones possess a large positive charge which allows them to neutralise some of the charge in DNA, and an electrostatic behaviour which means its structural and dynamic properties are affected by the presence of free ions. The degree of condensation is also known to be a function of osmotic stress, with hyperosmotic shock resulting in the hypercondensation of chromatin¹². As with other aspects of the cell nucleus these remain areas of ongoing research and the degree to which they affect the apparent dielectric permittivity is in need of both theoretical and experimental attention.

Validating the Behaviour of f_{x02}

Intracellular dielectric properties are difficult to measure in practice and typically require the fitting of multi-shelled dielectric models to data extracted by electro-impedance, electrorotation or DEP across a range of frequencies. Eq.(5.4) suggests that f_{x02} is directly proportional to intracellular conductivity; a parameter which can be understood directly in terms of potassium, as both the most abundant intracellular ion and whose efflux was implicated in the observed f_{x02} changes of Chapter Four. Potassium-binding benzofuran isophthalate (PBFI) is a potassium-sensitive fluorophore which has been widely used to measure changes to intracellular potassium concentration $[K^+]_i$ for a variety of cell types^{13,14}. A change in $[K^+]_i$ can be induced by applying hypotonic stress which will drive water into the intracellular compartment and thereby act to dilute the concentration of ions. The approach was first explored by Kregenow¹⁵ *et al.* to induce an efflux of potassium from duck erythrocytes and more recently by Chimote *et al.*¹⁶ with human lens epithelial cells. By first loading cells with the PBFI fluorophore, suspending them into a range of DEP solutions with various osmolalities and measuring both f_{x02} and PBFI fluorescence the nature of their correlation can be explored.

Method

SP2/O-Ag14 murine myeloma cells, as used in Chapter Four, were cultured as described previously. In preparation for these experiments 15 ml of the cells were suspended at a density of 0.5×10^6 cells/ml and incubated overnight for 24 hours. The acetoxymethyl (AM) ester form of PBFI was dissolved in dimethyl sulfoxide (DMSO) at a stock concentration of 10 μ M with a volume of 10 μ l added to the culture media. To facilitate loading, 10 μ l of Pluronic F-127 (20% w/v) was also added and the cells incubated for 100 minutes. Extracellular PBFI was then removed by washing cells in fresh culture media followed by

incubation for an additional 60 minute period, a step found to be necessary in producing a stable fluorescent signal over several hours. These loaded cells were then suspended into PBS and split for subsequent analysis by both DEP and fluorescent flow cytometry.

Culture media such as RPMI-1640 contain numerous chemical components vital for the long term maintenance and growth of cells. As discussed previously, DEP experiments require the near complete removal of salts which constitute the main source of free ions to ensure a low conductivity. In this experiment an isosmotic formulation (290 mOsm/kg) was developed which contained (in mM): 0.4 Ca^{2+} , 0.4 Mg^{2+} , 0.8 NO_3^- 0.4 SO_4^{2-} , 11.1 glucose, 10 HEPES and 269 mannitol. HEPES acted as a pH buffer in place of the standard sodium bicarbonate system used with CO_2 , the pH adjusted to a value of 7.4 using 1M sodium hydroxide. Hyposmotic solutions were prepared at osmolalities of 140, 190, 215 and 240 mOsm/kg by the removal of mannitol from the above formulation. The resulting osmolality was measured using an Advanced Model 3300 osmometer with the conductivity determined to be ~42 mS/m for all solutions using an Oakton CON-510 conductivity meter.

Relative changes in $[\text{K}^+]_i$ were determined using a ratiometric approach. The fluorescence of PBF1 is particularly sensitive to $[\text{K}^+]_i$ when excited at 340nm, but is invariant at an isosbestic point which exists in the region of 380nm. By measuring the ratio of fluorescent emissions at 500 due to excitation at these aforementioned wavelengths it is possible to deduce the relative change in $[\text{K}^+]_i$. PBF1 is relatively insensitive to changes in intracellular pH and intracellular sodium concentrations below 75 mM, exhibiting a fluorescent ratio with a near linear relationship to $[\text{K}^+]_i$ up to physiological levels. Ratiometric measurements were performed on cells suspended in the DEP solutions of various osmolalities using a BD Biosciences LRS II. Excitation wavelengths of 355 and 405nm were selected which are close to the PBF1 fluorescent maxima and isosbestic points discussed with their emission measured at ~500nm. The ratios were normalised to that of a PBS suspended control, expressed as a percentage to provide a measure of $[\text{K}^+]_i$ relative to that of cells in a physiological solution.

DEP measurements of f_{x01} and f_{x02} were performed in conjunction with optical measurements of cell diameter, the techniques being as described in Chapter Four. All measurements were performed within 30 minutes of cells becoming exposed to the DEP solution in the first wash step, with the solutions warmed to a temperature of 21°C prior to use. These steps act to minimise the observed decline in f_{x02} to less than 10 MHz but are unable to prevent the initial rapid equilibration of ions which occurs within minutes of exposure to the DEP solution. By

deriving cell volume from diameter measurements osmotic behaviour, intracellular dilution and ion efflux of murine myeloma cells can be analysed.

Cell Volume

The volume of cells loaded with PBFI is shown in Fig. 5.4 to decrease as the osmolality is increased. Of particular interest is the isotonic cell volume which was measured in PBS to be $900\mu\text{m}^3$, a measurement which suggests an isotonic DEP solution osmolality of 215 mOsm/kg for these cells in a mannitol based DEP solution. Higher osmolalities resulted in cell shrinkage with a roughly 30% decrease in volume at the isosmotic value of 290 mOsm/kg.

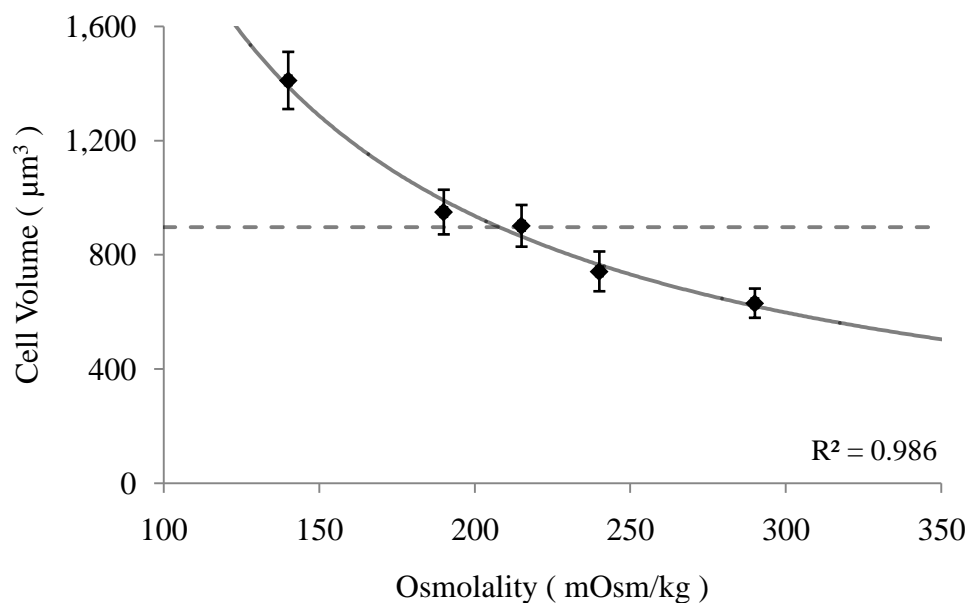


Figure 5.4 – Volumes derived from diameter measurements of murine myeloma cells suspended in DEP solutions of various osmolalities. Data points indicate the mean value \pm 95% confidence interval, based on 100 cells per datum and a spherical cell volume. The dashed horizontal line indicates the isotonic volume of cells measured in the PBS suspended control.

Kiesel *et al.*¹⁷ have made observations which are strikingly similar using human lymphocytes suspended in a sorbitol based solution. They determined that regulatory volume decrease (RVD), a process in which cells exposed to hypotonic stress are able to decrease their volume back towards their isotonic value, is inhibited below an osmolality of roughly 200 mOsm/kg. Their results also revealed isosmotic cell shrinkage, an observation made by Rouzair-Dubois *et al.*¹⁸ for murine glioma cells suspended in a solution where half of the

sodium chloride was isosmotically substituted by sucrose. Their study revealed a 15% decrease in cell volume within minutes of suspension which was attributed to the efflux of sodium and chloride ions due to their reduced extracellular concentration. Hamann *et al.*¹⁹ implicated the Na-K-Cl co-transporter NKCC1 in facilitating this isosmotic cell shrinkage under similar conditions with human epithelial cells. This mechanism appears to be implicated in the rapid ionic equilibration described previously, however the degree to which it affects the decline of $f_{x_{o_2}}$ over the subsequent two hours is not known. The additional hyposmotic stress acting beyond the observed isotonic point nevertheless increases the cell volume, acting to dilute the intracellular compartment.

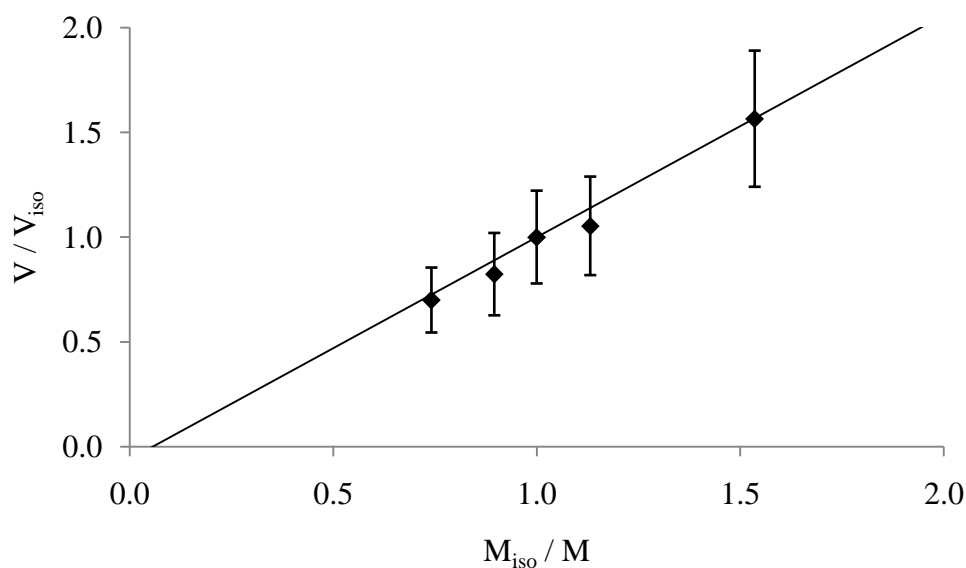


Figure 5.5 – Boyle-van't Hoff plot for the murine myeloma cells suspended in their DEP solutions and based on the data of Fig. 5.4. The volume V normalised to the isotonic volume V_{iso} is plotted against the inverse of osmolality M normalised to the isotonic osmolality M_{iso} .

Boyle-van't Hoff (BVH) plots are often used as a means of linearising an idealised relationship between cell volume and extracellular osmolality²⁰. The underlying relationship is based on the amount of impermeable solute, either side of a semi-permeable membrane, being constant. If we assume that the osmolality of solutes equals their molality and that no permeable solutes are present then the following relationship may be derived:

$$\frac{V_{BVH}}{V_{iso}} = (1 - v_b) \frac{M_{iso}}{M} + v_b \quad (5.5)$$

where V_{BVH} is the cell volume modelled by the relationship, M is the extracellular osmolality, V_{iso} is the isotonic volume, M_{iso} the corresponding isotonic osmolality and v_b the osmotically

inactive volume fraction. The volume of a cell can therefore be plotted as a function of the solution osmolality (both normalised to isotonic values) to determine the inactive volume and whether they behave as an ideal osmometer. When the data of Fig. 5.4 is fitted in this manner, such that the model passes through the isotonic datum, the plot of Fig. 5.5 is produced with an R^2 value of 0.971. The negative intercept represents an osmotically inactive fraction of -6%, an unusual result which may be the result of measurement error if the cells *in toto* are behaving close to ideal osmometers. Alternatively the cells may not be fully equilibrated and may be exhibiting active water transport, a conclusion which is reasonable based on the apparent ion effluxes occurring throughout these measurements. The result merits further study however the principal aim of controlling cell volume was achieved with the model providing an effective fit to the data for further analysis.

First Crossover and Membrane Capacitance

The behaviour of $f_{x_{o1}}$ is shown in Fig. 5.6 which displays its value increasing as the solution osmolality is decreased. It is noteworthy that the relationship appears linear, with an R^2 value of 0.999, from the isotonic osmolality of 215 mOsm/kg and below. At the time of writing, and to the authors knowledge, there is currently no known mechanism which explains the observed linear relationship between osmolality and $f_{x_{o1}}$ in the hypotonic range.

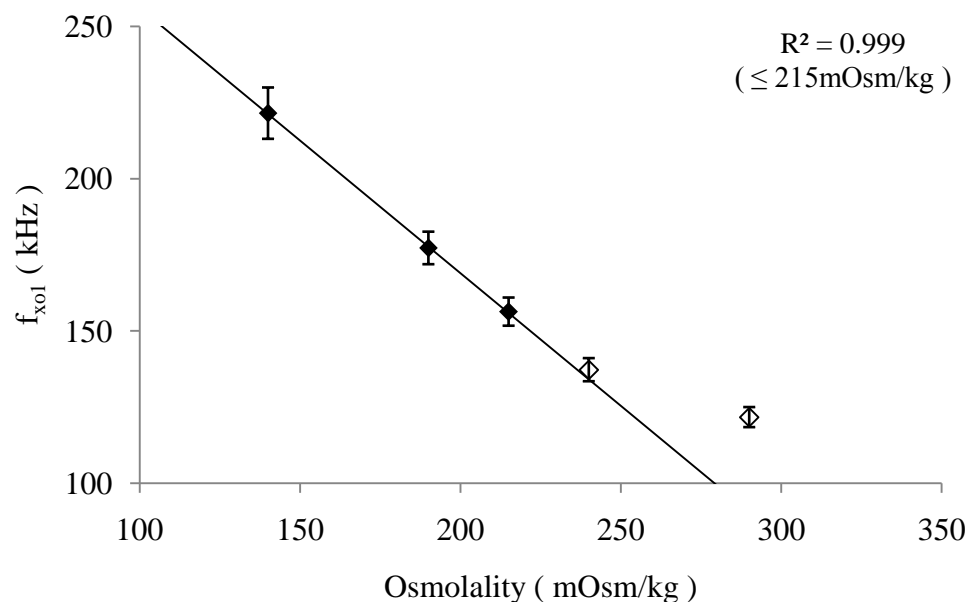


Figure 5.6 – $f_{x_{o1}}$ for the murine myeloma cells suspended in DEP solutions as a function of osmolality. Data points indicate the mean value \pm 95% confidence interval. The line of best fit has been applied to the isotonic and hypotonic data only (filled markers).

Healthy cells which are suspended in DEP solution for a short period of time exhibit a near zero membrane conductance. The membrane capacitance C_{mem} in F/m^2 may therefore be estimated by re-arranging Eq.(2.39):

$$C_{mem} = \frac{\sqrt{2}}{2\pi r f_{xo1}} \sigma_s \quad (5.6)$$

where r is half of the measured cell diameter, f_{xo1} the corresponding mean first crossover and σ_s is the solution conductivity measured at 41.5 mS/m. Calculation of the membrane capacitance C_{mem} produces the plot of Fig. 5.7, through which a straight line fit provides an R^2 value of 0.992. Cells with a smooth membrane such as erythrocytes typically exhibit membrane capacitances^{10,21} of between 6 and 8 mF/m^2 , with values closer to 14 mF/m^2 being typical of human lymphocytes suspended in isosmotic solutions²². The values encountered here are therefore within the expected range whilst the decrease in C_{mem} with osmolality is consistent with existing literature^{17,23}. At the lowest osmolality of 140 mOsm/kg the estimated value for C_{mem} is 6.1 mF/m^2 , a value which is close to the theoretical minimum and suggestive of cells approaching the point of cytolysis.

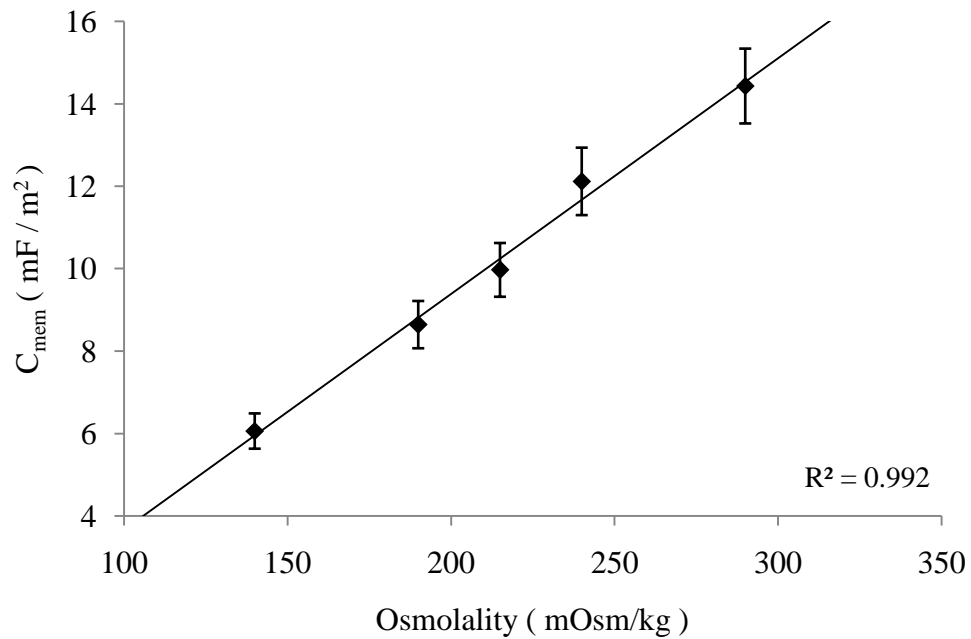


Figure 5.7 – C_{mem} derived from the data of Fig. 5.6 and Eq.(5.6) based on the measured solution conductivity of 41.5 mS/m. Data points indicate the mean value \pm 95% confidence interval.

Second Crossover

The value measured for $f_{x_{o2}}$ as a function of osmolality is plotted in Fig. 5.8 and suggests it is constant over the observed hypertonic range. In previous experiments the value of $f_{x_{o2}}$ was typically ≥ 200 MHz, higher than the value of approximately 170 MHz observed here. This difference may be the result of a change in culture conditions or the additional handling required for the loading of PBFI into cells prior to their suspension into DEP solutions. If RVD is occurring over the hypertonic range it will result in the efflux of K^+ , Cl^- and water, but apparently in such a manner as to maintain intracellular conductivity at the observed isosmotic value. By contrast, hypotonic stress results in $f_{x_{o2}}$ decreasing from its isotonic value of 166 MHz by 35%, to a value of 108 MHz at 140 mOsm/kg.

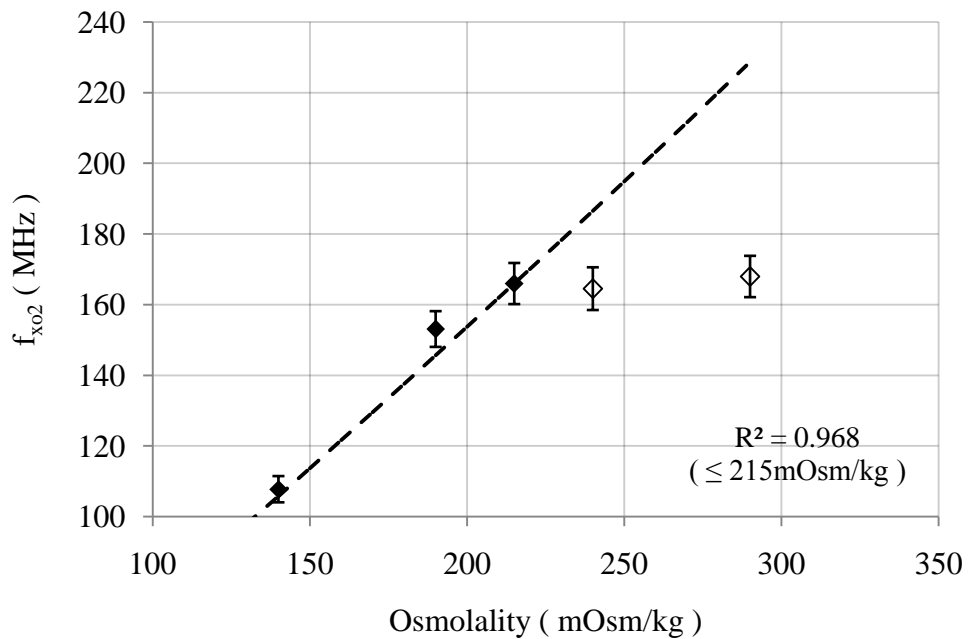


Figure 5.8 – $f_{x_{o2}}$ plotted as a function of solution osmolality. Data points indicate the mean value \pm 95% confidence interval. The dashed line is an estimate of $f_{x_{o2}}$ based upon the dilution of intracellular ions from the isotonic point of 215 mOsm/kg into the hypotonic range only (filled markers), as described by Eq. 5.7 and the fitted BVH model of Eq.(5.5).

If RVD is inhibited below the isotonic osmolality of 215 mOsm/kg it follows that there should be no significant efflux of intracellular ions. The concentration of intracellular ions will be diluted by the hypotonically induced volume increase, reducing the conductivity in a proportional manner and thereby reducing $f_{x_{o2}}$. By using the fitted BVH model described earlier with the isotonic datum an estimate of $f_{x_{o2}}$ may be defined as:

$$f_{xo2(BVH)} = f_{xo2(iso)} \times \frac{V_{iso}}{V_{BVH}} \quad (5.7)$$

where the isotonic second crossover value $f_{xo2(iso)} = 166$ MHz is scaled by the isotonic volume $V_{iso} = 900\mu\text{m}^3$ divided by the BVH modelled volume of Eq.(5.5). The resulting relationship produces the straight dashed line displayed in Fig. 5.8 with an R^2 value over the hypotonic range of 0.968. As the fit appears to be effective it suggests that a simple dilution model is appropriate for the prediction of f_{xo2} from the isotonic datum. Furthermore, it suggests that any apparent changes to intracellular permittivity due to structural changes induced in the nucleus are insignificant by comparison to those of conductivity. Under hypertonic conditions the model breaks down, as should be the case if an efflux of intracellular ions due to RVD is occurring, acting against any increase in conductivity. The degree to which f_{xo2} and therefore intracellular conductivity is regulated over this range is noteworthy and may have a broader significance in terms of cell electrophysiology. The product of f_{xo2} and cell volume will be constant if the total amount of intracellular ions remains the same. If an efflux of ions occurs in the hypertonic range, relative to that of the isotonic datum, an estimate of the relative intracellular ion losses can be made as:

$$(1 - n) \times f_{xo2(iso)} \times V_{iso} = f_{xo2(hyper)} \times V_{hyper}$$

$$\Rightarrow n = 1 - \frac{f_{xo2(hyper)} \times V_{hyper}}{f_{xo2(iso)} \times V_{iso}} \quad (5.8)$$

where n is the proportion of ions lost relative to the isotonic datum, $f_{xo2(iso)}$ and $f_{xo2(hyper)}$ are the isotonic and hypertonic second crossovers with V_{iso} and V_{hyper} their corresponding volumes, respectively. These estimates are based purely on the movement of monovalent ions with no account taken of higher charge carriers such as Ca^{2+} or Mg^{2+} . At 240 and 290 mOsm/kg, intracellular ion losses of 18 and 29% are estimated, respectively. If the formula is applied in the hypotonic region this value remains close to zero as expected.

Intracellular Potassium

Ratiometric flow cytometry was performed on the PBFI loaded cells following suspension into the various DEP solutions. These measurements were carried out in parallel to those of DEP, with loaded cells split from the same batch and re-suspended using the same protocol and solutions. As the conductivity is unimportant for flow cytometry a PBS suspended control was also used to normalise the fluorescence ratios against cells held in a close to

physiological solution. The fluorescence ratio of the cells was calculated from their mean signal area intensity and is quoted in Fig. 5.9 after normalisation to the control. In the hypotonic range, between 140 and 215 mOsm/kg, the ratio increases significantly from 71 to 94%. Beyond this isotonic point a marginal increase up to 99% occurs at the isosmotic point, a small change by comparison to the concomitant 30% decrease in cell volume. The dashed line in Fig. 5.9 represents a linear fit to the fluorescence ratio over the hypotonic range, a model which results in an R^2 value of 0.996.

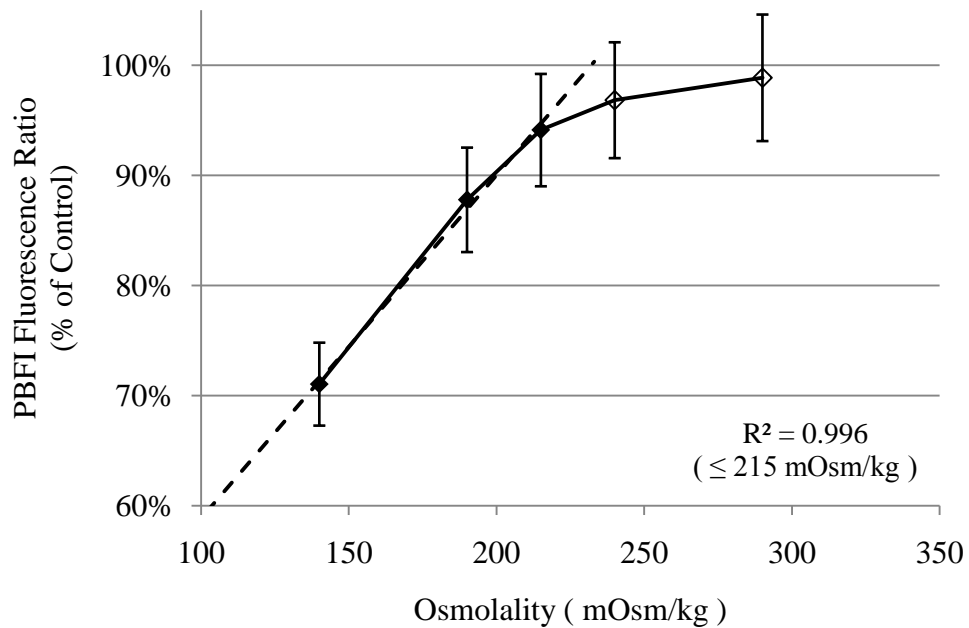


Figure 5.9 – Flow cytometry analysis of the PBFI fluorescence ratio for cells exposed to DEP solutions of various osmolalities. The ratios are normalised to that of a PBS suspended control. Data shown indicate the mean \pm 95% confidence interval. The dashed line is a linear fit of the normalised fluorescence ratio from the isotonic point of 215 mOsm/kg into the hypotonic range only (filled markers), modified from Eq.(5.7).

The linear relationship is again based on the assumption that ion efflux due to RVD is inhibited below the isotonic osmolality of 215 mOsm/kg. The fluorescent ratio of PBFI is also known to behave in a non-linear manner above physiological concentrations¹³, behaviour which could account for a small increase in fluorescence ratio. At the hypertonic osmolalities used here the fluorescence ratio remains less than that of the PBS suspended control, suggesting that $[K^+]_i$ remains below physiological concentrations and should therefore behave in a linear manner. Observations by Dezaki *et al.* of HeLa cells²⁴ suggest that the increase in hypertonic $[K^+]_i$ and $[Cl^-]_i$ is less than that expected from the associated

decrease in volume, a situation which implies that the osmotic water efflux drives an efflux of both ions during hypertonic cell shrinkage. The observations made here of f_{x02} , its relationship to intracellular conductivity and the measured volume changes also suggest a hypertonic efflux of ions. It is therefore reasonable to expect a linear relationship between the fluorescence ratio of PBF1 and f_{x02} , as both are expected to be linear functions of $[K^+]_i$. In Fig. 5.10 this fluorescence ratio is plotted against f_{x02} , for each of the respective osmolalities, and reveals a linear relationship between the two quantities. A straight line fit of the data provides an R^2 value of 0.967 and suggests that the changes in f_{x02} , intracellular conductivity and $[K^+]_i$ are both linearly related and proportional.

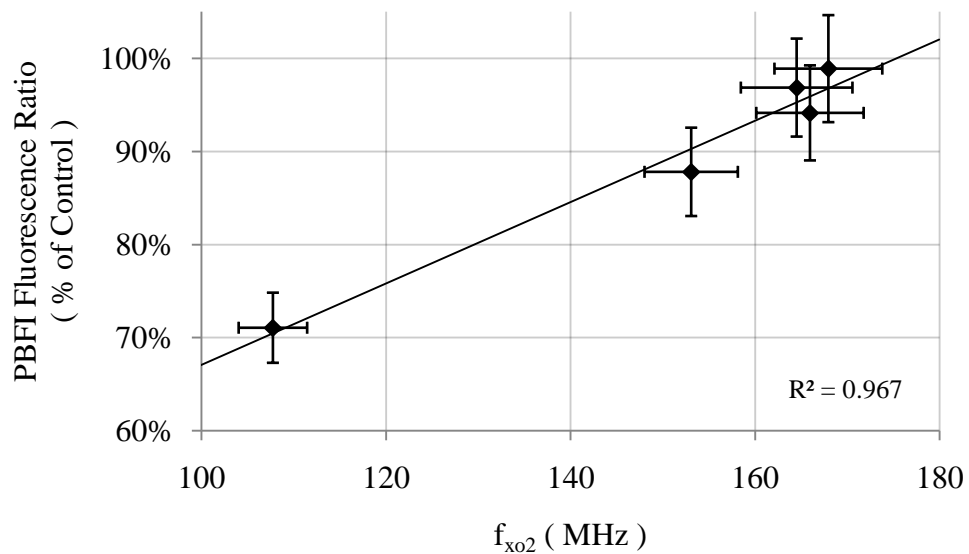


Figure 5.10 – PBF1 fluorescence ratio, relative to a PBS control, plotted as a function of f_{x02} . Data shown indicates the mean \pm 95% confidence interval for both quantities.

Conclusion

An analytical expression for f_{x02} has been derived based on a single shell model of a cell. This expression suggests a direct proportionality to the intracellular conductivity of a cell with a second dependency upon its intracellular permittivity. To determine its validity an experiment was undertaken involving dilution of the intracellular volume by applying hyposmotic stress, a process aimed at reducing the intracellular conductivity. A DEP solution based on the isosmotic substitution of sodium chloride by mannitol was used for this purpose. Murine myeloma cells were first loaded with the potassium-sensitive fluorophore PBF1 to allow for quantification of the intracellular potassium concentration $[K^+]_i$ relative to a PBS suspended control by ratiometric flow cytometry. Measurements of f_{x01} , f_{x02} and cell

diameter were undertaken in the DEP solutions simultaneously to provide a direct comparison to, and analysis of, the resulting dielectric changes.

The isosmotic DEP solution of 290 mOsm/kg induced cell-shrinkage relative to that of the control with an apparent isotonic osmolality of ~215 mOsm/kg, behaviour which appears to be consistent with inhibition of the regulatory volume decrease mechanism at and below this value. This behaviour implies the presence of both ion efflux and water transport out of the cell in the hypertonic region, including the isosmotic point. A Boyle-van't Hoff plot of the data suggests behaviour which is close to that of an ideal osmometer, with the discrepancy of a negative inactive volume fraction likely due to the unequilibrated state of the cells. It nevertheless provided an effective mathematical model of the cell volume to model intracellular dilution in the hypotonic range.

Membrane capacitance was calculated based on measurements of both f_{x01} and cell diameter, with values comparable to that of other published works on mammalian cells. A linear increase in its value was observed from the isosmotic point down to the theoretical minimum of 6 mF/m² at 140 mOsm/kg, corresponding to a near maximal dilution of the intracellular compartment. Measurement of f_{x02} revealed a plateau over the hypertonic range which, in conjunction with the observed volume reduction, indicates an efflux of both intracellular water and ions consistent with regulatory volume decrease. A model of ionic dilution from the isotonic point was found to accurately track the observed changes in f_{x02} over the hypotonic range. It provides evidence that f_{x02} does indeed scale with intracellular conductivity and that changes to the intracellular permittivity are negligible by comparison, under these conditions. At the isosmotic point an estimated 29% of the free charge is lost, a value which remains close to zero over the hypotonic range and is again consistent with the inhibition of regulatory volume decrease.

Ratiometric flow cytometry revealed trends in intracellular potassium concentration which are similar to those of f_{x02} . A dilution model from the isotonic point similar to that used for f_{x02} effectively tracked the observed hypotonic changes in its concentration, displaying a linear relationship with respect to osmolality which follows from the Boyle-van't Hoff formula. By plotting f_{x02} against the fluorescence ratio of PBF1 a linear relationship is suggested. Although f_{x02} does not discriminate between the various intracellular ions it offers a rapid and label-free means of evaluating the overall ionic state of cells.

References

- 1 Lei, U. & Lo, Y. J. (2011) Review of the theory of generalised dielectrophoresis. *IET Nanobiotechnology*, 5 (3), 86-106.
- 2 Pethig, R. (2010) Review Article-Dielectrophoresis: status of the theory, technology and applications. *Biomicrofluidics*, 4 (2), 022811.
- 3 Muratore, M., Srsen, V., Waterfall, M., Downes, A. & Pethig, R. (2012) Biomarker-free dielectrophoretic sorting of differentiating myoblast multipotent progenitor cells and their membrane analysis by Raman spectroscopy. *Biomicrofluidics*, 6, 034113.
- 4 Velugotla, S., Pells, S., Mjoseng, H. K., Duffy, C. R. E., Smith, S., Sousa, P. D. & Pethig, R. (2012) Dielectrophoresis based discrimination of human embryonic stem cells from differentiating derivatives. *Biomicrofluidics*, 6 (4), 044113.
- 5 Asami, K., Takahashi, Y. & Takashima, S. (1989) Dielectric properties of mouse lymphocytes and erythrocytes. *Biochimica et Biophysica Acta*, 1010 (1), 49-55.
- 6 Jones, T. B. (1995) *Electromechanics of Particles*, Cambridge: Cambridge University Press.
- 7 Schwan, H. P. (1957) Electrical properties of tissue and cell suspensions. *Advances in Biological and Medical Physics*, 5, 147-209.
- 8 Matzke, A. J. M., Weiger, T. M. & Matzke, M. (2010) Ion channels at the nucleus: electrophysiology meets the genome. *Molecular Plant*, 3 (4), 642-652.
- 9 Mazzanti, M., Bustamante, J. O. & Oberleithner, H. (2001) Electrical dimension of the nuclear envelope. *Physiological Reviews*, 81 (1), 1-19.
- 10 Gimsa, J., Müller, T., Schnelle T. & Fuhr, G. (1996) Dielectric spectroscopy of single human erythrocytes at physiological ionic strength: dispersion of the cytoplasm. *Biophysical Journal*, 71 (1), 495-506.
- 11 Broche, L. M., Labeed, F. H. and Hughes, M. P. (2005) Extraction of dielectric properties of multiple populations from dielectrophoretic collection spectrum data. *Physics in Medicine and Biology*, 50 (10), 2267-2274.
- 12 Finan, J., Leddy, H. & Guilak, F. (2011) Osmotic stress alters chromatin condensation and nucleocytoplasmic transport. *Biochemical and Biophysical Research Communications*, 408 (2), 230-235.
- 13 Kasner, S. E. & Ganz, M. B. (1992) Regulation of intracellular potassium in mesangial cells: a fluorescence analysis using the dye, PBFI. *American Journal of Physiology - Renal Physiology*, 262 (3), F462-F467.
- 14 Andersson, B., Janson, V., Behnam-Motlagh, P., Henriksson, R. & Grankvist, K. (2006) Induction of apoptosis by intracellular potassium ion depletion: using the fluorescent dye

- PBFI in a 96-well plate method in cultured lung cancer cells. *Toxicology in Vitro*, 20 (6), 986-994.
- 15 Kregenow, F. M. (1971) The response of duck erythrocytes to nonhemolytic hypotonic media. *The Journal of General Physiology*, 58 (4), 372-395.
 - 16 Chimote, A. A., Adragna, N. C. & Lauf, P. K. (2010) Ion transport in a human lens epithelial cell line exposed to hyposmotic and apoptotic stress. *Journal of Cellular Physiology*, 223 (1), 110-122.
 - 17 Kiesel, M., Reuss, R., Endter, J., Zimmermann, D., Zimmermann, H., Shirakashi, R., Bamberg, E., Zimmermann, U. & Sukhorukov, V. L. (2006) Swelling-activated pathways in human T-lymphocytes studied by cell volumetry and electrorotation. *Biophysical Journal*, 90 (12), 4720-4729.
 - 18 Rouzair-Dubois, B., Ouanounou, G., O'Regan, S. & Dubois, J. M. (2009) Sodium-dependent activity of aquaporin-1 in rat glioma cells: a new mechanism of cell volume regulation. *Pflügers Archiv: European Journal of Physiology*, 457 (5), 1187-1198.
 - 19 Hamann, S., Herrera-Perez, J. J., Zeuthen, T. & Alvarez-Leefmans, F. J. (2010) Cotransport of water by the Na⁺-K⁺-2Cl⁻ cotransporter NKCC1 in mammalian epithelial cells. *The Journal of Physiology*, 588 (21), 4089-4101.
 - 20 Katkov, I. I. (2011) On proper linearization, construction and analysis of the Boyle-van't Hoff plots and correct calculation of the osmotically inactive volume. *Cryobiology*, 62 (3), 232-241.
 - 21 Chan, K. L., Gascoyne, P. R., Becker, F. F. & Pethig, R. (1997) Electrorotation of liposomes: verification of dielectric multi-shell model for cells. *Biochimica et Biophysica Acta*, 1349 (2), 182-196.
 - 22 Pethig, R., Bressler, V., Carswell-Crumpton, C., Chen, Y., Foster-Haje, L., Garcia-Ojeda, M. E., Lee, R. S., Lock, G. M., Talary, M. S. & Tate, K. M. (2002) Dielectrophoretic studies of the activation of human T lymphocytes using a newly developed cell profiling system. *Electrophoresis*, 23 (13), 2057-2063.
 - 23 Tan, Q., Ferrier, G. A., Chen, B. K., Wang, C. & Sun, Y. (2012) Quantification of the specific membrane capacitance of single cells using a microfluidic device and impedance spectroscopy measurement. *Biomicrofluidics*, 6 (3), 034112.
 - 24 Dezaki, K., Maeno, E., Sato, K., Akita, T. & Okada, Y. (2012) Early-phase occurrence of K⁺ and Cl⁻ efflux in addition to Ca²⁺ mobilization is a prerequisite to apoptosis in HeLa cells. *Apoptosis*, 17 (8), 821-831.

Chapter Six

Cell Death and the Second Crossover Frequency

Introduction

The growth of cell cultures in labs is important for a wide variety of applications¹. Examples of this include the study of cell functions, the effect of chemicals upon them and the creation of artificially engineered tissues. This capability to culture cells *in vitro* has been explored since the early 20th century and became routine by the 1950s with development of defined culture media and the use of antibiotics to control microbial contamination. As cell cultures have expanded to industrial scales the ability to monitor their viability, and the critical factors underlying their growth, is of great importance. In this chapter we explore the culture of murine myeloma cells and their response to being unfed by looking at their viability, size and DEP crossovers. The second crossover appears to be correlated with the viability of a culture, tracking both its decline and recovery upon the resumption of feeding. Apoptosis was induced in the culture by the use of etoposide, a chemotherapy drug used to treat various cancers. The long term exposure of cells to this drug, at high concentrations for 24 hours, produced a noticeable decrease in viability which was tracked by the second crossover. A shorter exposure time of 6 hours provides no discernible change in viability, but results in subtle shifts to the distribution of both crossovers. Although explored in the context of the first crossover, measurements of the second crossover provide a more complete picture of the dielectric changes which occur during apoptosis induced by etoposide treatment.

Cell Growth and Death

Murine myeloma cells are frequently cultured for a variety of research purposes; however their use in the production of monoclonal antibodies (mAbs) has resulted in the need to culture them at an industrial scale¹. These mAbs are in principle capable of stimulating the immune system of a subject to defend against a variety of diseases such as multiple sclerosis, severe asthma and malignant tumours². During the 1970s the ability to culture these cells under controlled conditions *ex vivo* significantly improved their availability, an advance which led to the development of hybridomas where a B-cell lymphocyte possessing a desired immunity is combined by electrofusion with an immortalised murine myeloma cell. The resulting cells can be used in the mass production of these mAbs and are typically

maintained in incubated, agitated and fed vessels known as bioreactors with the principle aim of maximising mAb production. High yields are possible by maximising both cell density and viability³; however mechanisms which trigger cell death place an ultimate limit on this approach. These mechanisms are often described as either apoptosis or necrosis, where the former is actively controlled by the cell and the latter is uncontrolled or accidental⁴.

Specific triggers can initiate apoptosis, a cascade of processes which result in the programmed death of a cell⁵. In humans and animals this process is a normal part of development and ageing, involved in the maintenance of tissue cell populations and acting as a defensive countermeasure against the spread of disease. It is generally associated with condensation of the nucleus and fragmentation into smaller apoptotic bodies which are membrane bound. The release of specialised proteases, known as caspases, result in the cleavage and orderly destruction of proteins which can prevent the spread of disease. Membrane integrity is maintained throughout this process and surface molecules are expressed which mark these cells for phagocytosis. Apoptosis is also associated with the efflux of intracellular potassium⁶ which is understood to be a key stage in this process. Inhibition of Na^+/K^+ -ATPase prevents repolarisation of the cell membrane, suggesting a potential means by which electrokinetic techniques such as DEP can be exploited. Necrosis is a less well-defined term and generally refers to the accidental death of a cell without undergoing apoptosis. These cells are typically identified once they have undergone a complete loss of membrane integrity, a situation which may also be reached by apoptotic bodies in the absence of phagocytosis and is referred to as apoptotic necrosis⁴. Thus, although the presence of necrosis may be determined, it does not necessarily indicate the means by which death occurred.

In cell cultures, the deprivation of nutrients such as glucose and essential amino acids can intrinsically trigger the apoptotic process of a cell³. These triggers also include elevated osmolality, anoxia, reduced pH, serum deprivation and the build-up of waste products such as ammonia. Extrinsic triggers are also known to exist, where cell-to-cell signals are capable of initiating apoptosis in neighbouring cells and can lead to the collapse of a population. The maintenance of a viable cell culture therefore requires the addition of nutrients and removal of waste-products; however apoptosis can become an issue before any of these parameters deviate noticeably. A means of determining when cells are under stress and before any harm is caused is therefore desirable.

The potential for DEP to detect early stage apoptosis has been explored by several authors, typically involving the use of chemicals which artificially induce apoptosis. Pethig *et al.*⁷

exposed Jurkat T-cells to etoposide which caused a decrease in their membrane capacitance, a finding which corroborated earlier observations by Wang *et al.*⁸ for human leukaemia cells exposed to genistein. By contrast, the membrane capacitance of chronic myeloid leukaemia cells has been shown to increase after exposure to staurosporine⁹, a chemical agent known to induce apoptosis but whose mechanism of action remains the subject of ongoing research¹⁰. An apparent rise in the intracellular conductivity of these staurosporine exposed cells was simultaneously derived by curve fitting their DEP collection spectra across a range of frequencies. The issue of whether DEP can unambiguously distinguish between apoptotic and necrotic cells remains as necrotic cells may exhibit changes to f_{x01} , in response to both membrane breakdown and the release of intracellular ions. Given the range of observations and variety of chemical agents used to induce apoptosis an alternative approach was attempted here, by observing the collapse in viability for an unfed culture.

Apoptosis in an Unfed Culture

Although chemically induced apoptosis can produce rapid changes in the state of cells their relevance to standard cell culture conditions is debateable. In this experiment SP2/O-Ag14 murine myeloma cells were cultured, as described previously, in a standard T75 flask with an initial density of $\sim 1 \times 10^6$ cells/ml. Over a period of six days the cells were incubated under standard culture conditions, but without any feeding or splitting, to gauge changes in their viability, f_{x01} , f_{x02} and cell volume under extreme physiological stress. This stress is induced by the depletion of essential nutrients, the accumulation of waste-products and uncontrolled cell densities. Cell viability was determined by trypan blue, performed in the culture media using a haemocytometer, which is excluded by cells that possess an intact membrane. It is therefore able to distinguish necrotic cells from those which are either viable or undergoing apoptosis. Cell diameter and DEP measurements were performed as discussed previously in Chapter Five for an isosmotic solution of mannitol at room temperature, within 30 minutes of the first wash step.

The total cell count displayed in Fig. 6.1 increased consistently over four days before decreasing on days five and six. Apoptotic bodies were observed which were not included in the count, but clearly indicated the ongoing progression of apoptosis. Based on the exclusion of trypan blue the percentage viability was determined in Fig. 6.2. The initial viability of 63% increased to 78% after the first day, suggesting that the cells were not in an optimum condition to begin with. The viability then declines gradually over the following days, collapsing on the fifth to 29%. This behaviour correlates well to measurements of cell

viability in an unfed culture by Tey *et al.*¹¹ using NS0 myeloma cells, where cell viability collapsed from the fourth day onwards, albeit at an initial density roughly one-fifth of that used here. Both the depletion of amino acids and accumulation of ammonia were identified as contributing factors in their collapse, factors which are exacerbated at the higher cell densities used here. A maximum live cell density of 2×10^6 cells/ml achieved here using SP2/0 cells corresponds to a doubling of the population over three days, a result which is nearly identical to the maximum expansion exhibited by the myeloma cells of Tey *et al.*¹¹ over the same time period.

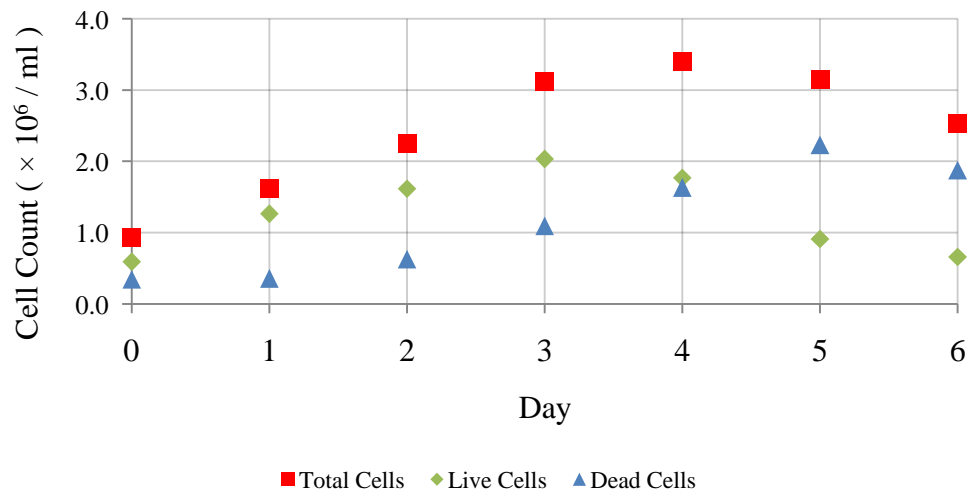


Figure 6.1 – Haemocytometer count of live and dead cells over a six day period, determined by the exclusion of trypan blue.

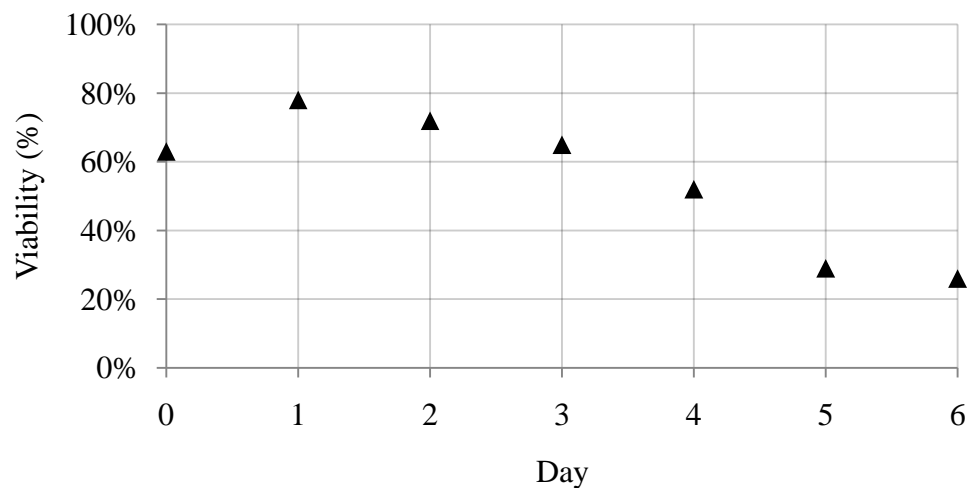


Figure 6.2 – Viability determined from the data of Fig. 6.1.

As the cell viability decreased their volume in both culture media and DEP solution reduced accordingly, as displayed in Fig. 6.3, which is generally expected¹² and in agreement with observations made by Pethig *et al.*⁷ for cells undergoing etoposide induced apoptosis. Isosmotic cell shrinkage in the DEP solution is apparent for all measurements however the degree of this shrinkage decreases with culture time, a factor which is likely due to the pre-existing shrinkage in culture media caused by the onset of apoptosis.

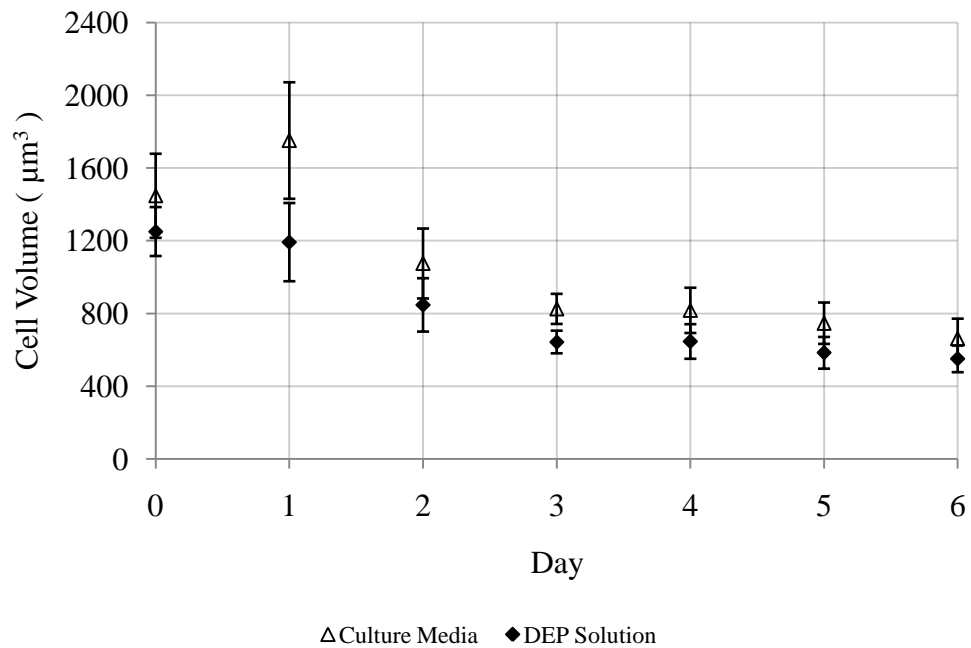


Figure 6.3 – Volumes derived from diameter measurements before and after suspension in DEP solution each day. Data points indicate the mean value $\pm 95\%$ confidence interval, based on over 50 cells per datum and a spherical cell volume.

DEP measurements were subsequently performed on these cells however their behaviour only represents those of the viable or apoptotic cell sub-population. The non-viable necrotic sub-population of cells identified by their uptake of trypan blue did not exhibit positive DEP with clearly defined crossover frequencies. Over six days the mean value of f_{x01} displayed in Fig. 6.4 varied by less than 15% throughout and displayed no clear trend. As a decrease in cell volume was observed over this period, and assuming cell membranes remain intact with a low conductance, it suggests a steady increase in the membrane capacitance shown in Fig. 6.5. This increase differs from the observations of decreasing membrane capacitance made by Pethig *et al.*⁷ and Wang *et al.*⁸, both of which indicated a smoothing of cell membranes with the onset of chemically induced apoptosis.

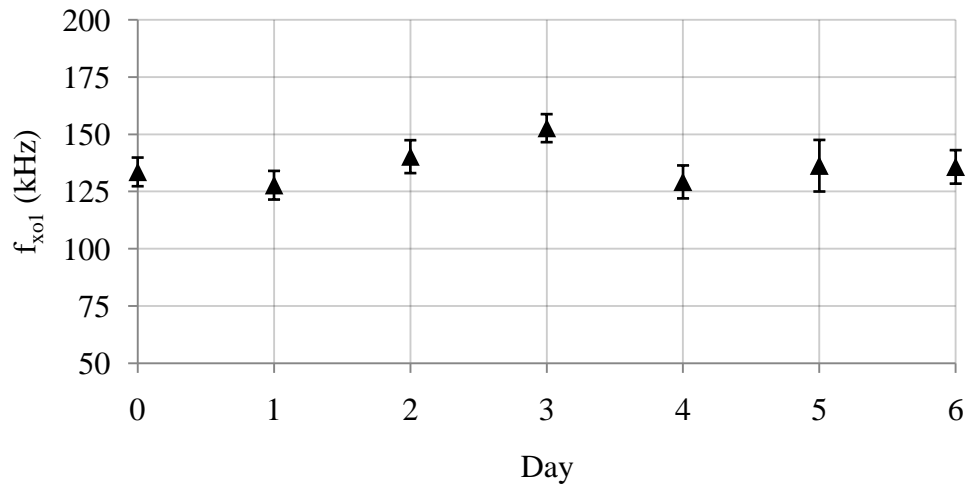


Figure 6.4 – $f_{x_{o1}}$ for murine myeloma cells suspended in DEP solutions as a function of time. Data points indicate the mean value $\pm 95\%$ confidence interval.

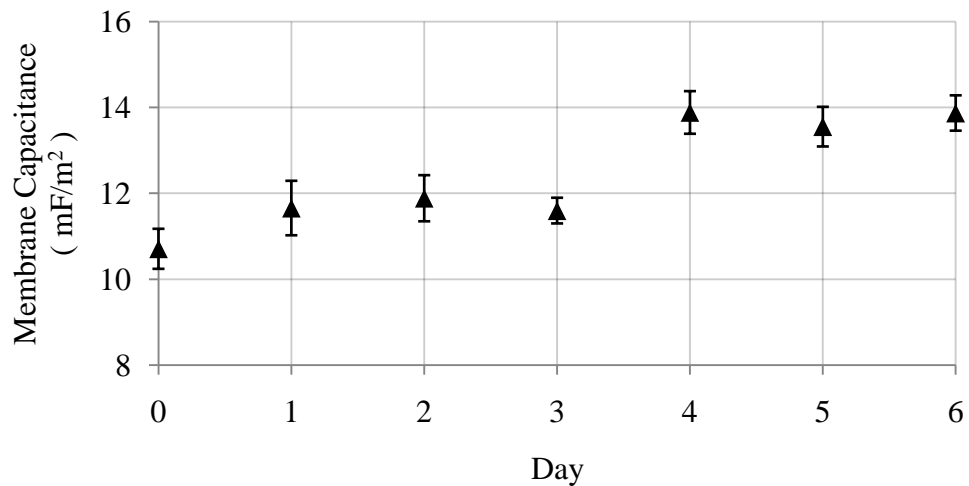


Figure 6.5 – C_{mem} derived from the data of Fig. 6.3, Fig. 6.4 and Eq. 5.6 based on the measured solution conductivity of 41.5 mS/m. Data points indicate the mean value $\pm 95\%$ confidence interval.

The possibility exists that membrane conductance could be increasing such that $f_{x_{o1}}$ remains constant with the observed decrease in cell volume, whilst maintaining the same or even lower membrane capacitance. Based on the $f_{x_{o1}}$ expression of Eq.(2.39), typical initial values for G_m due to ion channel conduction of 10 to 100 S/m² and static membrane capacitance throughout the experiment we can estimate the minimum membrane conductance required. These conditions imply membrane conductances of between 2000 and 8000 S/m² from the second to sixth days, respectively. Conductances of this order have previously been

suggested by Wang *et al.*⁸ based on the human leukaemia cells which were exposed to the apoptotic agent genistein for four hours; however a definitive determination of this behaviour requires further study and may depend on the trigger used to induce apoptosis.

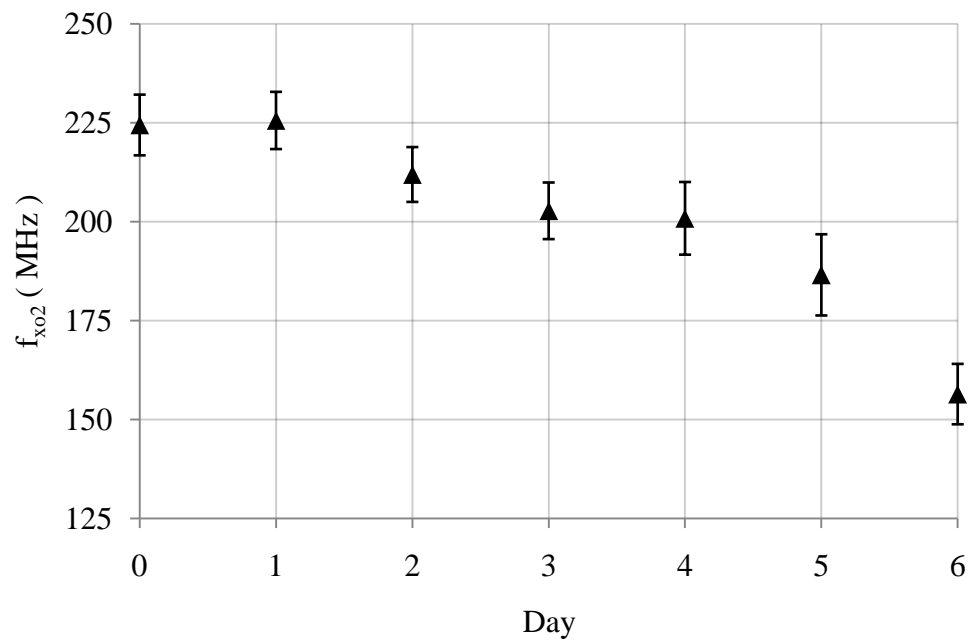


Figure 6.6 – $f_{x_{o2}}$ for murine myeloma cells suspended in DEP solutions as a function of time. Data points indicate the mean value $\pm 95\%$ confidence interval.

Measurements of the mean $f_{x_{o2}}$ value are displayed in Fig. 6.6 which broadly reflects the viability trend displayed in Fig. 6.2. The initial increase in viability after the first day is not reflected in $f_{x_{o2}}$ but may simply reflect a healthy intracellular ionic state for these cells, which remains static and would not indicate an increase in their population. As the culture time progressed their mean $f_{x_{o2}}$ value gradually decreased, collapsing rapidly from the fifth day onwards and concurring with both a collapse in viability and the maximum dead cell count. After six days the viability had reduced to 26% with the culture in a visibly poor state, with the presence of numerous apoptotic bodies and cell fragments. It is noteworthy that the behaviour displayed by the mean value of $f_{x_{o2}}$, derived from intact cells, reflects the overall viability of the population plotted in Fig. 6.2. This trend suggests that the mean value of $f_{x_{o2}}$ is an effective measure of necrosis in the wider cell population. It is not clear from this data whether the measurement of $f_{x_{o2}}$ can be used to assess the onset of apoptosis for individual cells, or whether it also reflects varying degrees of necrosis. A detailed analysis of this relationship requires a closer evaluation of both apoptotic markers and $f_{x_{o2}}$ together.

The cells were then washed twice and re-suspended into fresh culture media every two days in an attempt to restore their condition. This re-suspension was performed immediately following measurements on the sixth, eighth and tenth days at densities of 1.7 , 0.8 and 0.7×10^6 cells/ml, respectively. By doing so the proportion of live to dead cells exceeded unity following three days and continued to rise. On the eleventh day the culture viability shown in Fig. 6.8 had risen to 79%, matching the previous maximum on day two and at which point the experiment was ended.

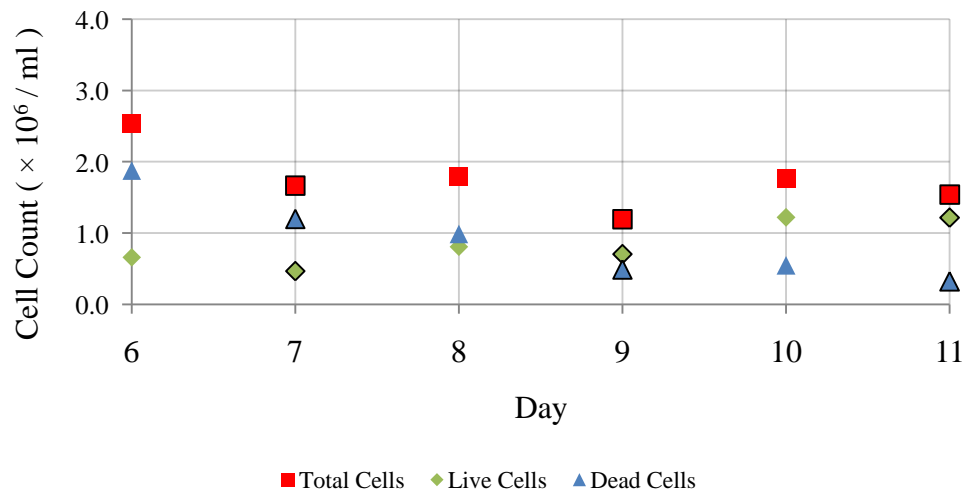


Figure 6.7 – Haemocytometer count of live and dead cells using trypan blue with re-suspension in fresh culture media performed following measurements on the sixth, eighth and tenth days. Bordered markers indicate measurements on the following day.

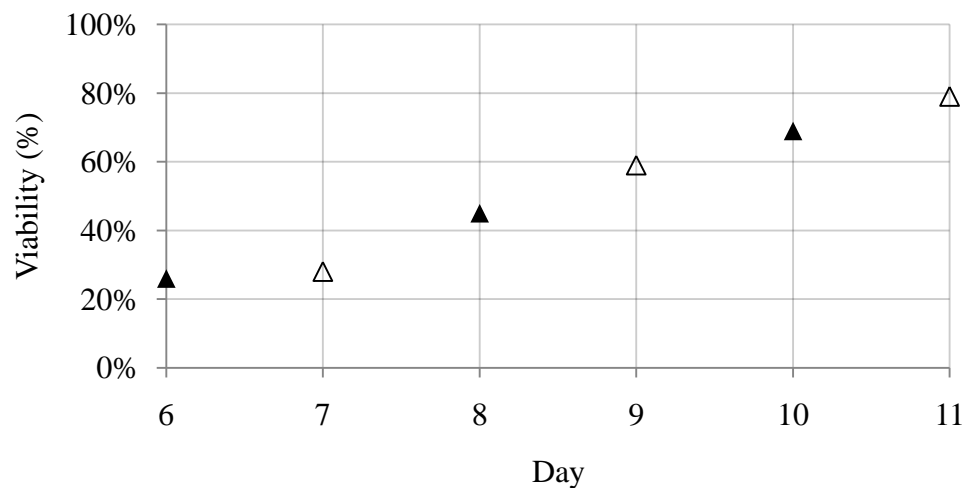


Figure 6.8 – Viability determined from the data of Fig. 6.7. Unfilled markers indicate measurements following re-suspension the previous day.

Restoration of the cell culture is further reflected in the cell volumes of Fig. 6.9, with a value in culture media of $1479 \pm 129 \mu\text{m}^3$ on the eleventh day being within 3% of the initial $1448 \pm 231 \mu\text{m}^3$ value. The data discussed thus far suggests a complete recovery of murine myeloma cells which are unfed for six days is possible, in terms of cell viability. The measurements of f_{x01} displayed in Fig. 6.10 again reveal no clear trend with the calculation of their membrane capacitance, displayed in Fig. 6.11, suggesting a full recovery and reduction back to their initial mean values. Fig. 6.12 shows the corresponding measurements of f_{x02} which further corroborate this recovery, with an apparent step increase in its value occurring after three days of feeding back to initial values.

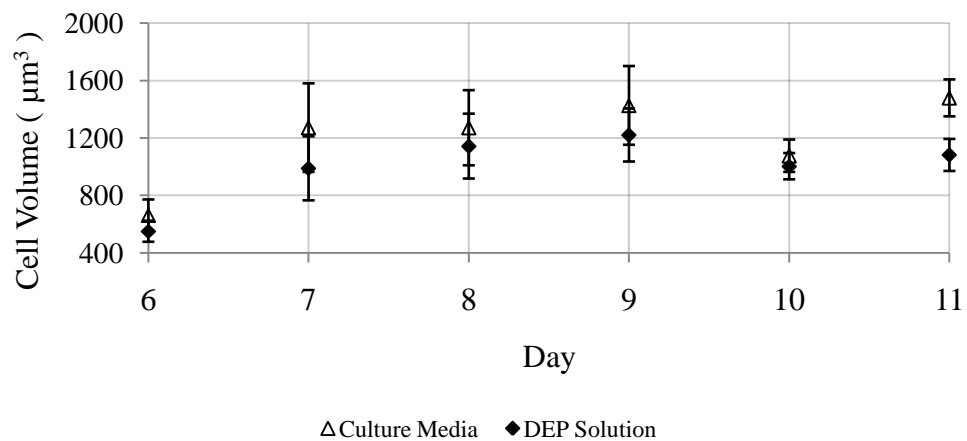


Figure 6.9 – Volumes derived from diameter measurements before and after suspension in DEP solution each day with re-suspension in fresh culture media performed following measurements on the sixth, eighth and tenth days. Data points indicate the mean value $\pm 95\%$ confidence interval.

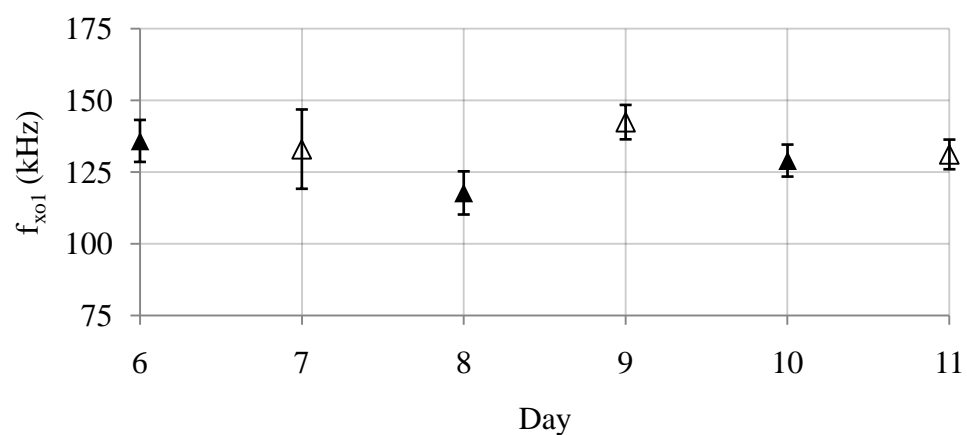


Figure 6.10 – f_{x01} for murine myeloma cells suspended in DEP solutions as a function of time. Data points indicate the mean value $\pm 95\%$ confidence interval.

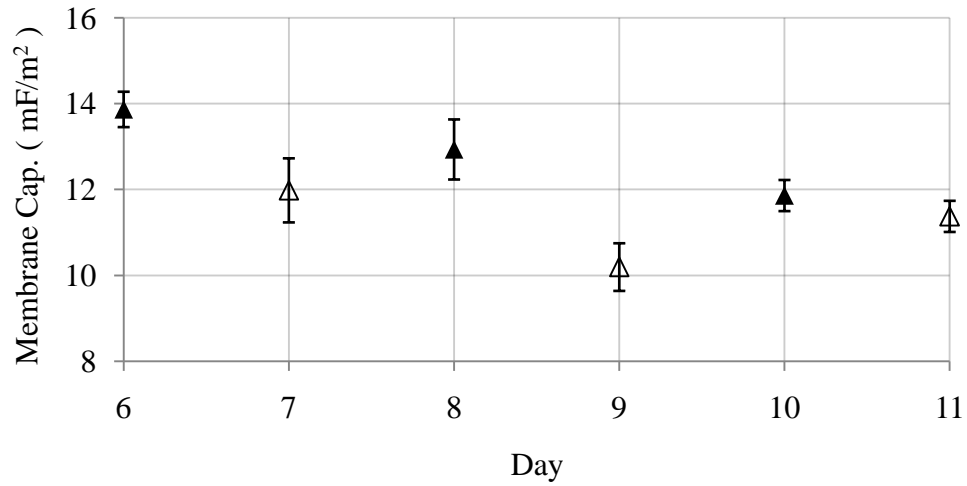


Figure 6.11 – C_{mem} derived from the data of Fig. 6.9, Fig. 6.10 and Eq. 5.6 based on the measured solution conductivity of 41.5 mS/m. Data points indicate the mean value \pm 95% confidence interval.

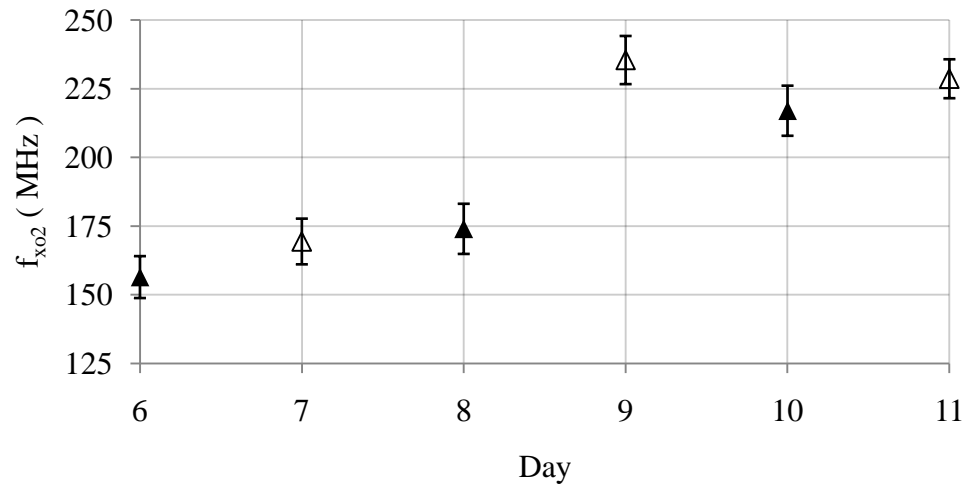


Figure 6.12 – $f_{x_{o2}}$ for murine myeloma cells suspended in DEP solutions as a function of time. Data points indicate the mean value \pm 95% confidence interval.

The experiment demonstrates an apparent correlation between the mean values of cell volume, membrane capacitance, and $f_{x_{o2}}$ with culture viability. Under these conditions the measurement of $f_{x_{o1}}$ alone is ineffective at distinguishing between cultures of high and low viability. By measuring cell diameter it is possible to make a distinction, however potential increases in the membrane conductance introduce ambiguity in its interpretation. The measurement of $f_{x_{o2}}$ on the other hand offers a single measurement which is independent of physical size and appears to correlate well to culture viability. A unique advantage is that the

frequency could be exploited to selectively filter out cells which appear to be undergoing apoptosis, without the need to measure their size. Plotting viability against f_{x02} produces Fig. 6.13 which appears to display a positive correlation. The Pearson correlation coefficient of this population is +0.86 which demonstrates a strong correlation. By comparison, a value of -0.62 between viability and membrane capacitance suggests a weaker correlation.

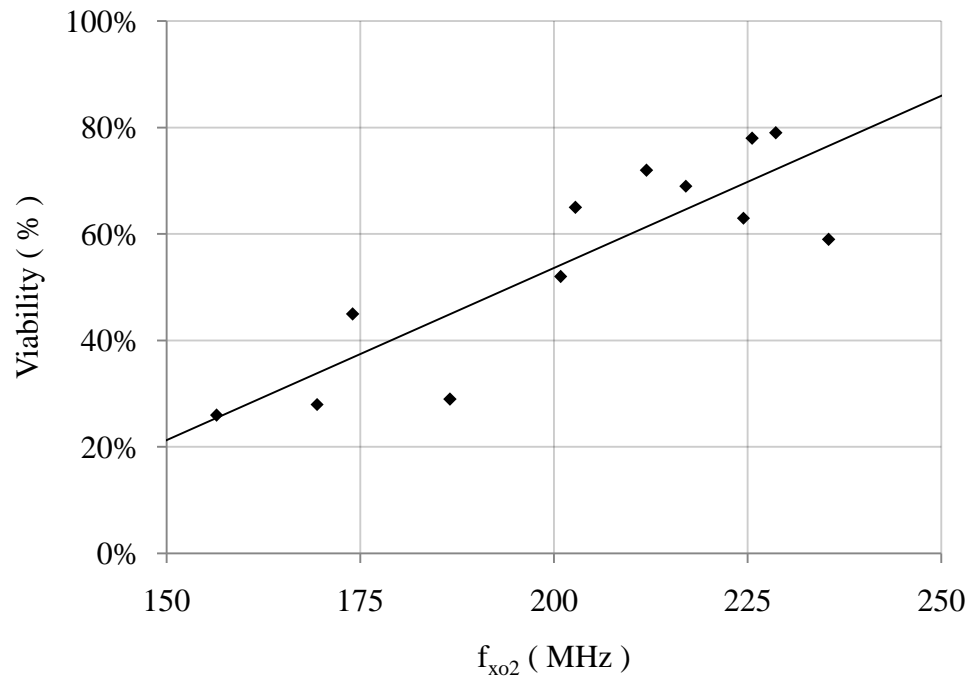


Figure 6.13 – Viability plotted against the mean value of f_{x02} for all twelve measurements. The solid line displays the best-fit by least squares regression.

Apoptosis Induced by Etoposide

Understanding the maintenance and behaviour of a cell culture is useful in a practical sense, however many variables exist which make it unattractive for research into the processes underlying cell death. Apoptotic chemicals provide a means of inducing apoptosis in a specific, controlled and reproducible manner. Several of these chemicals have already been the subject of research based on flow cytometry^{13,14}, electro-impedance^{15,16} and DEP^{7,8}. Etoposide is an a cancer therapy drug which inhibits a nuclear enzyme known as type II topoisomerase, an enzyme which plays an important role in the replication and transcription of DNA¹⁷. By interfering with this process, irreparable breakages in the DNA are introduced which can trigger the apoptotic process. Increases in the upper range of f_{x01} and corresponding decreases in membrane capacitance have been observed with Jurkat T-cells following six hours of exposure to etoposide, by which point approximately half of the cells

were identified as undergoing apoptosis using Annexin-V⁷. The efflux of potassium typically associated with the early stages of apoptosis provides a real motivation to investigate the response of $f_{x_{o2}}$ using the same approach.

Murine myeloma cells were cultured and split into standard six-well culture plates at a density of 1×10^6 cells/ml. Etoposide was dissolved in DMSO at a range of concentrations with 24 μ l of each solution added to individual wells containing 1.2 ml of culture media. By this method, cells were exposed to etoposide concentrations of 1, 10, 100 and 1000 μ M followed by incubation for 6 hours. Their viability was then determined by a haemocytometer count using trypan blue, a test which purely evaluated the prevalence of necrosis. Controls with and without DMSO were maintained in parallel as a reference for these viability measurements over the same period of time. These treated cells were then suspended into an isosmotic mannitol-based DEP solution in which measurements of $f_{x_{o1}}$, $f_{x_{o2}}$ and cell diameter were undertaken. Additional cultures were also incubated in parallel using the same etoposide concentrations but over a longer period of 24 hours before the same analysis.

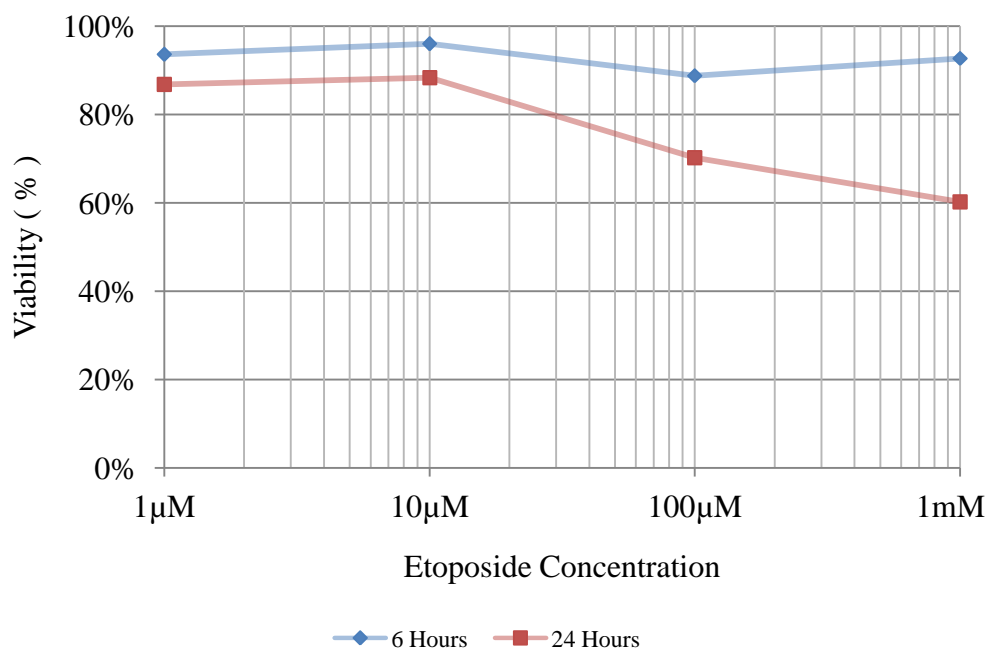


Figure 6.14 – Culture viability as a function of etoposide concentration after incubation for 6 and 24 hours.

After 6 hours of exposure the viability of cells displayed in Fig. 6.14 for the various etoposide concentrations revealed no significant variation. The cells retain their membrane

integrity and the test therefore provides no indication of whether apoptosis has been triggered. The viability of control samples both with and without DMSO remained close to 95% which is consistent with the values observed here. After 24 hours of exposure a clear trend emerges for etoposide concentrations of 10 μM and above, their viability decreasing from 88% down to 60% at 1 mM. As the apoptotic process is completed the cells, in the absence of phagocytosis, remain until their membranes break down and are unable to prevent the permeation of trypan blue. The observed behaviour is therefore consistent with apoptotic necrosis.

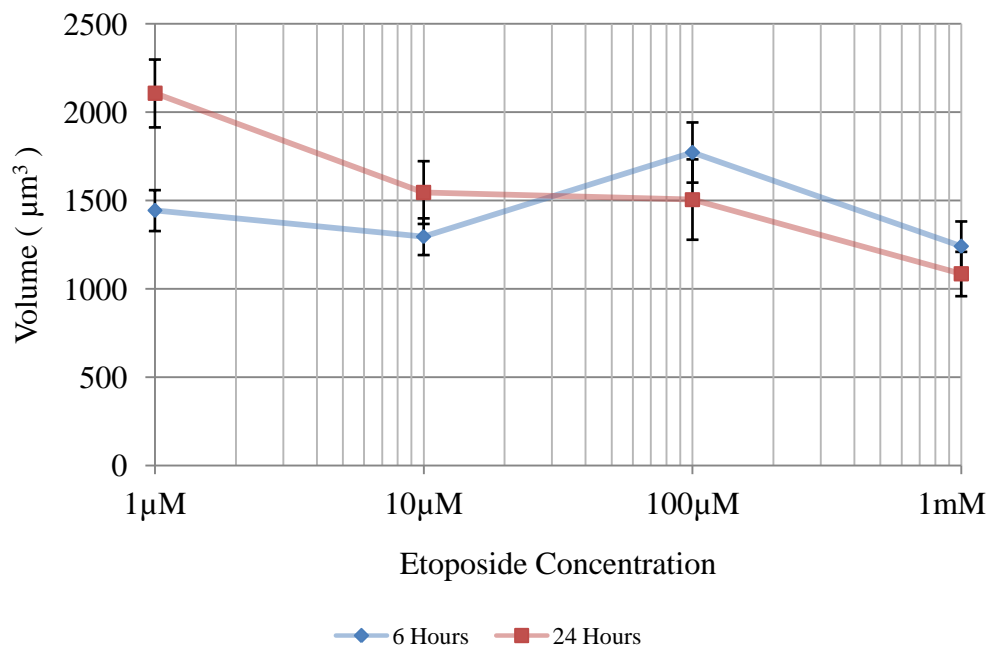


Figure 6.15 – Cell volume in DEP solution as a function of etoposide concentration after incubation for 6 and 24 hours. Data points indicate the mean value $\pm 95\%$ confidence interval.

In Fig. 6.15 the corresponding volume of cells following suspension into DEP solution revealed no clear trend after 6 hours. A modest decrease is apparent after 24 hours across the concentration range which is likely due to their continued shrinkage and necrotic break down. The corresponding mean volumes of cells with and without DMSO were 1343 and 1442 μm^3 , respectively, which suggests that their volume generally remains constant in response to this treatment. A similar response was observed by Yurinskaya *et al.*¹⁸ in histiocytic lymphoma cells undergoing the same treatment, suggesting that observations of cell shrinkage associated with apoptosis may not be fully understood.

DEP measurements were then undertaken which, as before, need to be interpreted with care as they represent the sub-population of cells which possess intact membranes and are

therefore capable of exhibiting crossover frequencies. After 6 hours of exposure there is no apparent difference in the mean value of $f_{x_{01}}$ above 10 μM although a clear trend does emerge after 24 hours - its value increasing with the concentration of etoposide and correlated with the decrease in cell viability. A useful view of $f_{x_{01}}$ after 6 hours is provided by the cumulative distribution of Fig. 6.17 for the DMSO control and etoposide concentrations of 10 μM and 1 mM. It indicates that a subtle shift in the distribution takes place with the presence of etoposide tending to reduce $f_{x_{01}}$. The result is interesting as it appears to contradict an observed increase in $f_{x_{01}}$ by Pethig *et al.*⁷ and therefore merits further study. Increases in the membrane conductance or intracellular conductivity could, in principle, produce such shifts.

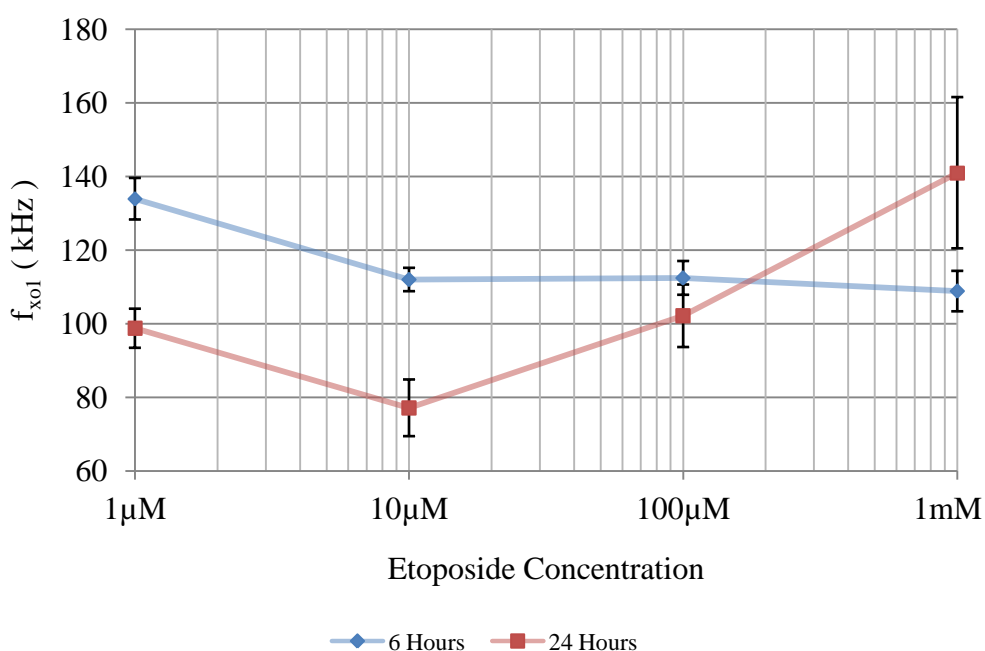


Figure 6.16 – $f_{x_{01}}$ for cells as a function of etoposide concentration after incubation for 6 and 24 hours. Data points indicate the mean value $\pm 95\%$ confidence interval.

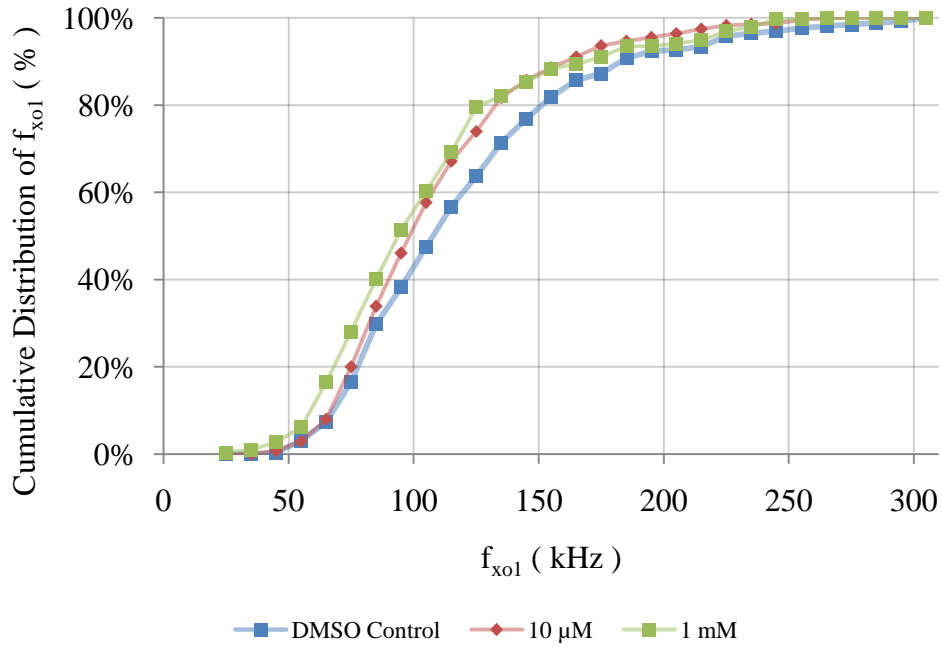


Figure 6.17 – Cumulative f_{xo1} distribution of the cells for the DMSO control and etoposide concentrations of 10 μM and 1 mM after 6 hours of exposure.

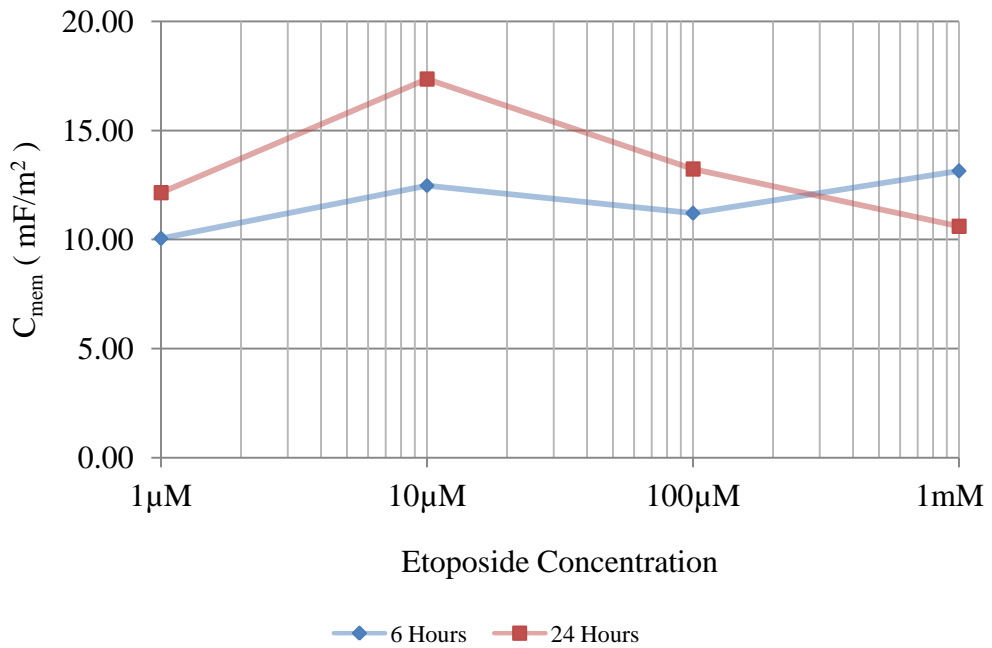


Figure 6.18 – C_{mem} derived from the data of Fig. 6.15, Fig. 6.16 and Eq.(5.6) based on the measured solution conductivity of 41.5 mS/m. Data points indicate the mean value \pm 95% confidence interval.

Based on the mean values of cell volume and $f_{x_{o1}}$ a corresponding reduction in the membrane capacitance occurs above $10\mu\text{M}$ after 24 hours, as displayed in Fig. 6.18, but provides no clear trend after only 6 hours. It is likely that the detection of subtle apoptotic changes requires the calculation of membrane capacitance on a cell by cell basis, a process which is more suited to a dedicated cell profiling system.

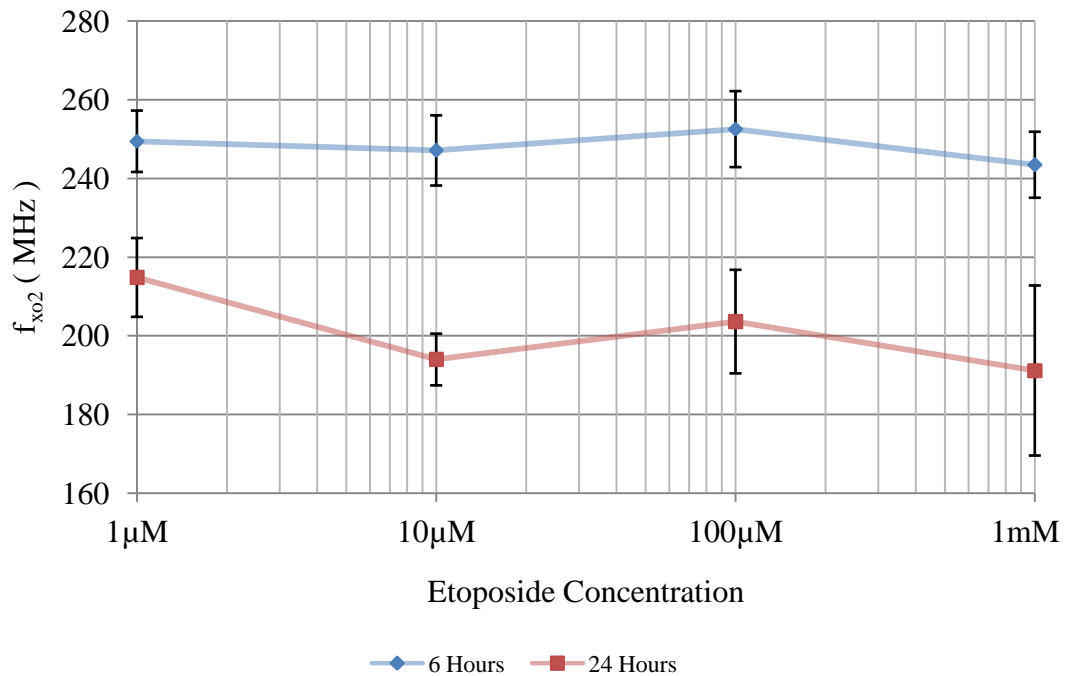


Figure 6.19 – $f_{x_{o2}}$ for cells as a function of etoposide concentration after incubation for 6 and 24 hours. Data points indicate the mean value $\pm 95\%$ confidence interval.

In contrast to the apparent trends in the mean value of $f_{x_{o1}}$ and C_{mem} displayed after 24 hours the mean value of $f_{x_{o2}}$, displayed in Fig. 6.19, did not appear to change appreciably regardless of the time exposed. The result is unusual when considering the expected apoptotic efflux of potassium. However, an increase in the concentration of intracellular sodium has been observed by Yurinskaya *et al.*¹⁸ with histiocytic lymphoma cells treated with etoposide. After four hours the ratio of the intracellular potassium concentration to that of sodium decreased, however their combined concentration remained the same. As $f_{x_{o2}}$ is dependent upon intracellular conductivity it is unable to distinguish between specific ions and thus, if the total concentration of free intracellular ions remains the same, we would not expect a change in $f_{x_{o2}}$. A plot of the cumulative $f_{x_{o2}}$ distribution in Fig. 6.20 reveals a subtle downward shift as the concentration of etoposide is increased, a change which would correlate to an overall efflux of free ions. It suggests that $f_{x_{o2}}$ is capable of detecting changes associated with the early stages of etoposide induced apoptosis in a similar manner to $f_{x_{o1}}$.

The implied decrease in intracellular conductivity is not consistent with a decrease in f_{x01} , unless the membrane conductance increased and became more permeable to ions.

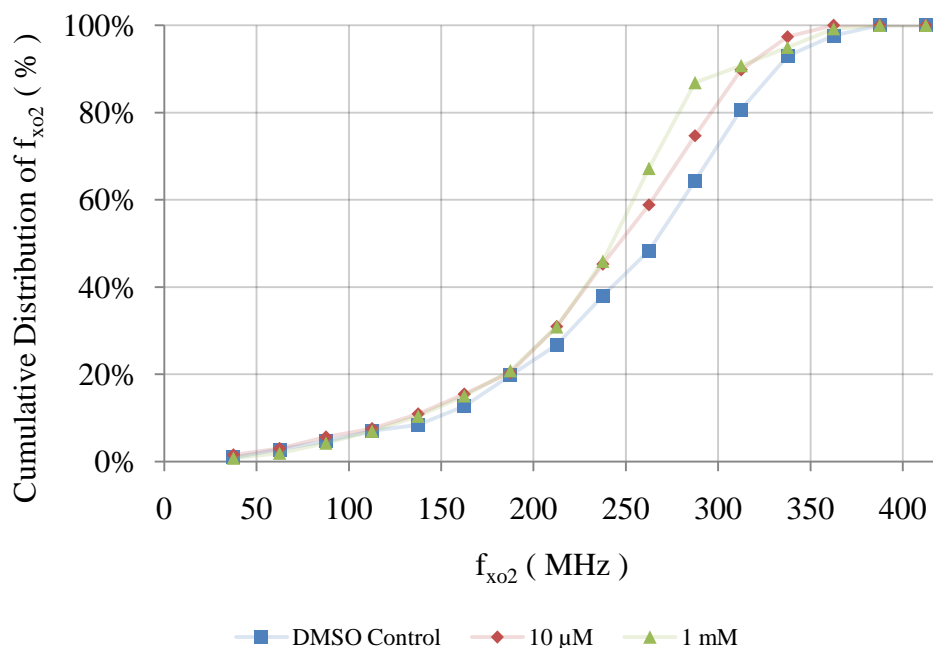


Figure 6.20 – Cumulative f_{x02} distribution of the cells for the DMSO control and etoposide concentrations of 10 μ M and 1 mM after 6 hours of exposure.

Conclusion

Murine myeloma cells were maintained in an unfed culture for a period of six days. A decrease in their viability was observed from a maximum of 78% to a minimum of 26% with a rapid decrease in their mean volume occurring over the first three days. The mean value of f_{x01} remained relatively constant over this period but the estimated membrane capacitance appeared to increase gradually, differing from published observations of etoposide induced apoptosis. A significant increase in membrane conductivity remains a possibility and highlights a fundamental difficulty in the interpretation of f_{x01} by itself. By contrast, the mean value of f_{x02} revealed an apparent correlation to their measured viability, behaviour which suggests that the intracellular conductivity of intact cells is related to the overall spread of necrosis in the culture. After six days the cells were washed in fresh culture media at two day intervals which allowed for a recovery of the culture to a viability of 79%. Both the mean cell volume and estimated membrane capacitance returned to their initial values, with the mean value of f_{x01} remaining relatively constant. The mean value of f_{x02} also returned to its initial value suggesting that – at least from a dielectric perspective – the cell

culture was fully recovered. By examining the relationship between viability and $f_{x_{o2}}$ across the entire experiment a high degree of positive correlation was observed with a Pearson correlation coefficient of +0.86. This experiment demonstrated that $f_{x_{o2}}$ may be an effective way to gauge the viability of a culture; however its ability to detect the more subtle processes underlying apoptosis remains an important question.

Etoposide was investigated as a chemical means of inducing apoptosis, an approach which has already been demonstrated by several authors using flow cytometry¹², electro-impedance¹⁴ and DEP⁷. After 6 hours of exposure to etoposide, by which point apoptosis is expected to be underway, the distribution of $f_{x_{o1}}$ shifts to lower frequencies in a manner that is proportionate to its concentration and in contradiction with an existing study. It draws attention to the difficulty distinguishing between changes in the membrane's capacitance and conductance. Following 24 hours of exposure a collapse in the viability of cells, proportionate to the concentration of etoposide above 10 μM , was correlated to a decrease in the mean value of $f_{x_{o2}}$ in a similar manner to that of unfed cells. It appears to represent the onset of necrosis following the induced apoptotic process as the culture media should otherwise be suitable for the growth of cells. The cumulative distribution of $f_{x_{o2}}$ has revealed shifts which are consistent with the efflux of intracellular ions associated with apoptosis after the first six hours. An influx of sodium may mask the detection of potassium efflux by $f_{x_{o2}}$, however the technique provides a means of quantifying the overall loss in intracellular conductivity – and is a useful tool in terms of understanding the changes to $f_{x_{o1}}$.

References

- 1 Davis, J. M. (2011) *Animal Cell Culture: Essential Methods*, Chichester: John Wiley & Sons.
- 2 Hansel, T. T., Kropshofer, H., Singer, T., Mitchell, J. A. & George, A. J. T. (2010) The safety and side effects of monoclonal antibodies. *Nature Reviews Drug Discovery*, 9 (4), 325-338.
- 3 Meshram, M., Naderi, S., McConkey, B., Ingalls, B., Scharer, J. & Budman, H. (2013) Modeling the coupled extracellular and intracellular environments in mammalian cell culture. *Metabolic Engineering*, 19, 57-68.
- 4 Fink, S. L. & Cookson, B. T. (2005) Apoptosis, pyroptosis, and necrosis: mechanistic description of dead and dying eukaryotic cells. *Infection and Immunity*, 73 (4), 1907-1916.
- 5 Elmore, S. (2007) Apoptosis: a review of programmed cell death. *Toxicologic Pathology*, 35 (4), 495-516.
- 6 Yu, S. P. (2003) Regulation and critical role of potassium homeostasis in apoptosis. *Progress in Neurobiology*, 70 (4), 363-386.
- 7 Pethig, R. & Talary, M. S. (2007) Dielectrophoretic detection of membrane morphology changes in Jurkat T-cells undergoing etoposide-induced apoptosis. *IET Nanobiotechnology*, 1 (1), 2-9.
- 8 Wang, X., Becker, F. F. & Gascoyne, P. R. C. (2002) Membrane dielectric changes indicate induced apoptosis in HL-60 cells more sensitively than surface phosphatidylserine expression or DNA fragmentation. *Biochimica et Biophysica Acta - Biomembranes*, 1564 (2), 412-420.
- 9 Chin, S., Hughes, M. P., Coley, H. M. & Labeed, F. H. (2006) Rapid assessment of early biophysical changes in K562 cells during apoptosis determined using dielectrophoresis. *International Journal of Nanomedicine*, 1 (3), 333-337.
- 10 Stepczynska, A., Lauber, K., Engels, I. H., Janssen, O., Kabelitz, D., Wesselborg, S. & Schulze-Osthoff, K. (2001) Staurosporine and conventional anticancer drugs induce overlapping, yet distinct pathways of apoptosis and caspase activation. *Oncogene*, 20 (10), 1193-1202.
- 11 Tey, B. T., Singh, R. P., Piredda, L., Piacentini, M. & Al-Rubeai, M. (2000) Bcl-2 mediated suppression of apoptosis in myeloma NS0 cultures. *Journal of Biotechnology*, 79 (2), 147-159.
- 12 Bortner, C. D. & Cidlowski, J. A. (2011) Life and death of lymphocytes: A volume regulation affair. *Cellular Physiology and Biochemistry*, 28 (6), 1079-1088.

- 13 Gorman, A. M., Samali, A., McGowan, A. J. & Cotter, T. G. (1997) Use of flow cytometry techniques in studying mechanisms of apoptosis in leukemic cells. *Cytometry*, 29 (2), 97-105.
- 14 Ullal, A. J. & Pisetsky, D. S. (2010) The release of microparticles by Jurkat leukemia T cells treated with staurosporine and related kinase inhibitors to induce apoptosis. *Apoptosis*, 15 (5), 586-596.
- 15 Atienzar, F. A., Gerets, H., Tilmant, K., Toussaint, G. & Dhalluin, S. (2013) Evaluation of impedance-based label-free technology as a tool for pharmacology and toxicology investigations. *Biosensors*, 3 (1), 132-156.
- 16 Xie, F., Xu, Y., Wang, L., Mitchelson, K., Xing, W. & Cheng, J. (2012) Use of cellular electrical impedance sensing to assess in vitro cytotoxicity of anticancer drugs in a human kidney cell nephrotoxicity model. *Analyst*, 137 (6), 1343-1350.
- 17 .Wu, C. C., Li, T. K., Farh, L., Lin, L. Y., Lin, T. S., Yu, Y. J., Yen, T. J., Chiang, C. W. & Chan, N. L. (2011) Structural basis of type II topoisomerase inhibition by the anticancer drug etoposide. *Science*, 333 (6041), 459-462.
- 18 Yurinskaya, V., Goryachaya, T., Guzhova, I., Moshkov, A., Rozanov, Y., Sakuta, G., Shirokova, A., Shumilina, E., Vassilieva, I., Lang, F. & Vereninov, A. (2005) Potassium and sodium balance in U937 cells during apoptosis with and without cell shrinkage. *Cellular Physiology and Biochemistry*, 16 (4-6), 155-162.

Chapter Seven

Methods

Electrode Fabrication

Interdigitated electrodes intended for biological DEP need to be fabricated from a durable material which is both resistant to corrosion and capable of acting as a good conductor. Platinum is a widely used metal in medical devices such as pacemakers, catheters and stents due to its properties as a noble metal¹. A range of techniques for the deposition and patterning of thin film platinum have been developed however the adhesion of noble metals to substrates such as glass is weak², an issue which can affect the durability of electrodes. An intermediate adhesion layer can be used involving a metal which is less noble than the platinum and allows a stable bond to be formed. A layer of titanium is often used between the glass and platinum³, with 10nm being sufficient to act as a form of "glue". The titanium atoms bond as an oxide layer on the glass surface and diffuse through grain boundaries in the platinum film, thereby promoting adhesion.

3" diameter glass wafers were prepared by cleaning them in a mixture of sulphuric acid and hydrogen peroxide, also known as piranha solution. The wafers were rinsed in deionised water and dried, ready for the deposition of a titanium adhesion layer. Electron beam evaporation was used to deposit both the titanium and subsequent platinum layers to depths of 10 and 100nm, respectively. The technique involves heating a metal target in a crucible which is subjected to an electron beam source. These electrons are accelerated under a high voltage and cause the target metal to evaporate from the crucible, forming a vapour which subsequently settles on any surfaces within line-of-sight. Once deposition of both metal layers was completed the wafer was exposed to hexamethyldisilazane (HMDS), a chemical which reacts with surface groups to form a hydrophobic layer. This hydrophobic layer prevents developer agents from undercutting a subsequent photoresist layer⁴.

The patterning of metal was performed by spin coating the wafers in SPR350, a chemical which can act as a positive photoresist. A clear field mask obscures regions of metal which are intended to form tracks and pads. Regions of the photoresist which are exposed to UV radiation become soluble to the developer. The mask was positioned over the wafer, brought into contact and exposed to UV light using a Karl Suss aligner. A developer is used which removes the photoresist from exposed regions, after which the wafer is baked. An argon

based reactive ion etch followed by a wet etch in aqua regia (a mixture of hydrochloric and nitric acid) is used to remove the exposed regions of metal. The remaining photoresist is removed by oxygen plasma ashing producing the final released structure.






Step	Description	Cross-Section
1	<p>Wafer Cleaning</p> <p>Exposure to piranha solution (3:1 ratio of H₂SO₄ to H₂O₂) for 10 minutes. Rinse in deionised water and dry in a Marangoni dryer.</p>	
2	<p>Metal Deposition</p> <p>10nm of titanium followed by 100nm of platinum using an ANS electron beam evaporator.</p>	
3	<p>Photolithography</p> <p>Wafer priming in an HMDS box for 10 minutes. Spin coat 1.5µm of SPR350 photoresist at 700 rpm for 10 seconds and 2350 rpm for 60 seconds. Soft bake at 90°C for 60 seconds.</p> <p>Clear field mask soft contact and 9 second exposure to UV light using a Karl Suss mask aligner.</p> <p>Exposure to photoresist developer and hard baking at 110°C for 60 minutes.</p>	
4	<p>Metal Etch</p> <p>Argon reactive ion etch for 17 minutes at 200W (25 sccm) using a JLS etcher. Wet etch in HCl:H₂O:HNO₃ at a ratio of 3:2:1 for 60 seconds at 45°C.</p>	
5	<p>Resist Strip</p> <p>Oxygen plasma strip of the remaining photoresist in a barrel asher for 75 minutes. Rinse in ACT for 15 minutes at 50°C and repeat. Rinse in isopropyl alcohol followed by deionised water and dry using compressed N₂.</p>	

Table 7.1 – Process flow for electrode fabrication

Measurement of Linewidth & Sheet Resistance

In Chapter Three a test structure was described which allowed for measurements of both the electrical linewidth and sheet resistance of platinum tracks deposited on a glass substrate. The structure is displayed in Fig. 7.1 and consists of two components, the first being a cross formed by two tracks which intersect at right angles and the second being a length of track referred to as a bridge. By forcing a current through two adjacent arms of the cross and measuring the resulting voltage arising across the two remaining arms it is possible to determine the sheet resistance, an approach known as the van der Pauw method. The bridge track is connected at two points, across which the voltage is measured when a known current is forced through, and provides a means of deriving the electrical linewidth. The combined cross and bridge is referred to as a cross-bridge test structure.

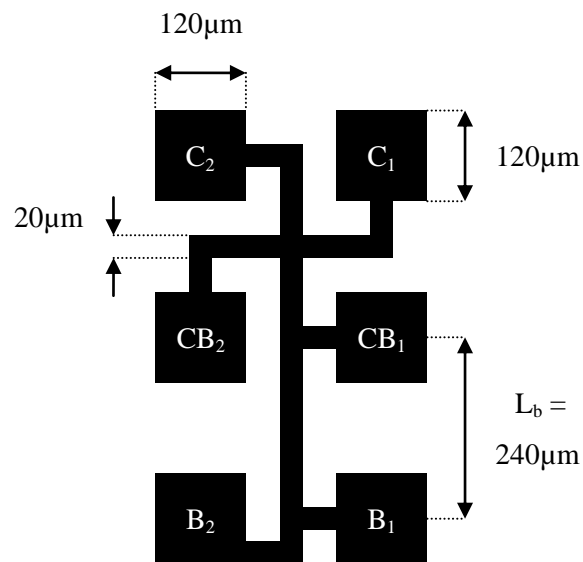


Figure 7.1 – Schematic of the cross-bridge test structure used in Chapter Three (not to scale).

A forcing current is first determined which allows for stable voltage measurements to be made without producing excessive joule heating of the cross structure. Standard guidelines⁵ suggest an initial current density of $0.2\text{MA}/\text{cm}^2$ which, for the track width of $20\mu\text{m}$ and platinum thickness of 100nm considered here, implies a current of 4mA . This current is first applied between terminals C_1 and C_2 such that a voltage can be measured across the terminals CB_1 and CB_2 to determine the cross resistance $R_{c1} = V_1/I_1$. The current is then halved to verify that no significant change in resistance occurs and thus joule heating is not an issue. Once the maximum measurement current has been determined it is reversed to determine $R_{c2} = V_2/I_1$. The procedure is repeated with current being applied between

terminals C_{B2} and C_2 with the voltage measured across terminals C_{B1} and C_1 , in both forward and reverse directions, to determine the cross resistances $R_{c3} = V_3/I_1$ and $R_{c4} = V_4/I_1$. A mean average of all four resistance measurements is taken and defined as the cross resistance R_c . The sheet resistance of the deposited platinum layer can then be determined by:

$$R_s = \frac{\pi R_c}{\ln 2} \quad (7.1)$$

The bridge section can then be used to derive an electrical linewidth for the track. A forcing current I_2 is applied between terminals B_2 and CB_2 , the current being set in the same manner as that for the cross to minimise joule heating. The resulting voltage drop V_5 is measured across terminals B_1 and CB_1 with the resistance $R_{b1} = V_5/I_2$. By reversing the direction of I_2 and measuring the voltage drop V_6 the resistance $R_{b2} = V_6/I_2$ can be calculated, the mean average of R_{b1} and R_{b2} providing the bridge resistance R_b . The mean electrical linewidth can then be determined by:

$$R_b = R_s \frac{L_b}{R_b} \quad (7.2)$$

where R_s is the sheet resistance derived from measurements of the cross and L_b is the distance between points which connect terminals B_1 and CB_1 to the bridge. If the cross section of the tracks are rectangular then the mean electrical linewidth will also equal the mean physical linewidth.

Two wafers were fabricated to measure the impedance of interdigitated electrodes with 20:20 and 20:40 μm mark-space ratios. These electrodes were surrounded by cross-bridge test structures, as displayed in Fig. 3.5, to provide electrical linewidths and sheet resistances for the impedance simulations discussed in Chapter Three. The wafers were each mounted into a mechanical probe station connected to an HP 4062UX process control system which provided current forcing and voltage measurement functions. In Table 7.1 the calculated sheet resistances and electrical linewidths for the test structures are displayed with sheet resistances of $\sim 1.8\Omega/\square$ for both wafers. Optical linewidth measurements were taken which indicate an error in their electrical measurement of less than 1%. A textbook value for the electrical conductivity of pure bulk platinum⁶ is 0.943×10^7 S/m which for the target deposition depth of 100nm suggests a sheet resistance of $1.1\Omega/\square$, only 61% of the measured value. The resistivity of thin film metals is known to exceed that of its bulk value as the film thickness decreases, a result of increased electron scattering⁷. This scattering in thin film metals highlights the importance of using simultaneous cross measurements to derive accurate impedance models.

Test Structure	Sheet Resistance (Ω/\square)		Electrical Linewidth (μm)	
	20:20 μm	20:40 μm	20:20 μm	20:40 μm
1	1.86	1.86	24.75	20.28
2	1.89	1.72	22.83	21.38
3	1.95	1.76	22.31	22.23
4	1.82	1.66	23.06	21.48
5	1.89	1.74	24.24	20.64
6	1.88	1.65	25.05	20.68
7	1.77	1.76	25.43	20.49
8	1.78	1.72	24.90	20.63
9	1.75	1.72	25.08	20.64
10	1.70	1.72	23.21	21.39
11	1.79	1.65	25.31	20.68
12	1.76	1.66	23.71	21.48
13	1.71		24.89	
14	1.77		24.64	
Mean (Optical)	1.81	1.72	24.16 (24.31)	21.00 (21.09)

Table 7.1 – Cross-bridge tests structure measurements for sheet resistance and electrical linewidth. The test structures were distributed around interdigitated electrode structures designed to evaluate the electrical impedance of 20:20 and 20:40 μm mark-space ratios.

Preparation of DEP Solutions

The DEP experiments performed in this thesis require that cells are suspended in a low conductivity solution, of typically less than 100mS/m in conductivity. The conductivity of mammalian culture media is typically⁸ in the region of 1.5 S/m, a value which is primarily due to the high concentration of sodium chloride present. By removing sodium chloride the conductivity can be reduced to a level where transitions to positive DEP in the frequency spectrum are observable. It is, however, considered important to match the osmolality of a DEP solution to that of the culture media in which the cells were grown. This isosmotic substitution of sodium chloride is undertaken to minimise the stress and damage to cells, with mannitol^{9,10} and sucrose^{11,12} being used both in the published literature and here. The addition of glucose at a concentration of ~2g/L is required as it provides metabolic fuel which is necessary for the maintenance of viability in mammalian cells¹³.

Preparation of the sucrose based DEP solution began by measuring the osmolality of cell culture medium using an Advanced Instruments Inc. Model 3300 osmometer. The osmometer operates by a technique known as freeze point depression, an approach based on determining the temperature at which the solid and liquid phases of a solution exist together, in equilibrium¹⁴. The freezing point of a solution occurs at a lower temperature than that of pure water, and at low concentrations¹⁵ this decrease is directly proportional to the total concentration of solutes, a 1 Osm/kg solution freezing at a temperature of -1.86°C. Based on a measured osmolality of ~310 mOsm/kg the required concentration of sucrose, in addition to glucose, was determined. A sterile beaker was filled with 700ml of deionised water, into which 100g of sucrose and 2g of glucose was dissolved prior to adding further deionised water to a final volume of 1 litre. Based on the molecular weights of sucrose (342.3 g/mol) and glucose (180.2 g/mol), both of which possess osmotic coefficients close to unity at the concentrations discussed here and therefore do not dissociate in water¹⁶, a solution is created with an osmolality of 309 mOsm/kg. Phosphate Buffered Saline (PBS) was added to increase the solution conductivity to 33 mS/m. PBS does not significantly affect the total osmolality as it is designed to replicate physiological conditions and only requires the addition of millilitres in volume. The solution pH was finally adjusted to a value of 7.4 by adding appropriate volumes of concentrated sodium hydroxide or hydrochloric acid, as required.

In Chapter Five, and onwards, a DEP solution based on the isosmotic substitution of sodium chloride with mannitol was used, a solution which also incorporated salts of both calcium and magnesium. Calcium is an important cation in culture media, with complete removal from mouse fibroblasts known to cause cell death within 48 hours¹⁷. Magnesium is another

cation included in culture media with its role in preventing the onset of senescence being demonstrated in human fibroblasts¹⁸. Although no definitive evidence exists for short term physiological effects due to the withdrawal of calcium or magnesium their inclusion, at culture media concentration, results in a DEP solution with an acceptable conductivity of ~42 mS/m. In the absence of PBS, which incorporates a phosphate based pH buffer, HEPES acted as a substitute. HEPES is a more effective pH buffering agent than phosphate at the hypothermic temperatures which DEP experiments are often performed in, an important consideration as the extracellular pH of mammalian cells is known to decrease under such conditions¹⁹. The inclusion of a pH buffer provides stability during the experiment and makes adjustment to a solution pH of 7.4 easier to achieve.

Due to the low concentrations of calcium and magnesium salts required, displayed in Table 7.2, the solution was prepared using an initial stock solution of 50× the final concentration. The stock solution consisted of calcium nitrate, magnesium sulphate, HEPES and glucose with an osmolality of 23.2 mOsm/kg at 1× concentration. A litre of DEP solution was constructed from 20ml of the stock solution, 48.6g of mannitol and the additional deionised water for an osmolality of ~290 mOsm/kg. The pH was adjusted to a value of 7.4 by adding 1M sodium hydroxide as required followed by measurements of both osmolality and conductivity (using an Advanced Model 3300 osmometer and Oakton CON-510 conductivity meter, respectively) for confirmation. Vacuum filtration through a 0.22µm membrane was performed in a laminar flow cabinet to prevent contamination due to bacteria or foreign particles. Unless sterilised by autoclaving the prepared solutions should be kept refrigerated and disposed within two weeks.

Component	Molecular Mass (g/mol)	Concentration (mM)	Concentration (g/L)
50× Stock Solution			
Calcium Nitrate (Tetrahydrate)	236.2	21.2	5
Magnesium Sulphate (Heptahydrate)	246.5	20.3	5
Glucose	180.2	555.1	100
HEPES	238.3	500.2	119
DEP Solution			
50× Stock Solution		2% (v/v)	
Mannitol	182.2	268.8	48.6
Sodium Hydroxide, 1M Solution		(as required for pH)	

Table 7.2 – Mannitol based formulation for stock and DEP solutions used in this thesis.

Cell Suspension

DEP experiments involving the detection of crossover frequencies require the suspension of cells into their solution at the intended conductivity. The following procedure describes the re-suspension of SP2/O murine myeloma cells from their RPMI-1640 culture media into the low conductivity DEP solution previously described. This procedure should be performed in a laminar flow cabinet under aseptic conditions to prevent contamination of both the cultured cells and reagents.

1. Warm the DEP solution up to 21°C or room temperature in a water bath. Lowering the temperature of cells from their incubated value of 37°C mitigates the loss of intracellular ions.
2. Murine myeloma cells were typically cultured for DEP experiments in T75 flasks (75cm² surface area) at a density of $\sim 5 \times 10^5$ cells/ml in 20ml of RPMI-1640 culture media. Cultured cells should be removed from their incubator and gently agitated using a pipette by drawing up and rinsing cells from the surface. This process acts to both release semi-adherent cells from the surface and break up any clumps.
3. Perform a cell count and viability check of a small sample using trypan blue and a haemocytometer. This measurement is important both to ensure the cell population is healthy and to estimate the final suspension volume required for a target cell density.
4. Centrifuge a volume of cells sufficient for the DEP experiment. As a rough guide, 0.5ml of the final DEP cell suspension at a density of 1×10^7 cells/ml was typically sufficient. At a culture media density of 5×10^5 cells/ml this requires an initial volume of 10ml which should be centrifuged at 300×g for 5 minutes.
5. A small pellet should form at the base of the centrifuged tube. Carefully aspirate the culture media to leave this pellet and gently tap the tube on a hard surface to loosen the pellet. Re-suspend the cells into 10ml of the warmed DEP solution and centrifuge the cells again.
6. Repeat the previous step to perform a second rinse in DEP solution. By repeating this process the concentration of culture media remaining is reduced significantly, ensuring that the target conductivity is achieved.
7. Carefully aspirate the DEP solution, gently tap the tube on a hard surface and re-suspend the cells to the final suspension volume, 0.5ml for the values quoted here.

DEP Experiment

The DEP experiments undertaken in this thesis used electrodes designed in Chapter Three, their performance being considered based on a 50Ω source operating at frequencies of up to 300MHz with cells suspended in an aqueous solution of 50 mS/m conductivity. An Agilent ESG-D4000A signal generator was used to generate a sinusoidal signal of $0.305 V_{pp}$ ($0.215 V_{RMS}$) as shown in Figure 7.2. The generator was controlled by PC over GPIB using LabVIEW software which applied each frequency for 10 seconds, from 425 to 25 MHz in 25 MHz decrements when evaluating the second crossover, f_{x02} . A Mini-Circuits ZHL-1A amplifier applied a power gain of $\sim 17.5\text{dB}$, which given the input and output impedances of 50Ω provided an output voltage of $\sim 5 V_{pp}$, as stipulated by the simulations of Chapter Three.

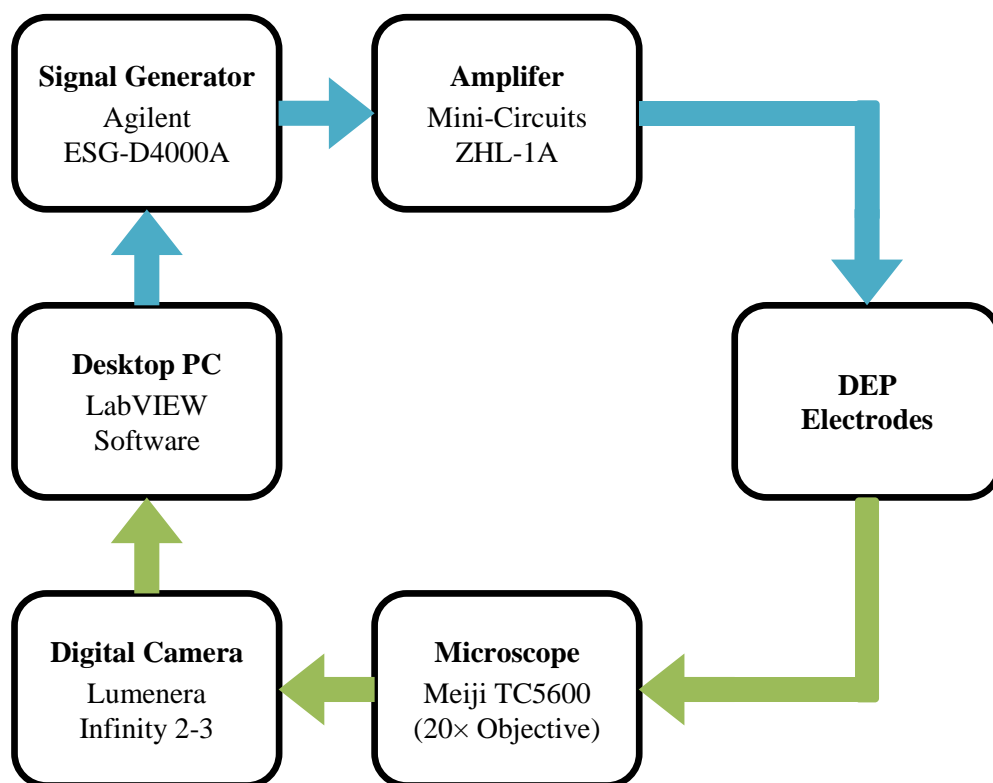


Figure 7.2 – Setup used to perform DEP experiments where blue and green arrows display the electrical signal and optical paths, respectively.

Cells were suspended into the DEP solution and a $5\mu\text{l}$ volume deposited over the electrodes. A small tape gasket and glass cover slip were used to form a sealed chamber which prevented evaporation of the sample with the electrodes mounted into an inverted microscope with a $20\times$ objective lens. After each frequency was applied for 10 seconds an image was automatically captured using a Lumenera Infinity 2-3 digital camera.

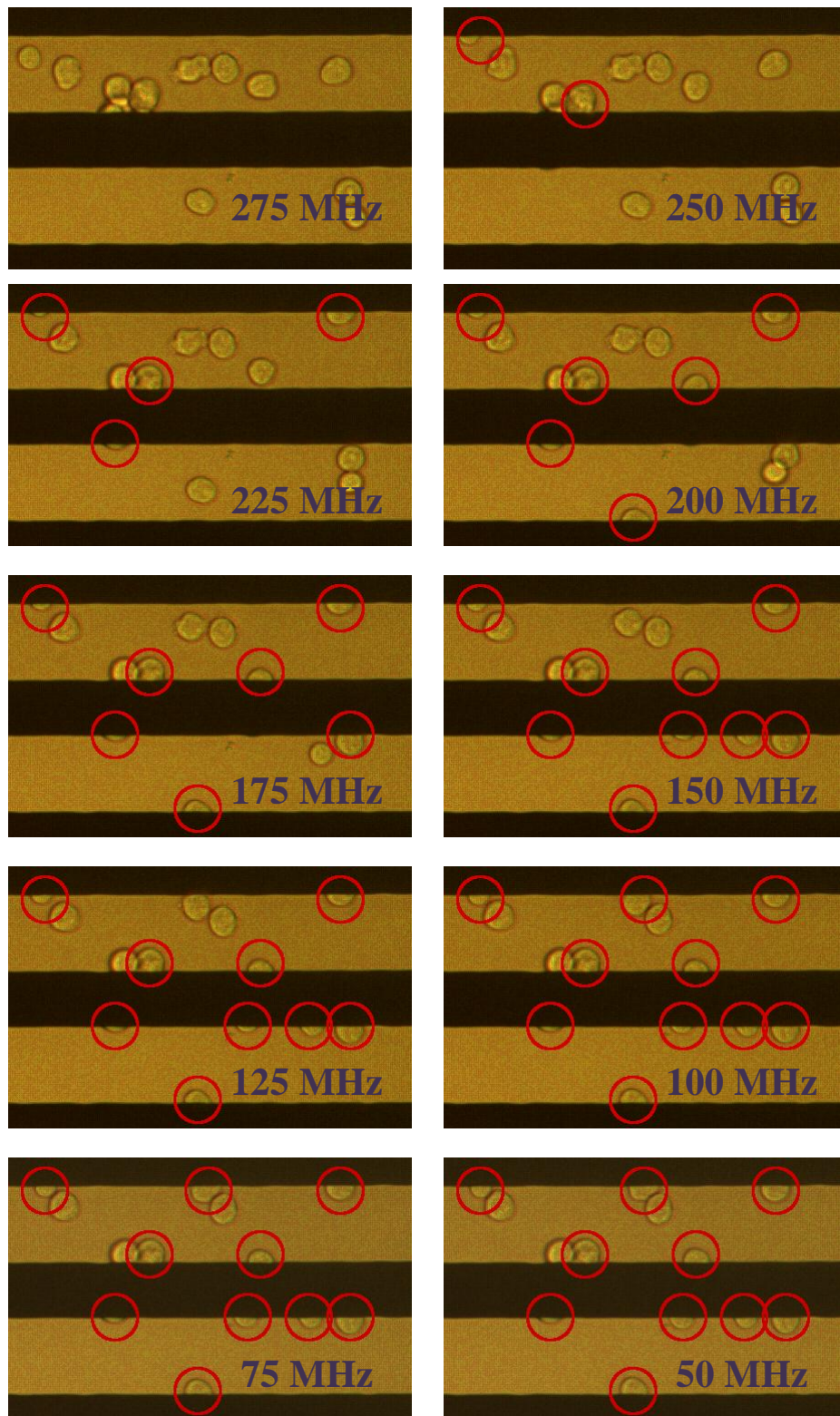


Figure 7.3 – Images captured following a frequency sweep to determine the f_{x02} distribution of a cell population. Cells circled in red are identified as having been attracted to an electrode edge under positive DEP.

In Figure 7.3 a series of images captured from a frequency sweep are displayed. At 275 MHz most of the cells are aligned between the electrode edges. Two of the cells appear close to an edge but it is unclear whether they have become attracted under positive DEP, as a result they remain uncaptured. When the frequency is decreased to 250 MHz it is easier to establish that two of the cells have transitioned into positive DEP as they have clearly moved towards an electrode edge. These cells are highlighted in red and are classed as having an f_{x02} value of between 275 and 250 MHz. This process of determining when cells have transitioned into positive DEP is repeated down to the finishing frequency, allowing a histogram of f_{x02} values to be built up as displayed in Figure 7.4.

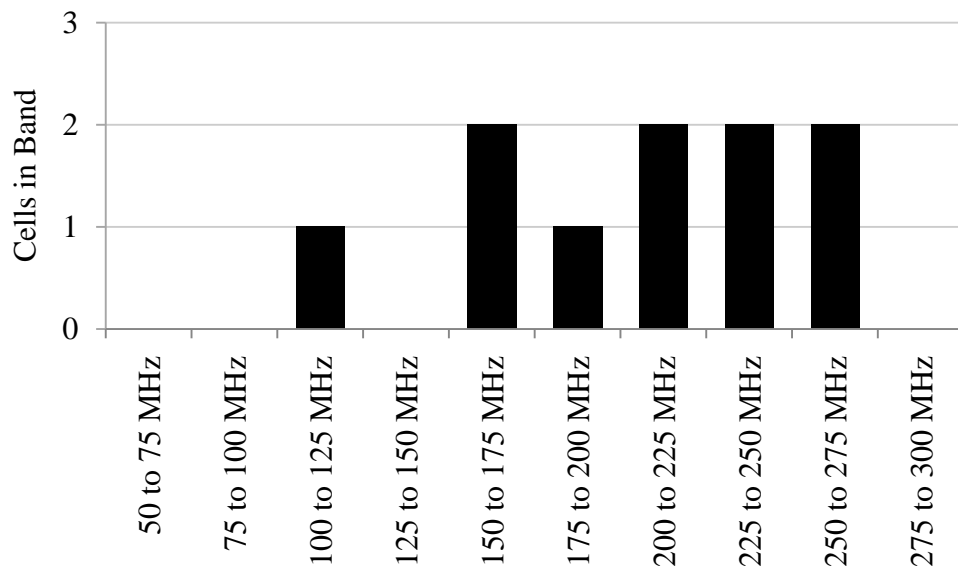


Figure 7.4 – An f_{x02} distribution derived from the images of Fig. 7.3.

In this thesis the mean value of these distributions are plotted with error bars displaying the 95% confidence interval of the mean, $\sim 1.96 \times$ the sample standard deviation divided by the square root of the number of cells (for both the upper and lower bounds). A range of 210 MHz was estimated in Chapter Three which, assuming it encompasses the mean value ± 3 standard deviations, requires a sample size of at least 50 to constrain the 95% confidence interval (for the mean) to within 10 MHz. As a general guideline, experiments conducted in this thesis used a cell sample size of at least 100 to minimise this confidence interval.

Measurement of Cell Size

The diameter of cells was measured to determine their volume, this approach assumes a spherical shape which is reasonable for cells which are freely suspended in solution. Images of the cells were taken using a 40× objective focused on a region outside of the interdigitated electrodes. The cells were allowed to settle onto the glass surface and the focusing adjusted to ensure they were measured accurately within the lens focal plane. In Fig. 7.5 a single cell is shown using the image processing program ImageJ, the plot displaying the intensity profile along a line bisecting the cell. The outer membrane is defined by two intensity minima on this line, the distance between which provides a measure of the cell diameter ϕ . Cells which appeared as aggregated clumps were avoided to prevent an inaccurate estimate of the diameter.

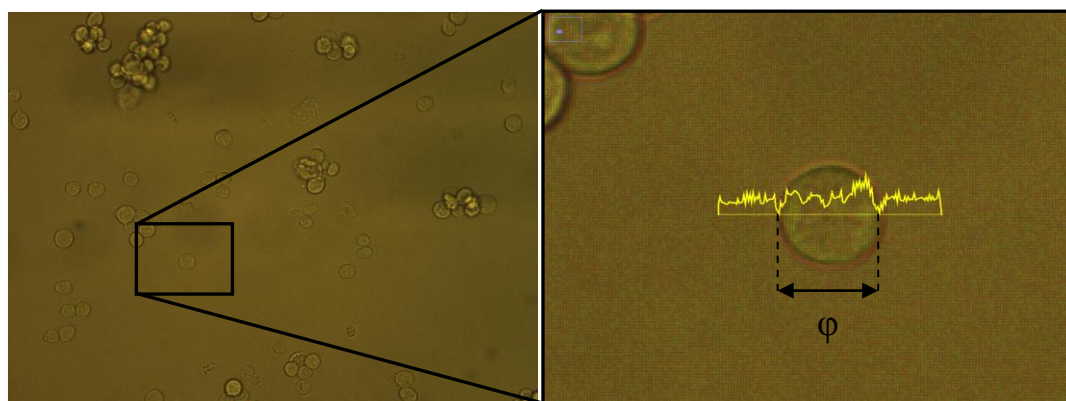


Figure 7.5 – The diameter of a cell as defined by the intensity minima of a bisecting line.

A graticule was used to determine the image resolution as ~ 4.9 pixels per μm . Based on a cell of $5\mu\text{m}$ radius, which is below the mean value for murine myeloma cells in DEP solution as displayed in Fig. 4.4, the volume error resulting from a half-pixel error is $\pm 6\%$. Throughout this thesis measurements of the cell diameter or the derived effective volume are quoted in terms of their mean value \pm the 95% confidence interval. These values are derived from the experimental data and as such incorporate variances from both the distribution of values and the error in their measurement. Uncertainty in the measured diameter will not bias the mean value of derived parameters, however the measured variance will be higher than the true value. As a result of the latter, the displayed 95% confidence intervals represent a worst case estimate²⁰. By measuring at least fifty cells from each sample this uncertainty in the estimated mean volume was kept to a practicable minimum, being on average $\pm 15\%$ of the cell volumes discussed in Fig. 6.3 & Fig. 6.9.

References

- 1 Cowley, A. & Woodward, B. (2011) A healthy future: platinum in medical applications. *Platinum Metals Review*, 55 (2), 98-107.
- 2 Tiggelaar, R.M., Sanders, R.G.P., Groenland, A.W. & Gardeniers, J.G.E. (2009) Stability of thin platinum films implemented in high-temperature microdevices. *Sensors and Actuators A: Physical*, 152 (1), 39-47.
- 3 Kondo, I., Yoneyama, T., Takenaka, O. & Kinbara, A. (1992) Formation of high adhesive and pure Pt layers on TiO₂. *Journal of Vacuum Science & Technology A*, 10 (6), 3456-3459.
- 4 Levinson, H.J. (2005) *Principles of Lithography*, Bellingham, WA: The Society of Photo-Optical Instrumentation Engineers.
- 5 American Society for Testing and Materials (2003). ASTM F 1261M-96 Standard test method for determining the average electrical width of a straight, thin-film metal line [Metric]. West Conshohocken, PA: ASTM International.
- 6 Giancoli, D.C. (1995) *Physics: Principles with Applications (4th ed.)*, Upper Saddle River, NJ: Prentice Hall.
- 7 Lacy, F. (2011) Developing a theoretical relationship between electrical resistivity, temperature, and film thickness for conductors. *Nanoscale Research Letters*, 6 (1), 636-649.
- 8 Pethig, R. (2010) Review Article-Dielectrophoresis: status of the theory, technology and applications. *Biomicrofluidics*, 4 (2), 022811.
- 9 Markx, G.H., Huang, Y., Zhou, X.F. & Pethig, R. (1993) Dielectrophoretic characterization and separation of micro-organisms. *Microbiology*, 140 (3), 585-591.
- 10 Hughes, M.P. & Morgan, H. (1998) Dielectrophoretic trapping of single sub-micrometre scale bioparticles. *Journal of Physics D: Applied Physics*, 31 (17), 2205-2210.
- 11 Gascoyne, P.R.C., Wang, X.B., Huang, Y. & Becker, F.F. (1997) Dielectrophoretic separation of cancer cells from blood. *IEEE Transactions on Industry Applications*, 33 (3), 670-678.
- 12 Becker, F.F., Wang, X.B., Huang, Y., Pethig, R., Vykoukal, J. & Gascoyne, P.R.C. (1994) The removal of human leukaemia cells from blood using interdigitated microelectrodes. *Journal of Physics D: Applied Physics*, 27 (12), 2659-2662.
- 13 Gascoyne, P.R.C. & Vykoukal, J.V. (2004) Dielectrophoresis-based sample handling in general-purpose programmable diagnostic instruments. *Proceedings of the IEEE. Institute of Electrical and Electronics Engineers*, 92 (1), 22-42.

- 14 Koumantakis, G. & Wyndham, L.E. (1989) An evaluation of osmolality measurement by freezing point depression using micro-amounts of sample. *Journal of Automatic Chemistry*, 11 (2), 80-83.
- 15 Krogh, A. (1939) *Osmotic Regulation in Aquatic Animals*, Cambridge: Cambridge University Press.
- 16 Stokes, R.H. & Robinson, R.A. (1966) Interactions in aqueous nonelectrolyte solutions. I. Solute-solvent equilibria. *The Journal of Physical Chemistry*, 70 (7), 2126-2131.
- 17 Yang, D.P. & Morton, H.J. (1970) Effect of calcium and magnesium on the morphology and growth pattern of L-M cells. *Journal of the National Cancer Institute*, 46 (3), 505-516.
- 18 Killilea, D.W. & Ames, B.N. (2008) Magnesium deficiency accelerates cellular senescence in cultured human fibroblasts. *Proceedings of the National Academy of Sciences of the United States of America*, 105 (15), 5768-5773.
- 19 Baicu, S.C. & Taylor, M.J. (2002) Acid-base buffering in organ preservation solutions as a function of temperature: new parameters for comparing buffer capacity and efficiency. *Cryobiology*, 45 (1), 33-48.
- 20 Hamilton, L.C. (1992) *Regression with Graphics: A Second Course in Applied Statistics*, Pacific Grove, CA: Duxbury Press.

Chapter Eight

Conclusions & Future Work

Introduction

In this thesis the first comprehensive study of dielectrophoresis on mammalian cells above 100 MHz has been conducted. The underlying theory was developed and explored to guide the design of experimental equipment. Initial observations of the second crossover frequency f_{x02} were made and followed by a systematic evaluation of its behaviour. In verifying and understanding its behaviour a new intracellular dimension has emerged for microfluidic devices based on DEP crossovers, the analysis of which complements existing dielectric measurements of the cell membrane.

Summary of Thesis and Results

Chapter Two presented the theory underlying dielectrophoresis, by first considering the force induced on a dipole under the influence of a non-uniform electric field. By determining the form of its surrounding electric potential the DEP force induced on any dielectric particle can be derived. A lossless dielectric sphere was first considered before being adapted to include both conductive losses and a thin dielectric shell, analogous to a mammalian cell. The model possessed regions of negative and positive DEP with transitions at two characteristic frequencies when suspended in a solution of sufficiently low conductivity. At low frequencies the first crossover f_{x01} has been extensively researched by others, its behaviour governed by the cell membrane. Higher frequencies model a second crossover, referred to as f_{x02} , which was expected to behave as a function of intracellular dielectric properties. By considering a rotating electric field the concept of electrorotation was also introduced, a technique which is capable of detecting intracellular properties but requires extensive analysis across multiple frequencies. The application of a single crossover is attractive both in terms of its simplicity and the ability to sort cells when combined with microfluidics.

In Chapter Three the process of adding shells was generalised, a technique previously exploited to extract detailed intracellular dielectric properties using impedance spectroscopy. Based on the dielectric properties of mouse lymphocytes derived by Asami *et al.*¹, involving impedance spectroscopy data from 100 kHz to 250 MHz, their DEP spectrum in a low

conductivity solution was predicted. The model incorporates dielectric properties of the nucleoplasm, nuclear envelope, cytoplasm and cell membrane; predicting a value for f_{x02} of ~215 MHz. Interdigitated electrodes were modelled using a distributed RCR network² incorporating track resistance, solution conductivity and inter-electrode capacitance. The approach was validated by comparing the impedance spectra of platinum test structures fabricated on glass wafers. A device capable of performing DEP experiments beyond the range required was designed and fabricated using these techniques. The levitation of particles under negative DEP, beyond f_{x02} , was simulated by finite element modelling and used to constrain the design. Due to the frequencies involved the capacitance, and therefore area, of the device was restricted to 1.84mm². By incorporating a parallel resistance for signal termination the design ensures a flat impedance response across a wide frequency range and consistency in the electric field strength.

The first experimental observations of f_{x02} were described in Chapter Four³. A computer controlled system was developed and used to sweep the applied frequency from 425 MHz down to 25 MHz. Images were automatically captured through an inverted microscope and used to determine the levitation and subsequent attachment of cells to the electrode edges under negative and positive DEP, respectively. Murine myeloma cells were cultured, suspended in an isosmotic low conductivity solution and deposited over the electrodes. By applying a 5 V_{pp} signal at 425 MHz the cells were observed levitating under negative DEP, above the electrodes. This observation confirmed the predicted high frequency response which requires an intracellular relative permittivity lower than that of water to occur. As the frequency was decreased the levitation height of cells was reduced until they transitioned to positive DEP around the predicted region of ~215 MHz, becoming attached to the electrode edges. This behaviour confirms the existence of f_{x02} and provides a degree of confidence in the dielectric parameters extracted by impedance spectroscopy for cells which are broadly similar to those used here. An unexpected observation was that the mean value of f_{x02} decreased over time when suspended in the low conductivity solution. This phenomenon affected all cells in a similar manner and continued until effective DEP forces could no longer be applied. Human red blood cells were subjected to the same experimental conditions, exhibiting a lower initial value for f_{x02} but undergoing a similar decrease in crossover frequency with time. In previous studies, by Gimsa *et al.* on murine myeloma cells and Lacelle *et al.* on human red blood cells, the isosmotic substitution of salt by a non-electrolyte resulted in the efflux of intracellular ions. By undertaking temperature controlled experiments the activation energy of a process reflected by this decrease in f_{x02} , during the first two hours of suspension in DEP solution, corresponded to that identified by Lacelle *et*

al. This correlation provided evidence that a breakdown in the ionic homeostasis of cells under these conditions is a critical issue faced in the measurement of $f_{x_{o2}}$. Exposure of murine myeloma cells to DEP solutions containing various combinations of major culture media salts revealed the importance of potassium chloride in this regard. Analysis of these cells by flow cytometry revealed that the isosmotic solution resulted in cell shrinkage upon suspension in a manner consistent with an initial efflux of ions. Cell viability was also shown to collapse but did not appear to trend with the corresponding decrease in $f_{x_{o2}}$ for intact cells after several hours of continued suspension. Based on these initial findings, measurements of $f_{x_{o2}}$ in subsequent experiments were performed within 30 minutes of suspension to mitigate this effect.

Chapter Five presented an analytical derivation of $f_{x_{o2}}$ which demonstrated its direct proportionality to the intracellular conductivity of a cell when suspended in a low conductivity solution, typically used for these experiments. An experiment was devised to directly control the value of $f_{x_{o2}}$ by applying hypotonic stress to the cells such that dilution of the intracellular compartment occurred. Measurements of cell diameter and $f_{x_{o1}}$ were conducted to provide complementary information about the morphological state and integrity of the cell membrane. In addition to these DEP techniques the cells were loaded with the potassium sensitive intracellular fluorophore PBFI. By performing ratiometric flow cytometry the fluorophore provided a determination of relative differences in the intracellular potassium concentration. DEP solutions were created which applied varying degrees of hyposmotic stress and used to identify an osmolality of 215 mOsm/kg as isotonic. Relative to this isotonic point, hypertonic stress resulted in cell shrinkage with an apparent increase in potassium concentration which was below that expected for the volume reduction, supporting the rapid efflux of ions upon suspension discussed in the previous chapter. Hypotonic stress drove an increase in cell size as intended which resulted in decreased intracellular potassium concentration, a decrease which is accounted for by the associated dilution. Membrane capacitances were determined from the measurements of cell diameter and $f_{x_{o1}}$, behaving as expected with an osmolality of 140 mOsm/kg resulting in capacitances close to the theoretical minimum. The behaviour of $f_{x_{o2}}$ generally reflected that of the intracellular potassium concentration determined from the ratiometric measurements. In the hypertonic region an increase in $f_{x_{o2}}$ occurred which was below that expected from the volume reduction, also supporting an efflux of ions. As intended, the application of hypotonic pressure resulted in intracellular dilution which accounts for the observed reduction in $f_{x_{o2}}$. Across the entire osmotic range explored a strong correlation was displayed between intracellular potassium concentration and $f_{x_{o2}}$. Although $f_{x_{o2}}$ will also depend upon

the concentration of other free ionic species its ability to track changes in the most abundant ion provides the potential to easily evaluate the intracellular state of cells in a non-invasive and label-free manner.

In Chapter Six the viability of cell cultures was discussed as being amongst the most important parameters concerning a cell biologist. The industrial production of murine myeloma cells in batch cultures highlights their importance and the requirement for methods to both monitor their viability and maximise productivity. A means of detecting changes to the intracellular ionic state of cells, which appeared to be demonstrated in the previous chapter, could provide a means of detecting if the collapse of a cell culture is underway such that corrective action can be taken. Murine myeloma cells were maintained in an unfed culture for six days, during which measurements of $f_{x_{o2}}$, $f_{x_{o1}}$, cell diameter and viability were made on a daily basis. The viability of cells was determined by the exclusion of trypan blue, a measure of necrosis, revealing a maximum viability of 78% which eventually collapsed to 26%. After this treatment the cells were washed and fed with fresh culture media at two day intervals resulting in the full recovery of their viability after five additional days. The mean value of $f_{x_{o1}}$ provided no clear trend over this experiment and, due to uncertainty regarding the membrane conductivity of cells undergoing apoptosis, a convincing determination of membrane capacitance was not possible. In contrast, the mean value of $f_{x_{o2}}$ displayed a strong correlation to viability across the entire experiment suggesting the technique could be applied with this in mind. By using the apoptotic agent etoposide, an experiment was undertaken to determine if $f_{x_{o2}}$ could reveal changes associated with the early onset of apoptosis. The mean values of $f_{x_{o1}}$ and $f_{x_{o2}}$ displayed no clear correlation with etoposide concentration following six hours of treatment. After a full day the mean value of $f_{x_{o1}}$ displayed an increase with etoposide concentration but at a stage where cell viability had already decreased and the onset of necrosis was underway. By inspecting their cumulative distribution plots, subtle shifts in both crossovers do occur following six hours of exposure, before any detectable change in cell viability. A decrease in $f_{x_{o1}}$ was indicated with respect to increasing etoposide concentration which appears to contradict an earlier published result; however a corresponding decrease in $f_{x_{o2}}$ does occur, consistent with the efflux of potassium ions associated with early stage apoptosis. Whether this approach can be applied to apoptosing cells under standard culture conditions requires further study, ideally involving time intervals shorter than those employed here.

Future Work

The efflux of ions is an issue which applies to the measurement of mammalian cells in low conductivity solutions, both in the use of $f_{x_{o2}}$ and other electrical techniques. In this thesis the issue was mitigated by reducing the exposure time, however this approach may not be practical if large cell populations require measurement or sorting. A temporary chemical means of “locking” these ions inside the cell would be an ideal solution, which may be achievable by exploiting the use of ion channel blockers. If, however, the efflux of ions is dominated by the permeability of the lipid membrane itself then such an approach may be ineffective. In Chapter Four, the presence of potassium chloride in the suspending solution was identified as critical in the prevention of this efflux and its introduction at low concentrations is worthy of further research. A compromise may be possible between the rate at which $f_{x_{o2}}$ decreases and the increase in solution conductivity associated with the addition of potassium chloride, such that an effective crossover remains. Alternatively, or in addition, the use of evaporative⁴ or Peltier⁵ based microfluidic cooling may be employed to reduce the temperature of both the device and samples to below that of the room. A temperature of 10°C in this work was able to reduce the decrease to ~13 MHz/hour however further reductions may be possible at even lower temperatures.

A further study of apoptosis under typical culture conditions is necessary to determine if the measurement of $f_{x_{o2}}$ can be used as an early warning system, beyond the ability to track viability. The experiment undertaken in Chapter Six could be repeated with shorter intervals between each measurement, such that the onset of apoptosis can be discriminated from the necrotic breakdown of the cell membranes. An alternative approach would be to extract a sub-population of cells in the early stages of apoptosis, by using fluorescence-activated cell sorting and Annexin V for example, to determine if their $f_{x_{o2}}$ values differ from those of the bulk population.

By designing electrodes capable of operating effectively in the second crossover region an unexplored area of the Clausius-Mossotti function became accessible. In this thesis the study of cells was restricted to that of the second crossover itself however, above this frequency, a plateau in the DEP spectrum is expected. At such frequencies the DEP force becomes a function of the difference between intracellular and extracellular permittivities, the former being poorly understood and the latter being relatively well characterised. By determining the levitation height of a cell at a given voltage, and using an estimate of the cell density, a value for the intracellular permittivity can be derived. The application of different voltages could be used to further eliminate cell density as a variable and provide a more accurate

estimate. In the dilution experiments of Chapter Five the induced changes to f_{x02} were accounted for by the estimated change in intracellular conductivity. Subtle changes in the structure of chromatin, such as those occurring throughout the cell cycle or even as the result of histone modification, may influence intracellular permittivity and result in detectable dielectrophoretic changes. If changes in the levitation height, as a function of both voltage and frequency, can be determined with sufficient accuracy the intracellular dielectric information derived may provide unique insights and provide new parameters to sort by.

Conclusion

This thesis has achieved its stated aim by both verifying the existence of a second DEP crossover, referred to as f_{x02} , in mammalian cells and exploiting its behaviour. A device capable of exploring the required frequency range was created which revealed a crossover whose location agrees with that predicted by theory. Its stability has been characterised and the practical conditions required for its reliable measurement determined. Control of f_{x02} was achieved by applying osmotic stress, demonstrating its relationship to both intracellular conductivity and potassium concentration. The viability of a cell culture is correlated to the value of f_{x02} and an apparent sensitivity to the early stages of chemically induced apoptosis has been demonstrated. Devices exploiting f_{x02} have the potential to characterise and sort cells at high rates of throughput based on subtle intracellular dielectric differences, in a manner which is both non-invasive and label free.

References

- 1 Asami, K., Takahashi, Y. & Takashima, S. (1989) Dielectric properties of mouse lymphocytes and erythrocytes. *Biochimica et Biophysica Acta*, 1010 (49), 49-55.
- 2 Chung, C., Smith, S., Menachery, A., Bagnaninchi, P., Walton, A. J. & Pethig, R. (2011) Interdigitated electrode modelling for applications in dielectrophoresis. *2011 IEEE International Conference on Microelectronic Test Structures. 4-7 April 2011. Amsterdam, Netherlands.* pp74-79.
- 3 Chung, C., Waterfall, M., Pells, S., Menachery, A., Smith, S. & Pethig, R. (2011) Dielectrophoretic characterisation of mammalian cells above 100 MHz. *Journal of Electrical Bioimpedance*, 2, 64-71.
- 4 Maltezos, G., Rajagopal, A. & Scherer, A. (2006) Evaporative cooling in microfluidic devices. *Applied Physics Letters*, 89 (7), 074107.
- 5 Maltezos, G., Johnston, M. & Scherer, A. (2005) Thermal management in microfluidics using micro-Peltier junctions. *Applied Physics Letters*, 87, 154105.

Appendix

Publications

Interdigitated Electrode Modelling for Applications in Dielectrophoresis

C. Chung, S. Smith, A. Menachery, P. Bagnaninchi, A.J. Walton and R. Pethig

Institute for Integrated Micro and Nano Systems, School of Engineering,
 Scottish Microelectronics Centre, The University of Edinburgh, EH9 3JF, UK

ABSTRACT

Electrical test structures have been designed to enable the characterisation of interdigitated electrode structures in conductive solutions, as used in dielectrophoresis. Test masks have been fabricated to explore the impact of array size, finger separation and solution conductivity on the applied electric field. A circuit model based on a distributed RC network is proposed and evaluated, demonstrating close agreement with actual impedance measurements. This provides the capability to readily predict the voltage and phase along the length of electrodes used for dielectrophoresis and other applications.

INTRODUCTION

Dielectrophoretic (DEP) separation systems for particles including cells and bacteria continue to be an area of intense research [1, 2]. These exploit the frequency dependent force applied to polarisable particles in a non-uniform electric field. This force is dependent upon differences in the dielectric properties of particles and their suspending solution with dielectrically distinct particles moving in opposite directions, known as positive or negative DEP. This is extremely attractive as a label free cell sorting technique. In the VHF range a crossover occurs (zero DEP force) dependent upon the dielectric properties of the nucleus and cytoplasm [3] providing the opportunity to fractionate cells based on factors such as cell cycle phase or degree of differentiation.

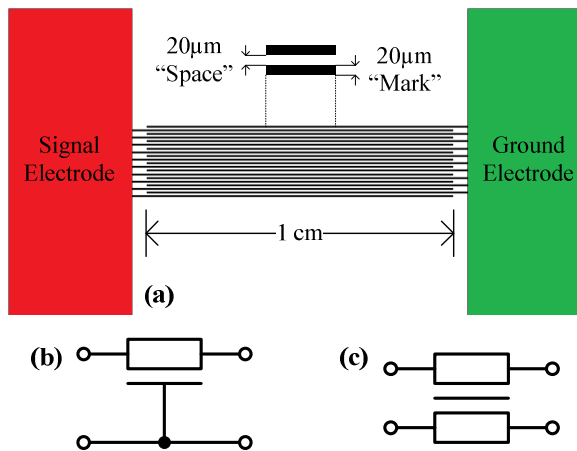


Fig. 1. (a) Typical interdigitated electrode test structure (b) Distributed RC network symbol (c) Distributed RCR network symbol

A variety of electrode geometries are used to generate these non-uniform fields, the most common being planar interdigitated electrodes (IDEs) as shown in Fig. 1(a), typically manufactured from 100-500nm thick gold or platinum and patterned using lift-off. Feature sizes in the μm range mean relatively low voltages can produce the large field gradients required for DEP induced cell motion. However, this motion also depends on the IDE layout, conductivity of the suspending solution and frequency at which it needs to be driven. This paper describes a model that can be used to both guide the design of and characterise this technology.

INTERDIGITATED ELECTRODES

IDEs are usually considered as simple lumped capacitors but this approximation breaks down at high frequencies and for lossy dielectrics. A single finger in an IDE has both resistance per unit length and capacitance per unit length with adjacent fingers. These constitute a distributed RC network [4], shown in Fig. 1(b), whose resistance and capacitance are distributed along the finger. This represents a low-pass filter with infinite poles meaning any AC signal applied at one end will be attenuated along the length of the finger, determined by the distributed RC value and operating frequency.

Zero attenuation along the fingers is clearly desirable to ensure the required field is applied but as this is unachievable the ability to electrically model IDEs is essential. However, the frequency response of these networks involves hyperbolic functions which do not readily lend themselves to simple analysis. The analysis of IDE electrodes is further complicated as the distributed capacitance is between fingers which both have resistances distributed along their length. This constitutes a distributed RCR network [5] whose symbol is displayed in Fig. 1(c).

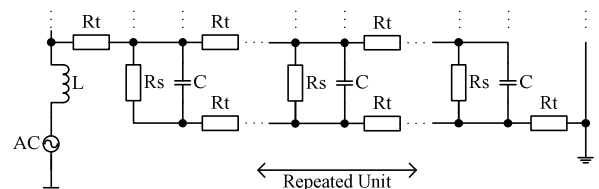


Fig. 2. Lumped equivalent circuit of a distributed RCR network

The challenge is to develop a model which can be used to predict the performance of these IDEs. Analytical solutions for distributed RC networks are available but difficult to integrate into modelling software such as SPICE. However, it is possible to develop models that provide good approximations for these networks [6]. In this work we have selected the RCR ladder network shown in Fig. 2 with lumped components representing track resistance, solution resistance and capacitance. This is attractive as the value of the lumped components is relatively simple to calculate and the accuracy may be increased by simply increasing the number of elements in the ladder. Another attraction of this ladder based model is that the effect of any lossy dielectrics can easily be incorporated as can the inductance of the electrode fingers. This model is used to examine the voltage attenuation along fingers with the goal of providing designers with critical aspects to consider relating to operating frequency as a function of IDE dimensions, sheet resistance and solution conductivity.

TEST STRUCTURES

Fig. 1(a) shows a schematic of the IDE test structures used in this work. The test chip layout displayed in Fig. 3 consists of IDEs with between 1 and 30 pairs of fingers with 1cm of overlap and two mark-space ratios, 20:20 μ m and 20:40 μ m, to characterise their capacitance and leakage resistance. These dimensions were selected for characterisation as cells are typically between 3 and 10 μ m in diameter.

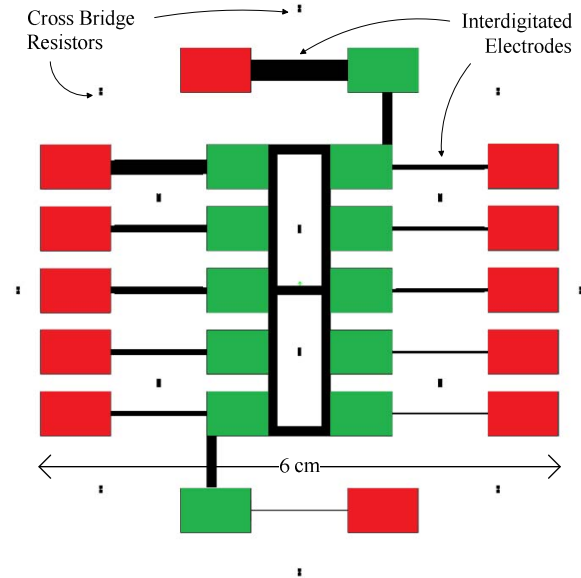


Fig. 3. Test mask layout with cross bridge resistors. The green and red contact pads correspond to those shown in Fig. 1(a)

The IDE test structures were interspersed with Kelvin cross bridge resistors of an identical trackwidth to the layout shown in Fig. 3. Using standard test methods [7] the electrical linewidth and resistivity were determined across the wafers. This enabled the

extraction of actual capacitance, track and solution resistances to be determined for the fabricated electrodes for input into the model.

Finite element modelling of an electrode cross-section was used to calculate the capacitance and current flowing between electrodes per unit metre. These values are multiplied by the number of pairs of fingers (P) and their length (L) to determine the total lumped capacitance and the solution resistance as shown in Fig. 4. This is simply adapted to calculate unit sections for the RCR ladder model.

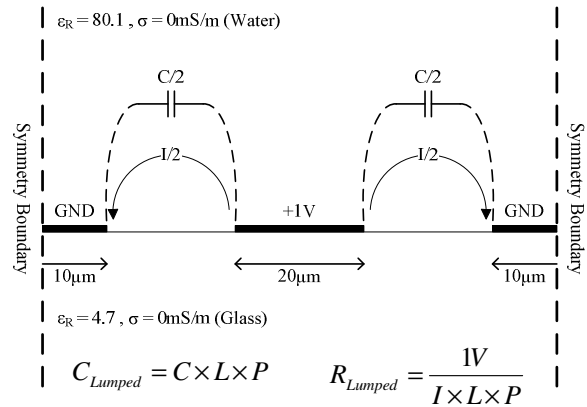


Fig. 4. COMSOL model for lumped capacitance and resistance

A 20:20 μ m (electrode-gap ratio) structure with a pure water dielectric produces a capacitance of 777pF/m. Fig. 5 presents the bandwidth for up to 30 pairs of fingers with a typical 50 Ω source and termination. It can be observed that the bandwidth decreases from 800 MHz for one pair of fingers down to 40 MHz for 20 pairs. It is clear that a trade-off exists between electrode area and bandwidth for a given output impedance, a potential issue for high volume particle trapping by DEP.

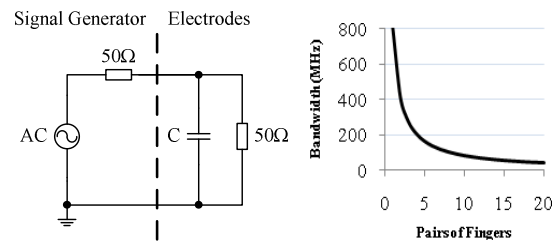


Fig. 5. Bandwidth reduction with increasing electrode area

CIRCUIT MODELS & FIT TO MEASUREMENTS

A simple lumped circuit model shown in Fig. 6 has been fitted to measured data for a 9 pair, 20:20 μ m IDE test structure, fabricated from 100nm thick platinum with a seed layer of 10nm titanium on glass. The lumped capacitance and solution resistances were estimated from cross bridge measurements which indicated a track width of 24 μ m (16 μ m spacing) and a sheet resistance of 1.8 Ω/\square (75m Ω/μ m track

resistance). A series inductance approximated the 1.3cm of wire connecting the device to an Agilent E4991A impedance analyser. The series resistance was adjusted to achieve a good fit over the 1 MHz to 1 GHz range.

The fit has three distinct regions. At low frequencies the impedance is determined by the series and solution resistances. As the frequency increases the impedance rolls off due to the parallel capacitance and at high frequencies the inductance dominates. This inductance must be minimised to ensure a sufficient voltage is dropped across the capacitance as a broad band is required for DEP measurements.

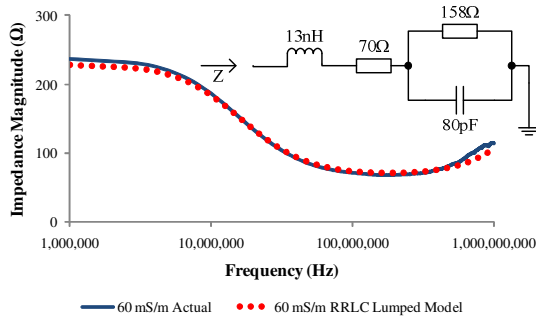


Fig. 6. 9-pair, 20:20µm device with 60 mS/m solution and lumped model fit

The need to empirically add a series resistance suggests that the model is missing an underlying parameter. Besides connections, this may be a function of track and solution resistances which all current paths encounter. While this lumped model fits the measured impedance it gives no insight into the IDE's operation as does the distributed RCR model proposed in Fig. 2 where the track resistance (R_t), solution resistance (R_s) and capacitance (C) between neighbouring electrodes can be readily identified. The accuracy of this ladder model may be improved by increasing the number of units. As with the lumped model a series inductance approximates the wire connections.

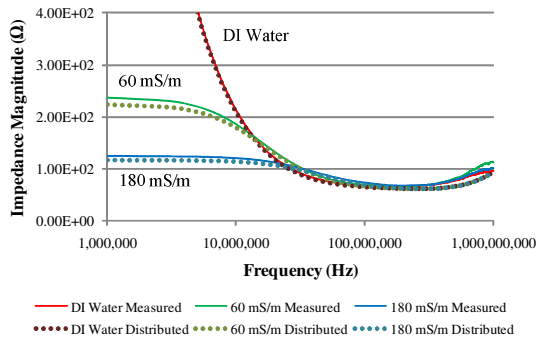


Fig. 7. Distributed model impedance magnitude and actual measurements for different conductivity solutions

Solutions with conductivities of 60mS/m and 180mS/m conductivity were prepared by adding

Phosphate Buffered Saline (PBS) to DI (De-Ionised) water and measured using a conductivity meter at 21°C. A PDMS gasket surrounded the device to ensure a solution depth greater than 500µm as over 99% of the current flows within 80µm of the electrode plane [8]. Electrodes were modelled in Spice using 20x 0.5mm unit sections per finger with the unit track resistance $R_t=37.5\Omega$ and capacitance $C=223fF$ based on the cross bridge measurements. R_s was 57kΩ and 19kΩ for 60mS/m and 180 mS/m conductivity solutions respectively.

Fig. 7 compares measured and modelled impedance magnitudes for the same electrodes as before. It can be observed that the impedance for DI water tends to infinity as the frequency approaches DC as expected with the distributed model providing a near perfect fit. At conductivities of 60mS/m and 180mS/m the impedance is closely matched by the model from DC up to 350 MHz. Approaching 1 GHz the measured impedance begins to level off, potentially due to uncompensated parasitic capacitances.

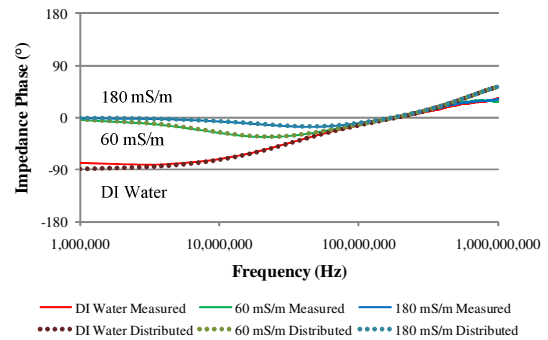


Fig. 8. Distributed model and measured impedance phase for different solution conductivities

Fig. 8 compares the measured impedance phase plots against those modelled and a good fit is observed with some deviation as the frequency approaches 1 GHz. The low frequency phase for DI water diverges from that of the distributed model where an infinite solution resistance was assumed. A phase shift in practice is reasonable as pure water has a finite conductivity in the region of 10µS/m. Based on the fit for both magnitude and phase responses the distributed RCR model appears to be effective with respect to different solution conductivities.

The impedance magnitude responses for IDE arrays with 1, 5 and 10 pairs of fingers, 20:20µm electrode-gap ratio and 33mS/m solution conductivity are displayed in Fig. 9. It should be noted that capacitances were determined for fingers not at the IDE edge. Hence it is expected that the model will perform best for larger array sizes where the symmetry boundary conditions applied in Fig. 4 are best approximated. Nevertheless the relationship is modelled well and highlights the impedance magnitude reduction as the number of fingers is

increased imposing limits based on the driving amplifier impedance. The associated impedance phase plot in Fig. 10 further illustrates the model's accuracy with respect to array size for frequencies up to and including the VHF range.

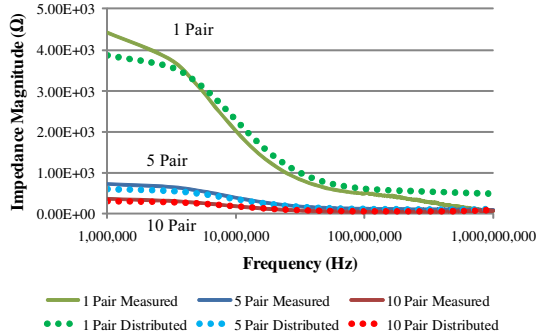


Fig. 9. Distributed model and measured impedance magnitude for different electrode array sizes (20:20 μm electrode-gap ratio, 33mS/m solution conductivity)

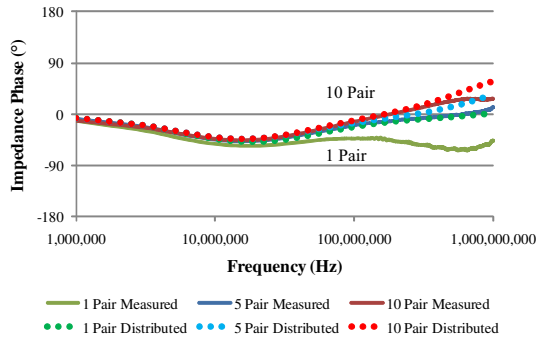


Fig. 10. Distributed model and measured impedance phase for different electrode array sizes (20:20 μm electrode-gap ratio, 33mS/m solution conductivity)

A comparison of impedance magnitude as a function of electrode spacing is displayed in Fig. 11 for IDE arrays with 5 pairs of fingers and a solution conductivity of 33mS/m. Electrode-gap ratios typical of cell based DEP work, 20:20 μm and 20:40 μm , have been selected for this. At low frequencies the modelled impedance magnitude in both cases is underestimated to a similar degree. This difference may arise due to inaccurate measurement of the solution conductivity or the electrode surface being less than ideal with respect to DC/low frequency conductivity. Irrespective of this the trend predicted at lower frequencies is accurate and the IDEs behaviour into the VHF range is in close agreement with the model. The associated impedance phase responses in Fig. 12 match the model with minimal differences.

DISCUSSION

By modelling IDEs using the proposed distributed RCR model it becomes possible to determine the voltage distribution along the electrode length and thus the electric field applied to particles undergoing DEP. This force is a function of the voltage difference

across the gap between adjacent electrodes indicated in Fig. 13, which will vary due to the track resistance and loading between electrodes. An important design consideration is identification of the minimum DEP force required. Devices based on the principle of capturing cells under positive DEP from the flow through a micro-fluidic channel need to take into account both the drag force and capture efficiency.

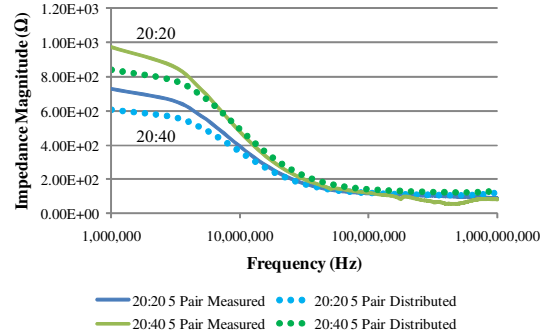


Fig. 11. Distributed model and measured impedance magnitude for different electrode spacings (33mS/m solution conductivity)

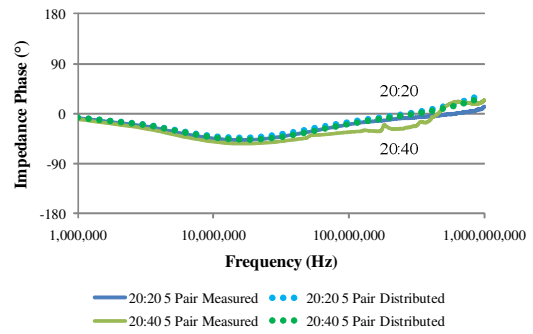


Fig. 12. Distributed model and measured impedance phase for different electrode spacings (33mS/m solution conductivity)

This will determine the minimum positive DEP force required for a given geometry and thus the required voltage difference between adjacent electrodes.

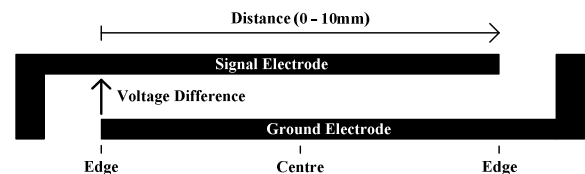


Fig. 13. Schematic of two fingers on an IDE indicating the voltage difference and distance along electrodes used in Fig. 14

Understanding this applied voltage difference is critical when the track is thin resulting in higher resistance or if long electrodes are employed, such as those used in spiral geometries for travelling wave DEP. Although these approaches are attractive to maximise the available surface area available and minimise fabrication costs the induced DEP force may be less than expected. The 9 pair, 20:20 μm electrode model may be substituted for the capacitor in Fig. 5 to analyse its behaviour in a 50 Ω matched system.

The resulting plot of the voltage difference as a function of position in Fig. 14 suggests a catenary style distribution with a minimum occurring midway along the fingers. The amplitude rolls-off with increasing frequency due to the low pass response formed by the distributed capacitance and resistance. At 100 MHz a “dead-zone” emerges with zero voltage difference between adjacent electrodes suggesting a collapse in the DEP force perpendicular to the electrodes at that location. At higher frequencies a region forms between “dead-zones” with a voltage difference (150 MHz). These voltage variations imply that an electric field gradient exists parallel to the electrodes capable of inducing a DEP force.

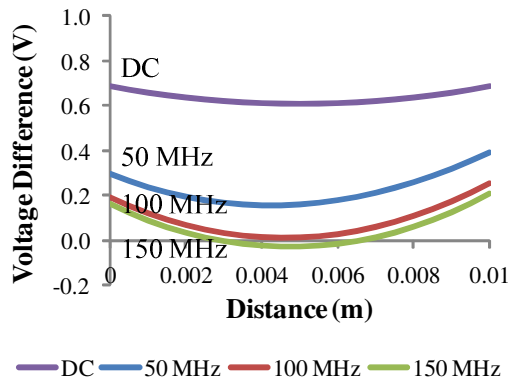


Fig. 14. Voltage difference along the 9-pair, 20:20 μ m device, 60mS/m Solution Conductivity

AC analysis of the voltage differences at the centre and edge of adjacent electrodes illustrate the factors influencing the formation of this catenary. Fig. 15(a) illustrates typical track and solution resistances with a catenary forming across the spectrum. Fig. 15(b), for an insulating solution, is matched at DC in the 50 Ω system but at higher frequencies the electrodes are loaded by their capacitance inducing a catenary.

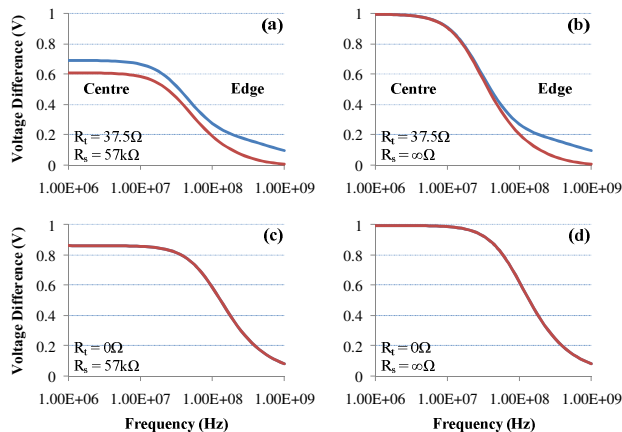


Fig. 15. Voltage difference spectra for various track and solution resistances. (a) Typical track and solution resistances, (b) An insulating solution, (c) Zero track resistance, (d) Infinite solution resistance and zero track resistance

A catenary is not observed for zero track resistance as the entire electrode is forced to the same voltage, shown in Fig. 15(c); the impedance match at DC is dependent upon the solution resistance. An infinite solution resistance in addition to zero track resistance results in the simple lumped capacitor response of Fig. 15(d). In practice, designs should operate below the cut-off frequency limiting the IDE electrode size and have sufficient track thickness to maximise the applied voltage difference.

It should be noted that the models reported in this paper do not account for dielectric dispersion or losses. The real permittivity of water remains constant up to 1 GHz with $\tan \delta$ increasing from 0.00485 to 0.0454 [9]. Using the proposed model it is relatively simple to include these effects. Track inductances may also be included although the improvement in accuracy is minor. Skin depth effects do not need to be considered over the frequency ranges concerned, the skin depth of platinum at 1 GHz being $\sim 5\mu$ m.

CONCLUSION

This paper has reported a method for modelling the impedance of interdigitated electrodes using a distributed RCR network with the capability of incorporating the effect of lossy dielectrics and track inductance. Impedance magnitude and phase responses for a range of solution conductivities, electrode array sizes and spacings have been compared with the proposed distributed RCR model and demonstrate a good agreement.

The physical implications identified in this paper using this model have been explored with respect to the resulting variation in the voltage difference between adjacent fingers along their length. Being able to readily model the impact of this voltage variation has real practical implications. One example where the application of the model may have been beneficial at the design stage is reported by Zhu et al [10] who observed the resultant motion of cells and their aggregation along spiral DEP tracks.

In summary the model and the results detailed in this paper are particularly important for the design of microelectrode structures intended for use in the dielectrophoretic manipulation of bio-particles, in particular those with thin electrode tracks or targeted at travelling wave DEP. The model provides a method of electrically simulating the complete experimental setup.

ACKNOWLEDGEMENTS

This work has been funded by the Wolfson Microelectronics Scholarship and the Institute for Integrated Systems.

REFERENCES

- [1] J. Voldman, "Electrical forces for microscale cell manipulation", *Annual Review of Biomedical Engineering*, vol. 8, pp. 425-454, 2006
- [2] R.S. Thomas, H. Morgan, and N.G. Green, "Negative DEP traps for single cell immobilisation", *Lab on a Chip*, vol. 9, pp. 1534-1540, 2009
- [3] R. Pethig, "Review Article – Dielectrophoresis: Status of the theory, technology and applications", *Biomicrofluidics*, vol. 4, 022811, 2010
- [4] P.L. Moran, "A Review of Distributed RC Thick Film Components", *Microelectronics International*, vol. 1, no. 1, pp. 17-21, 1993
- [5] F. Martorell, D. Mateo and X. Aragone, "Modelling and evaluation of substrate noise induced by interconnects", *IEE Proc-Comput. Digit. Tech.*, vol. 150, no. 5, September 2003
- [6] A.J. Walton, P.L. Moran, and N.G. Burrow, "The Steady State Analysis of Networks Containing Uniform and Non-Uniform Distributed Structures", *IEEE Transactions on Components, Hybrids and Manufacturing Technology*, vol. 10, no. 1, pp. 75-81, 1987
- [7] M.G. Buehler, S.D. Grant, and W.R. Thurber, "Bridge and Van der Pauw sheet resistors for characterizing the line width of conducting layers", *Journal of the Electrochemical Society – Solid State Technology*, vol. 125, no. 4, pp. 650-654, 1978
- [8] P. Van Gerwen et al., "Nanoscaled interdigitated electrode arrays for biochemical sensors", *Sensors and Actuators B*, vol. 49, pp. 73-80, 1998
- [9] T. Meissner, F.J. Wentz, "The complex dielectric constant of pure and sea water from microwave satellite observations", *IEEE Trans. Geoscience and Remote Sensing*, vol. 42, no. 9, pp. 1836-1849, September 2004
- [10] X. Zhu et al, "Electrode-rail dielectrophoretic assembly effect: formation of single curvilinear particle-chains on spiral microelectrodes", *Microfluidics and Nanofluidics*, vol. 9, no. 4-5, pp. 981-988, 2010

Dielectrophoretic Characterisation of Mammalian Cells above 100 MHz

Colin Chung^{1,4}, Martin Waterfall², Steve Pells³, Anoop Menachery¹, Stewart Smith¹ and Ronald Pethig^{1,4}

1. Institute for Integrated Micro & Nanosystems, School of Engineering, University of Edinburgh

2. Institute of Immunology & Infection Research, School of Biological Sciences, University of Edinburgh

3. MRC Centre for Regenerative Medicine, Chancellor's Building, Edinburgh

4. E-mail any correspondence to: colin.chung@ed.ac.uk or ron.pethig@ed.ac.uk

Abstract

Dielectrophoresis (DEP) is a label-free technique for the characterization and manipulation of biological particles - such as cells, bacteria and viruses. Many studies have focused on the DEP cross-over frequency f_{xo1} , where cells in a non-uniform electric field undergo a transition from negative to positive DEP. Determination of f_{xo1} provides a value for the membrane capacitance from the cell diameter, the means to monitor changes in cell morphology and viability, and the information required when devising DEP cell separation protocols. In this paper we describe the first systematic measurements of the second DEP cross-over frequency f_{xo2} that occurs at much higher frequencies. Theory indicates that f_{xo2} is sensitive to the internal dielectric properties of a cell, and our experiments on murine myeloma cells reveal that these properties exhibit temporal changes that are sensitive to both the osmolality and temperature of the cell suspending medium.

Keywords: Biodielectrics, Cytoplasm Conductivity, Dielectrophoresis, Myeloma Cells, Nucleus conductivity.

Introduction

Dielectrophoresis (DEP) is a technique that has been used to characterize and sort cells based on their distinct dielectric properties [1-3]. It refers to a force induced on polarisable particles in non-uniform electric fields. This force is proportional to both the field gradient and the real part of the particle's effective polarisability (per unit volume), described by the Clausius-Mossotti function:

$$\mathbf{p} = \frac{\epsilon_p^* - \epsilon_m^*}{\epsilon_p^* + 2\epsilon_m^*} \quad (1)$$

Here, ϵ_p^* and ϵ_m^* refer to the complex effective permittivities of the particle and suspending medium, respectively. Of particular interest to those studying the DEP properties of viable mammalian cells is measurement of the so-called DEP cross-over frequency - where the DEP force acting on a cell transitions from a negative to positive polarity. Measurement of this frequency and the cell diameter provides a determination of membrane capacitance and is typically observed in the 100~300 kHz range [2]. The majority of reported DEP studies have been limited to a maximum frequency of ~30 MHz, primarily

reflecting the limitation of most commercially available signal generators in delivering the required voltage (up to ~12 V_{pk-pk}) above this frequency. Under appropriate experimental conditions, a second cross-over is expected to occur at frequencies beyond 100 MHz, measurement of which is expected to reveal information regarding the dielectric properties of the cell interior [3]. To our knowledge no systematic investigation of this high-frequency DEP cross-over has been reported in the literature. In this paper we describe the circuitry and electrical load modeling for an interdigitated electrode array used to obtain, for the first time, measurements of this cross-over for mammalian cells as a function of time, suspending medium osmolality and temperature.

Multi-Shell Dielectric Model of a Cell

The effective dielectric properties of a mammalian cell can be modelled by applying the multi-shell method first described by Irimajiri [4]. The nucleoplasm, nuclear membrane, cytoplasm and cytoplasm membrane are represented as concentric spherical shells with distinct radii and dielectric properties (defined by their permittivity and conductivity). By successively merging these shells together an expression for the effective complex permittivity of an entire cell can be produced. Asami *et al* [5] used this method to determine the dielectric properties of mouse lymphocytes, based on impedance measurement of their suspensions. Inserting the dielectric parameters for these lymphocytes into equation 1 gives the DEP frequency response shown in figure 1.

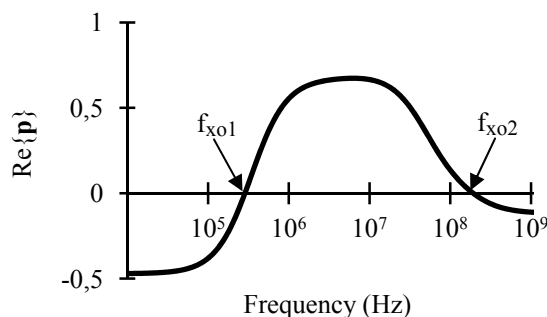


Fig.1: Frequency variation of the real part of the Clausius-Mossotti function for lymphocytes, derived from published dielectric data [5]. The DEP force is proportional to this function and shows two cross-over frequencies, f_{xo1} and f_{xo2} .

We use the form of figure 1 as a predictive guide to the DEP response of mammalian cells. The frequency regions exhibiting negative and positive DEP force correspond respectively to repulsion from, and attraction to, regions of high electric field concentration that occur close to the edge of electrodes. Between 100 kHz and 1 MHz this force transitions from negative to positive at the first (low frequency) cross-over frequency, f_{xo1} . The value of f_{xo1} depends upon the cytoplasm membrane capacitance and resistance, the cell diameter and the suspending medium conductivity [2, 6]. Determination of f_{xo1} for different cells and cell states has been the principle parameter for characterizing and sorting cells by DEP. In figure 1 it can also be seen that, at a frequency between 100 MHz and 1 GHz, a second cross-over, f_{xo2} , is predicted to occur. Above 100 MHz the membrane capacitive reactance should effectively short out the membrane resistance, so that the electric field penetrates into the cell interior [3]. The value of f_{xo2} for viable cells is thus predicted to depend on the intracellular dielectric properties.

A general expression for determining the DEP cross-over frequencies is derived by equating the real part of equation 1 to zero. This yields equation 2, where ϵ_m and σ_m represent the permittivity and conductivity of the suspending medium; ϵ_c and σ_c the effective permittivity and conductivity of the cell [7]:

$$f_{xo} = \frac{1}{2\pi} \sqrt{\frac{(\sigma_m - \sigma_c)(\sigma_c + 2\sigma_m)}{(\epsilon_c - \epsilon_m)(\epsilon_c + 2\epsilon_m)}} \quad (2)$$

The customary practice is to employ the DC approximations derived by Schwan [8] for the low-frequency effective values of σ_m and ϵ_m – namely $\sigma_m = rG_m$ and $\epsilon_m = rC_m$, where G_m and C_m are the conductance and capacitance, respectively, of the cell membrane, and r is the cell radius. This leads to a simple expression for f_{xo1} , from which values of the membrane capacitance and conductance can be derived [2, 6]. Above ~1 MHz, and certainly for the high frequencies of relevance to the work reported here, the DC approximations are not applicable. Instead, the frequency dependencies of the effective permittivity and conductivity of a cell must be taken into account. This can be accomplished using the multi-shell model, described in the Appendix, which with simplifying assumptions yields equations 3 and 4 that can be used to determine f_{xo2} :

$$\epsilon_c \approx \epsilon_{cp} \frac{2(1-\nu) + \frac{\epsilon_{np}}{\epsilon_{cp}}(1+2\nu)}{(2+\nu) + (1-\nu)\frac{\epsilon_{np}}{\epsilon_{cp}}} \quad (3)$$

$$\sigma_c \approx \sigma_{cp} \frac{2(1-\nu) + \frac{\epsilon_{np}}{\epsilon_{cp}}(1+2\nu)}{(2+\nu) + (1-\nu)\frac{\epsilon_{np}}{\epsilon_{cp}}} - \left[\frac{\epsilon_{np}\sigma_{cp} - \epsilon_{cp}\sigma_{np}}{\epsilon_{cp}} \cdot \frac{9\nu}{\left[(2+\nu) + (1-\nu)\frac{\epsilon_{np}}{\epsilon_{cp}} \right]^2} \right] \quad (4)$$

From equations 3 and 4 we find that the high frequency DEP cross-over f_{xo2} is determined by the internal cell dielectric parameters, namely the nucleoplasm permittivity (ϵ_{np}), nucleoplasm conductivity (σ_{np}), cytoplasm permittivity (ϵ_{cp}), cytoplasm conductivity (σ_{cp}) and nucleus volume fraction ($\nu = \text{nucleus volume/cell volume}$). Based on dielectric studies of mouse lymphocyte suspensions, Asami *et al* [5] derived the following dielectric values: nucleoplasm relative permittivity 52; nucleoplasm conductivity 1.35 S/m; cytoplasm relative permittivity 60; cytoplasm conductivity 0.32 S/m. Substituting these values into equations 2, 3 and 4, for the medium conductivity of 33 mS/m used in our experiments, we can predict a value for f_{xo2} in the range 90 to 320 MHz depending on the nucleus volume fraction.

Materials and methods

Interdigitated electrodes are commonly used in DEP experiments, but understanding their behaviour above 100 MHz requires accurate modelling of the electrical load being driven by the signal source. An overview of the electrical system used to conduct f_{xo2} measurements is shown in figure 2. The signal generator provides a sine wave between 2 MHz and 500 MHz at up to 2 V_{pk-pk}. This is fed to a high power amplifier with ~17.5 dB gain over this range when terminated into a 50Ω load. A 50Ω resistor in parallel with the DEP electrodes is used to approximate this termination, connected by a short ¼ metre length of co-axial cable. This prevents reflection issues with longer cables that reduce bandwidth. The interdigitated structure is fabricated from 100nm thick platinum deposited onto a Pyrex substrate, patterned using standard photolithographic techniques and etched by argon plasma milling.

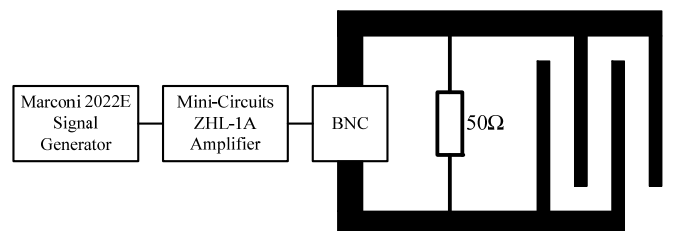


Fig.2: Schematic of the electrical system used to investigate the DEP properties of cells above 100 MHz.

Two interdigitated electrode ‘fingers’ are shown in figure 3, with a signal being applied to the left pad and grounded on the right pad. An example of a current path is displayed in red, flowing from the signal pad and along the top finger track. At some point this current crosses through the suspending medium to the bottom finger, along the remaining track to ground. A continuum of such current paths exist along the overlap length (L_O), determined by track resistance, suspending medium conductivity and capacitive coupling between the fingers.

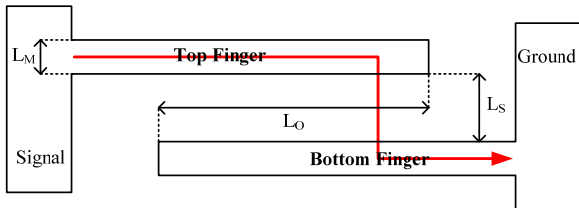


Fig.3: Interdigitated electrode fingers and example current path.

The distributed RCR network of figure 4 has been used to model these parameters. Track resistance (R_t), suspending medium resistance (R_s) and parallel track capacitance (C) components were used for sections of length $\Delta x - L_O$ divided by the number of sections. Sheet resistance from cross bridge resistor measurements was used to estimate R_t . Values for R_s and C per unit length along the fingers were determined by finite element models of a cross section in COMSOL Multiphysics software. The accuracy of this distributed network increases as Δx approaches zero, but beyond five sections the differences between impedance spectra were observed to be marginal. Ten sections were used to provide sufficient detail for voltage distribution plots.

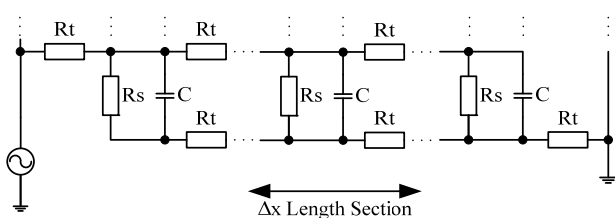


Fig.4: Distributed RCR interdigitated electrode model.

The voltage difference between the adjacent fingers creates the non-uniform electric field E , inducing a DEP force upon the cells. The DEP force is proportional to ∇E^2 , and needs to be maintained along the entire electrode structure at all frequencies of interest to ensure that cells, which have transitioned from negative to positive DEP, become attracted to the electrode edge in a practical time period, typically less than 10 seconds. At the 20 μ m electrode scale, for the purpose of DEP cross-over measurement, a minimum voltage difference of 3.5 V_{pk-pk} was found to be sufficient. The signal generator was adjusted for the amplifier to output 5 V_{pk-pk} when terminated into 50 Ω .

Specifications for two examples of interdigitated electrodes are given in table 1, fabricated from 50 and 100 nm thick platinum.

	Design 1	Design 2	
Number of Fingers	16	16	
Finger Overlap (L_O)	20	2	mm
Finger Width (L_w)	20	25	μ m
Finger Spacing (L_s)	20	35	μ m
Medium Conductivity	33	33	mS/m
Sheet Resistance	3.6	1.8	Ω/\square
Section Length (Δx)	2	0.2	mm
Section Medium Resistance (R_s)	30	340	k Ω
Section Track Resistance (R_t)	28.8	14.4	Ω
Section Track Capacitance (C)	1500	67	fF
Area	12.8	1.9	mm ²

Tab.1: Model parameters for two electrode design examples.

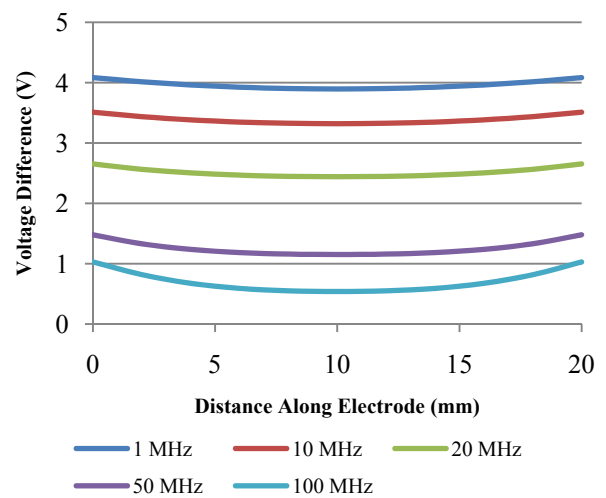


Fig.5: Voltage difference between adjacent fingers (Design 1).

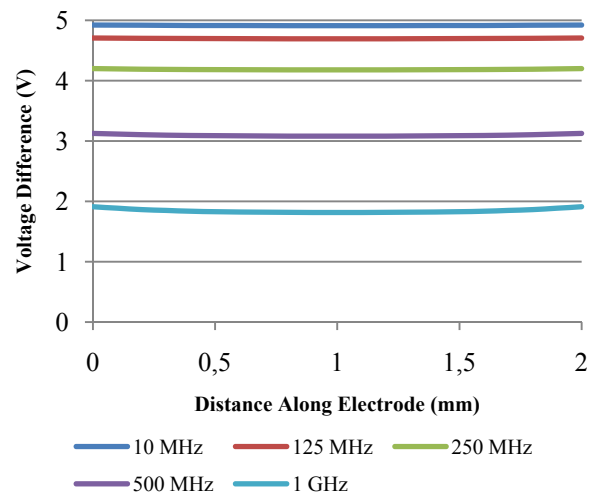


Fig.6: Voltage difference between adjacent fingers (Design 2).

The voltage difference profiles shown in figure 5 take the form of catenaries due to the resistive and capacitive loading along the length of the electrode fingers. The bandwidth, defined by a minimum voltage difference of 3.5V, is only 8 MHz and far below the upper range of 320 MHz predicted for f_{x02} . Electrode design 2 shown in table 1 features an increased finger width and spacing, which

reduces the finger overlap, and double the platinum thickness. As shown in figure 6, this flattens the voltage difference profile and increases the DEP operating bandwidth to 400 MHz. However, this is achieved at the cost of significantly reducing the electrode area. Electrode design 2 was used for the DEP studies described here.

Cell Culture

Murine myeloma SP2/O cells were grown in RPMI-1640 medium supplemented with 100 units/mL penicillin-streptomycin and 10% foetal calf serum (FCS). The cells were grown in suspension with 5% CO₂ in air at 37°C to a density of 1x10⁶ cells/mL. An iso-osmotic cell suspension medium for DEP studies was prepared by adding 3 g/L glucose and 100 g/L sucrose to DI water. Conductivity was adjusted to 33 mS/m with PBS, verified using a conductivity meter (Oakton CON 510) and the pH adjusted to 7.4 with NaOH/HCl. The osmolality of the final medium was 310 mOsm/kg, verified with an osmometer (Advanced Instruments Inc. Model 3300). DEP media of osmolality 250, 390, 435 and 480 mOsm/kg were also prepared by adjusting the sucrose concentration. The SP2/O cells were centrifuged (100g, 5 minutes) and washed twice in 10 mL of the DEP media, before final suspension at a density of 1x10⁷ cells/mL for analysis. The electrodes were mounted in an inverted microscope (Meiji TC5100). By focusing on the electrode plane discrimination between cells undergoing negative DEP (out-of-focus or between the electrodes) and positive DEP (in-focus at electrode edges) was possible.

Results

Figure 7 shows the distribution of values for the high-frequency crossover, f_{x02} , with a population sample of 418 SP2/O cells suspended in a DEP medium of osmolality 310 mOsm/kg. Under these conditions the vast majority of cells were observed to undergo the transition from negative to positive DEP when sweeping down the frequency range.

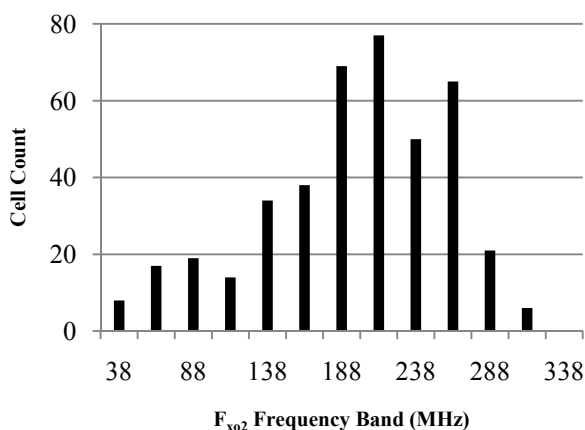


Fig.7: f_{x02} spectrum for SP2/O cells (n=418) suspended in DEP medium with 310 mOsm/L osmolality and 33 mS/m conductivity.

The mean value of f_{x02} for the cell populations shown in figure 7 is 195 MHz with a standard deviation of 63 MHz. An interesting finding, shown in figure 8, is the reduction of the f_{x02} values as a function of time after their suspension in the DEP solution.

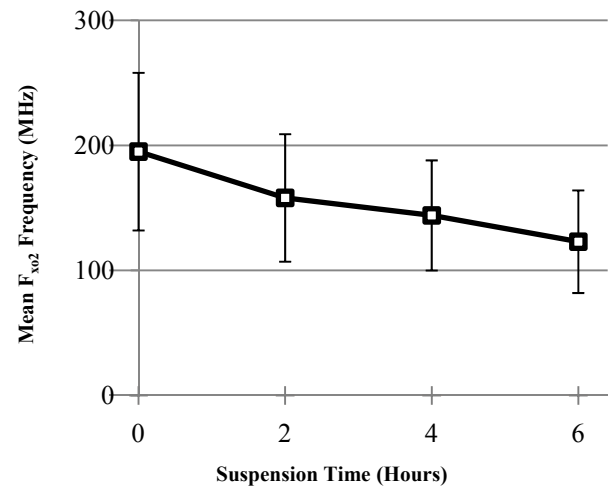


Fig.8: Mean f_{x02} frequency for SP2/O cells suspended in DEP medium with 310 mOsm/L osmolality and 33 mS/m conductivity over 6 hours. Single standard deviation bars shown.

A corresponding temporal change in the low-frequency cross-over, f_{x01} , was not observed, and is not expected unless the cell state is deliberately altered by adding chemical agents to the solution known to induce cell activation or apoptosis for example [2, 9].

The reduction in f_{x02} over time was found to be a function of temperature, as shown in figure 9. Cell suspensions were held in a temperature controlled water bath (situated in a refrigerated room for the 10°C run) between measurements. The rate of frequency reduction based on the first two hours clearly increases with temperature, more than doubling in rate (~2.4x) for increases of 10°C between 21°C and 37°C.

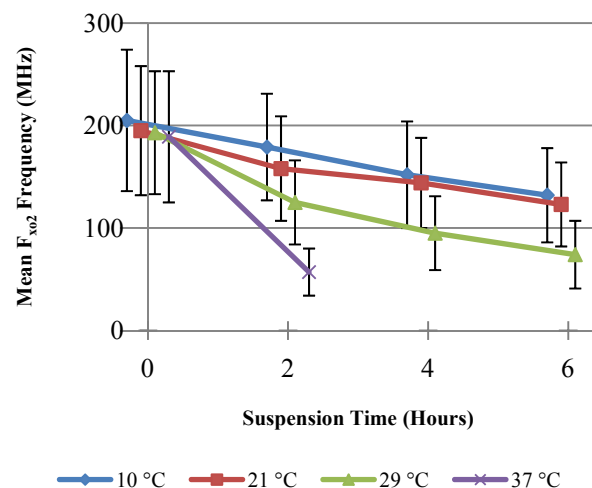


Fig.9: Mean f_{x02} frequency for SP2/O cells suspended in 310 mOsm DEP medium at 10°C, 21°C, 29°C and 37°C over 6 hours. Single standard deviation bars are shown.

At 37°C the rate of fall of f_{x02} was so great that accurate determination of it became difficult after two hours. The osmolality of the suspending solution was also found to influence the mean f_{x02} value, as shown in figure 10. The higher osmolality solutions tended to result in lower values of f_{x02} for the same period of cell suspension in the DEP solution.

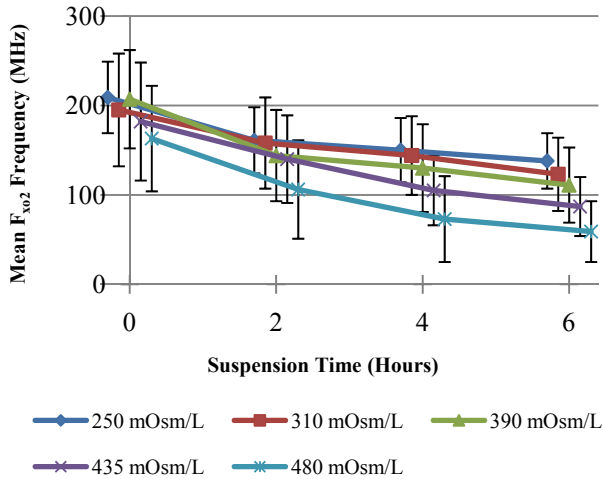


Fig.10: Mean f_{x02} frequency for SP2/O cells suspended in DEP media of 250, 310, 390, 425 and 480 mOsm/L. Standard deviation bars are shown.

Discussion

The distribution of high frequency cross-over, f_{x02} , values for SP2/O cells shown in figure 7 was obtained by slowly sweeping down from an applied signal frequency of 400 MHz. At this initial frequency all of the cells were observed to levitate above the electrode plane under the action of negative DEP, but on proceeding below 325 MHz subpopulations of the cells were attracted to the electrode edges by positive DEP. This behaviour confirmed that the predicted high-frequency DEP cross-over shown in figure 1 for mammalian cells can be observed under our experimental conditions, and that the designed electronics and electrodes are capable of exploring this high frequency region of the DEP spectrum. The mean f_{x02} value of 195 MHz shown in figure 7 falls well within the 90 MHz to 320 MHz range of values we predicted using the cell dielectric parameters given by Asami *et al* [5]. This provides a degree of validation for both the multi-shell model of a cell and our use of the extracted dielectric parameters. Our theoretical analysis - yielding equations 3 and 4 for the effective cell permittivity and conductivity at high frequencies - indicates that f_{x02} is sensitive to the effective dielectric properties of the cell interior. This distinguishes f_{x02} from the lower frequency DEP cross-over at f_{x01} which is sensitive to the suspending medium conductivity, the cell radius, and the effective permittivity and conductivity of the plasma membrane [2, 6, 9]. Extending DEP measurements

to include analyses of both f_{x01} and f_{x02} should therefore provide enhanced characterisation of the dielectric properties of cells, and enable more efficient manipulations of cells (e.g., subpopulation enrichment or selective separation) using DEP techniques.

Equations 3 and 4 inform us that the high frequency cross-over, f_{x02} , is determined by the permittivity and conductivity of both the nucleoplasm and cytoplasm, as well as the nucleus volume fraction. The nucleus volume fraction is known to change with cell cycle [10], and could be one factor responsible for the relatively wide distribution of f_{x02} values shown in figure 7. The relationships of the dielectric parameters to specific biological features of a cell are at present not clear, but an insight into the relative sensitivity of f_{x02} to them can be obtained.

	Permittivity	Conductivity
Medium	31%	0%
Nucleus	8%	13%
Cytoplasm	6%	1%
Nucl. Vol. Fraction		8%

Tab.2: Sensitivity of f_{x02} to dielectric parameters based on Asami *et al* [5] for a nucleus volume fraction of 0.7. The change in frequency for a $\pm 10\%$ variation in each parameter is normalised to the base f_{x02} value of 195 MHz.

Table 2 provides a measure of sensitivity in f_{x02} to each dielectric parameter based on the modelled values undergoing a $\pm 10\%$ variation. A nucleus volume fraction of 0.7 is used here with values approaching ~ 0.9 being typical of lymphocytes which are associated with our SP2/O cells [11]. Finally, the intracellular conductivity is scaled for a base f_{x02} value of 195 MHz to which these variations are normalised.

F_{x02} is unaffected by small changes in medium conductivity although a large increase, beyond ~ 300 mS/m, results in a collapsed DEP profile with no cross-over occurring. F_{x02} is most sensitive to the medium permittivity, a parameter which is dependent upon temperature but regulated precisely in these experiments [12]. The conductivity, permittivity and volume fraction of the nucleus are the most likely causes for the temporal change displayed in figure 8. A reduction in f_{x02} of the magnitude observed requires the effective conductivity of the cell interior to reduce by a factor of nearly 40%. This represents a significant alteration in cell state, and could be directly related to the fact that for our DEP experiments the cells were suspended in low ionic strength solutions, commonly used for the determination of f_{x01} , for example [2, 6, 9].

Processes that could be responsible for the temporal reduction in f_{x02} reported here could include the leakage of

ions, such as potassium, down their concentration gradients to the cell exterior, or the osmotic flux of water across the plasma membrane [13]. Such changes would not influence measurements of the lower frequency DEP cross-over at f_{x01} , unless they lead to significant changes in cell volume, morphology or viability [2, 3, 9]. Determination of the temporal behaviour of f_{x02} may prove to be a sensitive indicator of loss of cell viability, and a useful tool to be used when formulating the chemical composition of cell suspending media to be used in DEP studies [14].

Q_{10} is a widely used quantity in the study of metabolic activity and is the factor by which a 10°C increase in temperature alters a reaction rate [15, 16]. The temperature dependence results shown in figure 9 suggest Q_{10} is approximately 2.4 for the process in question, between 21°C and 37°C; and within the typical range for biological processes. Based on this data, the Arrhenius plot of figure 11 provides further detail regarding this process.

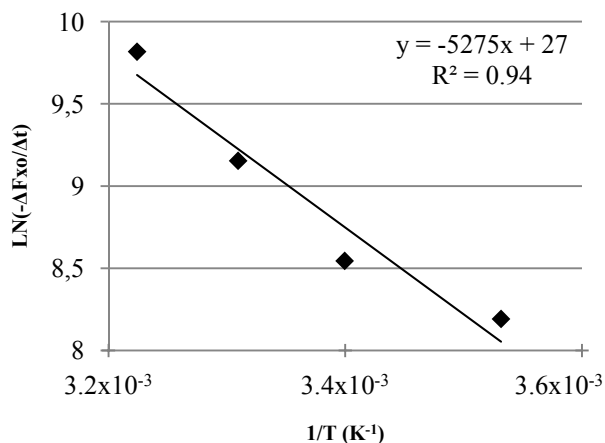


Fig.11: Arrhenius plot for the initial rate of mean f_{x02} roll-off.

The linear fit of the data gives an activation energy of ~44 kJ/mol for the underlying process leading to the temporal behaviour of the high frequency DEP cross-over. We note that the temperature dependence of the coefficient of water self-diffusion through lipid multilayers is also described by the Arrhenius law, with an apparent activation energy of ~41 kJ/mol [17], a coincidence which requires further study.

Finally, the trend shown in figure 10, of a decrease in f_{x02} with increasing osmolality of the cell suspending medium, suggests an associated decrease in internal cell conductivity and/or permittivity. The mechanism for this may be related to that of the aforementioned temporal reduction in frequency, however the initial rate of reduction appears to be unaffected by the change in osmotic pressure.

Conclusions

An electrical system comprising interdigitated electrodes and signal generator has been designed and tested to

observe, for the first time, cells undergoing DEP cross-over in the predicted frequency range above 100 MHz. Electrical modelling of the electrodes based on a distributed RCR network allowed us to determine the limiting factors for high frequency operation. Capacitive loading is the most critical factor, and results in an imposed limitation of the electrode area. The mean f_{x02} value of 195 MHz observed for murine myeloma SP2/0 cells agrees well with that predicted using the cell interior dielectric properties derived from impedance studies of lymphocytes [5]. This suggests that the internal dielectric properties derived from lymphocytes, and the multi-shell model of a cell, may be applicable for the study of other mammalian cell types using the electrodes and electronics described here.

The theory indicates that the high frequency DEP cross-over at f_{x02} is sensitive to changes in the dielectric properties of the cell interior, and especially those associated with the nucleus and the relative size of the nucleus to the cell volume. An interesting finding, and one not predicted from the large number of reported studies of the low frequency DEP cross-over at f_{x01} , is the rapid reduction of f_{x02} with time. At present we do not understand the changes of cell state that are responsible for this behaviour. Experiments to gain a further understanding are currently in progress in our laboratories. One important conclusion to be drawn is that measurements of both the low and high frequency DEP cross-over, at f_{x01} and f_{x02} , are likely to provide a better indicator of any changes in cell state during DEP experiments than through determination of f_{x01} alone. This could be of particular importance for DEP studies and manipulations of stem cells [18].

Acknowledgements

The authors thank Dr Martin Reekie for helpful discussions. This work was supported by a Wolfson Microelectronics Scholarship awarded to C.C., and the Edinburgh Research Partnership in Engineering and Mathematics (ERPem).

References

1. Voldman J. Electrical Forces for Microscale Cell Manipulation. *Annu. Rev. Biomed. Eng.* 2006;8:p. 425-54. doi: 10.1146/annurev.bioeng.8.061505.095739
2. Pethig R, Talary MS. Dielectrophoretic Detection of Membrane Morphology Changes in Jurkat T-Cells Undergoing Etoposide-Induced Apoptosis. *IET Nanobiotechnol.* 2007;1:p. 2-9. doi: 10.1049/iet-nbt:20060018
3. Pethig R. Review Article – Dielectrophoresis: Status of the Theory, Technology and Applications. *Biomicrofluidics* 2010;4:022811. doi: 10.1063/1.3456626
4. Irimajiri A. A Dielectric Theory of “Multi-Stratified Shell” Model with its Application to a Lymphoma Cell. *J. Theor. Biol.* 1979;78:p. 251-69. doi: 10.1016/0022-5193(79)90268-6

5. Asami K, Takahashi, Y, Takashima S. Dielectric Properties of Mouse Lymphocytes and Erythrocytes. *Biochim. Biophys. Acta* 1989;1010:p. 49-55. doi: 10.1016/0167-4889(89)90183-3
6. Pethig R, Jakubek LM, Sanger RH, Heart E, Corson ED, Smith PJS. Electrokinetic Measurements of Membrane Capacitance and Conductance for Pancreatic Beta-cells. *IEE Proc. Nanobiotechnol.* 2005;152:6:p. 189-193. doi: 10.1049/ip-nbt:20050040
7. Jones T. *Electromechanics of Particles.* Cambridge University Press; 1995. p. 56. doi: 10.1017/CBO9780511574498
8. Schwan, H.P., *Electrical properties of cells and tissues,* *Adv. Biol. Med. Phys.,* 1957, 5, pp. 147-209.
9. Wang X, Becker FF, Gascoyne PRC. Membrane Dielectric Changes Indicate Induced Apoptosis in HL-60 Cells More Sensitively Than Surface Phosphatidylserine Expression or DNA Fragmentation. *Biochim. Biophys. Acta* 2002;1564:p. 412-420. doi: 10.1016/S0005-2736(02)00495-9
10. Turgeon ML. *Clinical Hematology: Theory and Procedures.* Lippincott, Williams & Wilkins:2005. p. 67.
11. *CAP Proficiency Testing Handbook:1995. Serton 2, Hematology, Coagulation, Clinical Microscopy.*
12. Catenaccio A, Daruich Y, Magallanes C. Temperature Dependence of the Permittivity of Water. *Chem. Phys. Ltrrs* 2003;367:p. 669-671. doi: 10.1016/S0009-2614(02)01735-9
13. Ho SN. Intracellular Water Homeostasis and the Mammalian Cellular Osmotic Stress Response. *J. Cell. Phys* 2006;206:p. 9-15. doi: 10.1002/jcp.20445
14. Puttaswamy SV, Sivashankar S, Chen RJ, Chin CK, Chang HY, Cheng HL. Enhanced Cell Viability and Cell Adhesion Using Low Conductivity Medium for Negative Dielectrophoretic Cell Patterning. *Biotechnol. J.* 2010;5:p. 1005-1015. doi: 10.1002/biot.201000194
15. Lehninger AL. *Biochemistry.* 2nd ed. Worth Publishers, Inc; 1975. p. 196.
16. Bekku YS, Nakatsubo T, Kume A, Adachi M, Koizumi H. Effect of Warming on the Temperature Dependence of Soil Respiration Rate in Arctic, Temperate and Tropical Soils. *Appl. Soil Ecol.* 2003;22:p. 205-210. doi: 10.1016/S0929-1393(02)00158-0
17. Khakimova AM, Rudakova MA, Doroginitskiĭ MM, Filippov AV. An NMR Study of the Temperature Dependence of the Coefficient of Water Self-Diffusion through Lipid Bilayer Membranes. *Biofizika.* 2008;53(2):p. 271-80.
18. Pethig R, Menachery A, Pells S, De Sousa P. *Dielectrophoresis: A Review of Applications for Stem Cell Research,* *J. Biomed. Biotechnol.,* 2010;182581 (7 pages). doi: 10.1155/2010/182581

	Radius (r) / Thickness (t)	Complex Permittivity
Nucleoplasm	r_{np}	ϵ_{np}^*
Nuclear Envelope	t_{ne}	ϵ_{ne}^*
Cytoplasm	r_{cp}	ϵ_{cp}^*
Cell Membrane	t_{mb}	ϵ_{mb}^*

Each complex permittivity is composed of permittivity, ϵ , and conductivity, σ , with angular frequency, ω , and imaginary unit, i , by the relationship:

$$\epsilon_{xx}^* = \epsilon_{xx} - \frac{i}{\omega} \sigma_{xx}$$

We define the cell's effective permittivity, ϵ_c^* , in terms of the following intermediate parameters, E_x , and volume fractions, v_x :

$$\epsilon_c^* = \epsilon_{mb}^* \frac{2(1-v_1)+(1+2v_1)E_1}{(2+v_1)+(1-v_1)E_1} \quad v_1 = \left(1 - \frac{t_{mb}}{r_{cp}}\right)^3$$

$$E_1 = \frac{\epsilon_{cp}^* \frac{2(1-v_2)+(1+2v_2)E_2}{(2+v_2)+(1-v_2)E_2}}{\epsilon_{mb}^*} \quad v_2 = \left(\frac{r_{np}}{r_{cp}-t_{mb}}\right)^3$$

$$E_2 = \frac{\epsilon_{ne}^* \frac{2(1-v_3)+(1+2v_3)E_3}{(2+v_3)+(1-v_3)E_3}}{\epsilon_{cp}^*} \quad v_3 = \left(1 - \frac{t_{ne}}{r_{np}}\right)^3$$

$$E_3 = \frac{\epsilon_{np}^*}{\epsilon_{ne}^*}$$

Real solutions for equation 2 for a suspending medium of permittivity, ϵ_m , and conductivity, σ_m , must satisfy the condition [7]:

$$\frac{\sigma_m - \sigma_c}{\epsilon_c - \epsilon_m} > 0$$

Asami *et al* [5] derived the following dielectric parameters for mouse lymphocytes: $r_{np} = 2.6 \mu\text{m}$; $t_{ne} = 40 \text{ nm}$; $r_{cp} = 2.9 \mu\text{m}$; $t_{mb} = 7 \text{ nm}$; $\epsilon_{np} = 52\epsilon_0$; $\epsilon_{ne} = 28\epsilon_0$; $\epsilon_{cp} = 60\epsilon_0$; $\epsilon_{mb} = 6.8\epsilon_0$; $\sigma_{np} = 1.35 \text{ S/m}$; $\sigma_{ne} = 6 \text{ mS/m}$; $\sigma_{cp} = 0.32 \text{ S/m}$; $\sigma_{mb} = 3.2 \mu\text{S/m}$. Substituting these values into the expressions above, with $\sigma_m = 33 \text{ mS/m}$ and $\epsilon_m = 80.1\epsilon_0$, yields the effective conductivity and relative permittivity spectra of figure A1. The form of these spectra imply that real solutions for equation 2 exist below 5 MHz and above 120 MHz. Applying the simplification that $t_{ne} \approx 0$, and eliminating terms divided by ω^2 we obtain a simplified, high-frequency, expression for E_2 :

Appendix

Calculating the DEP cross-over frequency using equation 2 requires both the effective permittivity and effective conductivity of the particle. These need to account for both geometric and dielectric properties which, for suspended mammalian cells, may be modelled by a multi-shelled sphere [4, 5]. Defining first these properties for each shell consisting of the following elements:

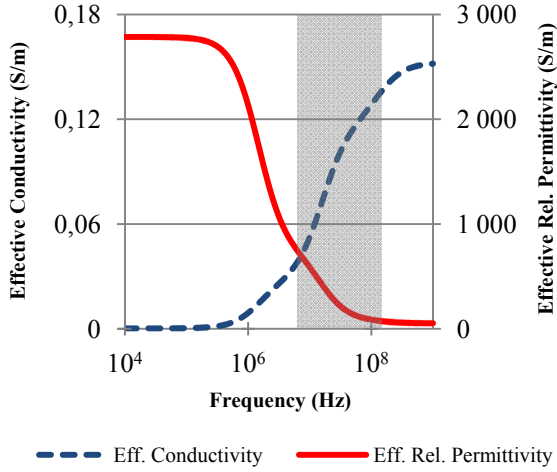


Fig.A1: Effective conductivity and relative permittivity of a cell based on the dielectric data of Asami *et al* [5]. The dark band indicates where real solutions for the DEP cross-over do not exist.

$$E_2 = \frac{\epsilon_{cp}\epsilon_{np} + \frac{\sigma_{cp}\sigma_{np}}{\omega^2}}{\epsilon_{cp}^2 + \frac{\sigma_{cp}^2}{\omega^2}} + i \frac{\frac{\epsilon_{np}\sigma_{cp} - \epsilon_{cp}\sigma_{np}}{\omega}}{\epsilon_{cp}^2 + \frac{\sigma_{cp}^2}{\omega^2}}$$

$$\approx \frac{\epsilon_{np}}{\epsilon_{cp}} + i \frac{\epsilon_{np}\sigma_{cp} - \epsilon_{cp}\sigma_{np}}{\omega\epsilon_{cp}^2} \stackrel{\text{def}}{=} X_1 + iX_2$$

For the sake of clarity we define the real and imaginary parts, respectively, as X_1 and X_2 here. Substituting these into E_1 with $t_{mb} = 0$ yields an expression for ϵ_c^* where terms involving $X_2^2 \propto \omega^{-2}$ can be eliminated.

$$\epsilon_c^* \approx \epsilon_{cp}^* \left[\frac{2(1 - v_2) + X_1(1 + 2v_2)}{(2 + v_2) + (1 - v_2)X_1} \right]$$

$$+ i \frac{X_2(1 + 2v_2)[(2 + v_2) + (1 - v_2)X_1]}{[(2 + v_2) + (1 - v_2)X_1]^2}$$

$$- i \frac{X_2(1 - v_2)[2(1 - v_2) + X_1(1 + 2v_2)]}{[(2 + v_2) + (1 - v_2)X_1]^2}$$

Expanding out ϵ_{cp}^* , substituting back for X_1 and X_2 and rearranging ϵ_c^* into the general form of complex permittivity gives:

$$\epsilon_c^* \approx \epsilon_{cp} \frac{2(1 - v_2) + \frac{\epsilon_{np}}{\epsilon_{cp}}(1 + 2v_2)}{(2 + v_2) + (1 - v_2)\frac{\epsilon_{np}}{\epsilon_{cp}}}$$

$$- i \left[\frac{\sigma_{cp}}{\omega} \cdot \frac{2(1 - v_2) + \frac{\epsilon_{np}}{\epsilon_{cp}}(1 + 2v_2)}{(2 + v_2) + (1 - v_2)\frac{\epsilon_{np}}{\epsilon_{cp}}} \right]$$

$$- \epsilon_{cp} \frac{\epsilon_{np}\sigma_{cp} - \epsilon_{cp}\sigma_{np}}{\omega\epsilon_{cp}^2} \cdot \frac{9v_2}{\left[(2 + v_2) + (1 - v_2)\frac{\epsilon_{np}}{\epsilon_{cp}} \right]^2}$$

Comparing the coefficients with the general form for complex permittivity, the real part of this expression corresponds to the effective cell permittivity of equation 3. The imaginary part, multiplied by $-\omega/i$, corresponds to the effective cell conductivity of equation 4.